Studies of a prototype of an Electro-Optic Beam Position Monitor at the CERN Super Proton Synchrotron

Alberto Arteche González

Department of Physics

Royal Holloway, University of London

A thesis submitted to the University of London for the degree of Doctor of Philosophy

March, 2018

Declaration

I confirm that the work presented in this thesis is my own. Where information has been derived from other sources, I confirm that this has been indicated in the document.

Signed:

Date:

Abstract

The commissioning, development and results of an Electro-Optic Beam Position Monitor (EO-BPM) prototype installed in the CERN Super Proton Synchrotron (SPS) are reported in this thesis. This technology is a diagnostic technique that aims to be capable of measuring the transverse intra-bunch position in 1 ns proton bunches with a time resolution less than 100 ps, in order to achieve the requirements of the High Luminosity Large Hadron Collider (HL-LHC).

The thesis details the mechanism that generates the electro-optic signal that results from the interaction of the Coulomb field with a lithium niobate crystal via the Pockels effect. The theoretical background leads to the introduction of the EO-BPM concept based on vacuum-integrated EO crystals in the context of the SPS machine. In conjunction with this, an analytical framework has been developed to estimate the EO pickup signal for the SPS beam parameters. This study also presents two different opto-mechanical pickup designs, pickup zero and one. Numerical electromagnetic simulations have been carried out to predict, more precisely, the performance of both proposals in relation to the modulating field. In addition, a detailed description of the experimental optical setup adjacent to the prototype and the acquisition system is presented. Further simulations have been applied to incorporate the response of the detection system to calculate the final signal delivered by the prototype. Results from measurements in December 2016 for pickup zero and over the summer 2017 for pickup one are reported and constitute the first detection ever of a proton beam by electro-optic means. Analysis verifies that the signal at a radial distance of 66.5 mm scales correctly as a function of the beam conditions and the pickup model, and is also sensitive to the beam transverse position. These results provide the first proof of concept, in preparation for future developments of the technology towards the LHC upgrade.

Acknowledgements

First and foremost, I would like to start by thanking my supervisor, Dr. Stephen Gibson for the continuous support throughout my research and holding his laugher in the rare occasions I mispronounced or mixed up, in funny combinations, some english words. Even in the toughest moments, his encouragement and help made possible to complete this work. Besides my advisor, I am too very grateful to my colleges of the EO-BPM team at Royal Holloway, with special mention to Alessio Bosco for his good handiness with optics and good skills filing off delicate crystals under pressure, the LabVIEW wizard Gary Boorman for dedicating some of his talent to this project, and Sophie Bashforth, for taking over this exciting idea, even though I abandoned her once alone down in the tunnel.

I would also like to express my gratitude to our comrade-in-arms at CERN, specially to Thibaut Lefévre for his patient guidance, and to Michal Krupa and Tom Levens for their tireless support and key contribution. More importantly, to them and all the good folks at CERN, thanks for being always ready to step in for a good piece of pizza and limonccelo somewhere downtown in Meyrin.

I want to thank my fellows at Royal Holloway for the insightful comments about the project, in particular to Stewart Boogert for making me discover the joy and satisfaction of a nice diagram, and my Scottish countryman Laurie Nevay who converted me to a devoted Python fan. Of course, I would not have enjoyed so much my time at Royal Holloway without the people I shared office with, coffee breaks, confidences, PhD frustration, and (a lot of) beer, some of those are William Shields, Héctor Garcia, and Franco la Zia.

Muchas gracias a mis amigos en España por fingir cierto interés en mi inestigación. Finalmente, quiero terminar dedicando esta tesis a mi familia, a mis hermanos, a mis padres y a Clara, a quienes agradezco, como siempre, todo su apoyo.

Contents

List of Figures

List of Tables

List of Symbols

γ	Lorentz factor
α	Angle subtended between the Coulomb field and the direction transverse to the beam velocity
ρ	Bunch charge density distribution
χ	Head-Tail correction factor in the charge density distribution
e_0	Charge of the proton
N_p	Number of protons per bunch
σ	Standard deviation of the Gaussian charge distribution of the bunch
r_0	Transverse radial distance to the bam direction
z_0	Distance from the pipe centre to the beam position
r_{centre}	Distance from the pipe centre to the crystal position
t	Time
v	Beam velocity
β	Relativistic $\beta = v/c$
σ_x, σ_z	Beam size projections in x and z
β_x, β_y	Beta functions along the x and y projections
D_{β_x}, D_{β_y}	Dispersion of the beta functions β_x and β_y respectively
r_{centre}	Radial distance from the pipe centre to the pickup position
Δ, Σ	Difference and sum signals between opposing pickups
Φ	Angle formed by colliding beams at the LHC interaction points
$R(\Phi)$	Reduction factor of the overlapping area between colliding bunches

$\epsilon_N^H,\ \epsilon_N^V$	Horizontal and vertical normalised emittance
$Q_h,\ Q_v$	Horizontal and vertical betatron tunes
k_B	Boltzmann constant
ϵ_0	Dielectric permittivity in vacuum
ϵ_{ij}	Relative dielectric permittivity tensor
$\epsilon_z^T,\ \epsilon_z^S$	Clamped and unclamped dielectric constant in z direction
$E_i,\ D_i$	Applied electric field and electric displacement vector components
$\mathbf{E}^{opt}$	Polarisation vectors
$E_p,\ E_{\text{bunch}}$	Propagating Coulomb field in vacuum of a single proton and a bunch
$E_{\text{LNB}},\ E_z$	Modulating electric field in the crystal
$r_{ij},\ s_{ij}$	Linear and quadratic electro-optic tensors
η_{ij}	Electric impermeability tensor
$n_{i,j}$	Refractive index tensor
$n_x,\ n_y,\ n_z$	Principal refractive indices
$n_o,\ n_e$	Ordinary and extraordinary refractive indices
v_p	Phase velocity
$L_x,\ L_y,\ L_z$	Electro-optic crystal dimensions
Γ_0	Offset phase retardation due to the crystal natural birefringence
ϕ_0	Offset phase retardation between two optical paths in the interferometric configuration
$\phi_x,\ \phi_z$	Dephase along the x and z directions of the crystal
$\phi_o,\ \phi_e$	Dephase along the ordinary and extraordinary directions of the crystal
V_π	Voltage applied required to shift the phase birefringence an amount π
E_π	Electric field required to shift the phase birefringence an amount π
$E_{\pi,\text{inter}}$	Electric field required to shift the phase difference between two optical paths an amount π
T_{crossed}	Light transmission function for the crossed polarisers configuration
S_{crossed}	Sensitivity of the crossed polarisers configuration
T_{inter}	Light transmission function for the interferometric configuration
S_{inter}	Sensitivity of the interferometric configuration

ω	Angular frequency
f	Linear frequency
τ	Transit time of the optical beam passing through the crystal
$f_{m,max}$	Maximum bandwidth of the crystal
ω_m	angular frequency of the field applied
φ , φ_{RF}	Modulation depth for phase and amplitude modulations
κ	Reduction factor of the modulation depth
k_{C-I}	Ratio between the sensitivities of the interferometric and crossed polarisers configurations
K_D	Decay factor of the propagating Coulomb field peak of the proton bunch along the radial distance
λ	Optical beam wavelength
θ_{TD}, θ	Orientations of the transmission direction of the analyser and the half wave-plate axis
P_{DC}	Optical power baseline
V_{DC}	DC voltage output of the fast detector
S_{DC}	DC Sensitivity of the fast detector
ΔP_{opt}	Beam-induced optical modulation
V_{RF}	RF voltage output of the fast detector
S_{RF}	RF Sensitivity of the fast detector
G_e	Effective gain of the amplifier
V_G	Amplifier output
R	Detector responsivity
η_{amp}	RMS noise of the amplifier
η_{PD}	RMS noise of the fast detector
η_{Total}	Total RMS noise of the detection system
μ_C	Ratio between the strengths of the propagating Coulomb field in vacuum and the modulating field in the crystal
μ_S	Ratio between the strengths of the propagating Coulomb field in vacuum and the field concentrated at the edge of the crystal

Chapter 1

Motivation

1.1 High Luminosity Large Hadron Collider

The Large Hadron Collider (LHC) is the largest and highest energy particle accelerator ever built [1]. The LHC is a 27-km circular accelerator based underground at a mean depth of 100 meters beneath the Franco-Swiss boundary near Geneva. The LHC is run by the European Organisation for Nuclear Research (CERN), and it has been designed to accelerate proton and ion bunches in opposite directions to produce head on collisions in the interaction points along the ring. The first long LHC run took place from 2010 to 2012 for proton collisions; during this time, a centre-of-mass energy of 8 TeV (4 TeV per beam) was reached at the collision points. A major achievement of this period was the successful confirmation of the Higgs Boson existence in 2012 [2,3], but also delivered other relevant discoveries such as the rare decay of the B_S^0 meson [4].

The European Strategy for Particle Physics set a plan to further increase its discovery potential [5]. According to this proposal, the LHC would get upgraded to improve the luminosity, that is, the rate of collisions at the Interaction Point (IP) by a factor 10 (from 300 fb^{-1} to 3000 fb^{-1}). This process is denominated as High Luminosity Large Hadron Collider (HL-LHC) project, which aims to provide more accurate measurements of the phenomena that occur below the current design sensitivity. For instance, beyond the Higgs discovery, the HL-LHC will explore the existence of the new particles predicted by the supersymmetry theory, while optimising the Higgs Boson production, too. That is why the luminosity must be improved, as the exploration of these new physics requires a higher collision rate.
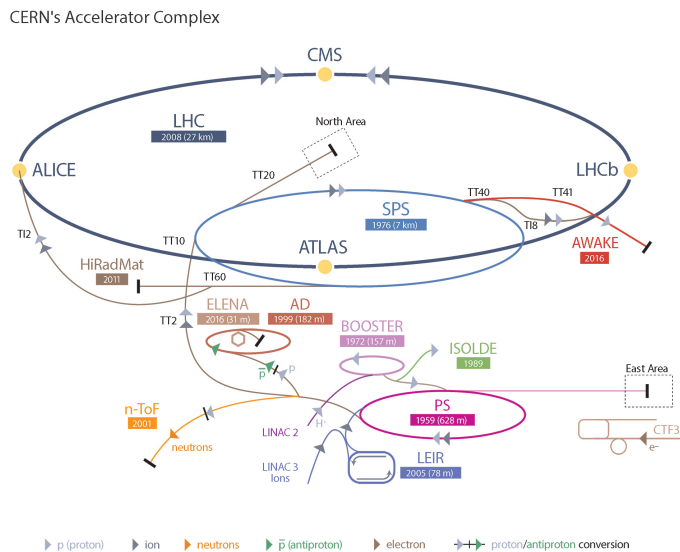
Figure 1.1: CERN accelerators chain [6].

As Figure 1.1 illustrates, the LHC machine is the culmination of a chain of accelerators that successively and steadily increase the proton beam energy [1]. The process starts with a Linac where the protons are accelerated up to 50 MeV, before being transferred to the Proton Synchrotron Booster (PSB) that reaches 1.4 GeV; it is then followed by the Proton Synchrotron (PS), reaching 25 GeV beam energy, and the Super Proton Synchrotron (SPS) where it achieves 450 GeV. The SPS is the second largest accelerator at CERN, being the penultimate step just before injecting two proton beams into the LHC that circulate in opposite directions so they collide in the interaction points.

1.1.1 Detection of crab cavity performance

The HL-LHC project relies on the implementation of innovative technologies that mainly aim, among other objectives, to heighten the rate of collisions. In this regard, the superconducting cavities known as crab-cavities emerge as an interesting proposal. This mechanism improves the previous type of interaction (Fig. 1.2(a)) by rotating or kicking the bunches circulating in opposite directions before and after the interaction point to make them collide purely head-on (Fig. 1.2(b)) [7]. This way, the overlapping area is reduced by a factor $R(\Phi)$, which is a function of the angle Φ between beams shown in Figure 1.2, and is given by:

$$R(\Phi) = \frac{1}{1 + \left(\frac{\sigma_z}{\sigma_x} \tan \frac{\Phi}{2}\right)^2}, \tag{1.1}$$

where σ_x and σ_z are the beam size projections in x, that corresponds to the direction of the particle beam, and also in z, which is the direction transverse to the accelerator plane. The crab cavity technology is envisioned to maximise the luminosity at the interaction point, but entails the need to implement some quite challenging diagnostics to monitor the induced fast transverse displacements:
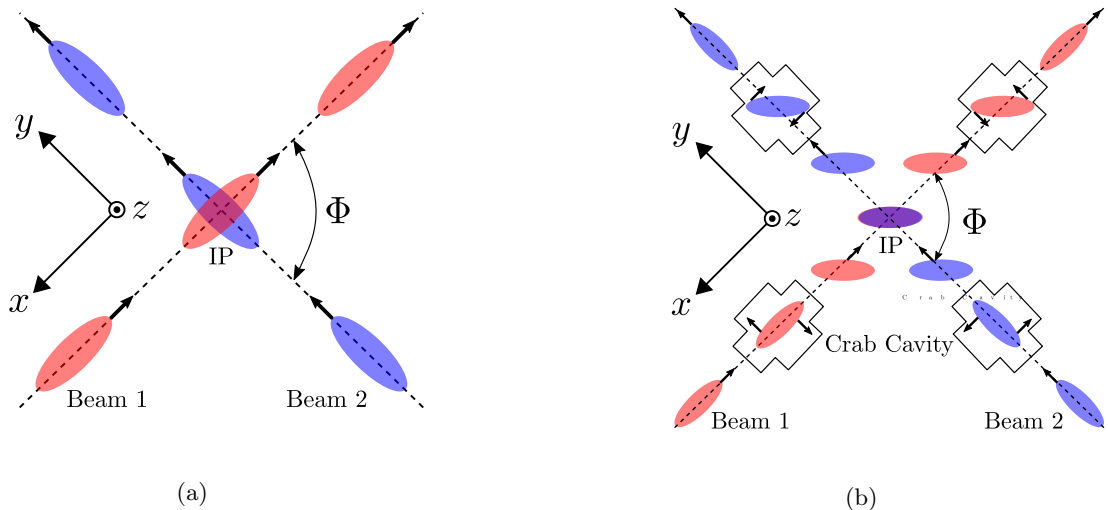
Figure 1.2: Diagrams of the current collision geometry (a), and the crab cavity mechanism (b): the bunch is rotated before the Interaction Point IP to orient the bunches head-on and is kicked back to the original position afterwards.

1.1.2 Detection of Head-Tail instabilities

The Head-Tail (HT) instability occurs when the Coulomb field propagating from the head of the bunch reflects in the pipe and interacts with the tail as it passes, inducing an energy shift in the whole bunch. As a result, this type of instability produces a standing wave-like distribution of charge determined by the number of modes m, that is, the number of zero crossings of the transverse charge position [8, 9]. This phenomena was first observed at the CERN Proton Synchrotron (PS) and Booster (PSB) [10] and has also recently been reported at the LHC, too [11]. Traditionally, the HT detection is based on the acquisition by fast oscilloscopes of the analog difference Δ and sum Σ of the RF signals generated by two opposing stripline electrodes [12]. It is important to monitor this type of instability since it constitutes a limiting factor on the maximum beam intensity that can be stored in the LHC.

The required bandwidth (BW) to detect a particular HT instability scales inversely with the bunch length, for instance, a 200 ns bunch (assuming a gaussian charge distri-

bution) would require a system with a bandwidth around 150 MHz [13]. Figure 1.3(a) illustrates some exemplary time-domain signals Δ obtained from the difference between opposing pickups. In the simulation the rigid mode is denoted as $m = 0$ and some typical intra-bunch HT modes ($m = 1$, 2, and 6) are also displayed assuming a Gaussian distribution where the bunch length is defined as $4\sigma = 1\,\text{ns}$ for LHC, where σ is the standard deviation. In addition, Figure 1.3 depicts the corresponding frequency-spectrum of the Δ signals, which indicates the detection bandwidth of each mode. The maximum of the HT motion in the frequency domain shifts towards higher frequencies as the mode number or the intra-bunch resolution increases.

(a)   (b)
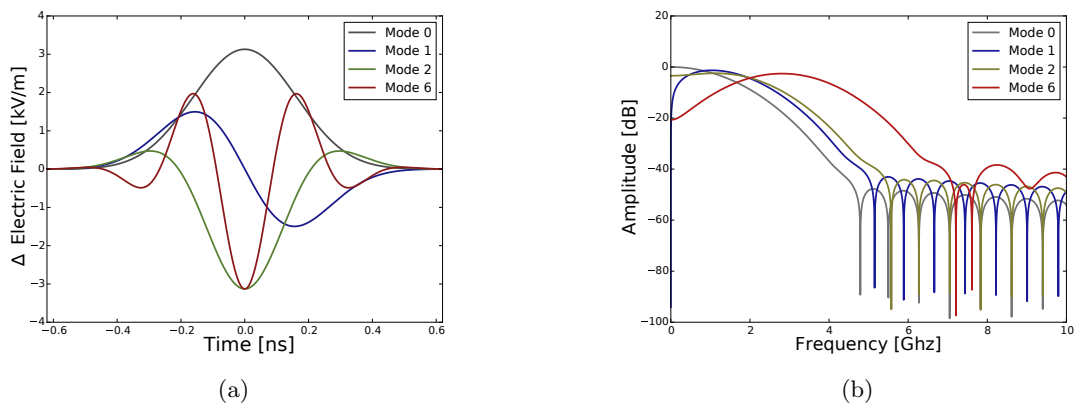
Figure 1.3: Typical HT signals for modes 0, 1, 2, and 6 in the time-domain (a) and the corresponding frequency bandwidth (b).

As mentioned previously, several of the so-called HT monitors based on traditional electromagnetic electrodes installed at LHC have already produced measurements. The performance is normally limited by the pickups, cables and acquisition system. For instance, according to the HL-LHC technical design report, these monitors typically present bandwidths of around $2\,\text{GHz}$ [14], however the current state-of-art of such devices is set to approximately 3-4 GHz being capable to detect mode 4 HT at LHC, as T. Levens reported in 2016 [11, 15]. In order to observe a highly detailed mode 6 HT instability in the order of at least $100\,\text{ps}$ resolution, a minimum bandwidth of $6\,\text{GHz}$ must be targeted [13], and according to the same HL-LHC technical design report, a $10\,\text{GHz}$ bandwidth is considered desirable [14].
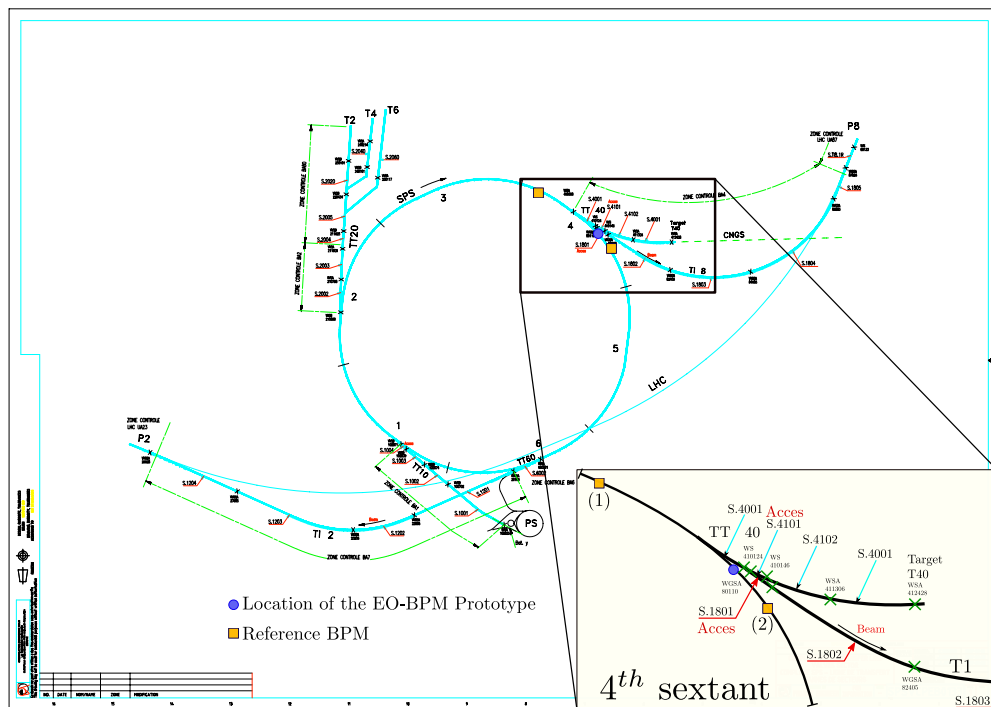
Figure 1.4: Layout of the SPS ring with a detail of the zoomed section that shows where the EO-BPM prototype was installed, and also the position of a pair of reference BPM (about 50 m upstream (1) and 14 m downstream (2)) employed to track the transverse beam offset in some experiments of this thesis [17].

1.2 Prototyping at Super Proton Synchrotron

Although this study is part of the HL-LHC project, the prototype has been first installed in the Super Proton Synchrotron (SPS) accelerator for development and testing, specifically in the 4th sextant as shown in Figure 1.4. One can observe that our installation is located between two BPM that were employed to interpolate the beam offset at the position of interest. The technical drawing displayed in Figure 1.5 also reveals an existing HT monitor about one metre upstream from the prototype. Figures 1.6 and 1.7 illustrate the optic lattice of the SPS by plotting the beta function projections $\beta_i = \beta_x$ and $\beta_i = \beta_y$ and their dispersions D_{β_x} and D_{β_y}, against the longitudinal accelerator position s [16]. The reason why the SPS was selected over the LHC for the first studies is the better availability of the former to gain access, incorporate new elements, and carry out interventions while the beam parameters are actually very similar in both of them.

As mentioned earlier, the SPS accelerates the beam to be injected into the LHC, and also provides the experiments NA61/SHINE, NA62, and COMPASS with a parti-

5
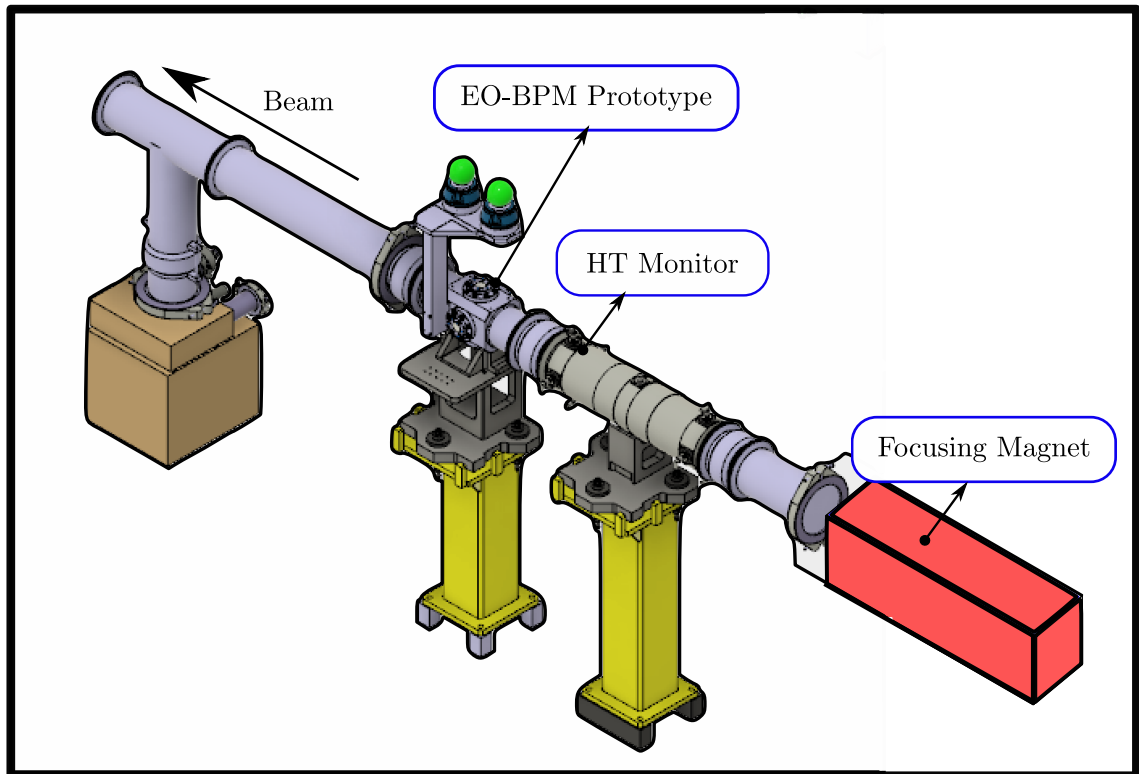
Figure 1.5: Representation of the section of the SPS ring where the EO-BPM was installed.

cle beam [18]. Moreover, the AWAKE experiment [19] also takes place at SPS and its favourable conditions specially in terms of intensity, can be exploited parasitically to study novel technologies, for instance, the Electro-Optic Beam Position Monitor (EO-BPM). In addition, the installation of the first crab cavities in the SPS for testing is planned. This constitutes an excellent opportunity as it allows us to check the performance of the EO-BPM measuring the kicks that will only be applied on the vertical plane of the beam.

For SPS, the number of protons of a nominal bunch is typically 1.15×10^{11}, which corresponds to a bunch charge of approximately $80\,\mathrm{nC}$. Also, the beam is accelerated from $26\,\mathrm{GeV}$ at injection to $450\,\mathrm{GeV}$ at maximum energy. The process of acceleration normally entails that the Gaussian bunch length, defined as 4σ, is shortened from $4\,\mathrm{ns}$ at low energy down to $1.6\,\mathrm{ns}$ at top energy. It should be noticed though, that most of the numeric-analytic calculations presented in this thesis to compare the performance of the different EO pickup models, have been done assuming $4\sigma = 1\,\mathrm{ns}$ for simplicity, but also because that value corresponds to the typical nominal bunch length at LHC, which is in fact the machine where the EO-BPM is foreseen to be eventually installed [20, 21]. It is a different situation when the simulations of the EO signal are compared to the experimental
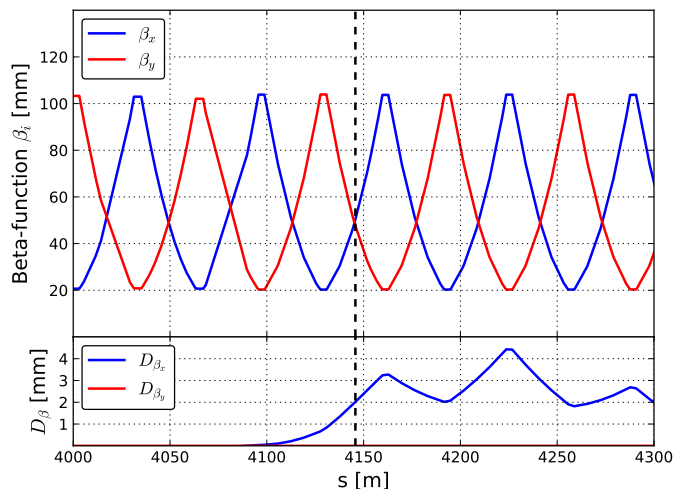
Figure 1.6: SPS lattice represented by the beta function projections β_x and β_y against s, and their dispersion values D_{β_x} and D_{β_y}, respectively.
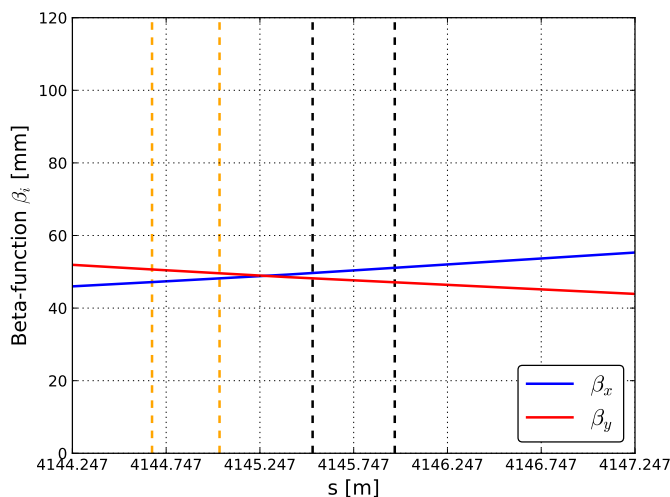
Figure 1.7: Zoomed in section of the lattice around the position of the EO-BPM and HT monitor.

measurements, since in that case the length input was retrieved from the logging system if possible. Additionally, a proton bunch with a length of that order emits a Coulomb field in the Radio-Frequency (RF) region that ranges up to several gigahertz. The beam parameters are summarised in Table 1.1 [22]. For completeness of all the main parameters involved in this project, it is important to mention that the pipe radius at the prototype location is 66.5 mm so the EO pickup was installed at that distance from the centre of the circular pipe section.

Table 1.1: SPS parameters [22].

Beam parameters at injection (pilot)	26 GeV
Horizontal Normalized emmitance ϵ_N^H	2.5 ± 0.3 μm
Vertical Normalized emmitance ϵ_N^V	3.0 ± 0.3 μm
Transverse Normalized emmitance ϵ_N^z	0.25 eV·s
Betatron Tunes $Q_{h,v}$	26.13, 26.19
SPS circumference	6.9 km
Bunch length	$4\sigma = 4.2 \pm 0.1$ ns (Gaussian distribution)
Revolution frequency	43.375 kHz
Voltage up to acceleration	from 2 MV to 3 MV
Momentum compaction factor	0.00192
Beam parameters at top energy (nominal)	**450 GeV**
Horizontal Normalized emmitance ϵ_N^H	3.0 ± 0.3 μm
Vertical Normalized emmitance ϵ_N^V	3.6 ± 0.3 μm
Transverse Normalized emmitance ϵ_N^z	0.6 ± 0.10 eV·s
Betatron Tunes $Q_{h,v}$	26.13, 26.19
SPS circumference	6.9 km
Bunch Intensity	1.15×10^{11} protons per bunch
Bunch length	$4\sigma = 1.6 \pm 0.1$ ns (Gaussian distribution)
Bunch separation	25 ns
Revolution frequency	43.478 kHz
Voltage up to acceleration	from 7 MV
Momentum compaction factor	0.00192

1.2.1 Project aims

Several EO-BPM systems could potentially be implemented around the interaction points in the HL-LHC to better understand the HT instabilities and to monitor the tuning of the crab cavities. One of the main objectives pointed out previously is to achieve a minimum bandwidth of 6 GHz that could enable, at least, the high resolution detection of mode 6 HT instabilities.

The crab cavity technology is currently under development at CERN SPS to carry out the first feasibility studies. According to some preliminary simulations [23] the change of the beam shape is energy dependent. In particular, a transverse displacement in the bunch vertical plane of about ~ 6 mm is expected at 26 GeV, while is reduced to ~ 0.6 mm at 270 GeV for a 5 MV RF quick from the cavity. Given this result, it has been reported that a minimum space transverse resolution of 100 μm is required to validate the crabbing mechanism in the SPS, which is in principle within the state-of-art of the traditional

HT monitors. In addition, internal communications with the beam instrumentation department at CERN have also confirmed the same objective of $100\,\mu$m resolution for the EO-BPM. However, the final requirements remain unclear at the moment, pending more detailed simulations and the outcome of the initial tests.

1.3 Overview on Electro-Optic diagnostic techniques

Several Electro-Optic (EO) techniques have extensively been reported regarding bunch-length monitoring in linear electron accelerators for Terahertz (THz) detection, such as Electro-Optic Sampling (EOS) [24], Spectral Decoding (EOSD) [25], Spatial Encoding (EOSE) [26], Temporal Decoding (EOTD) [27], and Spectral Unconversion (EOSU) [28]. Most of the aforementioned techniques use pulsed lasers to activate the second order response of the Pockels effect in crystals like ZnTe or GaP. As they are used for terahertz spectroscopy in very short electron beams, these techniques are generally capable to resolve time profiles within a picosecond or even sub-picosecond resolution, as for instance in the results obtained by B.R. Steffen in DESY in 2007 [29]. Some relevant experiments that rely on these technologies have been performed at CERN itself, in particular, Rui Pan successfully installed and tested a high-resolution EO bunch length monitor based on EO spectral decoding, in the CLIC in 2014 [30]. This experiment constitutes the most direct antecedent of an EO diagnostic tool developed at CERN.

The EO-BPM is a non-invasive beam diagnostic device that relies on the fast optical response of the EO crystal located in each pickup, whose birefringence is modified by the passing Coulomb field. In this thesis, the concept design comprises two opposing pickups on the same plane, each equipped with a vacuum-integrated $LiNbO_3$ (LNB) crystal illuminated by linear polarised light, that emerges out of it with a different polarisation state due to the action of the linear Pockels effect. If an analyser is set after the crystal and oriented perpendicular to the initial polarisation direction, the extent of the polarisation change translates into an optical modulation as the particle beam passes. Therefore, the EO-BPM is based on the excitation of the lithium niobate linear EO coefficients, also known as Pockels effect rather than the second order response offered by ZnTe and GaP. Also, the EO-BPM can in principle work with Continuous Wave (CW) light sources, in contrast to many terahertz detection techniques that normally employ pulsed lasers, with the exception of the EOSU method.

Moreover, the linearity exhibited by the Pockels effect implies that the optical modulation could potentially be a replica of the field-profile applied on the crystal, which would allow the device to operate in a traditional BPM fashion, by combining sum Σ and difference Δ signals from different pickups on the same plane. Alternatively, the system can work as an optical interferometer that produces a single signal per pair of opposing pickups by combining the phase retardations induced by each crystal. Although both methods are discussed and analysed theoretically in chapter 3, the prototype presented in this thesis is inspired by the crossed polarisers design.

Several studies on the EO-BPM concept have been conducted in electron machines delivering a Pockels-related EO signal, such as the results obtained in 2001 with LNB by T. Tsang et al. in Brookhaven ATF [31], proving time responses in the order of picoseconds, or using BGO by M.A. Brubaker et al. [32]. The studies carried out by Y. Okayusu in 2012 [33] at SPring-8 employ various organic DAST crystals, which have demonstrated a resolution of tens of femtoseconds. The application of this idea to a circular proton machine at CERN was first proposed by Ralph J. Steinhagen in 2013 [34], who initiated the investigations aiming to deliver a novel diagnostic tool capable to achieve a fast response ranging from 6 GHz up to 12 GHz with a time resolution between 50 ps and 100 ps for the High-Lumi LHC upgrade. Those preliminary studies gave rise to the present thesis, which represents the first attempt of a proton-induced measurement by EO means and set the grounds towards further improvements.

Recent investigations on hybrid EO solutions carried out mainly by A. Angelovski et al. at FLASH [35–37] have already shown fast responses working as Beam Arrival Monitors (BAM). In particular, those systems performed above 40 GHz cutoff frequencies and sub-picosecond resolutions, making this alternative technique another promising candidate to be investigated. According to this proposal, an electro-magnetic pickup transmits a voltage signal induced by the passing beam into an EO amplitude or phase modulator, depending on what configuration is used. From an opto-mechanical point of view, the main difference lies in the fact that the EO crystal would not be vacuum-integrated in the pipe this time. Obviously, this could simplify the installation and the maintenance of the system, although it should be noted that the models reported were not designed to deliver a field time-profile or a BPM sort of signal, but to work as BAM, so further investigations in future are required.

Chapter 2

Electro-Optic theory

2.1 Pockels effect

The fundamental working principle of the device prototype presented in this thesis is the Pockels effect, which is one of the main properties of lithium niobate (LNB). Such effect is the Electro-Optic (EO) mechanism that produces the modification of the refractive indices of the crystal by the action of an external electric field. This makes lithium niobate the key piece that could provide a signal potentially induced by a propagating Coulomb field. The theoretical background of the concept including some relevant optical layouts, and also a general characterisation of lithium niobate are presented in this chapter.

2.2 The electro-optic coefficients

The dielectric permittivity ϵ_{ij} determines the relation between the applied electric field $\mathbf{E}$ and the electric displacement $\mathbf{D}$ in the medium:

$$D_i = \epsilon_0 \sum_{j=1}^{3} \epsilon_{ij} E_j \, , \tag{2.1}$$

where ϵ_0 is the permittivity in vacuum, and ϵ_{ij} is a 2nd rank symmetric tensor with 6 independent elements when assuming a lossless, anisotropic, and optically non-active crystal such as lithium niobate, thus $\epsilon_{12} = \epsilon_{21}$, $\epsilon_{13} = \epsilon_{31}$ and $\epsilon_{23} = \epsilon_{32}$. Moreover, the dielectric permittivity tensor can be linearised to be represented in its simplest form when the principal coordinate axes are used, that is, the directions of the crystal along which $\mathbf{E}$ and $\mathbf{D}$ are found to be parallel:

$$
\begin{pmatrix} D_1 \\ D_2 \\ D_3 \end{pmatrix} = \begin{pmatrix} \epsilon_{11} & 0 & 0 \\ 0 & \epsilon_{22} & 0 \\ 0 & 0 & \epsilon_{33} \end{pmatrix} \begin{pmatrix} E_1 \\ E_2 \\ E_3 \end{pmatrix}. \tag{2.2}
$$

Let us recall that each element of the impermeability tensor $\eta_{ij} = \epsilon_0/\epsilon_{ij} = 1/n_{ij}^2$, where $n_{11} = n_x$, $n_{22} = n_y$ and $n_{33} = n_z$, are the refractive indices along the principal axes [38]. Expanding $\eta_{ij}(\mathbf{E})$ around $\mathbf{E} = 0$:

$$
\eta_{ij} = \eta_{ij}(\mathbf{E} = 0) + \sum_{k=1}^{3} r_{ijk} E_k + \sum_{k=1}^{3} \sum_{l=1}^{3} s_{ijkl} E_k E_l + \ldots, \tag{2.3}
$$

where the parameters r_{ij} and s_{ij} are the EO coefficients of first and second order, respectively. Therefore, r_{ij} are the linear coefficients responsible for the Pockels effect and s_{ij} causes the quadratic EO effect also known as the Kerr effect [39]. These tensors indicate how η_{ij} is modified by the action of an external electric field, thus:

$$
r_{ijk} = \left(\frac{\partial \eta_{ij}}{\partial E_k} \right)_{\mathbf{E}=0} \qquad s_{ijkl} = \frac{1}{2} \left(\frac{\partial^2 \eta_{ij}}{\partial E_k \partial E_l} \right)_{\mathbf{E}=0}. \tag{2.4}
$$

Since η_{ij} and ϵ_{ij} are symmetric ($\epsilon_{ij} = \epsilon_{ji}, \eta_{ij} = \eta_{ji}$), the indices i and j of the tensor r_{ijk} can be permuted, hence:

$$
r_{ijk} = r_{jik} = r_{hk}, \tag{2.5}
$$

where index $h = 1, 2, ..6$ contracts the elements of r_{ij} applying $(i, j) \rightarrow h$ as follows: $(1,1) \rightarrow 1$, $(2,2) \rightarrow 2$, $(3,3) \rightarrow 3$, $(2,3) \rightarrow 4$, $(1,3) \rightarrow 5$, $(1,2) \rightarrow 6$. This nomenclature reduces the independent values of the tensor r_{ijk} from 27 to 18, resulting in a 6×3 matrix. Furthermore, the coefficients r_{hk} are in the order of $\sim 10^{-12}$ m/V, whereas for instance $| s_{13} | \leq 2.3 \times 10^{-22}$ V^2/m^2 for lithium niobate [40, 41]. Consequently, unless an extremely high field activates the nonlinear coefficients s_{ij}, the Kerr effect can be neglected.

2.2.1 Review on the linear electro-optic effect for lithium niobate

Traditionally in the literature, the propagation of optical radiation is described in terms of the index ellipsoid represented in the principal coordinate system (x, y, z) [39]:

$$
\frac{x^2}{n_x^2} + \frac{y^2}{n_y^2} + \frac{z^2}{n_z^2} = 1, \tag{2.6}
$$

where the refractive indices n_x, n_y and n_z are the principal axes of the ellipsoid. By definition, within the volume of the index ellipsoid the energy density of an electromagnetic wave propagating throughout the crystal remains constant. Also, as stated earlier, the refractive indices are related to η_{ij}:

$$\eta_{ij} = \begin{pmatrix} \eta_{11} & 0 & 0 \\ 0 & \eta_{22} & 0 \\ 0 & 0 & \eta_{33} \end{pmatrix} = \begin{pmatrix} \frac{1}{n_x^2} & 0 & 0 \\ 0 & \frac{1}{n_y^2} & 0 \\ 0 & 0 & \frac{1}{n_z^2} \end{pmatrix}. \tag{2.7}$$

Therefore, the field-dependent impermeability tensor $\eta_{ij}(E_x, E_y, E_z)$ determines the direction of the ellipsoid axes and also their magnitudes, n_x, n_y and n_z, as a function of the field applied $\mathbf{E} = (E_x, E_y, E_z)$

Lithium niobate is an uniaxial crystal where the principal axes x and y are optically equivalent, and z, which is parallel to the lattice vector c, exhibits a different optical behaviour. This anisotropy makes lithium niobate a birefringent medium as it has two different refractive indices along the so-called fast (n_f) and slow axis (n_s). The fact that $n_f < n_s$ indicates that the phase velocity in the fast direction $v_{p,f}$ is higher than in the slow ones $v_{p,s}$ ($v_{p,f} > v_{p,s}$). Alternatively, the refractive indices can be referred as ordinary (n_o), for x and y directions and extraordinary (n_e) for z, thus $n_x = n_y = n_o$ and $n_z = n_e$. Quantitively, the extent of the birefringence is normally defined as $n_e - n_o$. According to this, lithium niobate exhibits negative birefringence, implying that $n_f = n_e < n_o = n_s$ as visually illustrated in Figure 2.1:
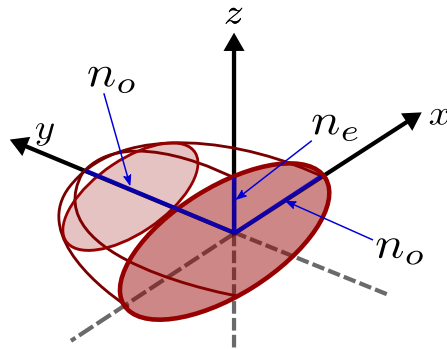
Figure 2.1: Section of the index ellipsoid on the y-cut (shaded) plane when the optical beam is propagating along the y axis. The ellipsoid axes are shown in blue: n_o is the refractive index along x and y, and n_e along z.

Additionally, the linear coefficients are determined by the crystallographic lattice of the medium. Being that lithium niobate exhibits 3m group symmetry, the coefficient

matrix r_{hk} in the principal coordinates has the following form [39]:

$$r_{hk} = \begin{pmatrix} 0 & -r_{22} & r_{13} \\ 0 & r_{22} & r_{13} \\ 0 & 0 & r_{33} \\ 0 & r_{51} & 0 \\ r_{51} & 0 & 0 \\ -r_{22} & 0 & 0 \end{pmatrix}. \tag{2.8}$$

Let us now consider an electric field E_z applied only along z to avoid crossed terms and exploit the coefficient r_{33}. Assuming $s_{ij} = 0$, equation 2.7 becomes:

$$\eta_{ij} = \begin{pmatrix} \frac{1}{n_o^2} & 0 & 0 \\ 0 & \frac{1}{n_o^2} & 0 \\ 0 & 0 & \frac{1}{n_e^2} \end{pmatrix} + \begin{pmatrix} r_{13}E_z & 0 & 0 \\ 0 & r_{13}E_z & 0 \\ 0 & 0 & r_{33}E_z \end{pmatrix}. \tag{2.9}$$

As shown before, the eigenvalues η_{11}, η_{22} and η_{33} of the tensor η_{ij} are the new axes lengths modified by the action of E_z. From equation 2.9, the index ellipsoid turn out to be as follows:

$$x^2 \left(\frac{1}{n_0^2} + r_{13}E_z\right) + y^2 \left(\frac{1}{n_o^2} + r_{13}E_z\right) + z^2 \left(\frac{1}{n_e^2} + r_{33}E_z\right) = 1. \tag{2.10}$$

The equation above shows that the shape of the index ellipsoid is modified when an electric field is applied parallel to z, or equivalently to the crystallographic direction c, for LNB. Let us note that there are no mixed terms such us xy, xz or yz. These terms would imply new directions for the refractive indices non-parallel to the principal axes. The new effective refractive indices n_x, n_y and n_z can be determined by comparison of the new ellipsoid (eqn. 2.10) with equation 2.6. For instance, the axis length along x:

$$\frac{1}{n_x^2} = \frac{1}{n_o^2} + r_{13}E_z, \tag{2.11}$$

which assuming the fact that $r_{13}E_z \ll n_0^{-2}$ and applying the relation $dn = -\frac{1}{2}n^3 d\left(\frac{1}{n^2}\right)$ leads to:

$$n_x = n_o - \frac{1}{2}n_o^3 r_{13}E_z, \tag{2.12}$$

14

similarly for n_y and n_x:

$$n_y = n_o - \frac{1}{2}n_o^3 r_{13}E_z \, , \tag{2.13}$$

$$n_z = n_e - \frac{1}{2}n_e^3 r_{33}E_z \, . \tag{2.14}$$

Figure 2.2 shows the different sections and axis lengths of the index ellipsoid when a light beam is propagating along y, for the LNB natural birefringence ($E_z = 0$) and also when the birefringence is modified by an applied electric field ($E_z \neq 0$). Let us note the direction of the new refractive indices remain unchanged when E_z is applied on the crystal, but the actual value changes by a certain extent given by equations 2.12, 2.13 and 2.14. It can also be appreciated that the axis length along the z direction is shortened by a greater extent than along x since the factor r_{33} is higher than r_{13} for LNB (Table 2.1).
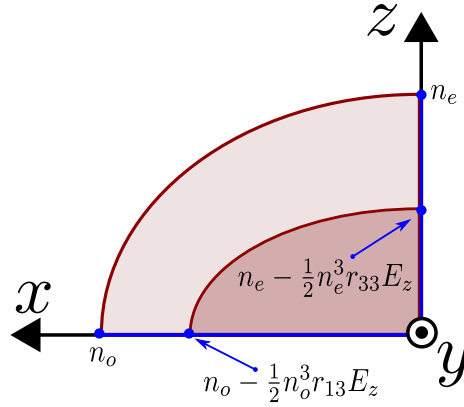
Figure 2.2: The index ellipsoid section with $E = 0$ occupies more surface (clearer) than when $E \neq 0$ (darker).

If a light beam is propagating along y under an applied field E_z, then the birefringence is obtained by substituting equations 2.14 and 2.12 in the definition:

$$n_z - n_x = n_e - n_o - \frac{1}{2}(n_e^3 r_{33} - n_o^3 r_{13})E_z \, , \tag{2.15}$$

where the factor $n_e - n_o$ represents the natural birefringence, and $\frac{1}{2}(n_e^3 r_{33} - n_o^3 r_{13})E_z$ is the term indicating the field induced birefringence change. As can be seen in equation 2.15, the value of the EO coefficients r_{13} and r_{33} play an important role in the extent of the birefringence modification. Table 2.1 shows the coefficients distinguished by the superscripts T and S, for LNB. The superscript T denotes that the crystal is unclamped and the superscript S denotes the crystal is clamped with an stress associated. The EO

coefficients r_{ij}^T for a free crystal are used when E_z is applied at low frequencies. The coefficients r_{ij}^S are used when the electric field is applied at high frequencies above the mechanical resonance of the lattice ($> 200\,\text{MHz}$) [42].

Table 2.1: Linear EO coefficients [$\times 10^{-12}\,\text{V/m}$] for LNB at $633\,\text{nm}$ [40].

r_{13}^T	r_{33}^T	r_{13}^S	r_{33}^S
10.0	32.2	8.6	30.8

As mentioned earlier, the key idea behind the detection is to use the Coulomb field from the particle bunch to induce a birefringence change as the optical beam propagates. Therefore, the election between the clamped or unclamped EO coefficients is determined by the scope of the frequency spectrum of the bunch.

2.3 Electro-optic modulation

The modification of the birefringence described in the previous section can be translated into a change in the polarisation state along the optical path before and after the crystal. The incoming light beam can be decomposed into different polarisation vectors, that travel through the crystal with different phase velocities $v_p = c/n$. This section studies the different optical configurations based on the input polarisation and the recombination after passing through it.

2.3.1 Geometry of the Electro-Optic modulator

The orientation of the beam propagation with respect to the applied field gives two main possible configurations: transversal modulation, when the propagating Optical Beam (OB) along one of the crystal axes is perpendicular to the field applied (Fig. 2.3(a)), or longitudinal modulation when both the direction of the OB and the field are parallel (Fig. 2.3(b)). The previous section discussed how the natural birefringence is modified as a function of the electric field applied across the z direction of a LNB crystal. According to this example, a transversal modulation would require the optical beam to propagate along either x or y; for the longitudinal modulation the field is applied in the same direction z as the OB propagation. In any case, the polarisation projections would be potentially affected by the new index ellipsoid.
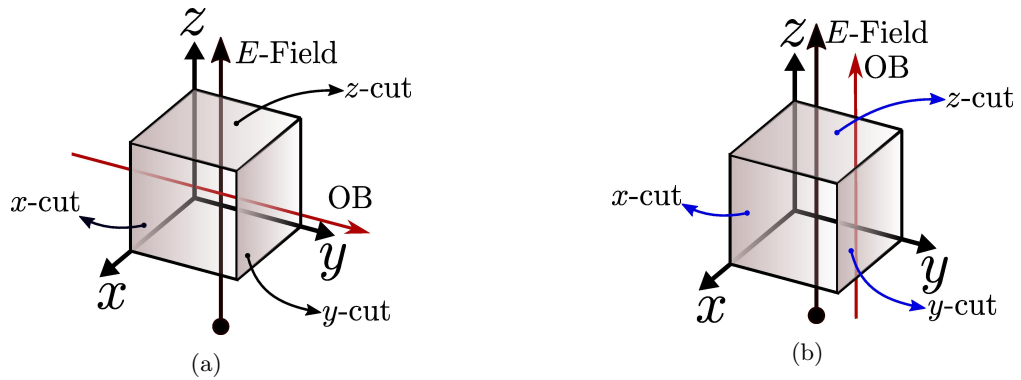
Figure 2.3: (a) Transverse modulation and (b) Longitudinal modulation geometries.

When the plane containing a crystal face is perpendicular to one of the principal axes, this plane is described as x-cut, y-cut or z-cut, depending on which corresponding direction is perpendicular to. In addition, it is common in the literature of commercial EO modulators to refer as z-cut and x-cut configurations, the geometries where the principal axes z and x are set vertically and perpendicular to the electrode plane. In Figures 2.4(a) and 2.4(b) the field is applied along z to make use of the higher coefficient r_{33}. Let us note that, the longitudinal modulation under x-cut configuration makes the directions of the OB polarisation vector E^{opt} and E_z to be perpendicular. This is normally known as Transverse Electric (TE) mode. Similarly, the transversal modulation of the polarisation vector E_z^{opt} in the z-cut configuration yields a Traverse Magnetic (TM) mode.
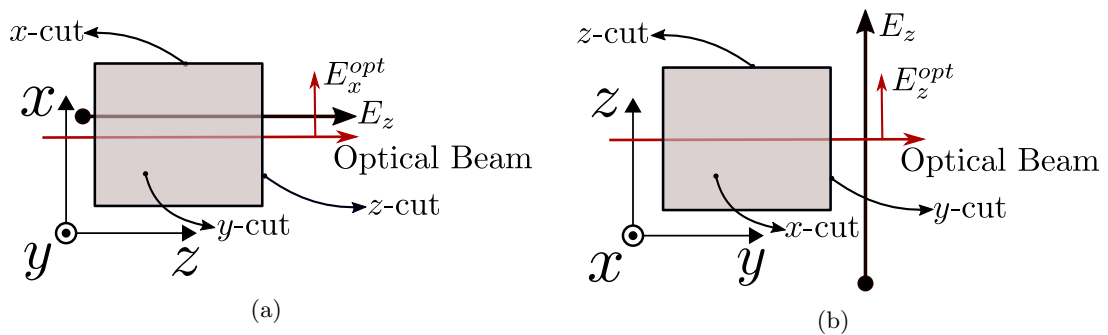
Figure 2.4: (a) x-cut in TE mode and (b) z-cut in TM mode for the polarisation vector E_z^{opt}.

For LNB in the x-cut configuration, the OB is incising on the XY face where only a unique refractive index n_0 can have an effect on the beam, and the crystal effectively behaves as a non-birefringent medium. Consequently, the optical modulation in x-cut configuration is not possible, making the z-cut geometry the only valid option.

2.3.2 Jones notation

Consider the z-configuration in transversal modulation (Fig. 2.4(b)), where the OB is propagating along the y axis, perpendicular to the electric field applied vertically across z. Before reaching the crystal, the electric field of the OB $\mathbf{E}^{opt}(t)$ can be represented as a polarisation vector:

$$\mathbf{E}^{opt}(t) = \begin{pmatrix} E_x^{opt}(t) \\ 0 \\ E_z^{opt}(t) \end{pmatrix} = \begin{pmatrix} E_x^{opt} e^{j(ky-\omega t)} \\ 0 \\ E_z^{opt} e^{j(ky-\omega t)} \end{pmatrix} = \begin{pmatrix} E_x^{opt} \\ 0 \\ E_z^{opt} \end{pmatrix} e^{j\Omega}, \qquad (2.16)$$

where k and ω are the wave number and angular frequency of the light beam and $\Omega(t) = ky - \omega t$ is the phase state of the incident light wave. Note that the physical field $\mathbf{E}^{opt}$ is the real part of this vector. Let the input light beam be vertically polarised, then, $E_x^{opt} = 0$ and $\mathbf{E}^{opt} = E_z^{opt}$. It can also be presented as a normalised Jones vector $\mathbf{E}_{vert}^{opt}$:

$$\mathbf{E}_{vert}^{opt} = \mathbf{E}_{vert}^{opt}(t) = \frac{1}{|\mathbf{E}_{vert}^{opt}|} \begin{pmatrix} 0 \\ E_z^{opt} \end{pmatrix} = \begin{pmatrix} 0 \\ 1 \end{pmatrix}. \qquad (2.17)$$

Also, the phase retardation due to different optical paths between the horizontal plane (x) and the vertical plane (z) can be represented by the following matrix M:

$$M = \begin{pmatrix} e^{-j\frac{\Gamma}{2}} & 0 \\ 0 & e^{j\frac{\Gamma}{2}} \end{pmatrix}, \qquad (2.18)$$

where $\Gamma = \Delta\phi = \phi_x$ - ϕ_z is a measure of the relative difference in phase retardation due to different optical paths caused by n_x and n_z in each direction. The Jones matrix M is the mathematical representation of an optical element with natural birefringence, for instance, a crystal of LNB. As pointed out earlier, $\Gamma = 0$ for the x-cut geometry so unless the opposite is mentioned, the z-cut configuration with the OB propagating along y (transverse modulation) will be assumed to be the configuration in the rest of the chapter.

2.3.3 Amplitude electro-optic modulation

In this scenario, the input linear polarisation $\mathbf{E}_{in}^{opt}$ is set at $45°$ with respect to x (or equivalently at $-45°$ with respect to z). In order to obtain this orientation a polariser can be used, or alternatively, the initial vertical polarisation $\mathbf{E}_{vert}^{opt}$ can be rotated by using

a Half Wave-Plate (HWP). A half-wave plate is a phase retarder (eqn. 2.18) such that the retardation is specifically equal to $\lambda/2$ for a given wavelength λ of incident light. The HWP is an optical element that induces a 2θ rotation when its fast axis is moved an angle θ with respect to the horizontal axis x. In Jones notation the passage of the beam through the HWP can be represented by a rotation matrix $R_\theta(2\theta)$, hence:

$$\mathbf{E}_{in}^{opt} = R_\theta(2\theta)\mathbf{E}_{vert}^{opt} = \begin{pmatrix} \cos(2\theta) & -\sin(2\theta) \\ \sin(2\theta) & \cos(2\theta) \end{pmatrix} \begin{pmatrix} 0 \\ 1 \end{pmatrix} = \begin{pmatrix} -\sin(2\theta) \\ \cos(2\theta) \end{pmatrix}. \tag{2.19}$$

Since the HWP interacts with the initial vertical polarisation, a negative rotation (clockwise) should be induced to obtain an input polarisation at $45°$ with respect x. Hence, $\theta = -\pi/8 = -22.5°$:

$$\mathbf{E}_{in}^{opt} = \frac{1}{\sqrt{2}} \begin{pmatrix} 1 \\ 1 \end{pmatrix}. \tag{2.20}$$

Let us note that $\theta = \pi/8 = 22.5°$ would result in $\mathbf{E}_{in}^{opt} = \frac{1}{\sqrt{2}}(-1, 1)^T$, making the input polarisation at $135°$ with respect to x. Equation 2.20 is used to illustrate the amplitude EO modulation in Figure 2.5. The incoming beam propagating along y is linearly polarised at $45°$ when it encounters the input face of the crystal set in z-cut configuration. The polarisation state $\mathbf{E}_{out}^{opt}$ of the emerging beam will be:

$$\mathbf{E}_{out}^{opt} = M\mathbf{E}_{in}^{opt} = \frac{1}{\sqrt{2}} \begin{pmatrix} e^{-j\Gamma/2} & 0 \\ 0 & e^{j\Gamma/2} \end{pmatrix} \begin{pmatrix} 1 \\ 1 \end{pmatrix} = \begin{pmatrix} E_x^{opt} \\ E_z^{opt} \end{pmatrix} = \frac{1}{\sqrt{2}} \begin{pmatrix} e^{-j\Gamma/2} \\ e^{j\Gamma/2} \end{pmatrix}. \tag{2.21}$$

The polarisation state after the crystal is then determined by Γ, which, depends upon the crystal birefringence defined in equation 2.15:

$$\Gamma(E_z) = \frac{2\pi}{\lambda}(n_z - n_x) = \frac{2\pi}{\lambda}(n_e - n_o)L_y - \frac{\pi}{\lambda}(n_e^3 r_{33} - n_o^3 r_{13})L_y E_z, \tag{2.22}$$

where L_y is the length of the crystal along the y direction and thus $n_e L_y$ and $n_o L_y$ are the optical paths followed by each of the components of the output polarisation vector in equation 2.21.
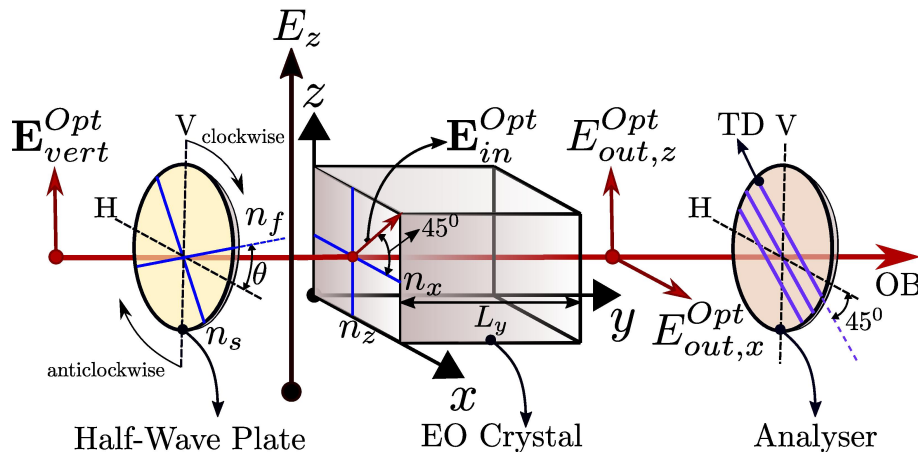
Figure 2.5: Amplitude modulation diagram.

The terms in equation 2.22 can be defined as:

$$\Gamma_0 = \frac{2\pi}{\lambda}(n_e - n_o)L_y\,, \qquad \Gamma(E_z) = \frac{\pi}{\lambda}(n_e^3 r_{33} - n_o^3 r_{13})L_y E_z\,. \qquad (2.23)$$

If $E_z = 0$, then, $\Gamma(E) = \Gamma_0 = \frac{2\pi}{\lambda}(n_e - n_o)L_y$ is the phase difference in absence of applied field, that is, caused by natural birefringence. After the crystal, the polarisation components get recombined, which results in a natural polarisation state without an E-field applied that is determined by Γ_0. Figure 2.6 depicts some relevant output polarisation cases. For instance, if $\Gamma = \pi$ the polarisation vectors along z and x are in anti-phase as case (a) shows. In anti-phase, $\mathbf{E}_{out}^{opt}$ in equation 2.21 is linear polarised at $-45°$, that is, perfectly perpendicular to the input polarisation $\mathbf{E}_{in}^{opt}$. In contrast, case (e) shows $\Gamma = 0$ where the polarisation vectors are now in-phase and then input and output polarisation states are equal ($\mathbf{E}_{in}^{opt} = \mathbf{E}_{out}^{opt}$). The intermediate points can be generally described as elliptical polarised states (cases (b) and (d)) where the main axes are always along the directions $\frac{1}{\sqrt{2}}(1,1)^T$ and $\frac{1}{\sqrt{2}}(-1,1)^T$, that is, at $45°$ and $-45°$ with respect x. When the contribution in $\frac{1}{\sqrt{2}}(-1,1)^T$ decreases, the projection on $\frac{1}{\sqrt{2}}(1,1)^T$ increases and vice versa, therefore, $\Gamma = \pi/2$ corresponds to circular polarisation.

In addition, the polarisation can be shifted along the different states shown in Figure 2.6 by activating the field-dependent term $\Gamma = \frac{\pi}{\lambda}(n_e^3 r_{33} - n_o^3 r_{13})L_y E_z$. From equation 2.23, the electric field required to obtain a relative difference $\Gamma = \pi$ is called E_π:

$$E_\pi = \frac{1}{L_y}\frac{\lambda}{n_e^3 r_{33} - n_o^3 r_{13}}\,, \qquad (2.24)$$

which is proportional to the optical beam wavelength λ and inversely proportional to the

crystal length L_y, for transverse modulation. Substituting E_π in equation 2.22 gives:

$$\Gamma(E_z) = \Gamma_o + \pi \frac{E_z}{E_\pi} \ . \tag{2.25}$$

Consider the analyser A with the Transmission Direction (TD) set at $-45°$ with respect to x located after the crystal along the optical path as drawn in Figure 2.5. Hence the polarisation vector $\mathbf{E}_{\text{trans}}^{opt}$ transmitted at the output of the analyser A:

$$\mathbf{E}_{\text{trans}}^{opt} = A\mathbf{E}_{out}^{opt} = \frac{1}{2} \begin{pmatrix} 1 & -1 \\ -1 & 1 \end{pmatrix} \frac{1}{\sqrt{2}} \begin{pmatrix} e^{-j\Gamma/2} \\ e^{j\Gamma/2} \end{pmatrix} = \frac{1}{2\sqrt{2}} \begin{pmatrix} e^{-j\Gamma/2} - e^{j\Gamma/2} \\ e^{j\Gamma/2} - e^{-j\Gamma/2} \end{pmatrix} \ , \tag{2.26}$$

using the definition $\sin(x) = \frac{e^{xj} - e^{-xj}}{2j}$, equation 2.26 simplifies to:

$$\mathbf{E}_{\text{trans}}^{opt} = \frac{j}{\sqrt{2}} \begin{pmatrix} -\sin(\Gamma/2) \\ \sin(\Gamma/2) \end{pmatrix} \ . \tag{2.27}$$

The normalised output transmission T_{crossed} after the analyser A is obtained from the polarisation vector in equation 2.27 as:

$$T_{\text{crossed}} = \mathbf{E}_{\text{trans}}^{opt,*} \cdot \mathbf{E}_{\text{trans}}^{opt} = \sin^2 \frac{\Gamma}{2} = \sin^2 \left(\frac{\Gamma_o}{2} + \frac{\pi}{2} \frac{E_z}{E_\pi} \right) \ , \tag{2.28}$$

where equation 2.28 above is known as the transfer function and is proportional to the transmitted intensity of the OB through the system formed by the crystal between crossed polarisers, in dimensions of power per unit area. Equation 2.28 is therefore equivalent to the ratio of power transmission between the point in the optical path just before the crystal and after the analyser A, that is, $T_{\text{crossed}} = |\ \mathbf{E}_{\text{trans}}^{opt}\ |^2 /\ |\ \mathbf{E}_{in}^{opt}\ |^2$. Of course, the curve T_{crossed} can be linearly scaled with the total light power employed in a particular experiment.

Figure 2.7 shows the transfer function from $\Gamma_0 = \pi$ (anti-phase, and parallel to the analyser) to $\Gamma(E_z) = 0$ (in-phase, so perpendicular to the analyser) along with some intermediate polarisation cases after the passage through the crystal. The polarisation shifts as the field increases from a maximum transmission $T = 1$ when the output polarisation and the analyser transmission direction are parallel. The transmission then decreases with the field, and thus the polarisation gets clockwise until hitting the minimum $T = 0$ when

$$\frac{1}{\sqrt{2}}\begin{pmatrix} -1 \\ 1 \end{pmatrix} \qquad \frac{1}{\sqrt{2}}\begin{pmatrix} e^{-\frac{3\pi}{4}j} \\ e^{\frac{3\pi}{4}j} \end{pmatrix} \qquad \frac{1}{\sqrt{2}}\begin{pmatrix} -j \\ 1 \end{pmatrix} \qquad \frac{1}{\sqrt{2}}\begin{pmatrix} e^{\frac{3\pi}{4}j} \\ e^{\frac{-3\pi}{4}j} \end{pmatrix} \qquad \frac{1}{\sqrt{2}}\begin{pmatrix} 1 \\ 1 \end{pmatrix}$$

(a)	(b)	(c)	(d)	(e)
$\Gamma_0 = \pi$	$\Gamma_0 = \frac{3\pi}{4}$	$\Gamma_0 = \frac{\pi}{2}$	$\Gamma_0 = \frac{\pi}{4}$	$\Gamma_0 = 0$
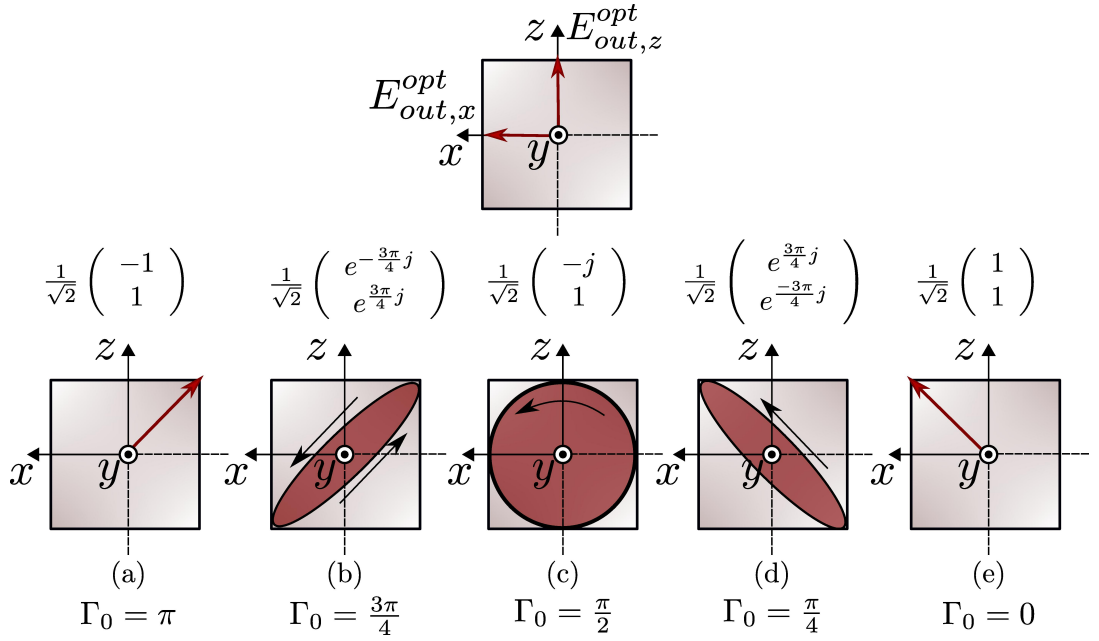
Figure 2.6: Crystal output face with some relevant polarisation states associated with the vector $\mathbf{E}_{out}^{opt}$: linear anti-phase parallel to the analyser ($\Gamma_0 = \pi$), circular ($\Gamma_0 = \frac{\pi}{2}$), in-phase perpendicular to the analyser ($\Gamma_0 = \frac{\pi}{4}$) and two half-way elliptical states ($\Gamma_0 = \frac{3\pi}{4}$ and $\Gamma_0 = \frac{\pi}{4}$).
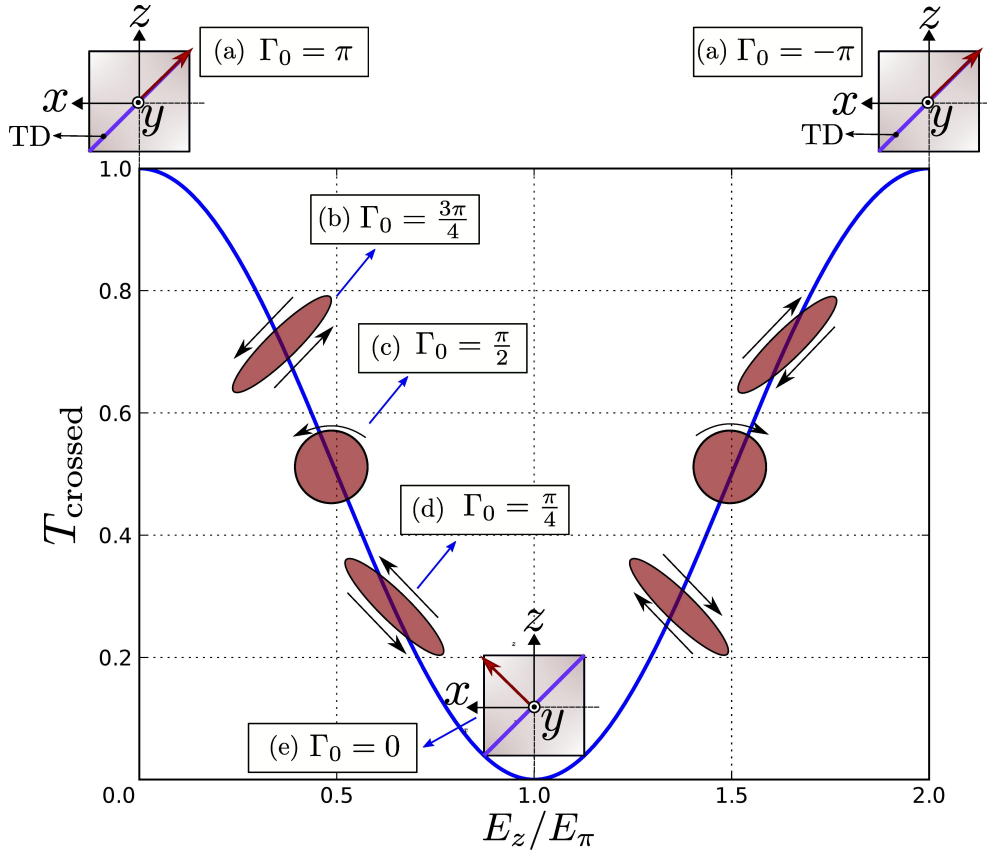
Figure 2.7: Transfer function (eqn. 2.28) with the associated output polarisation states after the crystal also depicted in Figure 2.6.

$E_z = E_\pi$ (the polarisation direction criteria is taken from Figure 2.5). Beyond this point the process is symmetric, but the ellipticity is anticlockwise.

2.3.4 Phase modulation

An alternative arrangement referred to as phase modulation is now considered. In contrast to the amplitude EO modulation, the input and output polarisation through the crystal remain vertical in this case. In order to optimise the modulation, the EO constant r_{33} will be exploited rather than the lower r_{13}, which leads to the z-cut configuration in purely TM mode. The incident optical beam is vertically polarised $\mathbf{E}^{opt}_{vert}(t) = \mathbf{E}^{opt}_{vert}$ in the direction of the extraordinary refractive index n_e (eqn. 2.17) when it enters the crystal sample, as shown in Figure 2.8. If an analyser were set after the crystal, the passing light power would be constant and electric field independent. The effect induced by the crystal is just a phase retardation ϕ_z in the output vertical polarisation vector $\mathbf{E}^{opt}_{vert,out}$:

$$\mathbf{E}^{opt}_{vert,out} = \begin{pmatrix} 0 \\ e^{-j\phi_z} \end{pmatrix} . \tag{2.29}$$

It is possible to use the phase modulator to obtain an interferometric signal. For instance, Figure 2.9 shows a Mach-Zehnder interferometer where a phase modulator has been located in the optical path of each arm of the system. As the optical intensity is split evenly, the initial field vector magnitude $\mathbf{E}^{opt}_{vert}$ becomes $\frac{1}{\sqrt{2}}\mathbf{E}^{opt}_{vert}$ when reaches arms 1 and 2. The optical paths are then phase retarded ϕ_1 and ϕ_2 at points (a) and (b) after the passage through the modulators of equal length L. Both arms are finally recombined at the Interferometric Point (IP). The polarisation is kept vertical along the whole sequence and then the polarisation vector, $\mathbf{E}^{opt}_{inter}$ will be the result of the interference:

$$\mathbf{E}^{opt}_{inter} = \frac{1}{\sqrt{2}} \left(\frac{1}{\sqrt{2}} \mid \mathbf{E}^{opt}_{vert} \mid e^{-j\phi_1} + \frac{1}{\sqrt{2}} \mid \mathbf{E}^{opt}_{vert} \mid e^{-j\phi_2} e^{j\phi_0} \right) = \frac{\mid \mathbf{E}^{opt}_{vert} \mid}{2} \left(e^{-j\phi_1} + e^{-j\phi_2} e^{j\phi_0} \right) , \tag{2.30}$$

where ϕ_0 is the random phase offset between arms. Now the transfer function T_{inter} at the IP is:

$$T_{inter} = \mathbf{E}^{opt,*}_{inter}\mathbf{E}^{opt}_{inter} = \frac{\mid \mathbf{E}^{opt}_{vert} \mid^2}{4} \left(2 + e^{j(\Gamma_{inter}+\phi_0)} + e^{-j(\Gamma_{inter}+\phi_0)} \right) , \tag{2.31}$$
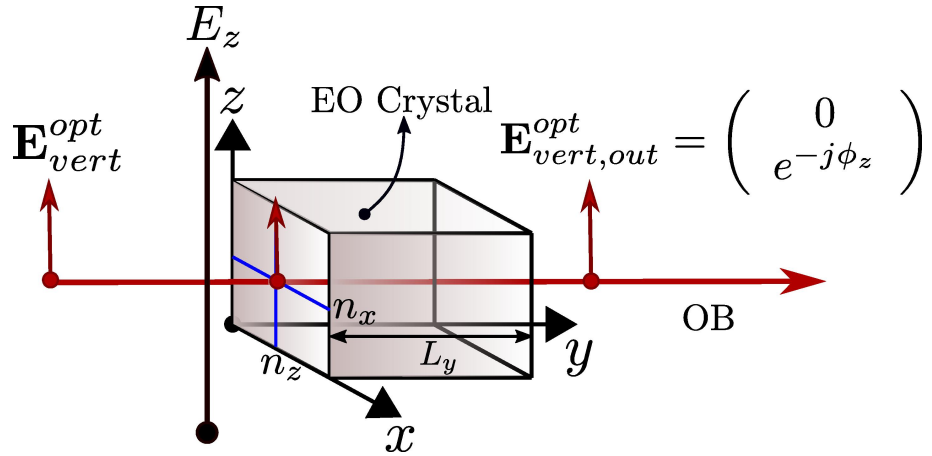
Figure 2.8: Phase modulator configuration where the input and output polarisation states are parallel to the z direction.
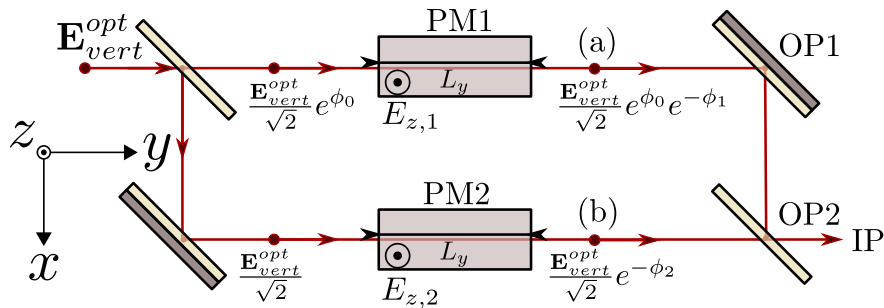
Figure 2.9: Mach-Zehnder interferometer with two LNB crystals (PM1 and PM2) acting as phase modulators placed in each of the two equally long arms.
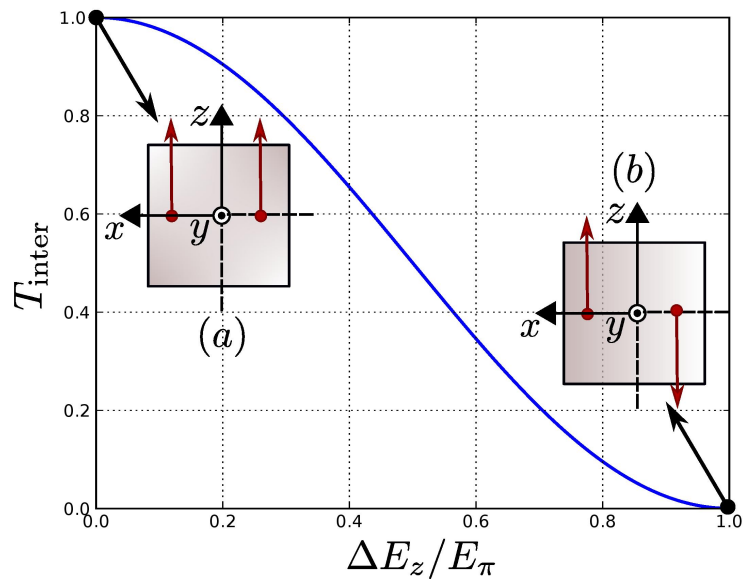
Figure 2.10: Transfer function (eqn. 2.37) for an interferometer phase modulation system from polarisation in phase (a) to anti-phase (b).

with $\Gamma_{\text{inter}} = \phi_1 - \phi_2$. By using the identity $\cos^2(\alpha) = \frac{1}{2}(1 + \cos(2\alpha))$, T_{inter} can be rewritten as:

$$T_{\text{inter}} = \cos^2\left(\frac{\Gamma_{\text{inter}}}{2} + \frac{\phi_0}{2}\right), \tag{2.32}$$

where is assumed that $\mid \mathbf{E}^{opt}_{vert} \mid^2 = 1$. If both arms of the interferometer are equally long, as in Figure 2.9, then $\phi_0 = 0$. Also, Γ_{inter} is a function of the refractive indices $n_{z,1}$ and $n_{z,2}$ of each crystal PM1 and PM2, respectively:

$$\Gamma_{\text{inter}} = \phi_1 - \phi_2 = \frac{2\pi}{\lambda} L_y(n_{z,1} - n_{z,2}), \tag{2.33}$$

where L_y is the crystal length, and the refractive indices $n_{z,1}$ and $n_{z,2}$ depend on the different electric fields applied in each arm $E_{z,1}$ and $E_{z,2}$. Equation 2.14 indicates how the refractive indices n_z change with the field, hence:

$$\phi_{1(2)} = \frac{2\pi}{\lambda} n_e L_y + \frac{\pi}{\lambda} r_{33} n_e^3 L_y E_{z,1(2)}. \tag{2.34}$$

Substituting the field-dependent phase of equation 2.34 in 2.30 and calculating the difference:

$$\Gamma_{\text{inter}} = \phi_1 - \phi_2 = \frac{\pi}{\lambda} L_y r_{33} n_e^3 \Delta E_z, \tag{2.35}$$

where Γ_{inter} is defined as the phase difference between the arms and $\Delta E_z = E_{z,1} - E_{z,2}$. If there were only one modulator in one arm and the other in free space, equation 2.32 can also be applied by simply taking E_z for that specific arm. Let us recall that, in this case, $E_{\pi,\text{inter}}$ is the field difference ΔE_z required to shift Γ_{inter} an amount π, then:

$$E_{\pi,\text{inter}} = \frac{\lambda}{r_{33} n_e^3 L_y}, \tag{2.36}$$

where the subscript "inter" was used to distinguish it from E_π (eqn. 2.24).

Similarly to T_{crossed} for the amplitude modulator configuration, the normalised transfer function T_{inter} is proportional to the transmitted intensity by scaling equation 2.32 properly. Also, the transfer function T_{inter} as a function of $E_{\pi,\text{inter}}$:

$$T_{\text{inter}} = \cos^2\left(\frac{\phi_0}{2} + \frac{\pi}{2}\frac{\Delta E_z}{E_{\pi,\text{inter}}}\right). \tag{2.37}$$

Figure 2.10 shows the transmission as a function of the electric field difference ΔE when $\phi_0 = 0$. If $\Delta E_z = 0$ then the transmission is maximum ($T_{\text{inter}} = 1$) because both arms are in phase. If $\Delta E_z = E_\pi$ the optical beams in both arms are in anti-phase and then the transmission is zero ($T_{\text{inter}} = 0$).

2.3.5 Sensitivity of the EO modulation

The sensitivity S of EO modulation can be defined as the derivative of the transfer function or equivalently, the normalised signal, with respect to the applied field. Let us consider the transfer functions for amplitude and phase modulation given in equations 2.28 and 2.37 respectively, then the sensitivity for each case will be:

$$S_{\text{crossed}} = \frac{dT_{\text{crossed}}}{dE_z} = \frac{\pi}{E_\pi} \sin\left(\frac{\Gamma_0}{2} + \frac{\pi}{2}\frac{E_z}{E_\pi}\right) \cos\left(\frac{\Gamma_0}{2} + \frac{\pi}{2}\frac{E_z}{E_\pi}\right) , \qquad (2.38)$$

$$S_{\text{inter}} = \frac{dT_{\text{inter}}}{d(\Delta E_z)} = \frac{-\pi}{E_{\pi,\text{inter}}} \cos\left(\frac{\phi_0}{2} + \frac{\pi}{2}\frac{\Delta E_z}{E_\pi}\right) \sin\left(\frac{\phi_0}{2} + \frac{\pi}{2}\frac{\Delta E_z}{E_{\pi,\text{inter}}}\right) . \qquad (2.39)$$

Using the identity $\sin\alpha\cos\alpha = \frac{1}{2}\sin(2\alpha)$ the sensitivity simply becomes:

$$S_{\text{crossed}} = \frac{\pi}{2E_\pi} \sin\left(\Gamma_0 + \frac{\pi E_z}{E_\pi}\right) , \qquad (2.40)$$

$$S_{\text{inter}} = \frac{-\pi}{2E_{\pi,\text{inter}}} \sin\left(\phi_0 + \frac{\pi\Delta E_z}{E_{\pi,\text{inter}}}\right) , \qquad (2.41)$$

which implies that the sensitivity changes dynamically when applying an electric field. However, if $E_z \ll E_\pi$ or $E_z \ll E_{\pi,\text{inter}}$, then:

$$S_{\text{crossed}} \simeq \frac{\pi}{2E_\pi} \sin(\Gamma_0) , \qquad (2.42)$$

$$S_{\text{inter}} \simeq \frac{-\pi}{2E_{\pi,\text{inter}}} \sin(\phi_0) , \qquad (2.43)$$

where the negative sign in S_{inter} comes from the fact that increasing the modulating field ΔE_z makes the cosine square function T_{inter} to decrease when $0 \leq \phi_0 \leq \pi$. The results in equations 2.42 and 2.43 show that the sensitivity of the signal depends on the initial offsets Γ_0 and ϕ_0 in the same way for both cases. The most sensitive points are obtained when $dS_{\text{crossed}}/d\Gamma_0 = 0$ and $dS_{\text{inter}}/d\phi_0 = 0$. It can thus be shown that those points are

found when $\Gamma_0 = \phi_0 = \pi/2$, which corresponds to the output circular polarisation for the amplitude modulation scenario. However, since $E_\pi \neq E_{\pi,\text{inter}}$, the interferometric signal is greater for a given same offset ($\Gamma_0 = \phi_0$), by the following factor:

$$k_{C-I} = \frac{S_{\text{inter}}}{S_{\text{crossed}}} = \frac{E_{\pi,\text{inter}}}{E_\pi} = \frac{r_{33}n_e^3}{r_{33}n_e^3 - r_{13}n_o^3} \ . \tag{2.44}$$

Assuming standard values of refractive indices n_o and n_e and EO coefficients r_{13} and r_{33} for LNB [40, 43], $k_{C-I} \simeq 1.45$. Figure 2.11 depicts the absolute sensitivities $|S_{\text{crossed}}|$ and $|S_{\text{inter}}|$ as a function of the phase offsets Γ_0 and ϕ_0 when $E_\pi = E_{\pi,\text{inter}} = 1\,\text{V/m}$ for simplicity:
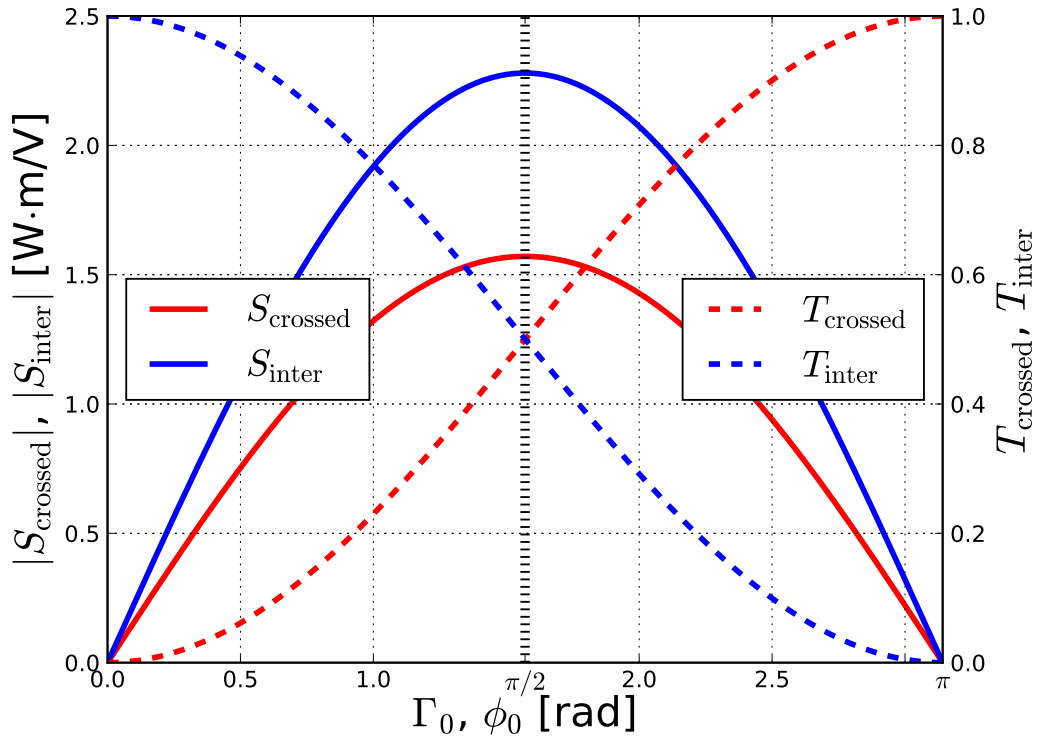
Figure 2.11: Sensitivity and transfer function versus the initial offset phase differences Γ_0 and ϕ_0 for the amplitude and interferometric modulator.

If $E_\pi = 1$ V/m, $S_{\text{crossed}} = \pi/2$ W·m/V and $S_{\text{inter}} = 1.45\pi/2$ W·m/V are the maximum achievable sensitivities by the amplitude modulator and the phase modulator, respectively. This point corresponds to the turning point of the transfer function when $\Gamma_0 = \phi_0 = \pi/2$. In contrast, the minimum sensitivity is zero when the phase offset is such that the transfer function is either maximum or minimum as $dT/dE_z = 0$ at that point.

It should be noted that this mathematical approximation is developed by assuming a small modulating field ($E_z \ll E_\pi$). The advantage of working under this condition is that the signal T is a faithful replica of the field $E_z(t)$ as they both keep a linear relation:

$$T_{\text{crossed}}(E_z) = S_{\text{crossed}}(\Gamma_0) \cdot E_z \,, \qquad T_{\text{inter}}(E_z) = S_{\text{inter}}(\phi_0) \cdot E_z \,. \qquad (2.45)$$

If the modulating field increases, the approximation is not valid anymore and equations 2.40 and 2.41 must be replaced by equation 2.45. It is still possible to couple the dynamic range of $E_z(t)$ to the linear region of the transfer function by selecting the right crystal length L_y and wavelength. Given the equations 2.42 and 2.43, the sensitivity increases with L_y and decreases with λ, so the signal improves by either enlarging the crystal or reducing the wavelength.

2.4   Crystal characterisation

After introducing the fundamentals of the electro-optic theoretical background, some important experimental aspects of LNB are presented. A sample of LNB is a natural birefringent dispersive material, and it also exhibits photorefractivity, ferroelectricity and pyroelectricity. Also, some studies on crystal characterisation are presented to check the agreement with the theory presented in the previous section.

2.4.1   Photorefractive effect

Photorefractivity consists of inducing a long-term modification of the refractive indices when the crystal is under illumination. This effect is caused by imperfections and charge carriers migration in the crystal lattice, however, the complete explanation is still under investigation [44, 45].

Furthermore, the photorefractivity effect is related to the average optical power, and it is wavelength and intensity dependent. In particular, LNB exhibits this effect strongly in the UV and visible parts of the spectrum, but tends to vanish in the infrared and beyond. The crystal must avoid the exposure to green light (533 nm) or shorter wavelengths. In order to prevent potential permanent damage, the crystal samples are usually doped with MgO typically in percentages from 3% mol up to 5% mol. Nevertheless, this only reduces the possibility of intensity-induced damage, but does not expand the usable wavelength range below the cutoff limit at 633 nm.

2.4.2 Lithium niobate as a dispersive material

Lithium niobate is a dispersive material and the refractive indices depends on the wavelength through the empirical Sellmeier equation:

$$n^2(\lambda) = 1 + \frac{B_1\lambda^2}{\lambda^2 - C_1} + \frac{B_2\lambda^2}{\lambda^2 - C_2} + -\frac{B_3\lambda^2}{\lambda^2 - C_3}, \tag{2.46}$$

where the coefficients A_i and B_i can be found in Table 2.2 [46] :

Refractive Index	B_1	C_1	B_2	C_2	B_3	C_3
n_o (LNB)	2.6734	0.01764	1.2290	0.05914	12.614	474.6
n_e (LNB)	2.9804	0.02047	0.02047	0.0666	8.9543	416.08
n_o (MgO:LNB)	2.4272	0.01478	1.4617	1.4617	9.6536	371.216
n_e (MgO:LNB)	2.2454	0.01242	1.3005	0.05313	6.8972	331.33

Table 2.2: Sellmeier parameters for undoped and 5-mol.% MgO doped lithium niobate.

Since LNB is a birefringent material, two sets of constants that correspond to the extraordinary e and ordinary o axes are shown Table in 2.2. Label LNB is used for the non-doped LNB crystal whereas MgO:LNB indicates the sample is 5% mol doped with MgO, which is in fact the same percentage of the crystals installed in the prototype. Figure 2.12(a) depicts the dispersion curve for both cases, and shows how the optical dispersion instead of being dramatically modified by the doping process, remains almost unchanged. Moreover, Figure 2.12(b) points out that the difference $r_{33}n_e(\lambda)^3 - r_{13}n_o(\lambda)^3$ decays very slightly with the wavelength, but from equation 2.24 the impact on E_π is insignificant when compared with the wavelength dependence.

(a)

(b)
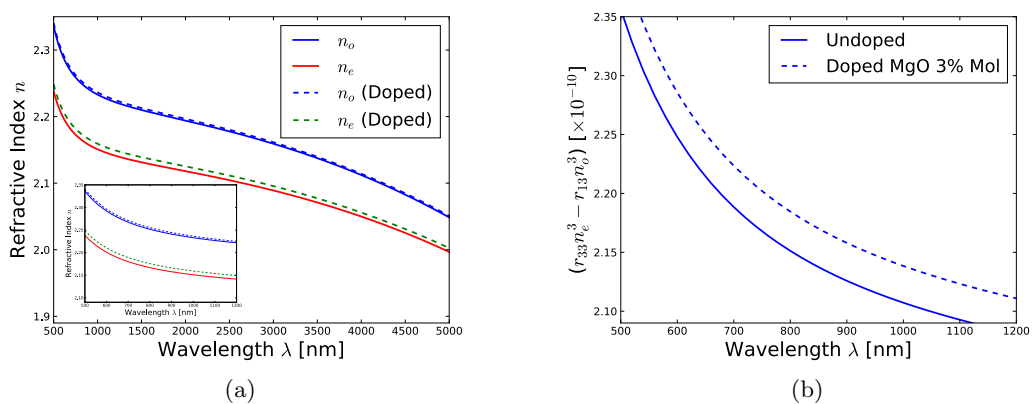
Figure 2.12: (a) Dispersion curve of undoped and 5-mol.% MgO doped lithium niobate; (b) difference $r_{33}n_e^3 - r_{13}n_o^3$ as a function of the wavelength [46].

2.4.3 LNB sample characterisation

This subsection presents the experimental EO characterisation of a LNB crystal of dimensions $(L_x, L_y, L_z) = (5\,\text{mm}, 10\,\text{mm}, 5\,\text{mm})$. Figure 2.13 is a photograph of the characterisation setup where a $633\,\text{nm}$ HeNe laser provides an optical beam to the sample while an electric field E_z is applied on the crystal through a high voltage safety cage. It should be noted that this type of laser has a short linewidth suitable for interferometric applications. The OB is vertically polarised after passing through a Polarising Beam Splitter (PBS) and the crystal is placed in a crossed polarisers system thank to a HWP and an analyser (Fig. 2.5). This arrangement replicates a z-cut configuration in transverse mode where the OB travels along y and the cage applies a voltage V_{applied} on the z-axis of the crystal, so $E_z = V_{\text{applied}}/L_z$.

The safety cage was connected to an external high voltage source that induced a modulation intensity registered by a Newport photodiode (PD) 818-BB-45. As a result, Figure 2.14 is the experimental transfer function using V_{applied} instead of E_z, which is equivalent to the scaled transfer function $I_0 T_{\text{crossed}}$. Here, $I_0 \simeq 64\,\mu\text{V}$ and $V_{\pi,exp} = (1410 \pm 19)\,\text{V}$ are measured experimentally, and are in good agreement with the theoretical value of $V_\pi = E_\pi/L_z = 1398.2\,\text{V}$ obtained from equation 2.24 and using $L_z = 5\,\text{mm}$. The parameter $V_{\text{bias}} = 200 \pm 18\,\text{V}$ accounts for the natural birefringence of the crystal, since it is the voltage required to shift back the output polarisation to an in-phase state ($\Gamma_0 = 0$).
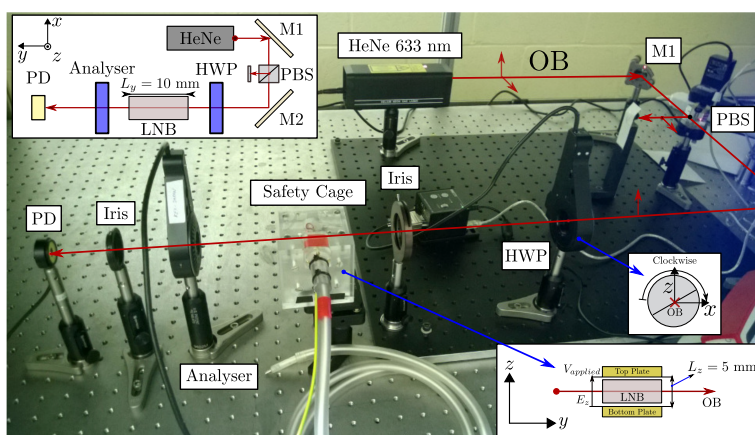
Figure 2.13: Experimental electro-optic characterisation setup.

The maximum I_0 and minimum power points in the experimental transfer curve correspond to the linear polarisation states, in particular, the parallel and perpendicular orientation of the analyser position, respectively. However, one can observe that the minimum of the curve does not reach a zero-light position. The reason can be explained
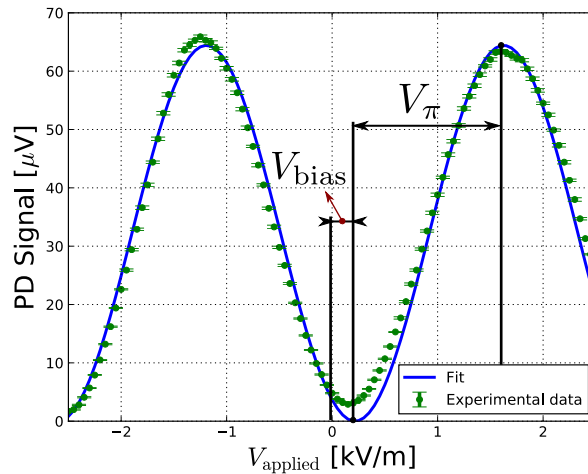
Figure 2.14: Experimental transfer function for a 10 mm long and 5 mm thick LNB sample.

from the rather poor contrast of the linear polarisation provided by the PBS, since some ellipticity still remains at the minimum point. The circular state is found to be in the half-maximum point (at ~ 38 μV), and the intermediate points correspond to transition elliptical states.

A polarisation scan is the plot of the transmitted power registered by a detector or a power meter while rotating the Transmission Direction (TD) of the analyser. In this thesis, the rotation is defined as anticlockwise by increasing the angle θ_{TD} (see Fig. 2.15). Also, if the input polarisation into the crystal is kept constant at $2\theta = 45°$ with respect to the x-axis (Fig. 2.13), then $\pm 45°$ are in principle the only two possible orientations of the major axis of the typical output elliptical polarisation after the crystal.
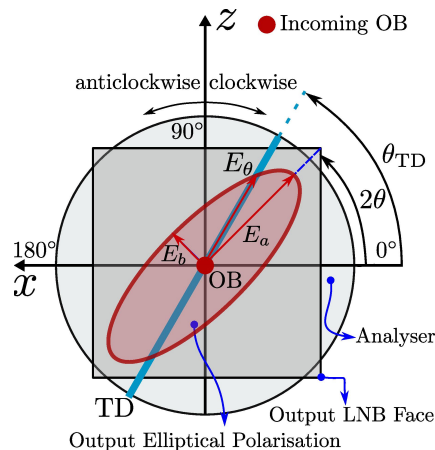
Figure 2.15: Polarisation scan mechanism represented from the crystal output face view. Angles θ_{TD} and 2θ determine the directions of the transmission direction of the analyser and the input polarisation, respectively.

Figure 2.16(a) is a set of various polarisation scans taken at different voltages, that is, different modulating fields. For each scan, the analyser position θ_{TD} determines the transmitted power in the way expressed in the following equation:

$$P_{\text{scan}}(V, \theta_{\text{TD}}) = P_{max}(V) \cdot \cos^2(\theta_{\text{TD}} - 2\theta) + P_{\text{offset}}(V) \cdot \sin^2(\theta_{\text{TD}} - 2\theta). \qquad (2.47)$$

Equation 2.47 was employed to calculate the fit curves that are plotted as continuous curves in Figure 2.16(a) along with the experimental scans. Furthermore, the polarisation projections $(E_a, E_b)^T$ can be calculated from the fit curve, since the square of the major E_a and minor E_b ellipse axes lengths are proportional to the power transmitted in their respective directions, hence, $E_a^2 \propto P_{max}$ and $E_b^2 \propto P_{\text{offset}}$. In fact, for a general position θ_{TD} of the analyser, $P_{\text{scan}}(V, \theta_{\text{TD}}) \propto | E(V, \theta_{\text{TD}} - 2\theta) |^2 = E_a^2 \cos^2(\theta_{\text{TD}} - 2\theta) + E_b^2 \sin^2(\theta_{\text{TD}} - 2\theta)$ leads to equation 2.47. Thereby, the polarisation projection can be obtained mathematically from the components E_a and E_b as follows:

$$\begin{pmatrix} E_x \\ E_z \end{pmatrix} = \begin{pmatrix} \cos 2\theta & -\sin 2\theta \\ \sin 2\theta & \cos 2\theta \end{pmatrix} \begin{pmatrix} E_a \cdot \cos \theta_{\text{TD}} \\ E_b \cdot \sin \theta_{\text{TD}} \end{pmatrix}. \qquad (2.48)$$

Equation 2.48 is used to fit the scans in Figure 2.16(a) to obtain the polarisation projections shown in Figure 2.16(b). Each scan corresponds to a particular position of the transmission curve (Fig. 2.14): for 158 V, the scan is taken close to the minimum and thus the expected linear polarisation leads to a high contrast curve. As the voltage increases, 566 V and 883 V, the contrast decreases meaning that the polarisation is becoming circular. At 1290 V, the voltage is near the maximum and the contrast has been inverted from the original position at 566 V. Finally, the polarisation is the most linear at 1600 V as it is even closer to the maximum.

It is interesting to observe that the analyser position for the minimum and maximum values of the scan curves in Figure 2.16(a) appear shifted for the almost circular states (566 V and 883 V) when compared to the linear states (e.g. 158 V). This means that the projections E_a and E_b are aligned close to the horizontal and vertical axes rather than the expected directions at $45°$ or $-45°(135°)$ (Fig. 2.15). In general, this tendency has been observed persistently when the output polarisation approaches to circular polarisation. This is due to the fact that in reality, the input polarisation is not totally linear but it
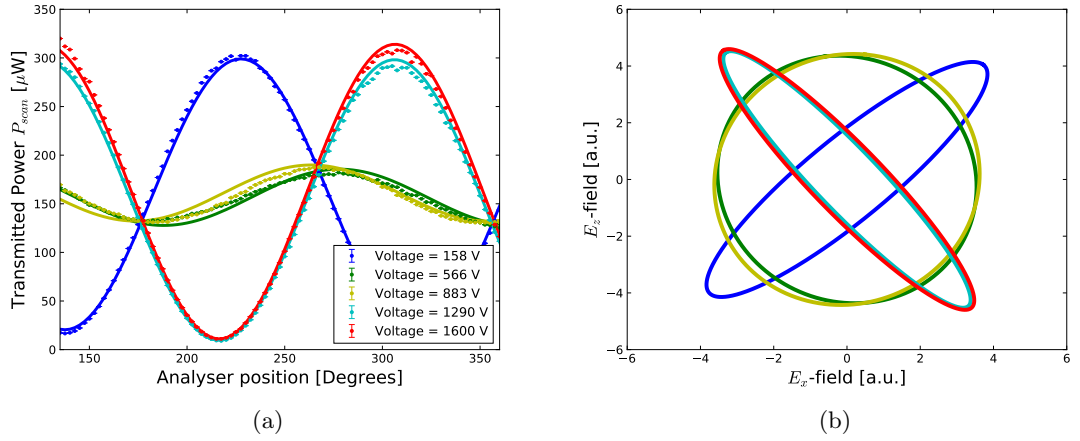
Figure 2.16: Experimental polarisation scans from $135°$ (points) and fits (continuous curve) (a) of the different polarisation states (b).

carries a certain degree of polarisation dispersion, in combination with the fact that its direction is not perfectly oriented at $45°$ with respect to the x-axis at the input face, which either way causes the initial state not to be split evenly among the x and z directions.

For instance, let us assume that the projection in z (E_z) of the input polarisation $\mathbf{E}_{in}^{opt} = E_x + E_z$ is slightly higher than in x (E_x), particularly $\mid E_z \mid = \mid E_x \mid + \mid E_V \mid$ where E_V is a very small extra contribution in the z direction, thus $\mid E_x \mid \gg \mid E_V \mid$. In this case the polarisation at the output face is effectively formed by the ideal projection with elliptical axes E_a and E_b obtained from a perfect split, accompanied with the minor vertical component E_V, as shown in Figure 2.17.
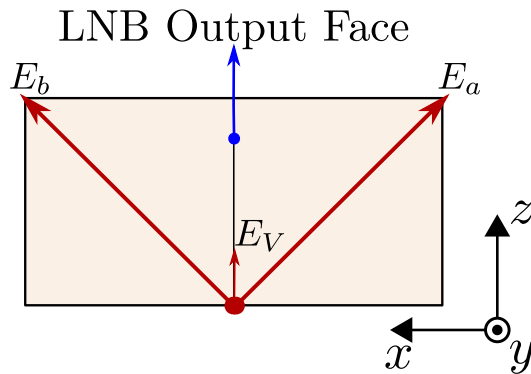
Figure 2.17: Diagram of the output face of lithium niobate along with the elliptical axes projections of the polarisation state oriented at $45°$ and $-45°$.

When $E_a \gg E_b$ the output state will be a high contrast linear polarisation with a maximum in the polarisation scan that corresponds to the direction of E_a, at $45°$. The

33

same argument can be applied vice-versa when the polarisation swaps to the opposite state ($E_b \gg E_a$), driving the maximum, equivalently, to $-45°$. However, when the output polarisation is approaching the circular state, the elliptical axes of the polarisation become comparable, and eventually $E_a \simeq E_b$. In this scenario, any projection of the output polarisation should lead to a flat polarisation scan. Nevertheless, the extra component E_V induces a small ellipticity, that effectively drifts the polarisation axes E_a and E_b to the vertical and horizontal directions. That is why the experimental scans for the most circular states reveal a maximum that corresponds to the major elliptical axis at $90°$.

2.5 High frequency modulation considerations

In the previous sections, the theoretical framework has been developed assuming a constant DC or low frequency f_m of the modulating field in the crystal. However, often the modulating field $E(t)$ applied is a very fast-changing function of time, the optical phase no longer follows the time-varying refractive index adiabatically. In this event, the light signal output is bandwidth-limited due to the phase velocity mismatch. Let us define the transit time τ for an optical beam propagating through an EO crystal and polarised on a direction of refractive index n to be:

$$\tau = \frac{n\,L_y}{c}\,, \tag{2.49}$$

where c is the speed of light and $n = n_z = n_e = 2.18$ at 780 nm (Fig. 2.12(a)) is the extraordinary index of refraction of LNB, since r_{33} is the most relevant EO coefficient used for phase modulation in the z-direction. Also, the modulation depth φ is the phase addition across the optical path through the crystal (eqn. 2.14) due to the modulating field E_z, hence:

$$\varphi(E_z) = \frac{\pi}{\lambda}\,n_e^3\,r_{33}\,L_y\,E_z = \frac{\omega_{opt}}{2c}\,n_e^3\,r_{33}\,L_y\,E_z = \Lambda \cdot L_y\,, \tag{2.50}$$

where ω_{opt} is the angular frequency of the OB and $\Lambda = \frac{\pi}{\lambda}n_e^3 r_{33}E_z$. Assuming the crystal is between electrodes in a lumped modulator fashion, the modulation depth is then reduced due to the finite transit time by a factor κ, defined as follows [39]:

$$\kappa = \frac{\sin\frac{1}{2}\omega_m\tau}{\frac{1}{2}\omega_m\tau} = \frac{\sin\frac{\omega_m n_z L_y}{2c}}{\frac{\omega_m n_z L_y}{2c}}\,, \tag{2.51}$$

where $\omega_m = 2\pi f_m$ is the angular frequency of the field applied. Therefore, the optical modulation extent in the crystal is frequency-dependent:

$$\varphi = \Lambda \cdot L_y \cdot \kappa = \Lambda \cdot L_y \cdot \frac{\sin \frac{1}{2}\omega_m\tau}{\frac{1}{2}\omega_m\tau} . \tag{2.52}$$

When $\tau \ll \pi/\omega_m$, that is, $\kappa \simeq 1$, the optical modulation is linearly proportional to the crystal length; in other terms, the crystal is operating in a low-frequency regime. As the transit time increases until being comparable to π/ω_m, the reduction factor κ becomes relevant to determine the bandwidth of the modulator. The κ-decay relation with $\omega_m\tau$ is illustrated in Figure 2.18:
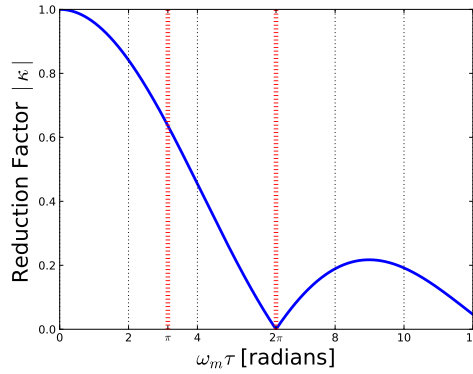
Figure 2.18: Reduction factor κ as a function of $\omega_m\tau$.

Given a crystal length L_y, the modulation is always maximum when applying a DC field ($\omega_m\tau = 0$, $\kappa = 1$). As soon as the field becomes time-varying, that is, $\omega_m\tau \neq 0$, the reduction factor drops from 1 to 0 at $\omega_m\tau = 2\pi$. Figure 2.19 shows the decay behaviour of the modulation depth as a function of the modulating frequency f_m for different typical crystal lengths. Alternatively, Figure 2.20(a) depicts φ against the crystal length for different frequency values of the modulating field. In this case, $\varphi = 0$ when the length is zero as a direct result of applying equation 2.52. In fact, the modulation extent increases linearly with the crystal length following equation 2.52 until κ is no longer almost 1. The criteria to establish the upper limit φ_{linear} of the linear regime is taking $\kappa = 0.95$ at a length L_{linear}. However, beyond that point enlarging the crystal still enhances the modulation due to the term L_y in equation 2.52. In particular, for $\omega_m\tau = \pi$ the reduction factor κ becomes more overriding and the curve reaches the maximum depth modulation φ_{max} (at this point, according to equation 2.51, $\kappa = 0.64$). Figure 2.20(b) also shows a detail of these parameters for $f_m = 12\,\text{GHz}$.
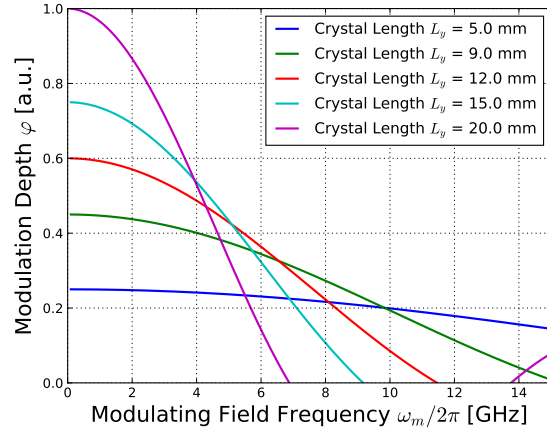
Figure 2.19: Modulation depth against frequency of the modulating field for the extraordinary refractive index n_e.

(a)

(b)
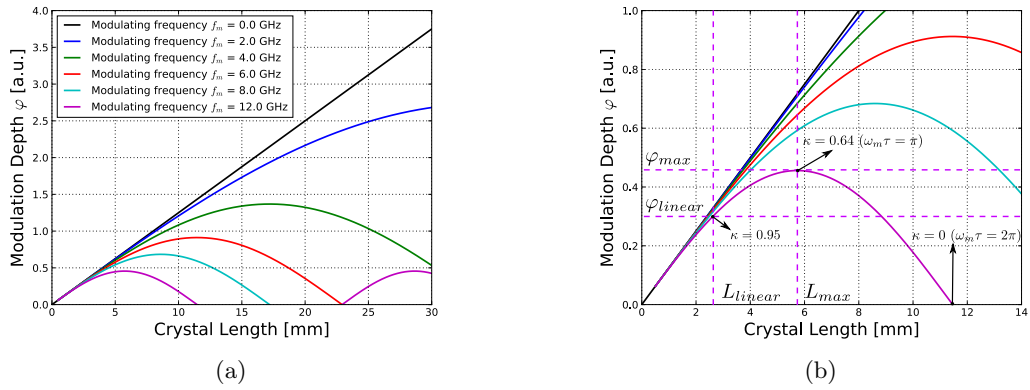
Figure 2.20: (a) Modulation depth against crystal length for the extraordinary refractive index n_e; (b) zoomed in amplification until $14\,\mathrm{mm}$ with labels to mark the linear and maximum modulation regimes for the case $f_m = 12\,\mathrm{GHz}$.
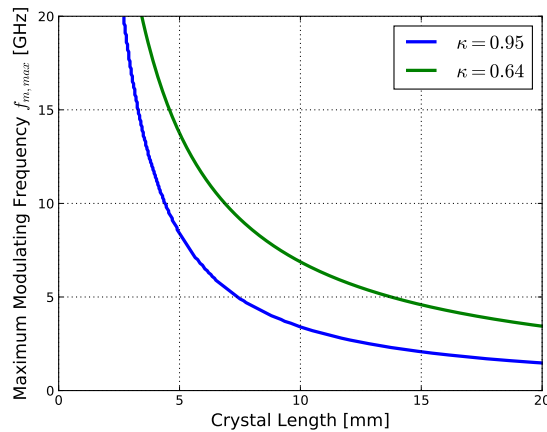
Figure 2.21: Maximum modulating frequency as a function of the crystal length L_y in the linear ($\kappa = 0.95$) and maximum modulation ($\kappa = 0.64$) regimes for LNB with $n_e = 2.18$.

In general, since $\omega_{m,max}\tau = \pi$ corresponds to the maximum bandwidth $f_{m,max}$, for a given crystal length:

$$f_{m,max} = \frac{c}{2L_y n_{o(e)}} \ .$$ (2.53)

Alternatively, the maximum length L_{max} for a given frequency f_m can be obtained from 2.53 by replacing $L_y = L_{max}$ and $f_{m,max} = f_e$. Inspecting Figure 2.21 provides a quick determination of the modulator bandwidth given a certain crystal length.

If we now consider the amplitude modulator configuration, the previous analysis can be repeated for the linear combination of both x and z projections. This means that, two different reduction factors κ_o and κ_e, caused by the refractive indices $n_{o(x)}$ and $n_{e(z)}$ (eqn. 2.51), are applied. Considering the phase difference presented in equation 2.22:

$$\varphi_{\mathrm{RF}} = \frac{\omega_m}{2c}\, E_z\, L_y\, (n_e^3 r_{33} \kappa_e - n_o^3 r_{13} \kappa_o)\,,$$ (2.54)

where φ_{RF} from equation 2.54 defines the modulation depth for an amplitude modulator in a high-frequency ω_m scenario. In reality, the difference between a single-direction φ and amplitude φ_{RF} modulations is rather minimal. For instance, Table 2.3 provides the maximum lengths L_{max} at different RF modulating frequencies for phase modulation φ_{max} in comparison to the amplitude modulation $\varphi_{\mathrm{RF,max}}$; in both cases, the results were obtained by applying the analysis shown in Figure 2.19.

f_m [GHz]	$L_{max}[\varphi_{max}]$ [mm]	$L_{max}[\varphi_{\mathrm{RF,max}}]$ [mm]
3	22.85	23.3
4	17.15	17.5
5	13.7	14.0
6	11.40	11.65
7	9.75	10.0
8	8.55	8.75

Table 2.3: Maximum lengths L_{max} for different RF modulating frequencies f_m.

This section presents a lumped EO modulator approach to the system. However, the modulating field E_z in the real scenario is not evenly distributed along the OB direction but follows the bunch shape. If the modulating signal travelled at the same speed as the OB, then the phase-matching would increase the bandwidth. The field propagation into the crystal will be studied in detail later in chapter 4 with numeric simulations.

2.6 Summary

This chapter presents the theoretical background that explains the optical modulation in lithium niobate. The fundamental principle of the prototype is the Pockels effect, whose main characteristic is the linear relation between the modulation and the electric field applied on the crystal.

Two possible optical systems are proposed: a crossed polarisers configuration that emulates an EO amplitude modulator, or an interferometric design inspired by an EO phase modulator. In both cases, the crystal is oriented in a z-cut configuration in transverse mode where the OB travels along the crystallographic y-axis. The pickups of the prototype replicate the crossed polarisers arrangement so the mechanism responsible for the optical modulation has been detailed. The output polarisation of the crystal is modified by an electric field applied across z, particularly, the polarisation shifts between two linear polarised states perpendicular one to the other, passing by intermedium elliptical states including a circular polarisation output at exactly the halfway point. This polarisation change is converted into a light intensity signal after passing the analyser. In addition, the sensitivity when the modulating field E_z is much lower than the crystal parameter E_π has been analysed, concluding that the linear states are almost insensitive at all whereas the circular state is the optimal point.

Lithium niobate is the key element of this project, this chapter also considers some relevant properties, such as the optical dispersion or the photorefractive effect that sets $633\,\mathrm{nm}$ as the lowest usable wavelength. Moreover, an experimental electro-optic characterisation of a LNB sample is presented as study case to validate the main crystal parameters that determine the output polarisation and the modulation performance, being those the natural birefringence and E_π.

Lastly, the dependency of the EO modulation with the frequency has been studied assuming a lumped modulator approximation. The main conclusion is that the crystal length L_y constrains the minimum bandwidth of the system, for instance, if the detection of a certain HT instability requires $6\,\mathrm{GHz}$ bandwidth, the crystal length cannot exceed $11.65\,\mathrm{mm}$. In the real scenario, the modulating field E_z at a given instant t is not evenly distributed along the OB direction in y but follows the bunch shape, then the phase-matching condition and bandwidth limitations would vary.

Chapter 3

Electro-Optic BPM concept at SPS

3.1 Coulomb field of a proton bunch at SPS

This chapter analyses the Coulomb field shape and strength of the proton bunch at the Super Proton Synchrotron (SPS) over the radial position. In particular, an analytical approach is presented to estimate the modulating field in the Electro-Optic (EO) crystal responsible for the optical modulation in the pickup.

3.1.1 Coulomb field of a relativistic proton

The Coulomb field time profile is strongly dependent on the particle energy. For a proton at rest, the Coulomb field $\mathbf{E}_p$ at a certain distance r spreads radially:

$$\mathbf{E}_p(\mathbf{r}) = \frac{e_0}{4\pi\epsilon_0 r^2} \cdot \mathbf{r}, \tag{3.1}$$

where e_0 is the proton charge, ϵ_0 is the vacuum permittivity and $\mathbf{r}$ the radial position vector. If the particle is accelerated to a velocity v close to the speed of light c ($\beta \to 1$), the Coulomb field is compressed along the bunch direction of travel. The propagating Coulomb field is no longer isotropic, in fact, the compactness along the transversal direction increases with the Lorentz factor γ $\left(\gamma^2 = \frac{1}{1-\beta^2}\right)$. At high energies, the electric field strength measured at a certain distance r will be now given as follows [47]:

$$\mathbf{E}_p(\mathbf{r}) = \frac{e_0}{4\pi\epsilon_0\gamma^2} \cdot \frac{1}{1 - \beta^2 \sin^2 \Psi} \cdot \frac{\mathbf{r}}{r^3}, \tag{3.2}$$

where the vector $\mathbf{r}$ is lined up along the direction from the observation point O to the

particle position, and Ψ is thus the angle subtended between the velocity $\mathbf{v}$ and $\mathbf{r}$, as Figure 3.1 illustrates:
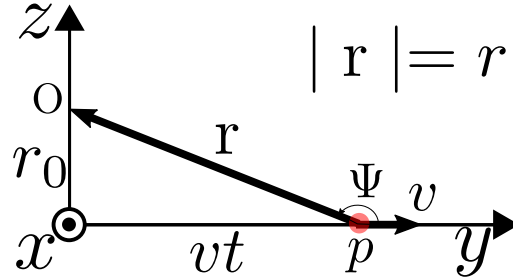
Figure 3.1: Relativistic proton diagram.

Equation 3.2 indicates how the Coulomb field lines are packed transversally with an opening angle $2/\gamma$ [47]. As a result of the compactness, the electric field projection along the motion direction y ($\Psi = 0, \pi$) decreases by a factor γ^{-2} compared to the isotropic field given in equation 3.1, whereas the transverse component along z ($\Psi = \pi/2$) is larger by a factor γ. Therefore, it turns out that the field along the longitudinal direction y can be omitted when γ is sufficiently high.

Using cylindrical coordinates (r_0, y, Θ) with $r_0 = \sqrt{z^2 + y^2}$ and $\Theta = \arctan(y/x)$, the radial transverse component E_{r_0} at the observation point O can be defined as [47]:

$$E_{r_0} = E_p(r_0, t) = \frac{e_0 \gamma}{4\pi\epsilon_0} \cdot \frac{r_0}{(r_0^2 + \gamma^2 v^2 t^2)^{3/2}} \,, \tag{3.3}$$

which, provides the transverse projection of the Coulomb field as a function of time t for a relativistic single particle at a certain distance r_0 from the motion direction. The longitudinal projection along the y direction is a factor $1/\gamma^3$ smaller than the transverse projection given by equation 3.3 and thereby, the contribution parallel to the bunch velocity will be negligible for ultrarelativistic particle bunches.

3.1.2 Time-profile field for a proton bunch

The charge density $\rho(t)$ for a bunch populated with N_p protons at SPS, typically follows a Gaussian distribution:

$$\rho(t) = \frac{N_p}{\sigma\sqrt{2\pi}} e^{-t^2/2\sigma^2} \,. \tag{3.4}$$

From equation 3.4 above, the bunch length can be defined in units of time as 4σ. Let us assume a perfectly on axis proton bunch, then, the transverse Coulomb field E_{bunch}

40

at a certain distance r_0, is given by the convolution of the single particle electric field E_p and the charge density $\rho(t)$:

$$E_{\text{bunch}}(r_0, t) = E_p(r_0, t) * \rho(t). \tag{3.5}$$

Equation 3.5 provides the time profile of the transverse electric field projection. Let α be the angle subtended by the propagating direction of the Coulomb field with the transverse direction z, then $\alpha = 1/\gamma$. Increasing γ enough implies that equation 3.5 becomes the total electric field strength as the longitudinal contribution vanishes. By increasing the energy, the bunch length 4σ gradually matches the time profile provided by equation 3.5 until becoming a replica of the bunch profile. Also, applying the Fourier transform over the equation 3.5 provides the electric field in frequency domain:

$$E_{\text{bunch}}(r_0, \omega) = \text{FT}[E_p(r_0, t) * \rho(t)](\omega) = \sqrt{2\pi} \cdot \text{FT}[E_p(r_0, t)](\omega) \cdot \text{FT}[\rho(t)](\omega), \tag{3.6}$$

where ω is the angular frequency, hence:

$$E_{\text{bunch}}(r_0, \omega) = \frac{N_p e_0}{2\sqrt{2}\pi^{3/2}\gamma v^2 \epsilon_0} e^{-\frac{1}{2}\sigma^2\omega^2} \mid \omega \mid \text{K}_1\left(\frac{\mid \omega \mid r_0}{\beta\gamma c}\right), \tag{3.7}$$

where K_1 is the modified Bessel function of the second type (see appendix A). Assuming a perfect on-axis position, Figures 3.2(a) and 3.2(b) show the time profile (eqn. 3.5) and the frequency components (eqn. 3.7) for the nominal $4\sigma = 1$ ns SPS bunch of $1.15 \cdot 10^{11}$ protons at top energy 450 GeV:

(a)   (b)
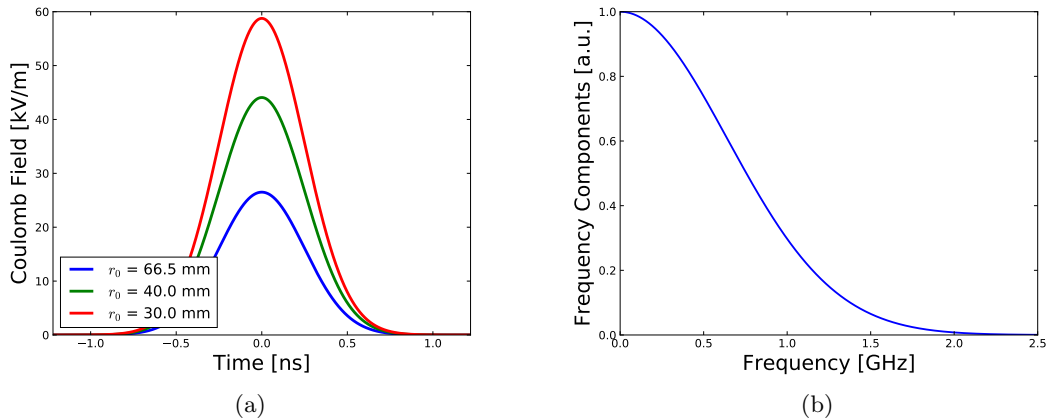
Figure 3.2: (a) Time profile and (b) frequency spectrum for a rigid mode bunch with the nominal SPS parameters.

Figure 3.2(a) shows that the peak value of the Coulomb field at 66.5 mm, which corresponds to the typical pipe radius of the SPS machine, is $\sim 24\,\mathrm{kV/m}$. Qualitatively, Figure 3.2(a) proves how the time profile obtained from equation 3.5 converges to the nominal 1 ns bunch length at 450 GeV. Also, the frequency range goes up to 1.2 GHz and depends exclusively on the bunch length. At this order of frequency components, the EO effect relies on the clamped EO coefficients r_{13}^S and r_{33}^S from Table 2.1. It is also important to consider the wide dynamic range in terms of bunch charge in a SPS scenario, that comes from $5 \cdot 10^9$ protons (0.80 nC) for the pilot bunch up to $5 \cdot 10^{11}$ protons (80 nC) for the nominal, which will be considered the general case in the rest of the chapter.

3.1.3 Coulomb field decay and crystal interaction at SPS

This section studies the shape and peak field decay of the Coulomb field over the transverse distance given the SPS parameters, as well as the interaction with a LNB sample placed at a certain distance r_0 from the passing bunch. As seen in Figure 3.2(a) from the previous section, the field time-profile is almost perfectly coincident with the bunch length. This result implies that the angle subtended by the propagating Coulomb field shown in Figure 3.3(a), that is $2\alpha = 2/\gamma \simeq 1/240$ ($\gamma = 480$), can be considered insignificant for a SPS bunch. Thereby, the electric field lines are almost perfectly transversal as sketched in Figure 3.3(b):

(a) (b)
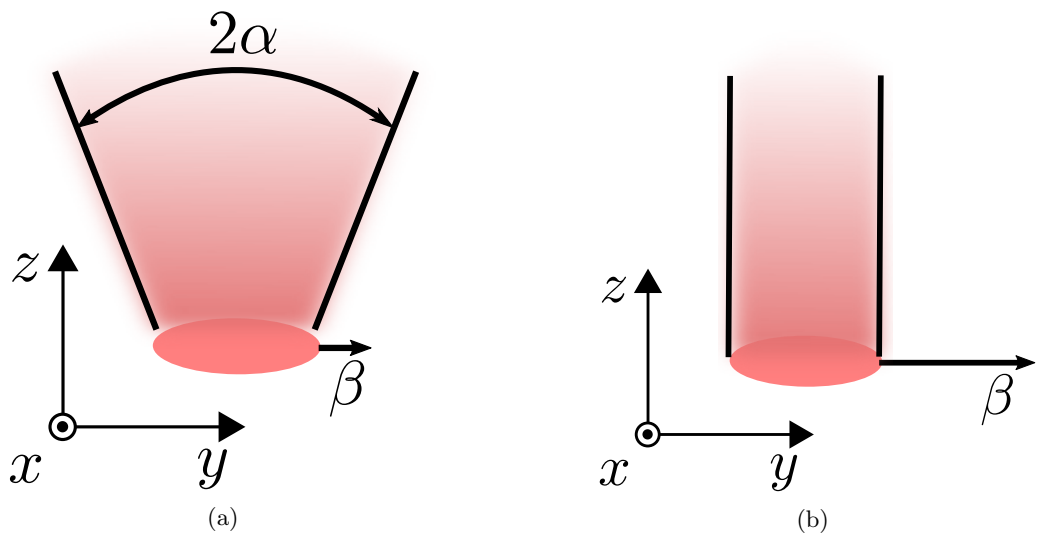
Figure 3.3: Propagating Coulomb field for (a) $\beta \ll 1$ and (b) $\beta \simeq 1$.

Figure 3.4 shows the angle α as a function of the energy in a range that covers up to the SPS top energy, at $450\,\mathrm{GeV}$. The angle subtended α is never greater than about $\sim 2°$ between $26\,\mathrm{GeV}$, which is the SPS pilot energy, and 450 GeV. This implies that the length of the field time-profile and the charge density function $\rho(t)$ are almost equal. In consequence, the electric field lines can be assumed to propagate totally transversal for any energy value at SPS and also for the LHC.

Moreover, applying the Fourier transform properties over the equation 3.5, the time-profile can be obtained as an inverse Fourier of $E_{\mathrm{bunch}}(r_0, \omega)$ (eqn. 3.7):

$$E_{\mathrm{bunch}}(r_0, t) = \frac{N_p e_0}{2\sqrt{2}\pi^{3/2}\gamma v^2 \epsilon_0} \cdot \mathrm{FT}^{-1}\left\{ e^{-\frac{1}{2}\sigma^2\omega^2} |\omega| \mathrm{K}_1\left[\frac{r_0 \cdot |\omega|}{v\gamma}\right] \right\}, \tag{3.8}$$

expanding $\mathrm{K}_1\left[\frac{r_0 \cdot |\omega|}{v\gamma}\right]$ around the maximum at $\omega = 0$:

$$\mathrm{K}_1\left[r_0\omega/c\gamma\beta\right] = c\gamma\beta/r_0\omega + ... \tag{3.9}$$

Since $e^{-\frac{1}{2}\sigma^2\omega^2}|\omega|\mathrm{K}_1\left[\frac{r \cdot \omega}{c\gamma\beta}\right]$ is a well-behaved, real, and even function, the expansion around $\omega = 0$ corresponds to the maximum electric field value E_{max} at $t = 0$ in the time profile when operating the inverse Fourier transformation. Therefore, substituting $\mathrm{K}_1\left[r_0\omega/c\gamma\beta\right] \simeq c\gamma\beta/r_0\omega$ in equation 3.8 gives [48]:

$$E_{\mathrm{bunch}}(r_0, t) = \frac{N_p e_0}{2\sqrt{2}\pi^{3/2}v\epsilon_0 r_0} \cdot \mathrm{FT}^{-1}\left\{ e^{-\frac{1}{2}\sigma^2\omega^2} \right\}, \tag{3.10}$$

which leads to a gaussian-like first-order approximation of the time-profile with the same maximum as equation 3.5:

$$E_{\mathrm{bunch}}(r_0, t) = \frac{N_p e_0}{2\sqrt{2}\pi^{3/2}v\sigma\epsilon_0 r_0} \cdot e^{-\frac{t^2}{2\sigma^2}}, \tag{3.11}$$

therefore, the peak-field E_{max} is obtained when equation 3.11 is evaluated at $t = 0$:

$$E_{max}(r_0, t = 0) = E_{max} = k_0 \cdot \frac{N_p}{\beta\sigma} \cdot \frac{1}{r_0}, \tag{3.12}$$

with:

$$k_0 = \frac{e_0}{2\sqrt{2}\pi^{3/2}c\epsilon_0}. \tag{3.13}$$
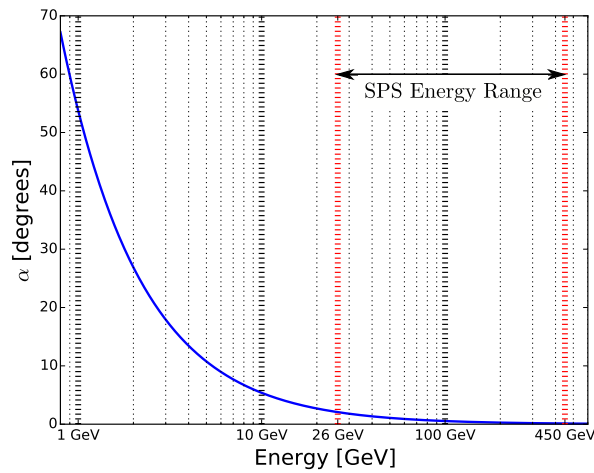
Figure 3.4: The angle α subtended by the bunch Coulomb field as a function of proton energy. The SPS energy range covers from injection at $26\,\mathrm{GeV}$ up to $450\,\mathrm{GeV}$.
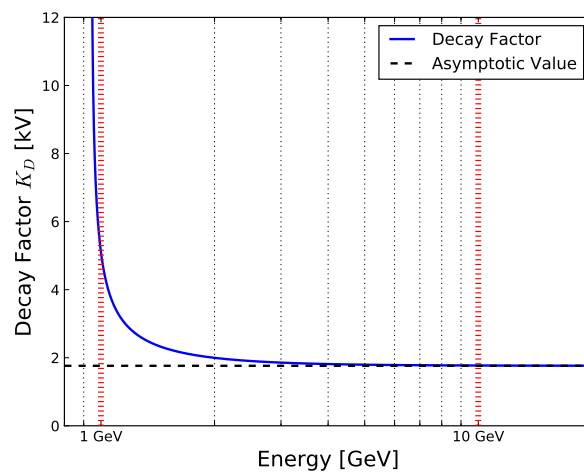
Figure 3.5: Decay factor K_D as a function of energy for a nominal SPS bunch.
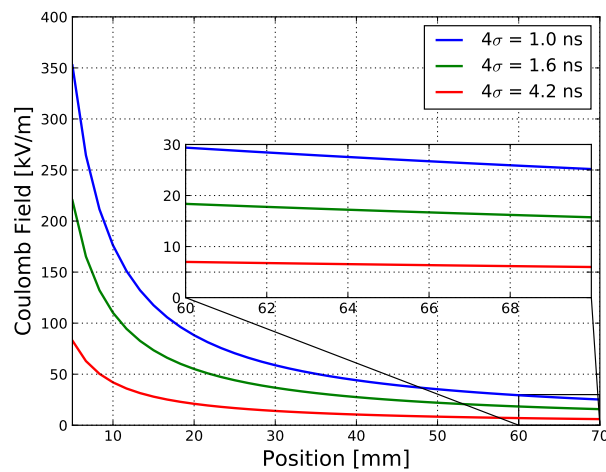
Figure 3.6: Coulomb field peak as a function of the transverse radial distance r_0.

44

Considering $\beta \simeq 1$ for SPS proton bunches, the maximum electric field at a given position r_0 depends strictly upon the charge and also the bunch length through σ. Equation 3.12 accurately predicts how the maximum strength of the Coulomb field E_{max} decays with $1/r_0$ as it propagates in vacuum. In fact, equation 3.11 replicates almost perfectly the profiles shown in Figure 3.2(a) that are obtained from the convolution in equation 3.5. Figure 3.5 shows the tendency of the decay factor, defined as $K_D = k_0 \frac{N_p}{\beta \sigma}$, to reach the asymptotic value $K_D = 1.76\,\text{kV}$, when $\beta \simeq 1$, as the energy increases. For energies beyond $10\,\text{GeV}$, the peak field does not depend on energy anymore but on the charge and length. Therefore, the Coulomb field lines are distributed transversally from the lowest energy at the pilot bunch scenario. Needless to mention, this profile will remain unchanged or may be even shorter after the injection into the LHC machine.

Let us consider now an EO crystal located at $r_0 = r_{\text{crystal}}$. Equation 3.12 is valid for a Coulomb field propagating in vacuum before reaching the crystal ($r_0 < r_{\text{crystal}}$). When passing into the dielectric material ($r_0 > r_{\text{crystal}}$), the field now propagates through a medium with a permittivity $\epsilon = \epsilon_0 \epsilon_{\text{crystal}}$, where $\epsilon_{\text{crystal}}$ is the relative permittivity of the crystal that will also be referred as dielectric constant in this thesis. The substitution of the permittivity ϵ in the equation 3.12 indicates a discontinuity of the propagating field $E_{\text{bunch}}(t)$ at the interface point $r_0 = r_{\text{crystal}}$. If the crystal is anisotropic, the permittivity is defined by a tensor, and the field is expected to drop by a factor $1/\epsilon_{\text{crystal}}$.

The EO modulation is caused by the electric field propagating inside the crystal. For instance, Figure 3.6 depicts the peak field as a function of the transverse distance r_0 for nominal SPS parameters. It clearly shows the $1/r_0$ decay of the maximum field for different bunch lengths. Using $r_{\text{crystal}} = r_{\text{LNB}} = 66.5\,\text{mm}$ the position where the propagating field encounters the LNB interface of dielectric constant $\epsilon_{\text{crystal}} = \epsilon_{\text{LNB}} = 30$, then the order of the electric field strength inducing the EO modulation is $0.56\,\text{kV/m}$ and $0.89\,\text{kV/m}$ for pilot and nominal bunches of lengths $1.6\,\text{ns}$ and $1.0\,\text{ns}$, respectively.

3.2 Concept of electro-optic pickup design

3.2.1 Mechanism of Coulomb field attraction

Externally, the EO pickup resembles a metallic button that can potentially produce an EO signal on its own or in combination with another EO pickup in the same plane. The EO crystal is the key component that encodes the bunch field strength according to the

Pockels effect and it is embedded in the very core of the EO pickup. The crystal is located between two right angle prisms that conduct the optical path through the crystal and reflect it back. The optical state of the emerging light after the crystal is modified by the passing particle bunch, due to EO modulation, which according to equations 2.28 and 2.24, increases with the crystal length L_y. The fundamental concept of an EO pickup is depicted in Figure 3.7.
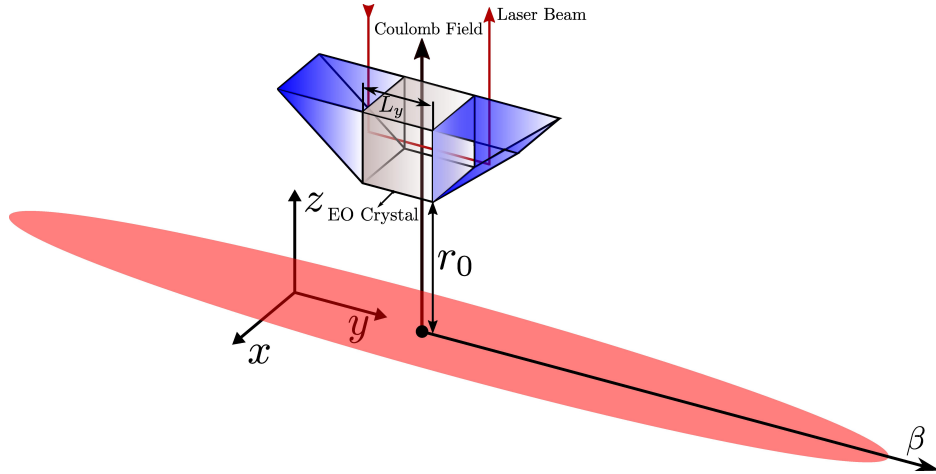
Figure 3.7: Interaction between the Coulomb field of the passing bunch and the conceptual EO pickup.

The electric field penetration into the crystal is limited by the crystal dielectric constant. In fact, a very small modulating field is expected in the crystal ($< 1\,\mathrm{kV/m}$), which translates to a very weak modulation. Thereby, a good Pockels crystal candidate combines, if possible, a low dielectric constant with high linear EO coefficients. Figure 3.8(a) shows the setup in Figure 3.7 integrated into a pipe section, where the crystal sample is directly facing the on-centre beam in vacuum. In this case, the field propagates radially and the time-profile at the face of the crystal is given by equation 3.5. At that point, the propagating field causing the EO modulation drops by the action of the dielectric constant $\epsilon_{\mathrm{crystal}}$. To enhance the field strength to a value closer to E_π, a floating electrode below the crystal is implemented. The Coulomb field lines propagate towards the crystal position, as indicated in Figure 3.8(b). The outer side of the floating electrode touching the crystal is smaller than the inner side facing the beam, thus the collected Coulomb field induces an electric polarisation in the electrode that delivers a higher density of field lines between the bottom and top electrode. This results in an increment of the field strength compared with the non-electrode case, although the drop due to the dielectric constant remains in both cases.
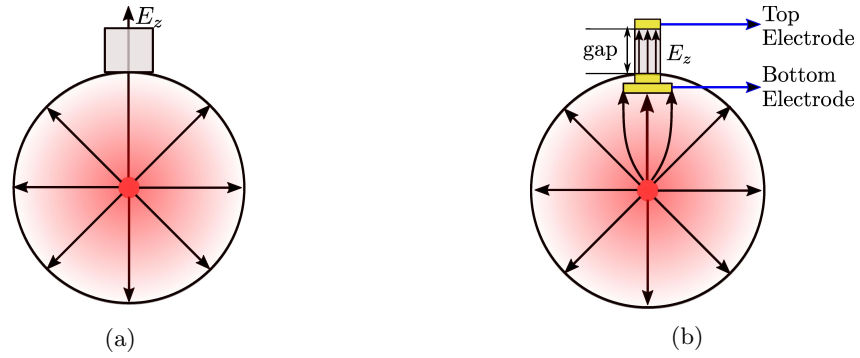
Figure 3.8: Concept designs for (a) the EO pickup with no electrode and (b) with electrode.

Ideally, under the assumption that the electric field lines always remain in the gap between the bottom and top electrode, the electric field is kept constant and independent of the crystal thickness. In reality, some field lines tend to escape out of the gap as it widens, thus, a thinner crystal may produce a certain increment in the field strength, but definitely not in inverse proportion to the thick reduction.

3.2.2 Optical layout for the EO pickup concept

The EO BPM comprises two opposing pick-ups in a single plane, each equipped with a birefringent EO crystal, illuminated by polarised light. The input polarisation depends on the working configuration: either the so-called crossed polarisers configuration or the interferometric one [49]. The former option follows the amplitude modulator scheme presented in the previous chapter, whereas the latter is inspired by the phase modulator arrangement.
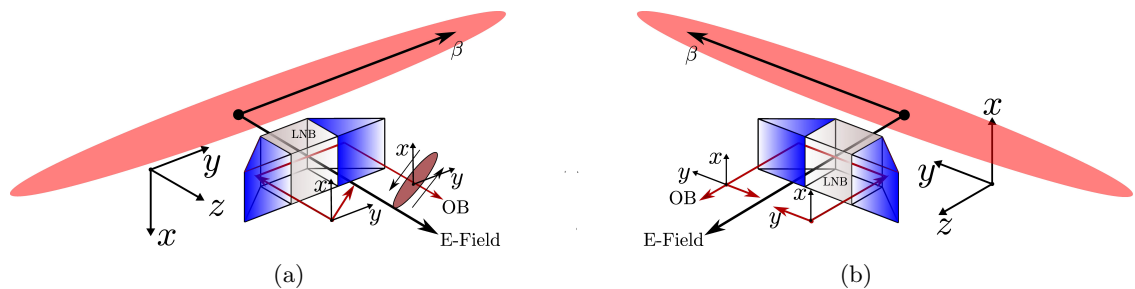
Figure 3.9: Conceptual designs for (a) a crossed polarisers pickup and (b) a phase modulator pickup.

Figures 3.9(a) and 3.9(b) represent the polarisation state along the optical path through the pickup for each configuration. For the crossed polarisers case, the input polarisation goes into the crystal at $45°$ with respect to the crystallographic x direction

47

and as a result of the crystal birefringence, the output polarisation is most likely elliptically polarised with the axes oriented at 45° and -45°.

In the phase modulator pickup (Fig. 3.9(b)) the input and output polarisation remains vertically polarised parallel to the crystal z direction, while the Coulomb field induces a phase-delay in the outcoming beam. The phase-delayed output polarisation can potentially produce an interferometric signal when combined with a non-delayed vertical polarised beam propagating in parallel, as shown in Figure 3.10(a). In this case, the input beams A and B feeding each pickup are split evenly into two different pairs of optical beams: 1 and 2, and 3 and 4, respectively. Each pair on the same plane produces an interferometric signal when the particle beam is passing at two different interaction points (IPA and IPB).

Furthermore, the phase-delayed output can be combined with another phase-delayed beam emerging from the opposite pickup in the same plane as sketched in Figure 3.10(b). Let us note that this diagram resembles the Mach-Zehnder interferometer plotted in Figure 2.9. In fact, it follows the same principle: the initial optical beams A and B are feeding both pickups, after passing through the EO crystals the input beams get converted into the phase-shifted optical beams 1 and 2, respectively, to get combined in a single IP. It should be noted that this configuration cannot work as a BPM because requires both a Σ and a Δ signal, however, it can potentially detect HT instabilities.
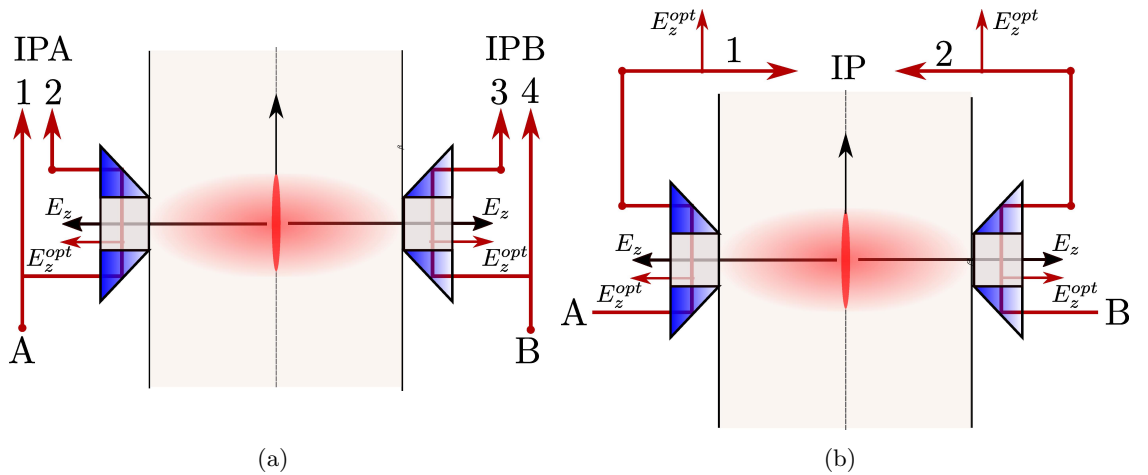
Figure 3.10: Concept of the optical layout for the interferometric design with (a) two different IP in the same plane and (b) with a single interferometric IP per plane outside the pipe.

3.2.3 Analytical studies on the EO pickup concept

At this point, three different strategies of EO detection have been presented. Let us set the horizontal plane as the detection framework where two EO pickups are facing each other, one on the left and one on the right. Each pickup can potentially produce an EO signal T_{pickup} based on either the crossed polarisers or the interferometric layout. The crossed polarisers signal results from applying equation 2.28, and similarly, the interferometric signal is obtained from equation 2.37, where now ΔE_z is simply the modulating field in the crystal for each pickup $E_{z,\text{left}}$ and $E_{z,\text{right}}$. The proton beam position can be calculated from the signal difference over the sum, $\Delta/\Sigma = (T_{\text{left}} - T_{\text{right}})/(T_{\text{left}} + T_{\text{right}})$, following the method used for traditional BPMs.

Table 3.1 summarises all the parameters employed in the analytic simulation to estimate the EO signal for a 5 mm LNB cubic crystal mounted in a typical SPS pipe of 133 mm aperture diameter, with the pickup located 66.5 mm from the beam position in the centre. The super-relativistic passing proton beam is assumed to compress the Coulomb field transversally, and then propagate homogeneously and radially over the pipe section, that is, the simulation is considering the non-electrode pickup scenario described in Figure 3.8(a). The list of parameters also includes the optical wavelength $\lambda = 780$ nm, although according to equation 2.24, a shorter wavelength implies a smaller E_π, and therefore a greater signal modulation, the chosen value reduces the photorefractive effect in the LNB sample. The negative value of the signal for the interferometric design, comes from the fact that the transfer function T_{inter} depends on the cosine square (eqn 2.37) whereas in the crossed polarisers signal, T_{crossed} follows a sine square function (eqn. 2.28).

Table 3.1: Input parameters to the analytic head-tail simulation.

SPS bunch intensity	$1.15 \cdot 10^{11}$	protons per bunch
Bunch length 4σ	1.0	ns
SPS beam energy	450	GeV
Instability modes	0, 1, 2 and 6	
Instability amplitude	0 to 2.5	mm
Pipe radius	66.5	mm
OB wavelength λ	780	nm
Crystal type	LNB	$\epsilon_{\text{crystal}} = 30$
Crystal length L_y	5	mm
E_π	711.35	kV/m

Figure 3.11(a) shows four different cases of HT instabilities where the orders 0, 1, 2 and 6 are represented for amplitudes from $0\,\mathrm{mm}$ to $2.5\,\mathrm{mm}$. The field-profile inside the dielectric LNB then drops by a factor $\epsilon_{\mathrm{crystal}} = 30$ (at $r_0 = 68\,\mathrm{mm}$), which is the dielectric component in the propagating direction z for LNB, as will be seen in the following chapter [40]. For each HT case previously represented, the modulating fields of each crystal on the left and right are given by equation 3.5, where the charge density $\rho(t)$ is defined by the SPS nominal parameters, that is, a bunch length of $4\sigma = 1\,\mathrm{ns}$ and the charge produced by $1.15 \cdot 10^{11}$ protons of Lorentz $\gamma = 480$. The factor $1/\epsilon_{\mathrm{crystal}}$ is then multiplied by the result of the convolution of the charge density $\rho(t)$ and $E_p(r_0, t)$, to determine the profiles inside the crystal shown in Figure 3.11(b). In fact, it can be shown that the peak field is given by equation 3.12 if ϵ_0 in the decay factor K_D is now replaced by $\epsilon_0 \epsilon_{\mathrm{crystal}}$ [49].

Finally, Figures 3.11(c) and 3.11(d) depict the signals expected on each side for an amplitude modulator pickup (Fig. 3.9(a)) with a natural birefringence such that $\Gamma_0 = \pi/2$, and a phase modulator pickup (Fig. 3.9(b)) with $\phi_0 = \pi/2$, so it corresponds to the most sensitive working points in both cases. It should be noticed that in this simulation the phase modulator pickups are supposed to work in a double IP configuration (Fig. 3.10(b)). Also, let us recall that when comparing Figures 3.11(c) and 3.11(d), the interferometric signal is more sensitive as $k_{\mathrm{C-I}} = T_{\mathrm{inter}}/T_{\mathrm{crossed}} \simeq 1.45$ according to equation 2.44.

Figure 3.12(a) presents the field difference between the profiles of each pickup shown in Figure 3.11(b). One can observe that the bunch position then relies on a field difference between opposing pickups in the order $\Delta \sim 0.5\,\mathrm{kV/m} \ll \mathrm{E}_\pi$ for the LHC scenario when using a non-electrode pickup. Putting the modulating field difference aside, the signal strength also depends on λ and the crystal length L_y. Figures 3.12(c) and 3.12(d) show the normalised difference between the pickup signals for the crossed polarisers configuration and the double IP layout respectively. These delta signals are obtained from the direct subtraction defined as $T_{\mathrm{left}} - T_{\mathrm{right}}$ of each corresponding case shown in Figures 3.11(c) and 3.11(d). Once again, as expected, the sensitive factor between both methods remains being $k_{\mathrm{C-I}} = 1.45$ after applying the difference.

The detection of HT instabilities has also been proposed using a single interferometric point per plane, following the scheme shown in Figure 3.10(b), and the result is presented in Figure 3.12(b). This sort of signal is simulated analytically resulting in a replica of the interferometric signal difference $\Delta T_{\mathrm{inter}}$ plotted in Figure 3.12(d). If $E_{z,\mathrm{left}}, E_{z,\mathrm{right}} \ll E_\pi$, as in this case, both results must be almost equal since applying
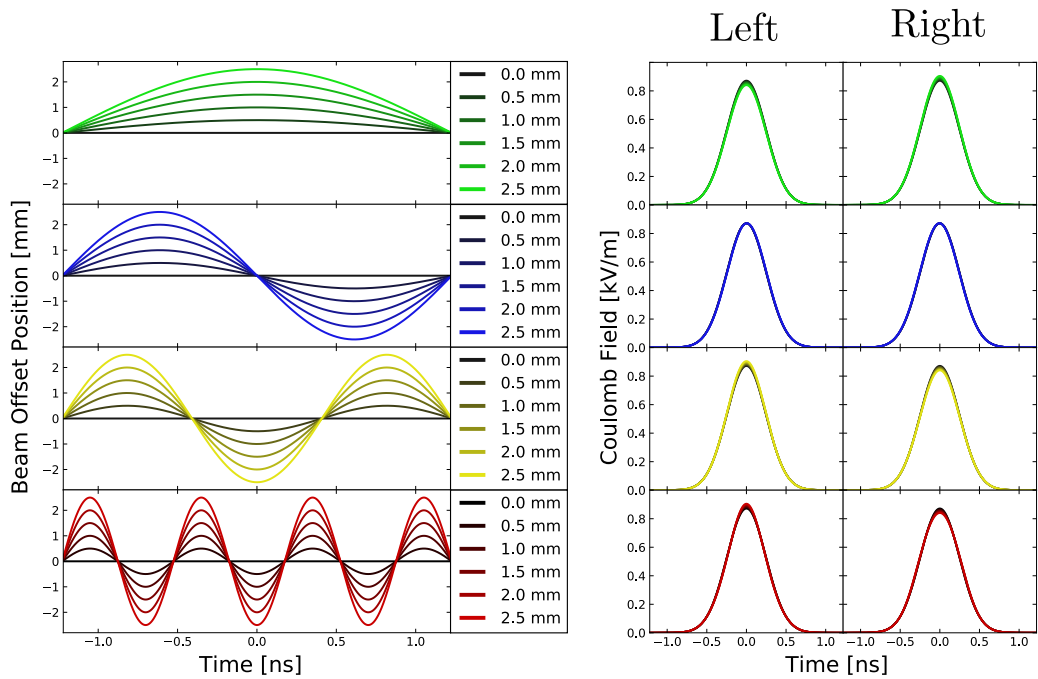
(a) Representation of the HT instabilities of modes 0, 1, 2 and 6.

(b) Modulating field inside a LNB crystal located at 30 mm from the beam.
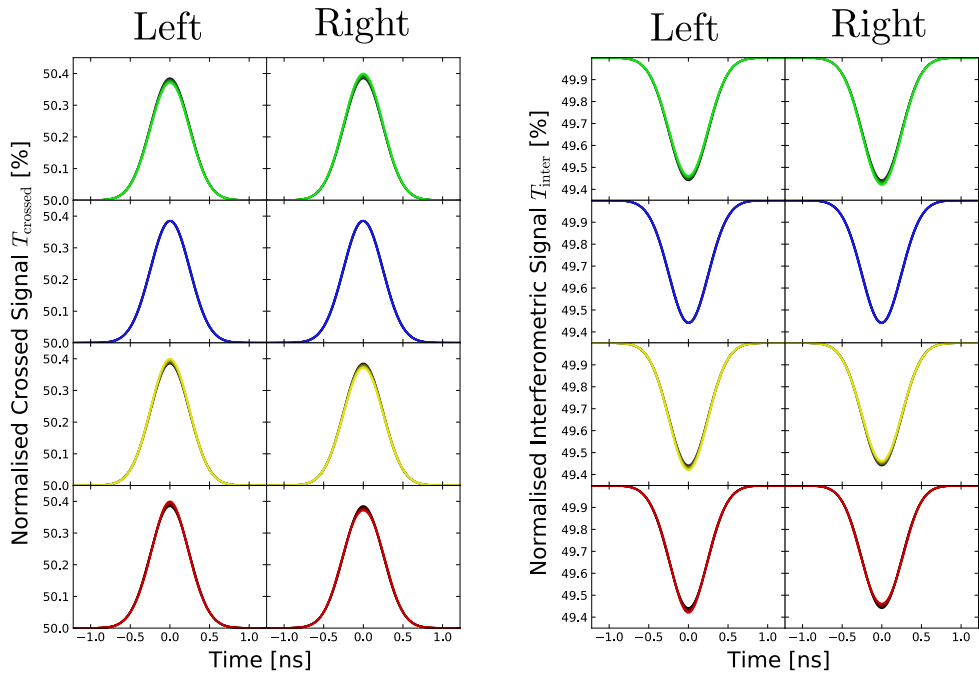
(c) Signals for the crossed polarisers pickups.

(d) Signals for an phase modulator pickups.

Figure 3.11: Analytic simulations of HT instabilities and the corresponding pickup signals at $r_0 = 68.0$ mm (inside the crystal), when assuming the field propagates totally radial.
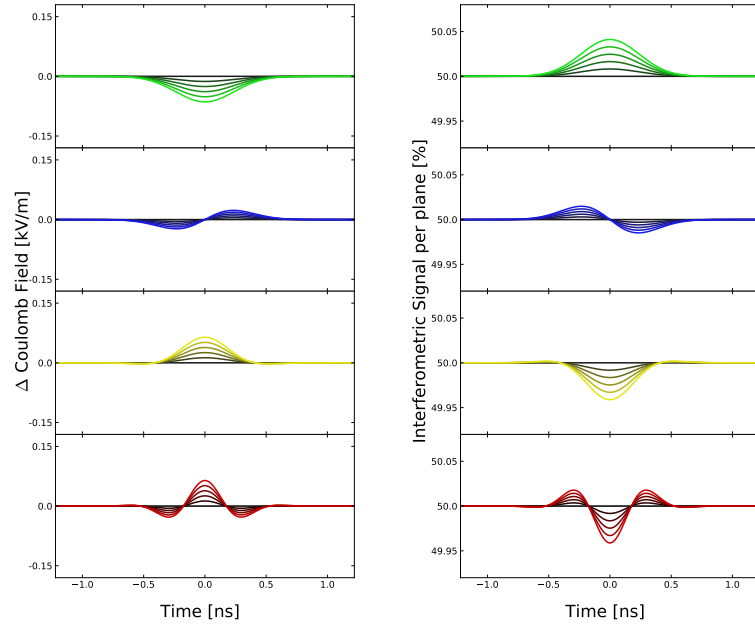
(a) Δ Modulating field (Left - Right). (b) Interferometric signal combined from two pickups in the same plane.
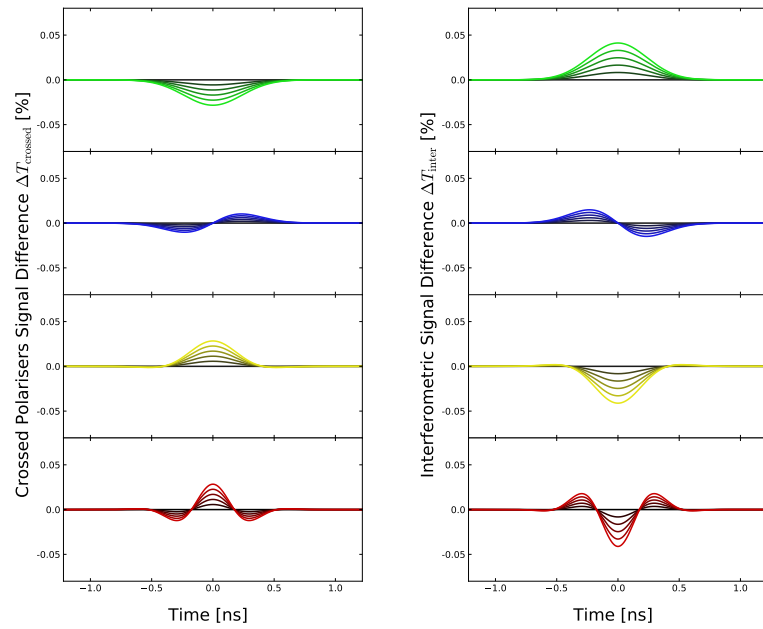
(c) $\Delta T_{\mathrm{crossed}}$ (Left - Right).   (d) $\Delta T_{\mathrm{inter}}$ (Left - Right).

Figure 3.12: Analytic simulation of the field and signal difference, and also the single interferometric signal.

the interferometric modulation equation 2.37 on ΔE_z, is equivalent to the signal difference obtained independently from the same equation for $E_{z,\text{left}}$ and $E_{z,\text{right}}$, that is, $T_{\text{inter}}(\Delta E_z) = \Delta T_{\text{inter}}(E_z)$.

Above all, the major advantage of a single interferometer is that the difference is obtained directly at the detector, instead of having to get a signal per pickup and post-process the subtraction. This way the EO signal can be amplified by pumping as much light power as the detector limit allows. In contrast, in the double interferometer (and also in the crossed polarisers configuration), each pickup modulation can be adapted to the maximum permitted by the detector, but then the final signal is dramatically reduced since it is obtained from the subtraction of those two large numbers. Therefore, the resolution of the signal with the field difference is better in the single IP model.

3.2.4 Summary

This chapter has introduced a detailed theoretical background to characterise the Coulomb field of a relativistic particle bunch. Using the SPS parameters, the Coulomb field at SPS can be assumed to be perfectly transversal, which implies that the force lines are parallel to the z-axis of the crystal. Moreover, some useful set of equations were derived to calculate the field strength and profile. This allowed us to estimate the Coulomb field to be about $\sim 24\,\text{kV/m}$ at the crystal face located 66.5 mm away from the beam, and a frequency spectrum not beyond 2 GHz for a rigid nominal bunch in SPS.

Two types of pickups are proposed: in the first proposal the crystal is located on the pipe at the radius distance so the Coulomb field propagating in vacuum simply encounters the crystal face, where it is reduced by a factor $1/\epsilon_{\text{crystal}}$, being $\epsilon_{\text{crystal}}$ the relative permittivity or dielectric constant value of the EO crystal in the direction of the propagating field E_z. For Lithium Niobate $\epsilon_{\text{crystal}} = 30$, then the modulating field is expected to drop to $\sim 800\,\text{V/m}$. Precisely to overcome this constrain, in the second proposal an electrode that attracts field lines towards itself and becomes electrically polarised is attached to the z-cut face. This way the density of electric field lines in the crystal is increased, and therefore the modulating field strength too.

Finally, from the point of view of the optical configuration the EO pickup can potentially work as an amplitude modulator or a phase modulator. Some analytical simulations have been carried out to estimate the performance of both models and confirmed the phase modulator pickup is a factor $k_{\text{C–I}} = 1.45$ more sensitive with respect to the amplitude

modulator. Not just that, a pair of phase modulator pickups in a plane can be arranged to produce a double or single interferometric signal, where the latter system offers a better signal-field resolution as a single IP makes the subtraction of opposing signals unnecessary.

Chapter 4

Prototype design of the EO pickup

4.1 Lithium Niobate orientation

This chapter presents the two variants of the first EO pickup prototype installed in CERN Super Proton Synchrotron (SPS), which will be referred as pickup or model zero and one for the rest of this thesis. Let us recall that the SPS was chosen to test the prototype because it is a more accessible machine than LHC, but with similar beam parameters.

The key piece of the EO pickup is a sample of MgO:LNB assembled in the core of the opto-mechanical design. As indicated in chapter 2, Lithium Niobate (LNB) crystals exhibit the Pockels effect, a property that is widely exploited in telecom systems as phase and amplitude modulators (see subsections 2.3.3 and 2.3.4). Moreover, LNB crystals also exhibit higher linear EO coefficients than other possible candidates such as $LiTaO_3$, but with a lower dielectric constant [40, 43]. In conclusion, the easy access in the market to these type of crystals, and its well-known properties reported in the large amount of literature due to its popularity in the industry, made LNB a suitable and sensible candidate for the first EO pickup prototypes.

The interaction between the EO crystal, the laser beam, and the Coulomb field defines the most optimal crystal orientation in terms of the optical modulation. As it has been demonstrated in the previous chapter, the Coulomb field from the proton bunch travels quasi perfectly perpendicular to the bunch velocity direction. Let us assume that the z-cut of the cubic sample is contained in a plane perpendicular to the incoming electric field. The conceptual diagram in Figure 3.7 indicates how a system formed by a pair of prisms direct the laser beam along the normal direction to the applied field E_z, throughout the crystal. Therefore, in terms of the Optical Beam (OB) orientation with respect to the

field lines, the induced modulation is defined as transversal, following the geometry shown in Figure 2.3(a). The electric field lines cross the crystal through the z-cut plane and the OB goes along y, as shown in Figure 4.1(a). In this configuration, the modulator EO theory developed in chapter 2 can be applied. In fact, the design proposed in this thesis is based on the amplitude modulator geometry rather than the phase modulator one. This implies that the input polarisation into the crystal for the prototype is linear at 45° degrees with respect to the crystal x direction, projecting evenly the optical components E_z^{opt} and E_x^{opt} into z and x directions, respectively.
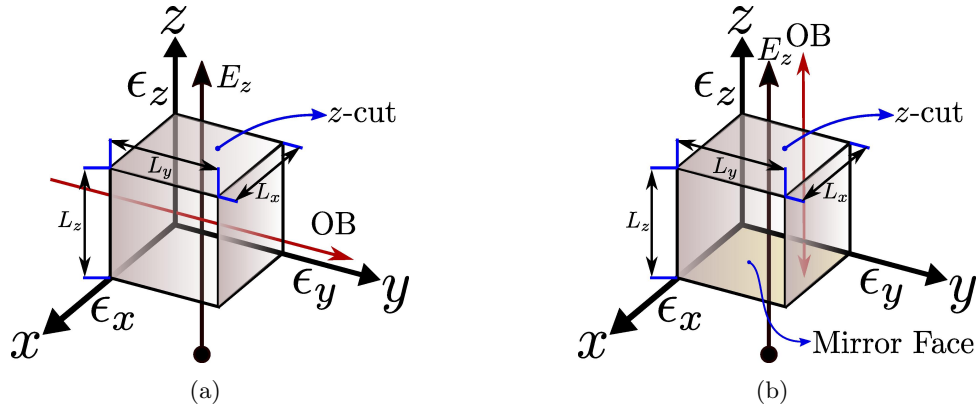
Figure 4.1: Orientation diagram of the LNB sample in the (a) transverse and (b) longitudinal configurations.

Let us recall that a good crystal candidate must compromise a low dielectric constant to minimise the field drop inside the crystal, with the highest possible Pockels coefficients, to maximise the modulation. In the theory developed in the chapter 2 was shown that the modulation of the optical components E_z^{opt} and E_x^{opt} along the z and x directions is proportional to $n_e^3 r_{33} E_z$ and $n_o^3 r_{13} E_z$ respectively, where E_z is electric field inside the crystal. However, the value of E_z depends inversely on the dielectric constant along z, as it decreases by a factor $1/\epsilon_z$ when the Coulomb field propagates through the dielectric interface. Since LNB is a uniaxial crystal, axes x and y are equivalent, and thus $\epsilon_x = \epsilon_y$. The equation 4.1 is the permittivity tensor with the dielectric constants for LNB in terms of the principal axes:

$$\epsilon = \epsilon_0 \begin{pmatrix} \epsilon_x & 0 & 0 \\ 0 & \epsilon_y & 0 \\ 0 & 0 & \epsilon_z \end{pmatrix} = \begin{pmatrix} \epsilon_{11} & 0 & 0 \\ 0 & \epsilon_{11} & 0 \\ 0 & 0 & \epsilon_{33} \end{pmatrix}. \tag{4.1}$$

Another different proposal consists in working in the longitudinal configuration (Fig. 4.1(b)) by keeping the same crystal orientation with respect to the Coulomb field, but setting the OB parallel to z and making it back reflect from the inner z-cut mirror face. In this scenario, the phase difference between the x and y projections is zero, due to the equal optical path, $2L_z n_o$, in both of them. Therefore, this solution would not make sense when the system is designed to work as an amplitude modulator pickup, since the crystal effectively loses the field-induced birefringence property and consequently, the input and output polarisation would not change with the passing beam [39]. It could be used though as a phase modulator system, but then, it would rely on the smaller r_{13} coefficient. Finally, if the field was applied in one of the other crystal directions x or y, some crossed terms would arise from multiplying the tensor in equation 2.8 by the new field E_x or E_y and subsequently, the direction of the index ellipsoid axes would be modified. Furthermore, the field would drop by a greater factor ϵ_x^{-1} or ϵ_y^{-1}, as can be appreciated in Table 4.1 [40]:

Table 4.1: Relative dielectric constant values of LNB [40].

$\epsilon_x^T = \epsilon_{11}^T/\epsilon_0$	$\epsilon_z^T = \epsilon_{33}^T/\epsilon_0$	$\epsilon_x^S = \epsilon_{11}^S/\epsilon_0$	$\epsilon_z^S = \epsilon_{33}^S/\epsilon_0$
84	30	44	29

In this context, the superscripts T and S denote whether the crystal lattice is unclamped or clamped depending on the frequency of the modulating field. For the nominal SPS bunch that produces the radio-frequency spectrum given by Figure 3.2(b), the clamped values can be assumed to be $\epsilon_z = \epsilon_{33}^T/\epsilon_0 = 30$ and $\epsilon_x = \epsilon_y = \epsilon_{13}^T/\epsilon_0 = 84$. Let us note that the clamped dielectric constants ϵ_z, happened to be ~ 2.5 times smaller than the other constants ϵ_x and ϵ_y, which reinforces the geometry presented in Figure 4.1(a) as the best possible configuration for LNB. In conclusion, a low value of the dielectric constant is key to optimise the EO signal and must be considered carefully along with the linear EO constants when selecting a crystal candidate in the EO-pickup design. In addition, the LNB samples that were used in the prototype pickups are 5%-mol doped with MgO (MgO:LNB) to minimise the photorefractive effect (section 2.4) and also improve the damage threshold.

4.2 Pickup design

4.2.1 Modulating field in the crystal samples

Both EO pickup designs rely on the amplitude modulator configuration. In a standard EO modulator the electric field E_z is generated by a voltage source, whereas the field of a proton beam in an EO pickup depends upon the bunch parameters and geometry conditions. For instance, pickup zero is a non-electrode pickup (Fig. 3.8(a)) where the EO crystal is a 5 mm cubic LNB sample ($L_x = L_y = L_z = 5$ mm) oriented as illustrated in Figure 4.1(a). Section 3.1.3 explained how the proton Coulomb field can be estimated as a free space propagation until reaching the crystal, when the field strength drops by the action of the dielectric constant, $E_{\text{bunch}}(r_0 = r_{\text{crystal}} = \text{radius})/30$, for LNB. In fact, Figures 3.11 and 3.12 predict very weak modulations in this scenario because the modulating field inside the crystal is much smaller than the parameter E_π. Therefore, the modulation will improve if the modulating field becomes comparable to E_π.

The field limitation can be partially overcome by placing electrodes to collect more field lines towards the crystal (Fig. 3.8(b)). In this case, the density of electric field lines within the gap between the electrodes increases, which yields an enhancement in the electric field strength inside the crystal. Pickup one is an attempt to follow this strategy in order to obtain a field increment and thus, more optical modulation. The crystal orientation remains equal but with different dimensions, now the crystal front section is smaller ($L_x = 2.5$ mm, $L_y = 3$ mm), but is longer in the OB direction ($L_z = 9$ mm), which potentially leads to a greater modulation according to equations 2.24 and 2.28.

Table 4.2: Crystal dimensions summary.

LNB Dimension [mm]	L_x	L_y	L_z
Pickup zero	5	5	5
Pickup one	3	9	2.5

A commercial EO modulator system is similar to the one shown in section 2.4.3, the mechanism relies on charging the electrodes by applying a voltage source to reach an applied field $E_{\text{LNB}} = \frac{V_{\text{applied}}}{L_z}$, as represented in 4.2(a). This way, when the field strength inside the crystal drops by a factor $1/\epsilon_z$, the value is effectively independent of the dielectric constant, mathematically, $E_{\text{LNB}} = E_z = \frac{V_{\text{applied}}}{L_z}$.
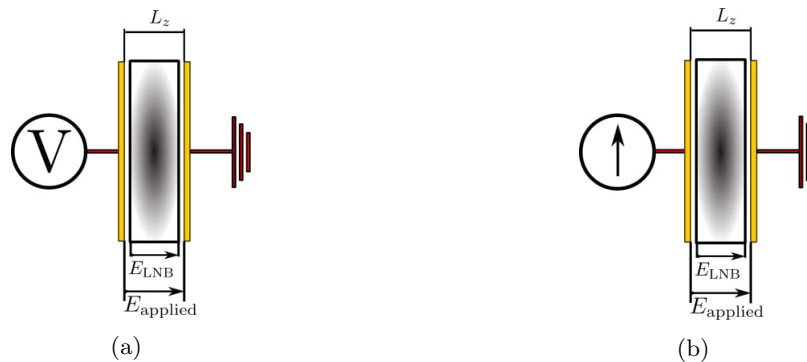
Figure 4.2: Equivalent circuits for (a) an optical modulator and (b) a EO pickup.

On the contrary, the electrodes in pickup one are not charged, but electrically polarised, which implies that the applied field on the crystal is limited. Figure 4.2(b) is an equivalent circuit where a current source constrains the charging capacity of the electrode plates as it occurs in the pickup. In consequence, the field applied through the crystal can be defined as follows:

$$E_{\text{LNB}} = \frac{E_{\text{bunch}}(r_0) \times \mu_C}{\epsilon_z}, \tag{4.2}$$

where $E_{\text{bunch}}(r_0)$ is the propagating Coulomb field value at the transverse position r_0 of the electrode pickup, and μ_C is the coupling factor that relates the Coulomb field with the field applied on the crystal E_{applied}, which eventually drops by $1/\epsilon_z$ to produce the modulating field E_{LNB}. The coupling factor μ_C depends on the electrode pickup design.

4.2.2 General overview of the pickup

Let us recall in the first place that the prototype reported in this thesis was installed in a pipe of $66.5 \, \text{mm}$ radius in the SPS. In order to meet the requirements of the machine, a collaboration between CERN and Royal Holloway, University of London (RHUL) was launched to design and manufacture the pickups. The technical drawings were produced with the assistance of the Engineering & Equipment Data Management Service (EDMS) at CERN [50–52], whereas the device was manufactured in the Physics Department workshop at RHUL. After the production, the pickups were also vacuum tested at CERN to ensure that they could accomplish the SPS requirements of maximum pressure $P_{\text{Limit}} < 1 \times 10^{-7} \, \text{mbar}$ before the installation [53].

Figure 4.3(a) shows the three different pieces of the button (3) gathered along with the viewport (1) and the central flange (2), which are the three main stainless steel com-

ponents for high vacuum that both pickup designs have in common. As a consequence, the aspect from outside (Fig. 4.3(b)) when the prototype is mounted in the SPS pipe, is the same for both pickups. The technical drawings allow us to analyse how the different elements of each model are arranged inside once it is installed. For instance, Figures 4.4(a) and 4.5(a) are the view section along the radial axis for pickups zero and one, respectively. They are depicted from outer to inner side of the pipe section in the following order: the viewport (1), the central flange (2), and the button (3).

The viewport is a transparent fused silica window with a broadband ($650\,\text{nm} - 1050\,\text{nm}$) Anti-Reflective (AR) optical coating framed in a vacuum-seal DN40CF flange, that allows the OB to pass from outside the pipe into the vacuum medium inside the pickup. The central flange is the piece responsible for holding the button and vacuum-seal the pickup-pipe attachment. It follows the standards of a DN63CF flange and the customised design also includes two channels (labeled by the letter 'A') highlighted in red of 5 mm diameter, in order to permit the light beam to go in to and out of the button body. Finally, the button is the component equipped with the optical system formed by the EO crystal and two prisms.

Figures 4.4(b) and 4.5(b) are the front section drawings for pickups zero and one respectively [54, 55]. The LNB sample is held by a ceramic piece (5) of Macor shown in salmon to isolate electrically the crystal from the metallic surroundings. The objective of this element is to minimise both the distortion of the penetrating Coulomb field inside the crystal caused by electric currents conducted along the button, and also the deflection of the field lines towards the metallic surroundings. The contact between the crystal surface with a metallic conductor different of the electrodes in the z-cut faces could make the field lines bend towards the x direction instead of keeping them straight parallel to z.

In Figures 4.4(b) and 4.5(b) [54, 55], one can see the incoming OB is deflected 90° into the LNB sample (4) in purple and then reflected back with a separation width w_L. The optical path is aligned by a pair of 10 mm side right angle prisms (6) in blue, placed at both sides of crystal. Due to this mechanism, a wider laser beam separation w_L yields into a larger separation between the segment of the laser path along the crystal, and the inner edge of it. The prisms are fused silica to avoid the risk of radiation damage in the SPS that would imply a dramatic loss of optical transmission. The button is in turn composed of three different pieces to facilitate the assembly of the prisms, EO crystal, and the ceramic holder inside of it.

Figures 4.6 and 4.7 are the assembly drawings for pickups zero and one including the OB depicted superimposed throughout the system [54, 55]. The crystal, prisms and ceramic holder are pieced together along with the three parts of the button to obtain a single body (3), that is then bolted to the central flange (2). Once the system flange and button is put together, it is attached as a single body to the pipe with a copper gasket in between to seal the vacuum. Similarly, the viewport (1) is then attached, with a silver gasket in between, to the central flange. The OB encounters various interfaces along the optical path, and in all of them an optical AR coating at 780 nm has been applied. The pickup components and their main characteristics are summarised in Table 4.3.
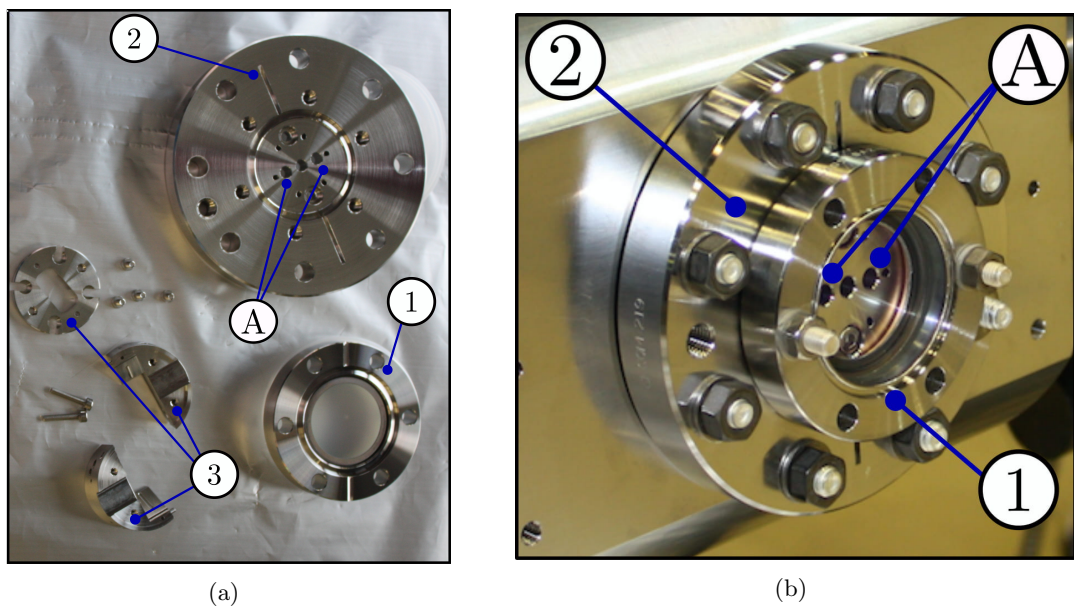
Figure 4.3: (a) Button pieces, central flange and viewport; (b) EO pickup mounted in the horizontal plane of the SPS pipe.

4.2.3 Button Configuration

The prototype pickup versions differ when comparing the shape dimensions of the crystal and the ceramic holder, and also the use of electrodes. The Macor part where the crystal is embedded was modified as a direct consequence of the different crystal dimensions in each pickup plus the incorporation of electrodes. The electrodes (7) shown in yellow in the technical drawings 4.5(a), 4.5(b) and also in Figure 4.7 represent one of the main divergencies between models zero and one. In conclusion, the difference between the pickups can be simply explained by describing how the system combines the ceramic holder, the LNB sample, and the electrode, altogether in the button, in each case.

(a) Side view section.

(b) Front view section.

Figure 4.4: Technical drawings of pickup zero (all the units are in millimetres) [54].
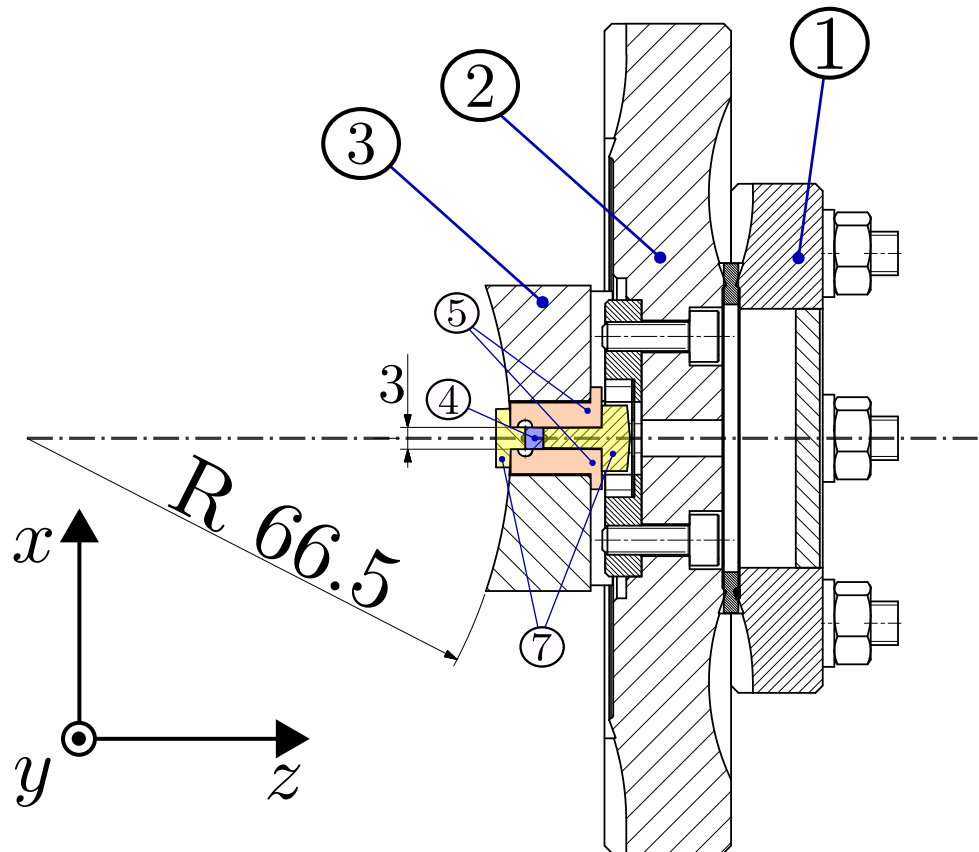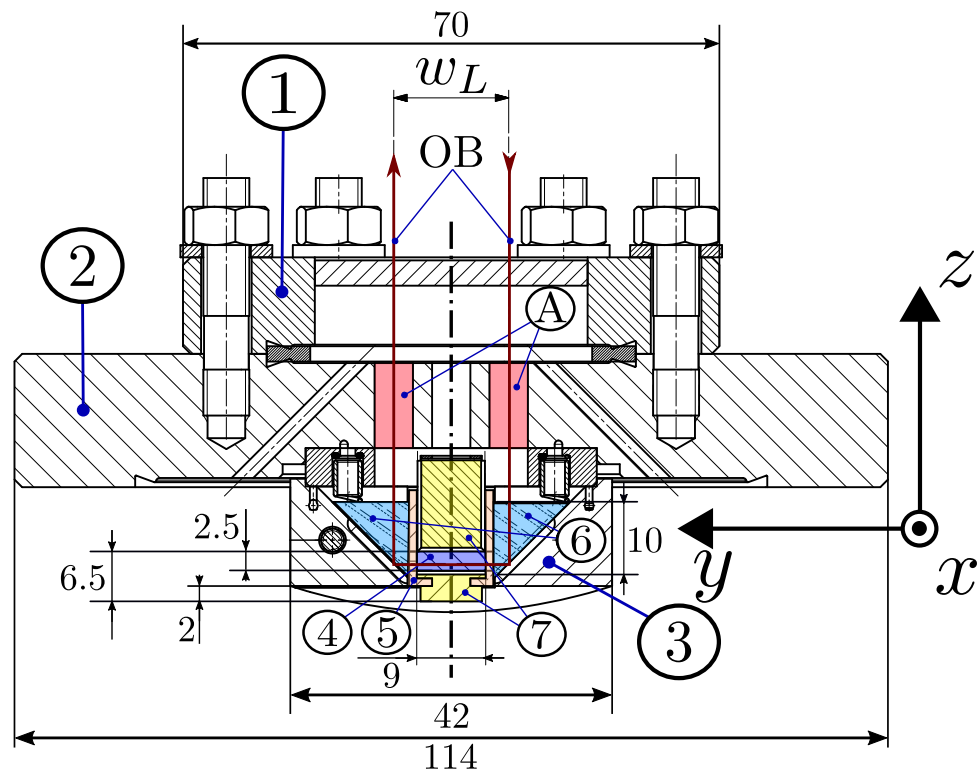
(a) Side view section.

(b) Front view section.

Figure 4.5: Technical drawings for pickup one (all the units are in millimetres) [55].

Figure 4.6: Assembly drawing of the pickup zero (all the units are in millimetres) [54].

Figure 4.7: Assembly drawing of the pickup one (all the units are in millimetres) [55].

Table 4.3: Summary of the main pickup components characteristics. The numeric labels correspond to the same ones employed in Figures 4.3, 4.4, 4.5, 4.6, and 4.7; similarly, the alphabetic labels refer to Figure 4.8. The symbol (*) denotes a broadband AR coating with a specific range $650\,\text{nm} - 1050\,\text{nm}$.

Label	Item	code	Coating	Material	Weight [g]
1	Viewport	DN40CF	AR*	Steel & fused silica	~ 110
2	Central flange	DN63CF	-	Steel	~ 1250
3	Button	-	-	Steel	~ 160
4	EO Crystal	-	AR*	MgO:LNB	~ 5
5,b,c	Crystal holder	-	-	Macor	~ 5
6,i	RA prism	Thorlabs PS61	AR	Fused silica	~ 1
7,g	Electrodes	-	Au	Copper	~ 5
j	Spring	HPC - CD2116	-	Steel	~ 1
k	holding plate	-	-	Cu Be	~ 1
-	Viewport bolts	M6 [x6]		Steel	
-	Flange bolts	M8 [x8]		Steel	
-	Button bolts	M4 [x2], M3 [x6]		Steel	

Figure 4.8 illustrates the assembly of the ceramic holder in the button (a) alongside a summary of the holder dimensions for each case. In both pickups, models zero and one, the ceramic holder is formed by two equivalent pieces, which are assembled along the y direction and hold the crystal in between. They are adapted to the crystal dimensions and therefore, the central channel where the crystal fits in is $5\,\text{mm}$ wide for pickup zero (b) and $3\,\text{mm}$ for pickup one (c). Additionally, both designs have a similar T-shaped piece represented in grey as a concept element, which, is also Macor-made for pickup zero (d) and as can be seen in Figure 4.4(a), pushes the crystal on his top z-cut face towards the bottom. Moreover, the T-shaped piece in pickup zero has a 4 mm diameter cylindric channel (e) that would go from the top crystal face all along its longitudinal axis, allowing to observe the crystal from outside when the button is totally assembled. Once the holder and the crystal are mounted together, there exists a clearance at the bottom z-cut face of the $5\,\text{mm}$ cubic sample, that is ledge-framed to hold the crystal in place (Fig. 4.9(a)). The design of this pair of ceramic pieces for pickup zero, includes two holes of $3\,\text{mm}$ diameter (f) that permit the OB to pass through the crystal along the y direction. Let us note that the crystal is in contact exclusively with ceramic material in this case.

65

For pickup one, the crystal sample is a rod of $9\,\mathrm{mm}$ long (L_y) with a rectangular base of $2.5\,\mathrm{mm} \times 3\,\mathrm{mm}$ ($L_x \times L_y$). The new dimensions yield thinner walls in the Macor part (c) on y, but thicker for the ones along x. The design keeps the T-shaped element but is now replaced by copper material (g), to convert this piece into the top electrode of the crystal. On the bottom face, Figure 4.5(b) shows the ceramic ledges along the y direction now holding an electrode that is facing the inside part of the pipe. Similarly, the ceramic pieces keep narrower holes (h) of $2.5\,\mathrm{mm}$ diameter to let the beam pass through the crystal before and after reflecting in the prisms (i), which are in turn pushed downwards against the ceramic holders to put them in a right angle position by a pair of springs (j). In both pickups the T-shaped piece is pressed against the top part of the crystal by a flexible copper holding plate (k) with a $4\,\mathrm{mm}$ diameter hole that is coaxial with the channel (e).
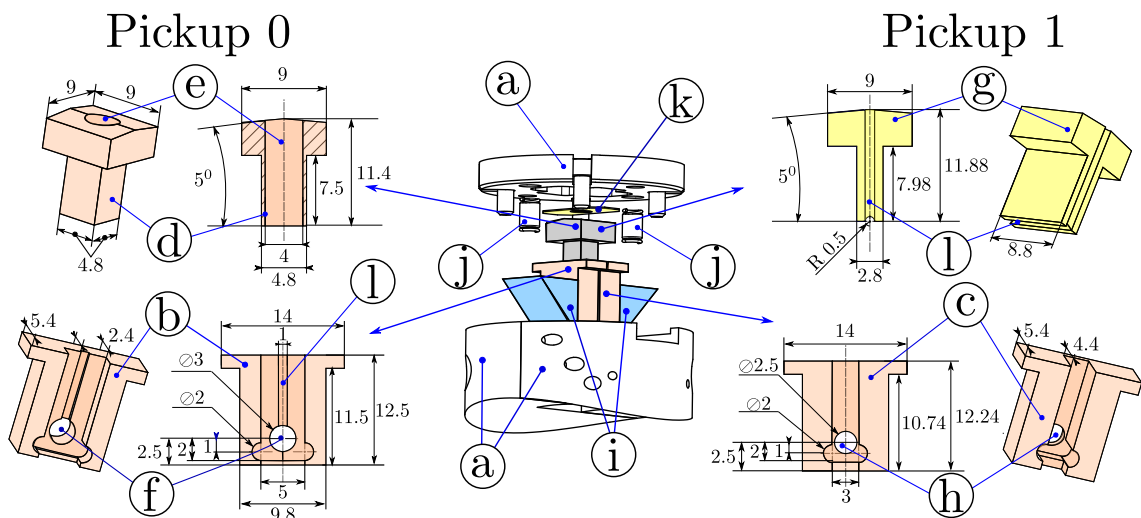
Figure 4.8: Assembly drawing of the ceramic holder and the button [56, 57].

For pickup one, the crystal is in touch with ceramic material on its sides, but in contrast with pickup zero, there is also contact with the two electrodes on the top and bottom faces along the z direction (Fig. 4.9(b)). This configuration has been designed to couple the Coulomb field into the crystal and guide the field lines parallel to z, as will be studied in detail in the following section. Finally, it is important to mention the presence of channels (l) for outgassing during the vacuum pumping in the top and bottom electrodes (g), and both ceramic holders (b) and (c).

Figure 4.10(a) shows the main elements that characterise the configuration for pickup zero. The main picture in the centre shows the 5 mm cubic LNB sample mounted in one of the corresponding ceramic holders to illustrate how it is designed to fit in during the as-
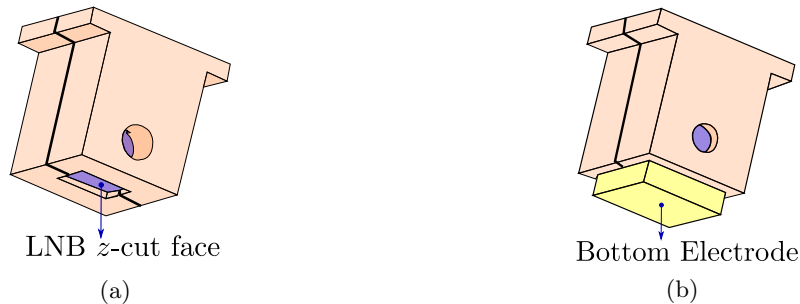
Figure 4.9: Depiction of the crystal sample embedded in the ceramic holder for pickup zero (a), and the bottom electrode for pickup one (b).

sembly process. In this image, the z-cut faces are metallic coated by a thin gold-chromium (Cr/Au) layer whereas the y-cut planes of the crystal are polished and transparent as they correspond to the OB input and output faces. In fact, these faces are put against the hole in the Macor pieces where the incident optical beam is supposed to pass through. As mentioned earlier, the polished faces are also coated with a type AR-B optical layer to avoid back reflections from the incoming light. On the bottom left of this figure appears the detail of the cubic crystal, the holders and the T-shaped piece along with the fused silica Right Angle (RA) prisms and the springs, being the two latter common elements with pickup one. A top view of the Macor holders and the prisms assembled in the button is shown in Figure 4.11. The image of the Macor holders created by the reflexion of the prisms has been highlighted, which indicates the optical path of the beam coming perpendicular to the sheet plane and emerging back.

Similarly, Figure 4.10(b) is a detail of the modified Macor holders, the electrodes, and the new crystal sample that characterise this design. On the top right there is a zoomed in image of the semi-mounted configuration with a removed holder (left) and also covered (right). The polished $2.5\,\text{mm} \times 3\,\text{mm}$ input faces of the crystal are again adjacent to the holder holes to make the optical beam pass through the crystal, and as in pickup zero, an AR coating at $780\,\text{nm}$ has been applied to avoid back reflections. The longest dimension of the LNB sample ($L_y = 9\,\text{mm}$) is parallel to the OB and perpendicular to the hole plane. The image shows how the crystal is held in between the bottom and top (T-shaped piece) electrodes touching the z-cut faces of the crystal, which are also gold-chromium (Cr/Au). The electrodes material is Oxygen-Free Copper (Cu-OFE) to avoid the oxygen molecules escaping out the copper lattice during the vacuum pumping, as this process could potentially make the pieces crack. The electrodes have also been coated by a thin gold layer by deposition that gives them a pallid golden colour.
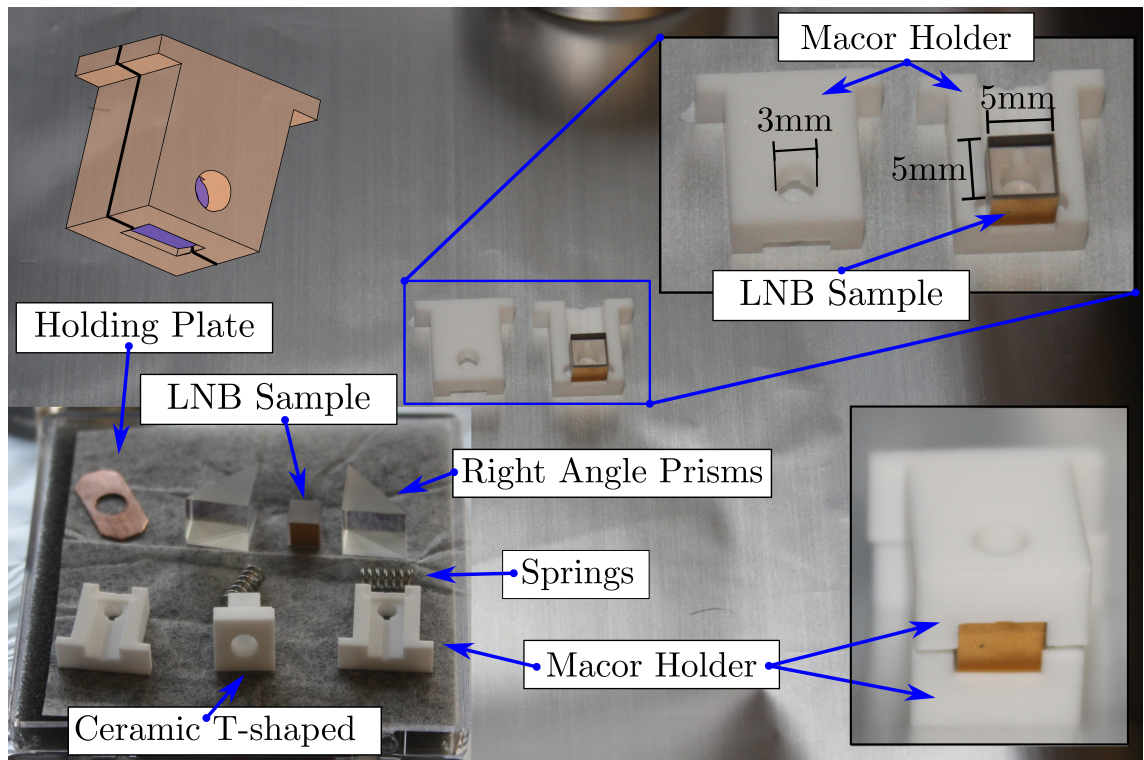
(a) Detail of the ceramic pieces, prisms, springs and crystal for pickup zero.
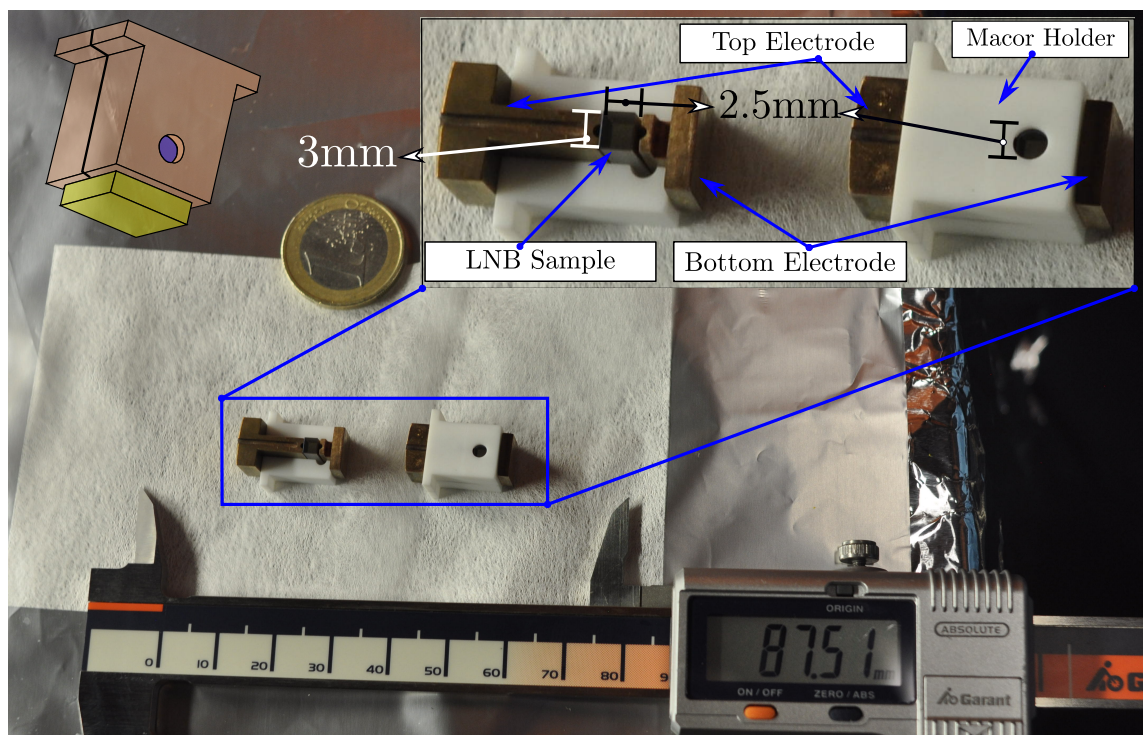
(b) Detail of the electrodes, ceramic holder and crystal for pickup one.

Figure 4.10: Pictures of the characterising elements for pickups zero (a) and one (b).
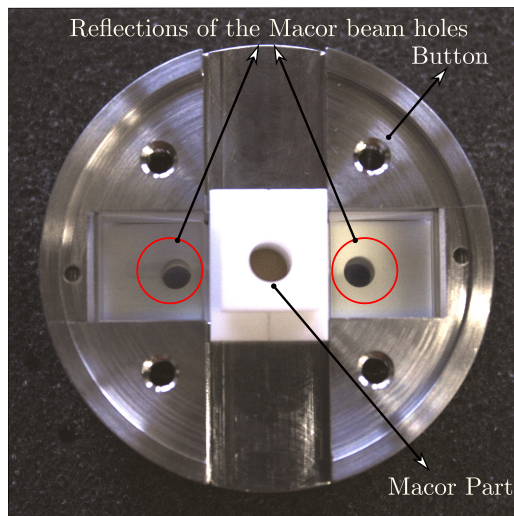
Figure 4.11: Top view of the button zero partially assembled.
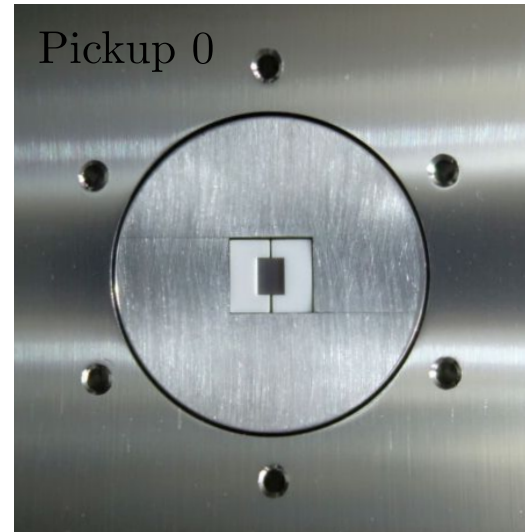
Figure 4.12: Button zero from inside the pipe.
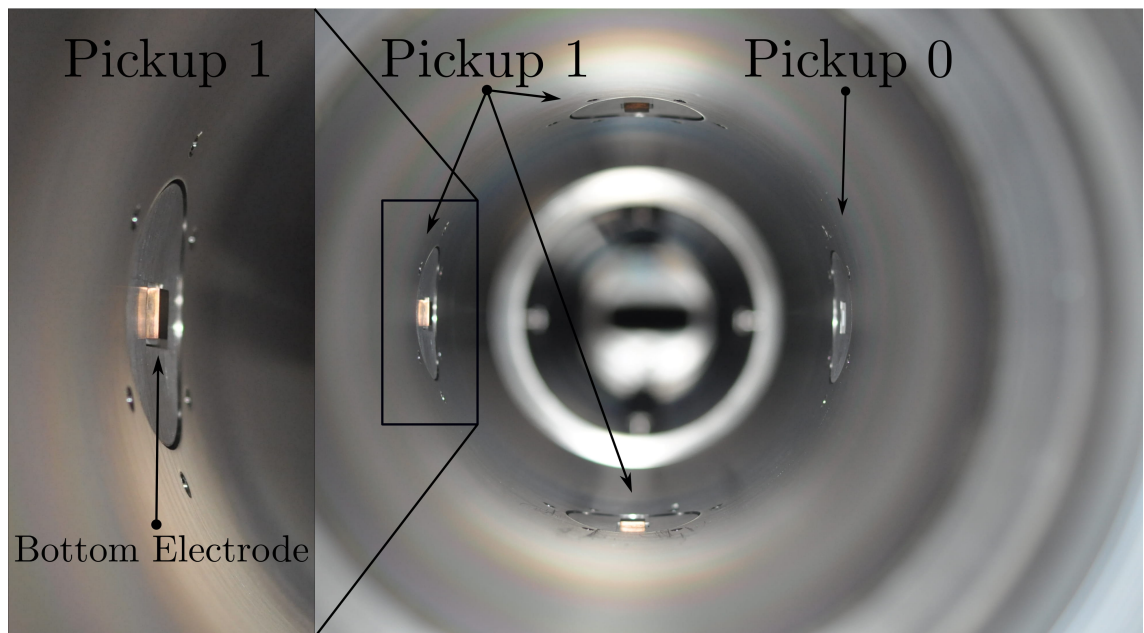
Figure 4.13: Buttons one and zero from inside the pipe.

An important feature of the button is the curvature on the inside part. Figures 4.13 is a picture from inside the pipe that illustrates how the button adapts its shape to the 66.5 mm pipe radius. A pair of pickups one can be observed on the vertical plane, and also the models zero and one on the left and right of the horizontal plane, respectively. Pickup zero follows the curvature of the pipe whereas the other three pickups have the bottom electrode sticking out by 2 mm. Figure 4.11 is a front image of pickup zero on the left where the crystal surface is retracted by about 0.5 mm, according to the technical

drawings. In this case, the z-cut face is not metal-coated, nor polished either, but is just a bare face of the crystal. The following section will analyse the impact of the coating in terms of electric field inside the crystal.

4.3 Electromagnetic simulations

The EO signal is dependent on the modulating field strength E_{LNB} inside the crystal according to equation 2.28. The numeric Electromagnetic (EM) simulations allow us to study more precisely the field propagation throughout the crystal after the analytical approach developed in chapter 2. The EM simulations presented in this thesis were carried out by a commercial software named Computer Simulation Technology (CST) particle studio, which is a package based on numeric finite elements methods widely used in particle accelerator research [58].

For each pickup version, a simplified geometry of the button was defined, as only the interactions with the crystal and the Macor holders are relevant. In fact, since the background is considered a Perfect Electric Conductor (PEC) in the CST scenario, it was pointless introducing the central flange and the viewport elements in the simulation. The inclusion of these steel objects only imply much longer computation time with no significant impact on the results. The main purpose of the simulation is to investigate the Coulomb field propagation over the pipe section and the crystal generated by an SPS nominal bunch (Table 1.1), that is, $4\sigma = 1\,\mathrm{ns}$ bunch of 1.15×10^{11} protons at $450\,\mathrm{GeV}$.

4.3.1 Electromagnetic simulations of pickup zero

The outside aspect of the general geometry for pickup zero is depicted in Figure 4.14(a). The simulation comprises a 200 mm long segment of pipe, represented as a cylindrical body of vacuum totally surrounded by a PEC background except for a single EO button placed on the top. In the simulation, the button represents the simplified steel body depicted in the technical drawings, having the same diameter and thickness, but the small elements such as the screws or small holes have been removed to shorten the computation time. Figure 4.14(b) shows the longitudinal cut section of the pipe and button, where the trajectory of the simulated proton bunch appears on-centre along the y-axis. The right-angle prisms that are highlighted in orange are defined as a fused silica material and the ceramic holder in pink is defined as Macor. However, the CST material library does

not offer LNB in its repository and therefore, the crystal sample was defined through the dielectric constants given in Table 4.1, that is, $\epsilon_y = \epsilon_x = 86$, and $\epsilon_z = 30$. All the figures of 4.14 have been extracted from the CST user interface to illustrate how this software displays the geometry.

Figure 4.14(c) is a zoomed in image of the front section of the button in the CST interface. The prisms, ceramic holder and the 5 mm square section of the crystal can be observed. Figures 4.14(d) and 4.14(e) show the detail of the front section view, where the ceramic holder and its holes perpendicular to the y-axis have been highlighted in the first one, and the crystal section in the second figure.

Putting aside the geometry, two main different simulation scenarios have been considered for pickup zero: the z-cut faces of the LNB sample can be either pristine or metal-coated. The purpose of introducing this nuance, is to investigate the impact on the field strength and quality through the crystal when there exist a deposited layer of copper on the bottom part of the crystal facing the particle bunch. In CST, this element is created as a $200\,\mu$m copper body attached to the z-cut faces of the sample. Finally, once both the geometry and the SPS proton bunch are correctly defined, it is then possible to proceed with the EM numeric simulation.
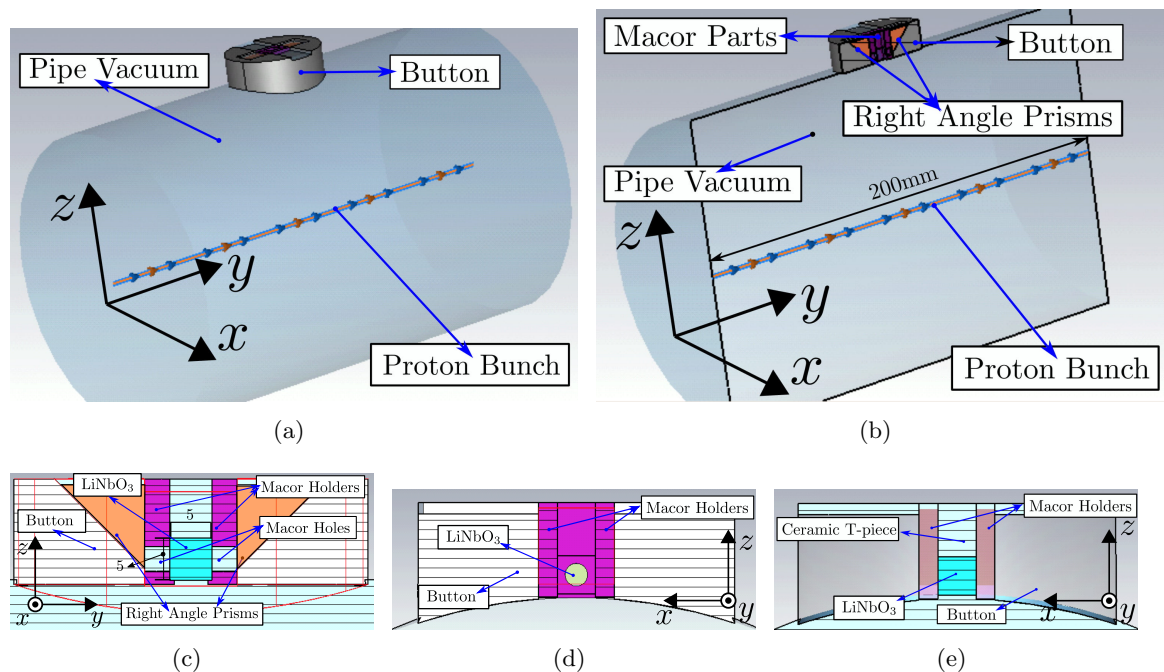
Figure 4.14: Screenshots of different views of pickup zero in the CST user interface.

Figures 4.15(a) and 4.15(b) show the Coulomb field peak against the radial distance r_0 for two study cases: crystal uncoated and metal-coated, respectively. The analytical calculation in blue is the maximum value of equation 3.5 given a certain r_0, which is the time-profile curve resulting from the convolution of the Gaussian charge density $\rho(t)$ (eqn. 3.4) and the proton energy $E_p(t, r_0)$ (eqn. 3.3), when applying the SPS parameters. The EM calculation in red is also the maximum value of the field time-profile curve, but in this case, the profiles are obtained from the output generated by CST.

The blue curve is the characteristic $1/r_0$ field-peak decay that obeys equation 3.12 when free space propagation is assumed, whereas the numeric simulation in red is a more realistic result that takes into account the interaction with the pickup. The two vertical discontinuous red lines indicate the segment of the radial distance occupied by the crystal. Since the 5 mm cube sample is placed slightly retracted with respect to the edge of the SPS 66.5 mm radius pipe, the Coulomb field penetrates into the dielectric crystal when the radial position goes from 66.65 mm to 71.65 mm.

Let us now recall from the previous chapter that the peak-field inside the crystal can be analytically approximated to $E_{max}(r_0 = 66.5\,\mathrm{mm})/\epsilon_z \simeq 800\,\mathrm{V/m}$, just as depicted in Figures 4.15(a) and 4.15(b), and indeed, the numeric simulation also exhibits the expected sudden decrease due to the dielectric discontinuity at the crystal interface. The numerical values are compared to the analytical estimation in Table 4.4 for both coated and uncoated scenarios, and also for a longer proton bunch $4\sigma = 1.6\,\mathrm{ns}$, which is the typical bunch length at 25 GeV injection energy into the SPS. The only significant difference when adding the metallic layer on the z-cut faces of the crystals is just the expected zero-field value found at the metallic surface, according to the results provided by CST.

Both calculations agree for most of the radial position r_0 and differences appear approaching the dielectric interface. In particular, from Table 4.4 and Figure 4.15, it is clear that the numeric calculation differs below the analytic prediction for pickup zero. The mismatch is caused by the elements that distort the ideal isotropic propagation symmetry shown in Figure 3.8(a). Particularly, the mechanism responsible for the peak field drop in the area nearby the pickup is described in Figure 4.16: instead of propagating evenly along the pipe section perimeter, the Coulomb field lines approximating the crystal are directed towards the metallic surroundings rather than through the crystal. The extent of such a mismatch can be quantified by a shape factor μ_S defined as the ratio between the numeric and analytic simulations at the crystal face, for pickup one, it results $\mu_{S,\mathrm{uncoated}} = 0.76$.
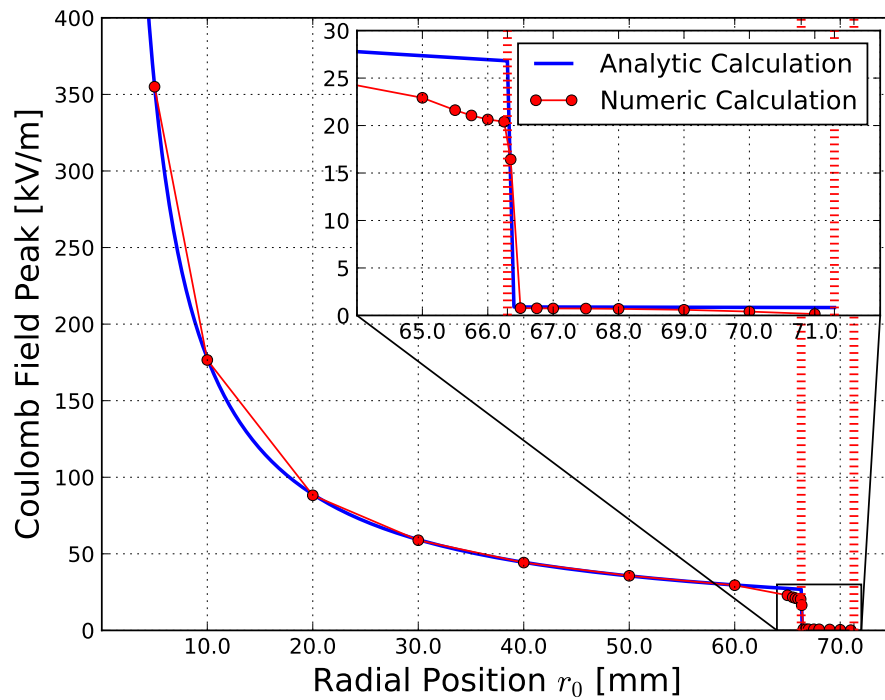
(a) Uncoated crystal.
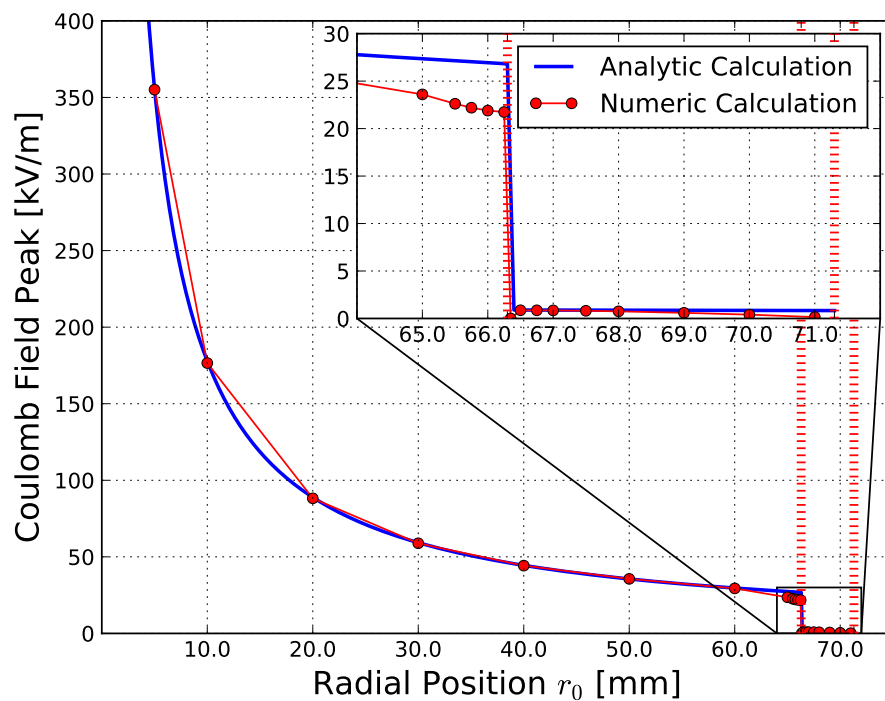
(b) Coated crystal.

Figure 4.15: Numerical electromagnetic and analytic simulations of the peak Coulomb field along the radial transverse position r_0 over the pipe section for pickup zero.

Figure 4.16: Vector field map produced by CST over the crystal section XZ at $y = 0$ for pickup zero. The instant corresponds to the peak field at $r_0 = 68.0\,\mathrm{mm}$.

In the light of the comparison between both simulation methods, the analytical approach turns out to be a fairly reasonable estimation of the field strength in the crystal when a radial propagation from an on-centre particle beam can be assumed (Fig. 3.8(a)).

Table 4.4: Analytical prediction for a shape factor $\mu_S = 1$, and the numeric result for the peak field at different radial positions inside the crystal under on-centre nominal SPS bunch conditions for pickup zero, except from the case denoted by (*), which corresponds to the simulation of an SPS bunch of length $4\sigma = 1.6\,\mathrm{ns}$.

Position [mm]	67.0	67.5	68.0	69.0	70.0
Analytical prediction [kV/m]	0.88	0.88	0.87	0.86	0.85
Modulating Field Peak E_{LNB} [kV/m] (uncoated)	0.75	0.76	0.73	0.59	0.41
Modulating Field Peak E_{LNB} [kV/m] (coated)	0.85	0.81	0.75	0.59	0.40
Modulating Field Peak E_{LNB} [kV/m] (uncoated*)	0.49	0.50	0.47	0.38	0.26

Another important aspect is to determine whether or not the time-profile shape inside the crystal is distorted when the field propagates through the dielectric. Figure 4.17 is the field profile inside the LNB sample for pickup zero under SPS nominal bunch conditions, according to CST. The simulation reveals that the Gaussian shape remains unchanged with identical length inside the crystal, but reduced by a factor $\sim 1/\epsilon_z$.

There exists a certain discrepancy between the coated and uncoated study cases as the former is slightly above the latter. This difference can be explained considering that the shape factor for the metallic coated scenario is greater ($\mu_{S,\mathrm{coated}} = 0.81 > 0.76 =$

$\mu_{S,\text{uncoated}}$), which means that the capacity of directing field lines towards the crystal is improved due to the presence of the metallic layer.
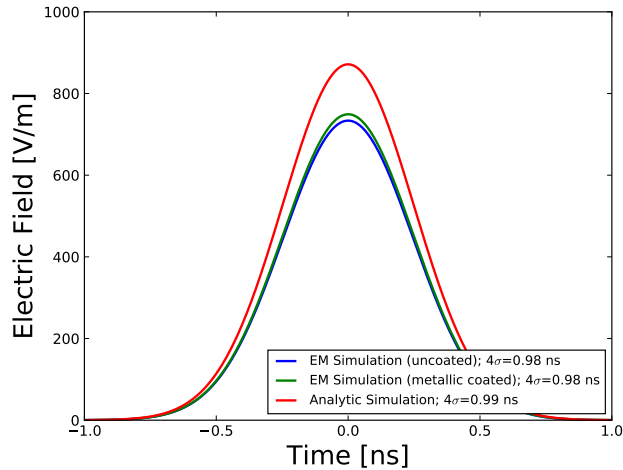
Figure 4.17: Coulomb field time-profile curve inside the LNB sample for pickup zero ($r_0 = 68.0\,\text{mm}$).

4.3.2 Electromagnetic simulations of pickup one

The EM characterisation of pickup one follows the same procedure as pickup zero. Figure 4.18 shows different images of pickup one in CST particle studio; 4.18(a) is an screenshot image of the general pickup at the user interface where the top and bottom electrodes can be appreciated along with the prisms and the longer ($L_y = 9\,\text{mm}$) LNB sample. Figures 4.18(b) and 4.18(c) are the front and side view section of the button for pickup one. In this instance, the input and output optical faces have smaller sections ($3\,\text{mm} \times 2.5\,\text{mm}$) and the crystal is enclosed between copper electrodes highlighted in yellow.

Similarly, once the geometry was defined for the same nominal SPS bunch conditions (Table 1.1), the numeric simulation was carried out and the results are presented in Figure 4.19 and summarised in Table 4.5. The radial distance between the vertical red lines in 4.19 represents again the peak-field inside the crystal, and the space that goes from the vertical blue line until the edge of the crystal corresponds to the space occupied by the electrode, where the electric field is zero. Whereas in pickup zero the field decays across the crystal, one can observe in Table 4.5 that the peak-field is kept more constant along the propagating direction z inside the LNB sample. This effect is caused by the grounding of the top electrode, which fixes the electric field difference and thus makes the strength
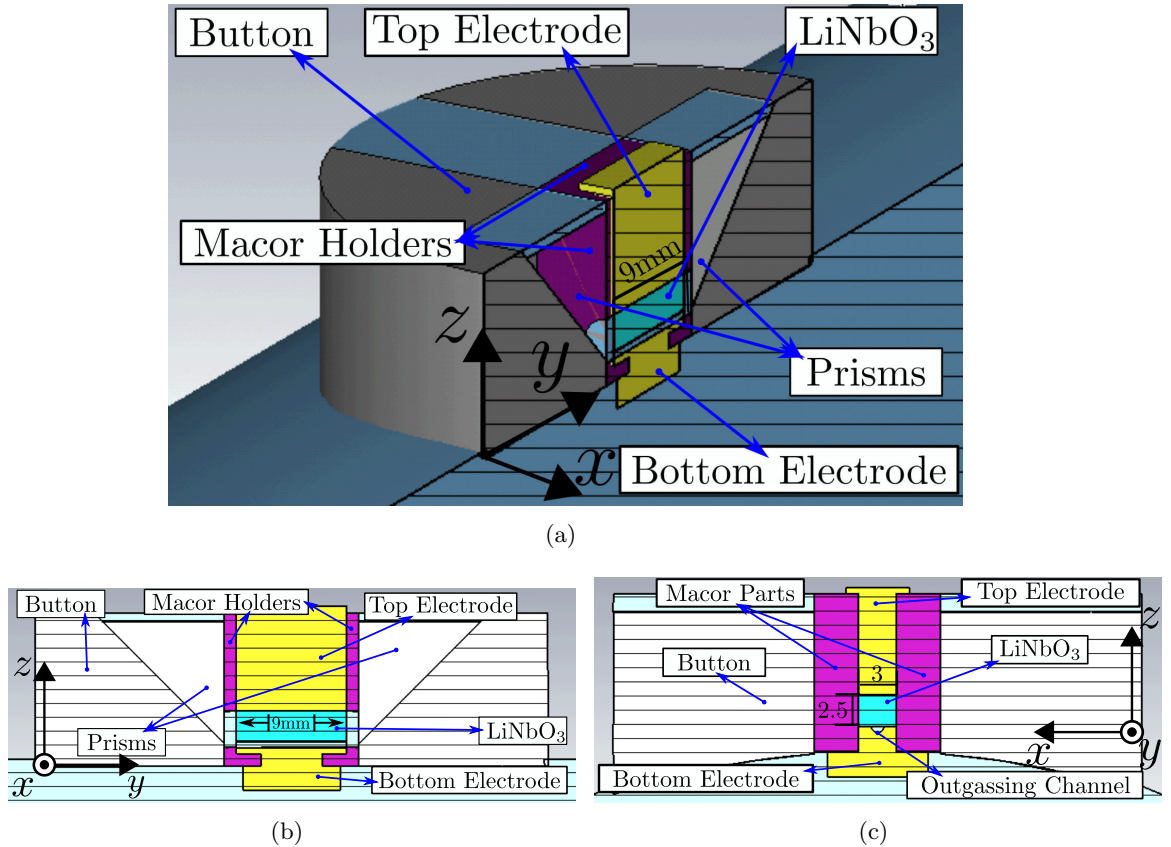
Figure 4.18: Screenshots of different views of pickup one in the CST user interface.

field lines be more uniform and parallel in between the electrodes, in the same fashion as described in Figure 3.8(b). In contrast, the lack of a grounded top electrode in pickup zero leads to a decay in the propagating peak-field crossing the crystal.

Table 4.5: Analytical prediction for a shape factor $\mu_S=1$, and the numeric result for the peak field at different radial positions inside the crystal under on-centre nominal SPS bunch conditions for pickup one.

Position [mm]	68.0	68.5	69.0	69.5	70.0
Analytical prediction [kV/m]	0.87	0.86	0.86	0.85	0.85
Modulating Field Peak E_{LNB} [kV/m]	2.93	2.86	2.80	2.76	2.77

On this occasion, the field strength when approaching the button along the radial distance is greater than the analytical estimation. This field enhancement is due to field lines concentrated near the electrode (Fig. 3.8(b)), which yields a shape factor $\mu_S \simeq$ 1.3. The mechanism ruling the field propagation is presented in Figure 4.20: the bottom electrode becomes an attraction point of field lines, in contrast to the pattern shown in
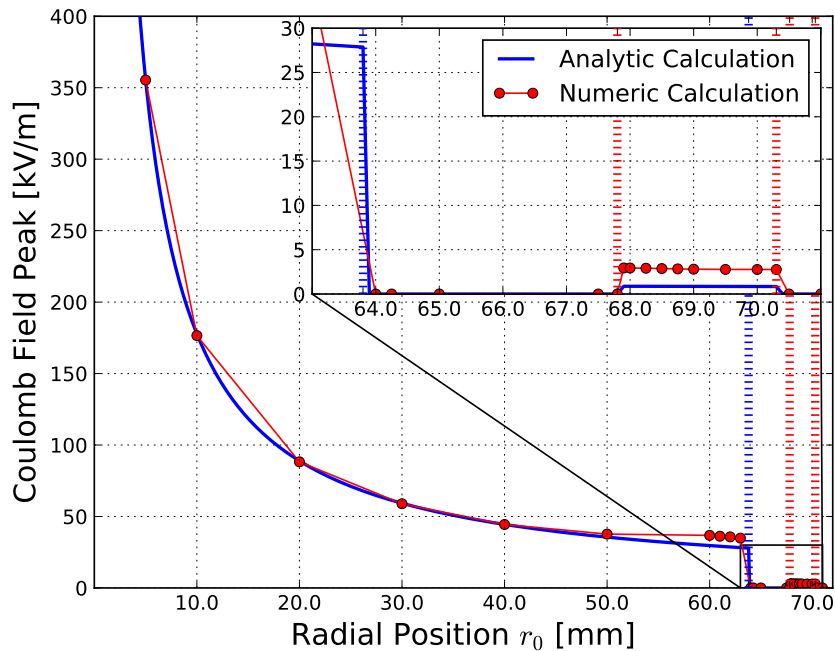
Figure 4.19: Numerical electromagnetic and analytic simulations of the peak Coulomb field along the radial transverse position r_0 over the pipe section for pickup one.

model zero. The Coulomb field polarises the electrode and creates a more uniform field distribution between the positive charge accumulated below the bottom face of the crystal and the grounded top electrode. In addition, the field collected is delivered in a smaller section, which increases the modulating field in the crystal. Zones A and B in the plot also reveal areas of high field where the lines escape towards grounded elements instead of going through the crystal. Future electrode and pickup designs must minimise those effects in order to achieve further increments of the modulating field.

Likewise pickup zero, Figure 4.21 proves that the enhanced field time-profile remains Gaussian-shaped inside the LNB crystal with a bunch length slightly shorter of $4\sigma = 0.93$ ns. Although the presence of the electrode does not produce any relevant distortion in the main signal, a small resonance appears after the beam transit. The residual periodic signal that follows the beam transit was not present in previous rigid mode simulations for pickup zero, so then the first conclusion is that the residual oscillations are induced somehow by the electrodes. This phenomena will be analysed in the following section.

Finally, from Table 4.5, one can notice that the modulating peak-field inside the crystal for pickup one rises with respect to the analytical prediction by a factor greater than its shape factor $\mu_S = 1.33$. For instance, the electric peak-field at $r_0 = 68.5$ mm is 3.35
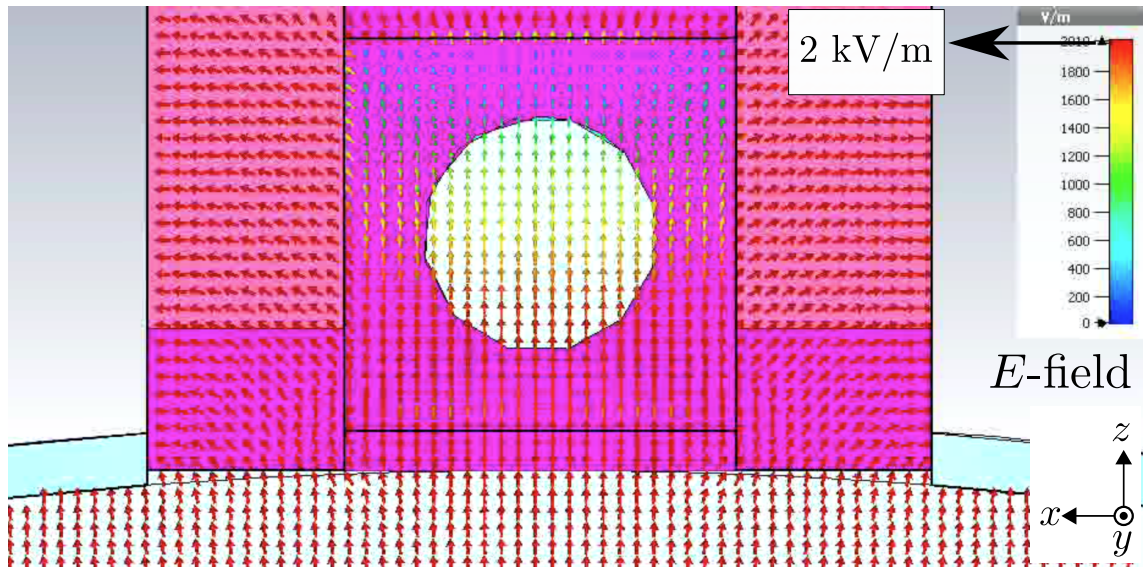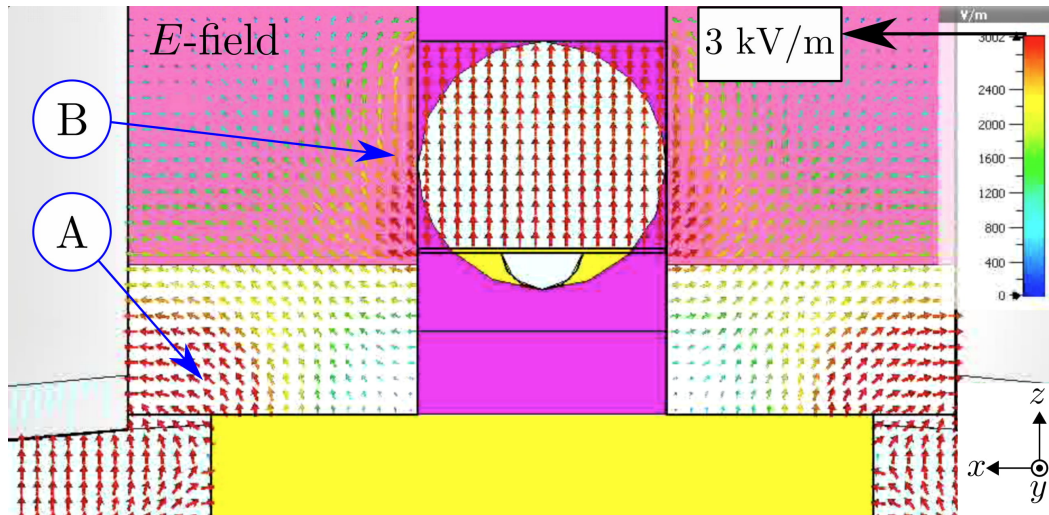
Figure 4.20: Vector field map produced by CST over the crystal section XZ at $y = 0$ for pickup one. The instant corresponds to the peak field at $r_0 = 68.5\,\mathrm{mm}$. The field goes through a shorter path A towards the grounded pipe and through B due to the lower dielectric constant of Macor.
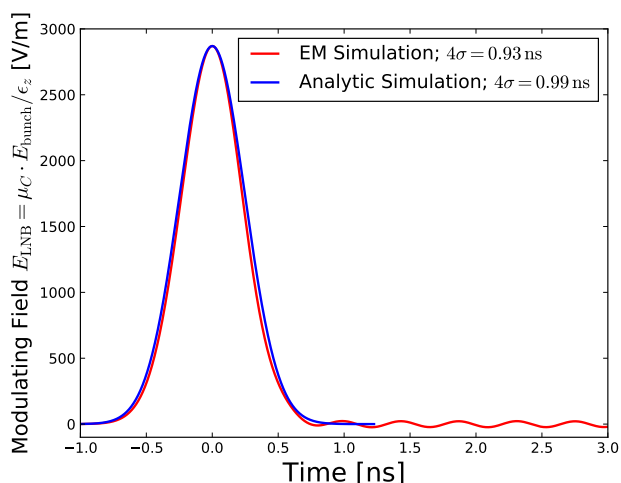
Figure 4.21: Modulating field time-profile curve inside the LNB sample for pickup one.

times higher than the analytical prediction. This indicates the efficiency of the electrodes to modify the density of field lines from the inner part facing the proton bunch to the outer part in contact with the crystal (Fig. 3.8(b)). Particularly, the electrode design is capable of gathering more Coulomb field that polarise electrically the electrode itself, delivering the collected field into the crystal with more compacted lines, leading to an increase even greater than the shape factor. This coupling factor was already introduced in equation 4.2 as μ_C, where here $E_{\mathrm{LNB}}(r_0) = E_{\mathrm{bunch}}(r_0) \cdot \mu_C/\epsilon_z$, and E_{bunch} is the analytical prediction at the radial position r_0. Therefore, for pickup one, $\mu_C = 3.35$.

4.3.3 Electromagnetic simulations of Head-Tail instabilities

At this point, both pickup models zero and one have been simulated for a rigid mode ($m = 0$), however, this prototype is a first contribution towards a system capable of detecting high order beam instabilities, as well as crabbing. With this objective in mind, numeric simulations of different proton beam instabilities under SPS parameters have been performed (Table 1.1). In particular, simulations of HT modes 1, 6 and 8 are presented, all of them with an amplitude of 3 mm. Modes 1 and 6 represent two significant scenarios, at least, in terms of bandwidth response at Hi-Lumi LHC: the charge distribution for a HT mode 1 is similar to the effect induced by a crab cavity kick, so this case allows us to also explore the modulating field profile for a crabbed-like beam. The aim of simulating mode 6 is to investigate the prediction presented in section 2.5, where it was stated that a modulating field in a 9 mm LNB crystal following the time structure of such a mode ($\leq$ 6 GHz) should be detectable, making possible the observation of high order instabilities in LHC. Therefore, considering mode 1 and the limiting case mode 6 covers the intermediate cases in between, and it is sufficient to investigate the reliability of the goals demanded by the Hi-Lumi project. Apart from modes 1 and 6, the mode 8 simulation is an step forward beyond the Hi-Lumi requirements to explore the detection limit of this technology. Also, the performance of pickup zero is limited by its low modulating capacity under LHC parameters, therefore the HT simulations are focused on investigating the novelty of introducing a floating electrode in pickup one, and its potential impact on bandwidth.

Importantly, CST defines the particle beam as a straight transmission line, so it is not possible to reproduce the beam offset functions shown in Figure 3.11(a). Since this feature is not available in the software, as confirmed in consultation with CST engineers, a workaround solution is necessary. It is possible though, to modify the charge distribution ρ over the transmission line to overcome this constraint. In fact, there exists a way to replicate the field profile of a HT instability at a given transverse radial distance r_0, multiplying ρ by a factor χ:

$$\chi = \frac{r_0}{r_0 \pm A \cdot \sin\left[\left[t - (t_0 - \frac{\mathrm{HT_{width}}}{2})\right] \cdot \frac{\pi}{\mathrm{HT_{width}}} \cdot (m+1)\right]} \, , \tag{4.3}$$

where A is the instability amplitude with the same units of r_0, m is the HT order, and $\mathrm{HT_{width}}$ is the distance between the boundary nodes of the HT instability centred at t_0. The parameter $\mathrm{HT_{width}}$ is relatively important for the simulation because the HT

oscillations are packed within that distance, so its variation also modifies the HT frequency. In these calculations, $HT_{width} \simeq 2.5$ ns, which is a reasonable value according to previous measurements in LHC [11]. Equation 4.3 is simply an approximation that provides a faithful replica of the HT field profile only for a particular radial distance. For all the cases, the same value of $r_0 = 68.5$ mm was taken, which corresponds approximately to the crystal centre in pickup one. Then, the transmission line distribution ρ_{TL} in these simulations is redefined as $\rho_{TL} = \rho \times \chi$, where ρ is a Gaussian distributed charge density given by equation 3.4 with $4\sigma = 1$ ns. Since there is no physical offset over the beam, the Coulomb field propagation would be radially symmetric in all directions, leading to exactly the same field profile in opposing pickups. However, it is possible to simulate the signal in the opposite pickup of the pipe by swapping the sign ($\pm$) in equation 4.3, which inverts the function along $\chi = 1$.

4.3.3.1 Head-Tail modes 1 and 6.

Figure 4.22 shows a comparison, between the CST output and the corresponding analytic calculation, of the modulating field inside the crystals in opposing pickups and the difference $E_{LNB,right}(t) - E_{LNB,left}(t)$ between them, for modes 1 and 6. The analytic result was obtained following the same procedure described in previous sections for an on-centre beam, but now the proton field E_p has been convoluted by ρ_{TM} in equation 3.5. Also, the coupling factor μ_C has been applied on E_{bunch} to scale the expected modulating field correctly, in particular for pickup one, $\mu_C = 3.35$ at $r_0 = 68.5$ mm (Table 4.5).

The modulating field inside the LNB crystal for mode 1 is shown in Figures 4.22(a) and 4.22(c). Apart from the periodic structure (A_{right}, A_{left}) that was already observed with $m = 0$, it is hard to distinguish at first glance the main signal from one induced by a Gaussian on-centre beam. This is due to the fact that a HT instability effectively induces a very small pattern overlapping the rigid mode-like distribution, as was shown in Figure 3.11(b). The residual periodic artefact that follows the rigid mode transit in Figure 4.21 exhibits a similar amplitude and the same period $T \simeq 0.44$ ns, which is within the same order of the mode 1 period in this case, $T \simeq 1$ ns. Also, the oscillation remains during the time window simulated ($t \simeq 10$ ns).

Figure 4.22(e) shows the modulating field difference between opposing pickups for mode 1. The reader can observe that at position B the analytic field does not follow the expected mode 1 shape (Fig. 3.12(b)). This is probably caused by an asymmetry
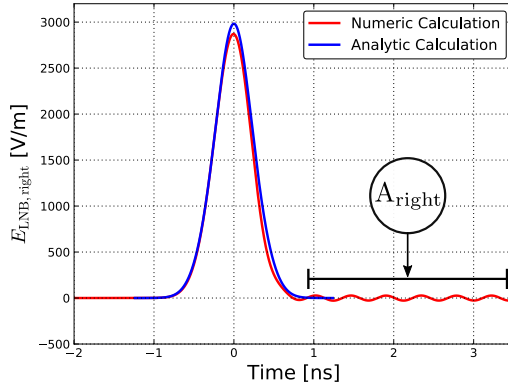
(a) Right pickup, mode = 1.
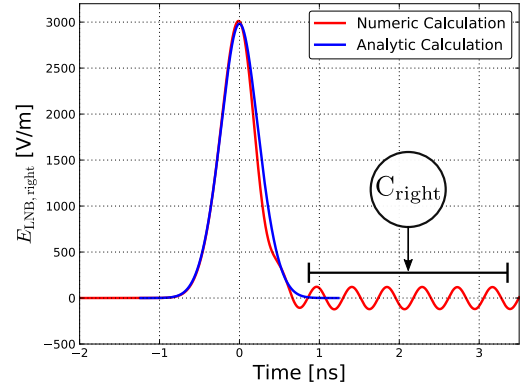
(b) Right pickup, mode = 6.
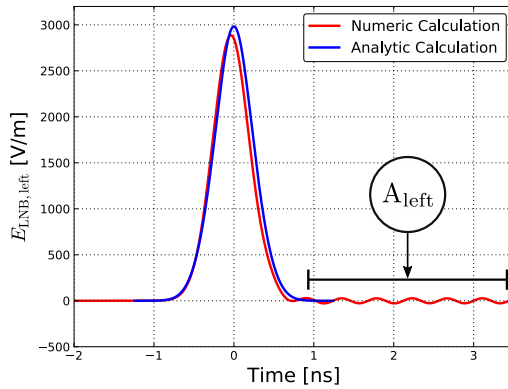
(c) Left pickup, mode=1.
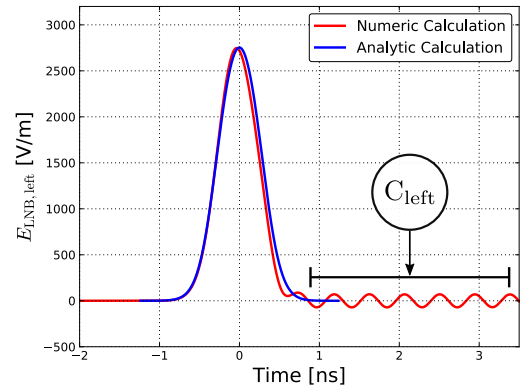
(d) Left pickup, mode = 6.
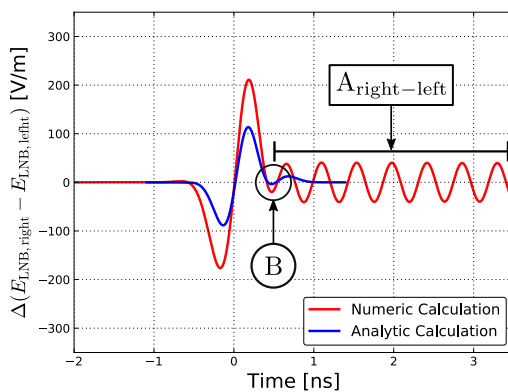
(e) $E_{\mathrm{LNB,right}} - E_{\mathrm{LNB,left}}$, mode = 1
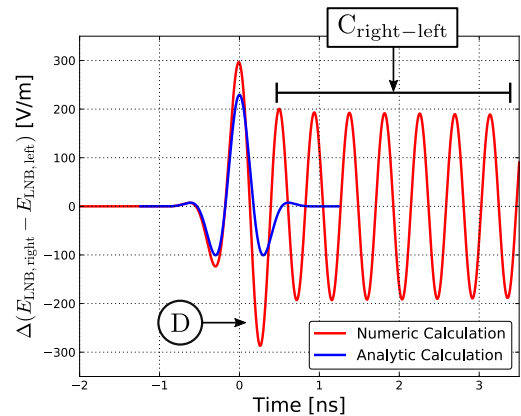
(f) $E_{\mathrm{LNB,right}} - E_{\mathrm{LNB,left}}$, mode = 6.

Figure 4.22: Comparison between the numeric and analytic simulations of HT instability modes 1 and 6, both of $3\,\mathrm{mm}$ amplitude.

difference between the functions $\rho_{\mathrm{TL}}(+)$ and $\rho_{\mathrm{TL}}(-)$ when swapping the sign in equation 4.3 to calculate the field in the opposite pickup (the difference $\chi(+) - \chi(-)$ should be a standing-wave function, perfectly even-symmetric). Although the difference may be small, the convolution of equation 3.5 could be amplifying the source of error. Nevertheless, apart of this nuance the profile is correct and more importantly, both CST and the analytic calculations used exactly the same functions $\rho_{\mathrm{TL}}(\pm)$ so both curves can be fairly compared. The output indicates the after-beam artefact is comparable in size to ΔE_{LNB}, and the way the resonance pattern is reduced in B indicates that it overlaps the HT signal itself.

Figures 4.22(b), 4.22(d), and 4.22(f) represent an equivalent result for HT mode 6. The modulating field E_{LNB} inside the crystal for a single pickup also reveals similar resonances (C_{left}, C_{right}) after the passing beam, which are now almost in anti-phase one each other. The period is the same as in mode 0 and 1, that is, $T \simeq 0.44\,\mathrm{ns}$, but the amplitude is visibly higher. Then, the period of the after-beam pattern seems independent of the order of the HT, but the amplitude increases with it. For modes 0 and 1, the resonance may be slightly excited by the main charge distribution, but is not driven in phase, so the amplitude is small. For mode 6, the charge distribution in time is similar to the period of the oscillations, so it drives the resonance to a higher amplitude. Once again in this case, the amplitude of the minimum at point D in Figure 4.22(f) clearly indicates that the HT signal and the resonance are overlapped.

The amplitude of the resonances in the CST output is slightly different in each pickup with respect to the opposite in every mode, and do not cancel out each other in the differential field ΔE_{LNB} because the resonance is not in-phase. The reader must bear in mind that instead of subtracting fields from opposing pickups in a single simulation, the same pickup is simulated twice after swapping the sign in $\chi(\pm)$ to reproduce the left and right modulating fields. Figure 4.23 is a illustrative diagram of the approximative charge distribution for HT mode 1 using χ from equation 4.3 as an on-centre beam, where the charge distributions $\rho_{\mathrm{TL}}(+)$ (case (a)) and $\rho_{\mathrm{TL}}(-)$ (case (b)) generate signals in opposing pickups. For each case, a first order resonance takes place when the maximum charge passes, and therefore do not occur at the same instant for $\rho_{\mathrm{TL}}(+)$ and $\rho_{\mathrm{TL}}(-)$. However, if we were able to simulate a real physical offset mode 1 as in case (c), then the resonance in both pickups due to the charge distribution would be perfectly in-phase, and they would, to first order, cancel each other in ΔE_{LNB}.
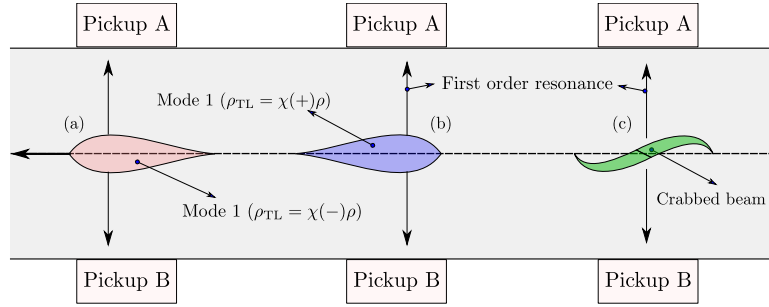
Figure 4.23: Diagram of the resonance mechanism.
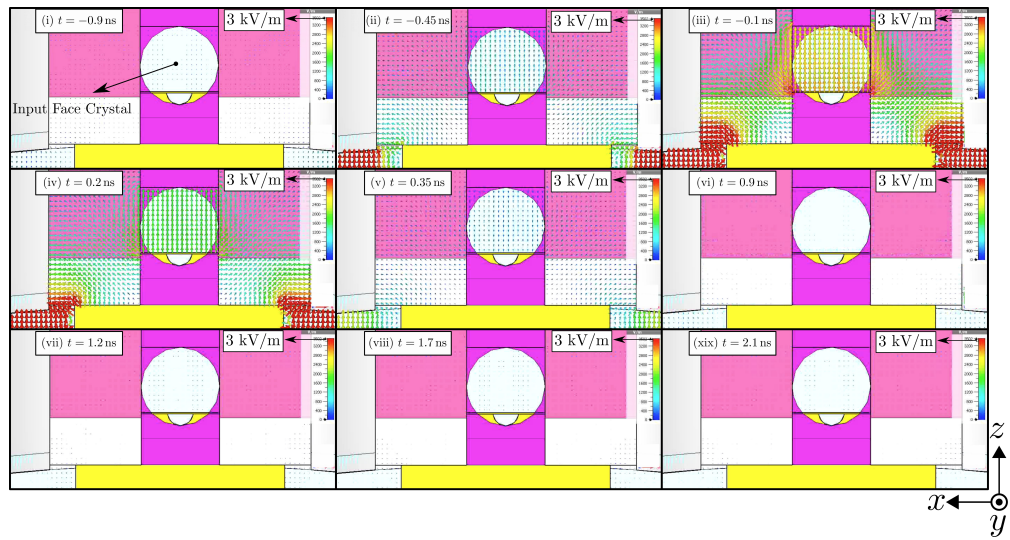
(a) Mode 1.
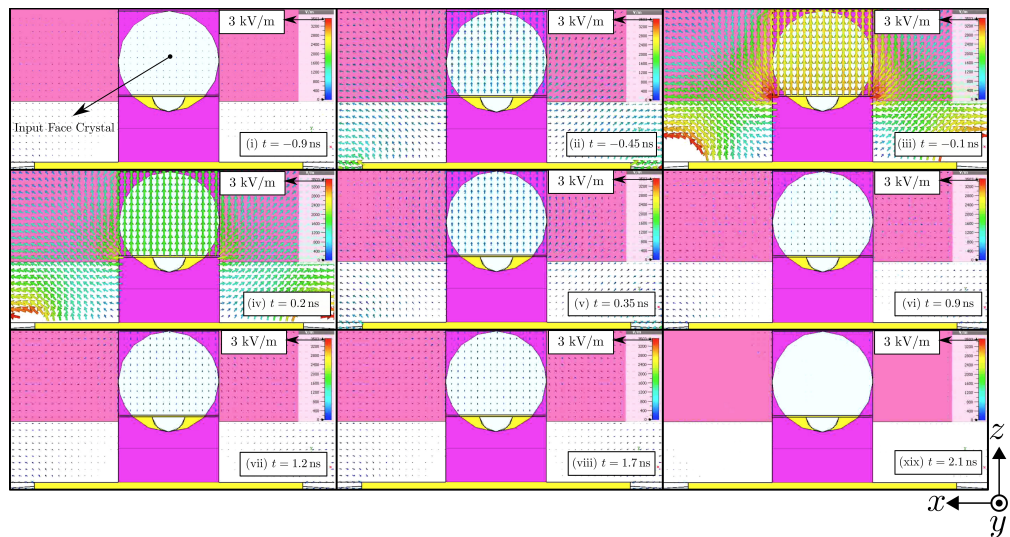
(b) Mode 6.

Figure 4.24: Vector field map evolution over the XZ plane at $y = 0$ for modes 1 and 6. The maximum field strength in the colour scale (red) corresponds to $3\,\mathrm{kV/m}$.

Figure 4.24 shows the temporal evolution of the field lines distribution over the crystal section in the plane XZ at $y = 0$, for modes 1 and 6. As pointed out for the rigid mode, there is field escaping through the edges of the electrode, and also around the crystal due to the lower dielectric constant of Macor. The main signal is depicted over the screenshots (i), (ii), (iii) and (iv), and the field lines turn fainter for the resonance in the rest of cases. The time stamp corresponds to the time values overlaid on the profiles shown in Figures 4.22(a) and 4.22(b), for modes 1 and 6, respectively.

According to these results, the main outcome is the confirmation by numeric means that the modulating field inside the crystal is able to follow a mode 6 HT time structure. Nevertheless, a residual after-beam field inside the crystal has also been detected, that overlaps and interferies partially with the HT profile itself. Although the amplitude of this persistent resonance is small in relation to the main signal in a single pickup, it is comparable to the difference ΔE_{LNB} between opposing pickups. However, it is important to highlight that the presence of the first order resonance doubles up in ΔE_{LNB} instead of disappearing due to the method applied to simulate the HT modes. Therefore, this part of the outcome is not realistic, but still this artefact may potentially mask high order modulation modes, unless the resonance is mitigated in future designs. The period of this pattern is the same for modes 0, 1 and 6, which suggests it is intrinsic to the pickup design and may be amplified when resonant with the HT frequencies.

4.3.3.2 Investigation of resonance.

Interestingly, the period of the resonance T could seem related to the SPS pipe, since $c \times 0.44\,\mathrm{ns} \simeq 132\,\mathrm{mm}$, which is almost perfectly coincident with the pipe diameter (133 mm). Nevertheless, when pickup one is attached to an LHC pipe of 30 mm radius the period remains very constant ($T \simeq 0.42\,\mathrm{ns}$), just as the zoomed in depiction proves in Figure 4.25. Therefore, the resonance is independent of the pipe diameter. Figure 4.26 shows how the period of the rigid mode resonance varies as the crystal gets thinner along the z direction. In this parametric study, the top electrode is kept grounded and its original length $l_0 = 7.98\,\mathrm{mm}$ increases by steps Δl equal to the crystal reduction to keep it right in between the electrodes. In this particular set of simulations, the T-shaped bottom electrode has been replaced by a roof-shaped one. From $T = 0.44\,\mathrm{ns}$, the period reaches $T = 0.54\,\mathrm{ns}$ for a $50\,\mu\mathrm{m}$ thick LNB crystal so the impact is higher than changing the pipe diameter.
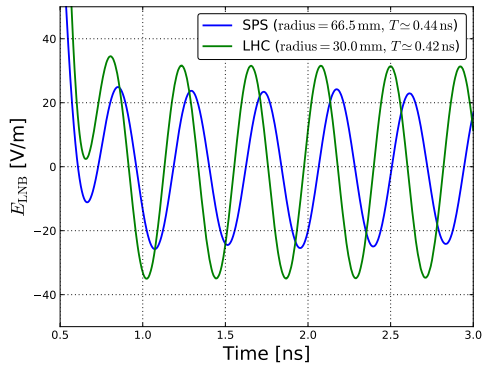
Figure 4.25: Resonances of the rigid mode for a pickup one installed in the LHC (30 mm) and the SPS (66.5 mm).
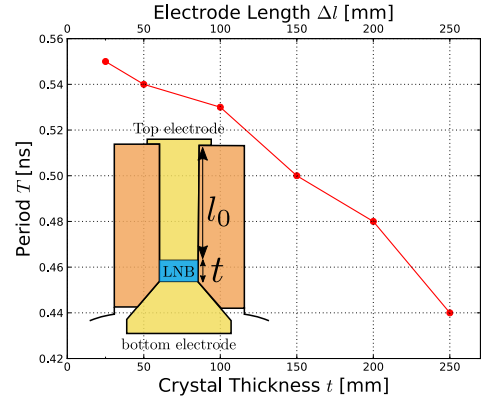
Figure 4.26: Period of the resonance at rigid mode against the crystal thickness.

Figure 4.26 shows that the resonance period correlates with the electrode length $l_0 + \Delta l$. Therefore, the element causing the resonance might be the top electrode shape, which reminds us a long thick wire. A possible hypothesis is the following: as the beam passes the polarised charge flows through the electrode towards the ground and generates a self-inductance along l_0 that makes the current oscillate. For instance, this effect would occur during the main signal illustrated in Figure 4.24 for modes 1 and 6, when the vertical field lines polarise the top electrode vertically, making the current flow parallel to z along the metallic rod. The fact that the period increases with the electrode length reinforces this hypothesis. Then, if the top electrode is widened in x, the current-induced magnetic field should be blocked and also the inductance along the wire-like shape.

Three different modifications have been implemented in different pickup one simulations to study the impact of the top electrode in the resonances. Figure 4.27(a) shows the modulating field produced in every case: in the V1 design the bottom electrode facing the beam has been removed. One can observe that now the peak field has decayed because the concentrating effect is attenuated; In V2 both top and bottom electrodes have been removed, then the field strength is even lower than in pickup zero, because the crystal is more retracted; V3 is the same as pickup one, but the top electrode has been extended along the x direction until touching the button body to prevent field lines around the electrode. In this case the peak field is very similar to previous simulations for an unmodified pickup one ($\sim 2.8\,\text{kV/m}$). It can be appreciated in Figure 4.27(b) that the resonance remains in V1, only noise can be seen in V2, and the modification introduced in V3 has dramatically attenuated the pattern shown in previous Figure 4.25. In summary, the bot-

tom electrode is not causing the perturbation, in fact, it is only when the T-shaped top electrode is removed in V2 or in pickup zero that the resonance disappears. Therefore, it is fair to conclude that the top electrode in pickup one was causing the resonance.
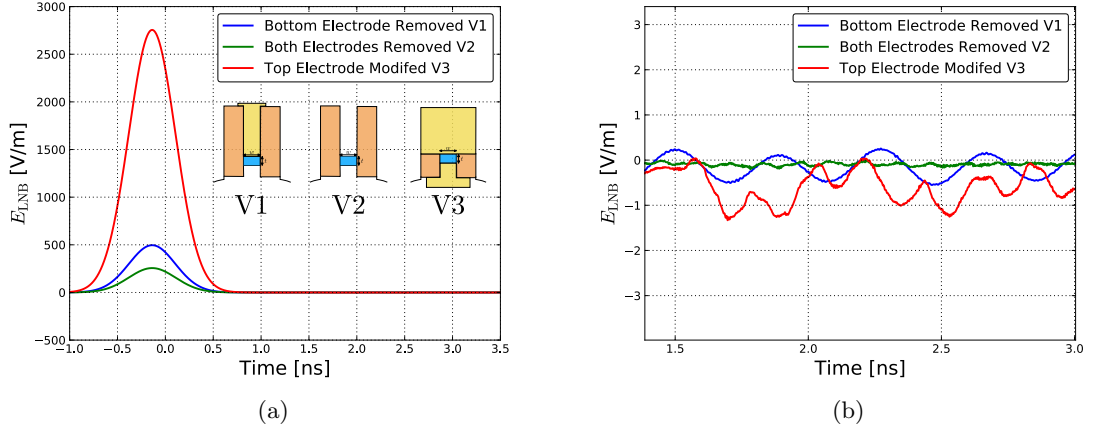
Figure 4.27: Modulating field for different modifications of pickup one: (a) standard single pickup signal; (b) zoomed in depiction of the resonance.

4.3.3.3 Head-Tail mode 8.

Figure 4.28 shows a vector field map depicted over the longitudinal section of the crystal in pickup one when a mode 8 HT beam is passing. The instant reflects a non-homogenous distribution at $x = 0$ on the ZY plane. Figures 4.29(b) and 4.29(a) account this phenomena by representing the modulating profile at different points along the y direction inside the crystal. The resonances between opposing pickups are in anti-phase as expected in the simulations, the peak profile changes vertically, and they are also shifted with respect to $t = 0$. Also, the position of the maxima are not symmetric with respect to $t = 0$ because once again, the first order resonance does not occur at that instant. The time offset between positions $y = -3\,\text{mm}$ and $y = 3\,\text{mm}$ is approximately $\Delta t \simeq 0.085\,\text{ns}$ for the left pickup and $\Delta t \simeq 0.03\,\text{ns}$ for the right one. Similar offsets are also observed at lower HT order modes 1 and 6 in pickup one, where the time difference is in the order of $\Delta t \sim 0.07\,\text{ns}$. Figures 4.30(b) and 4.30(a) are equivalent results for a HT mode 8 with the modified version V3. The effect of the resonance has almost been removed, so the profiles present less distorted shapes. In this case, the time difference between maxima along the crystal is $\Delta t = 0.097\,\text{ns}$ on the left, and $0.085\,\text{ns}$ on the right. Ideally, a photon that takes $\sim 0.043\,\text{ns}$ ($n_z \simeq 2.18$) to travel along those $6\,\text{mm}$ through the crystal should
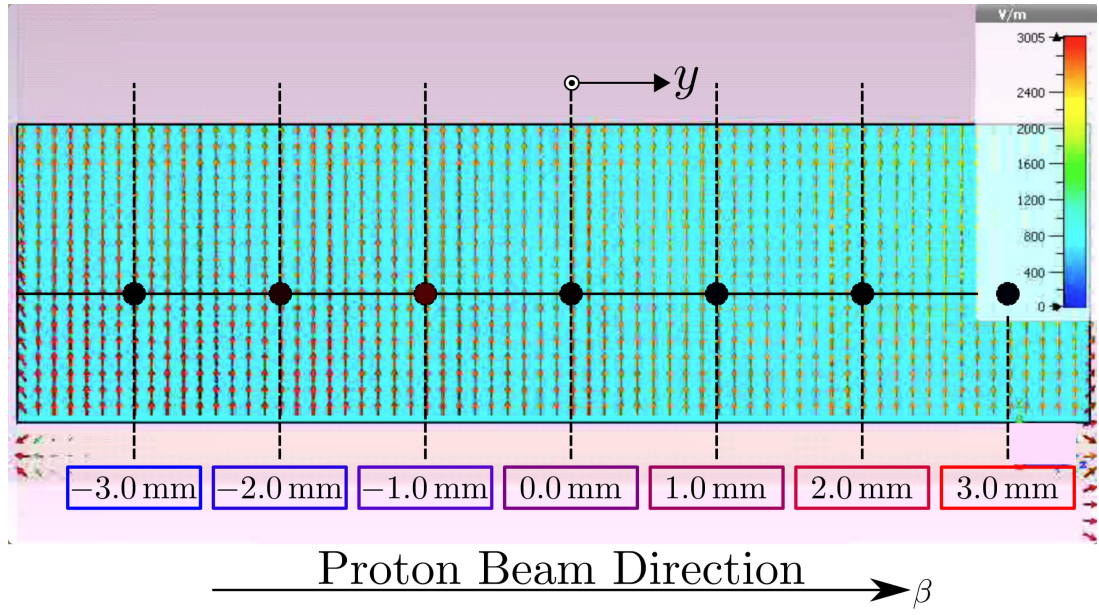
Figure 4.28: Vector map of the modulating field over the longitudinal section of the crystal for HT mode 8.

(a) Left pickup.

(b) Right pickup.
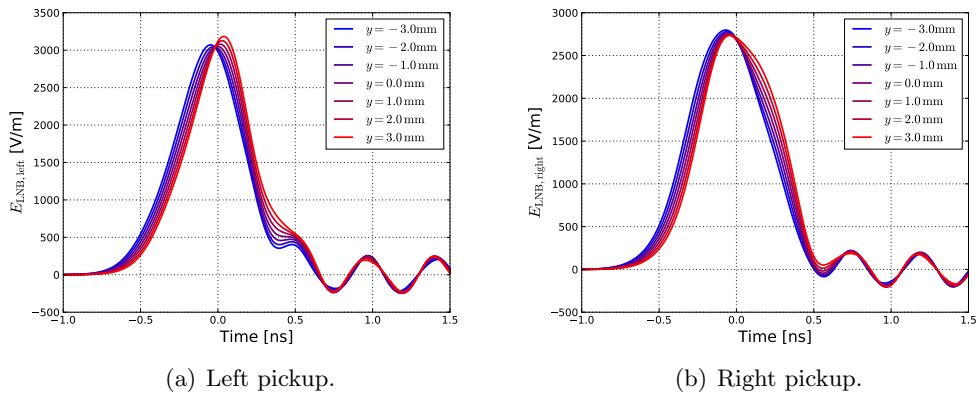
Figure 4.29: Modulating field in opposing pickups for mode 8 at different positions over the y axis for pickup one.

(a) Left pickup.

(b) Right pickup.
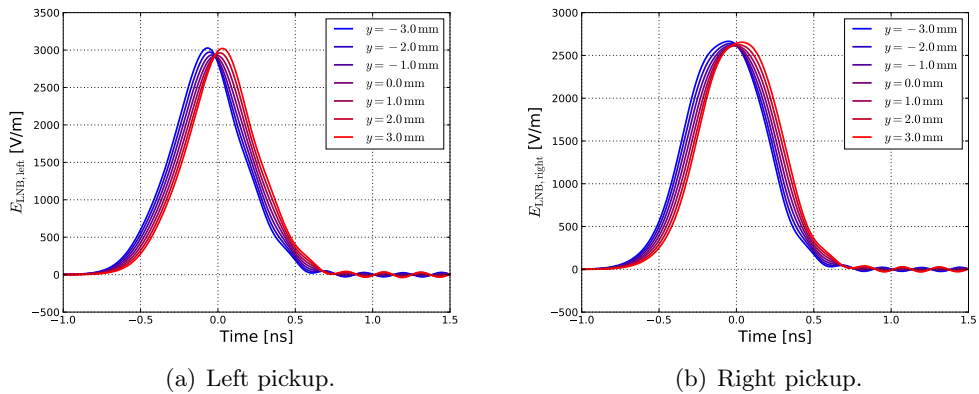
Figure 4.30: Modulating field in opposing pickups for mode 8 at different positions over the y axis for the modified pickup one, V3.

87

be modulated by exactly the same field strength to ensure a perfect phase matching with the modulating field. The discrepancy with the offset Δt indicates a certain degree of mismatch that implies a loss of modulation capacity.
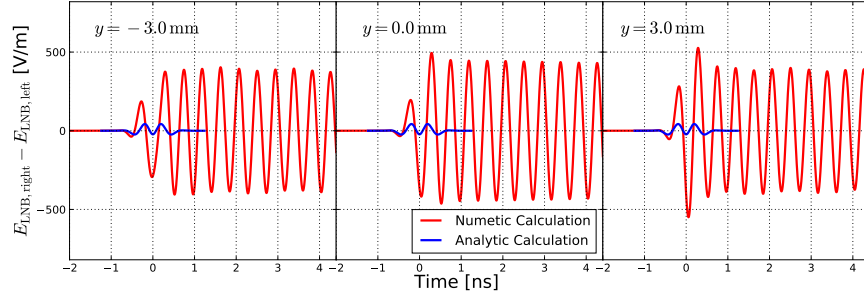
(a) Mode 8 pickup one.
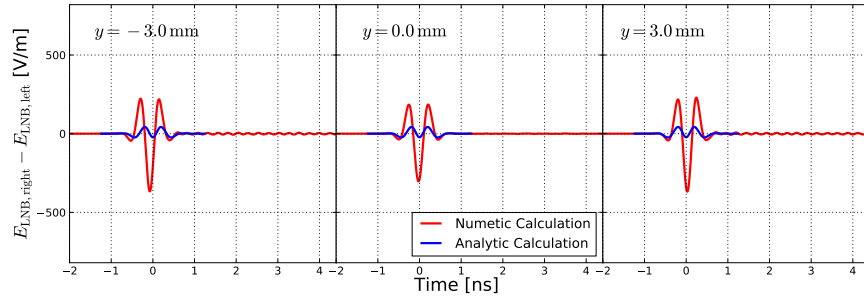
(b) Mode 8 with V3.
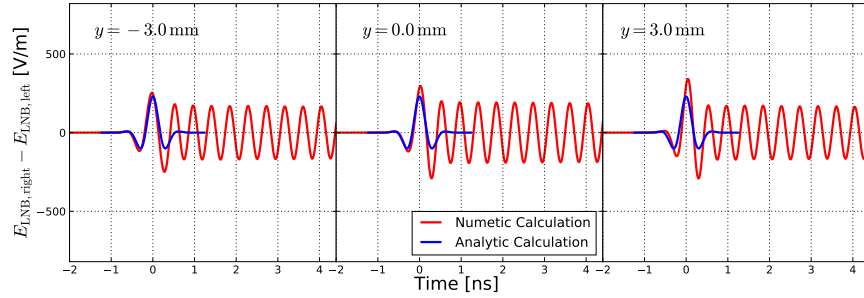
(c) Mode 6 with pickup one.

Figure 4.31: Modulating field difference ΔE_{LNB} in different positions along the longitudinal y axis. The analytic prediction used the original pickup one coupling factor μ_C also for the V3 result, so the field amplitude may change with the correct μ_C in (b).

Figure 4.31(a) shows the differential signal ΔE_{LNB} of a mode 8 HT instability for pickup one. The amplitude of the resonance has reached the maximum as the period of the applied field is about $T \simeq 0.55\,\mathrm{ns}$, almost totally in-phase with the resonance $T \simeq 0.44\,\mathrm{ns}$. The anti-phase resonances from opposing pickups sum up producing an overwhelming signal that masks completely the HT-induced field. However, as mentioned for modes 1

and 6, this output does not represent the real case scenario where the first order resonance should cancel out. The interference with the train changes along the y direction reducing ($y = -3\,\mathrm{mm}$) and expanding ($y = 3\,\mathrm{mm}$) the resonance amplitude. Comparatively, Figure 4.31(b) is also a mode 8 HT output for a V3 version, where the resonance is almost gone. Also, a mode 6 simulation with pickup one still produces a remaining HT profile on the left of the train in Figure 4.31(c), but the mode 8 investigation is totally limited by the simulation method.

Although the interference in Figure 4.31(a) is probably produced by a hidden mode 8 profile, the overlapping with the resonance makes impossible to check the time structure, then it is pointless to simulate higher modes with pickup one. In conclusion, assuming the crystal is capable to follow mode 6 and even higher orders, it is important for the performance of the system to redesign the top electrode and the pickup in general in order to mitigate or even remove completely the resonance, so also higher modes can be investigated by CST simulations.

4.4 Pickup sensitivity

This section presents the numeric calculations of the variation of the modulating field E_{LNB} as a function of the proton beam position. The study basically consists in repeating the numeric simulations in CST for pickup zero (Fig. 4.14) and one (Fig. 4.18), keeping the same conditions defined previously for SPS but varying the bunch offset position z_0 (Fig. 4.32). For instance, Figure 4.34 shows the peak field value at $68.0\,\mathrm{mm}$ and $68.5\,\mathrm{mm}$ away from the pipe centre for pickups zero and one, respectively, which represents approximately the middle point of the LNB crystal sample in each case.

The positive offset indicates the particle bunch is traveling along a direction placed closer to the pickup and consequently, a negative value means the traveling bunch direction is further away. It should be noticed that Figures 4.15 and 4.19 illustrate an equivalent result of the peak field strength when assuming an on-centre proton bunch ($z_0 = 0$). The points in the $10\,\mathrm{mm}$ offset range in Figure 4.34 follow a quasi-linear behaviour, however the off-fit points at $\pm 5\,\mathrm{mm}$ reveal the general $1/r_0$ decay at higher offset positions z_0. Assuming the linearity, the gradient in electric field for the non-electrode case is $22.1\,\mathrm{Vm^{-1} \cdot mm^{-1}}$, whereas the incorporation of the electrode in pickup one increases, not just the peak-field, but also the position gradient up to $88.6\,\mathrm{Vm^{-1} \cdot mm^{-1}}$.
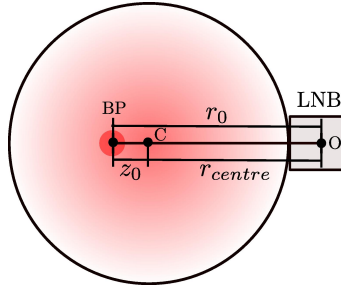
Figure 4.32: Diagram with the main geometrical parameters in the gradient calculation: BP is the beam position; C is the centre of the pipe; O is the crystal position.

The field-gradients simulated numerically by CST (Fig. 4.34(a) and Fig. 4.34(b)) are expected to match the analytical approximation obtained from applying equation 4.2. Nevertheless, the CST simulations demonstrates that the coupling factor μ_c also varies slightly when the position of the proton beam offset z_0 changes, just as Figures 4.33(a) and 4.33(b) illustrate. One can observe how the field concentrating factor μ_C, which is determined by the electrode shape, is also linearly dependent on the beam position. Therefore, the parameter μ_C can be expressed as a function of the gradient g_C and the beam offset z_0:

$$\mu_C(z_0) = z_0 \cdot g_C + \mu_C(r_0) = (r_0[\text{mm}] - r_{\text{centre}}[\text{mm}]) \cdot g_C[\text{mm}^{-1}] + \mu_C(r_{\text{centre}}), \quad (4.4)$$

where r_{centre} is the distance from the centre of the SPS pipe section to the observation point situated approximately at the centre of the crystal, as illustrated in Figure 4.32. In particular, these values shown in 4.33(a) and 4.33(b), for pickups zero $\mu_{C,0}$ and one $\mu_{C,1}$, have the following fits:

$$\mu_{C,0}(r_0) = (68.0 - r_0[\text{mm}]) \cdot 0.013 + 0.85 \,, \qquad \mu_{C,1}(r_0) = (68.5 - r_0[\text{mm}]) \cdot 0.052 + 3.35 \,, \quad (4.5)$$

where equation 4.4 has been reformulated as a function of r_0, and r_{centre} has been chosen to be 68.0 mm for pickup zero, leading to a gradient $g_C = 0.013 \, \text{mm}^{-1}$, and 68.5 mm for pickup one, giving a gradient $g_C = 0.052 \, \text{mm}^{-1}$. By virtue of the equations 4.5 and 4.4 above, equation 4.2 is rewritten as:

$$E_{\text{LNB}} = \frac{E_{\text{bunch}}(r_0) \cdot \mu_C(r_0)}{\epsilon_z} \,. \quad (4.6)$$
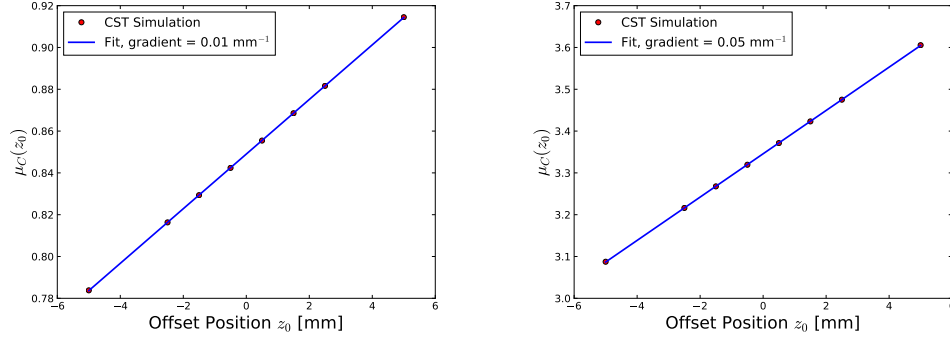
(a) $\mu_C(z_0)$ at $r_{\mathrm{centre}} = 68.0\,\mathrm{mm}$ for pickup zero. (b) $\mu_C(z_0)$ at $r_{\mathrm{centre}} = 68.5\,\mathrm{mm}$ for pickup one.

Figure 4.33: Coupling factor μ_C as a function of the beam offset z_0 according to the CST simulations.
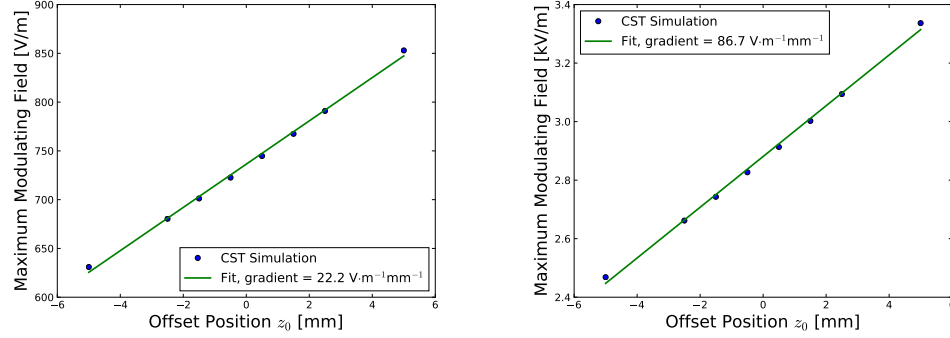
(a) Peak field at $r_{\mathrm{centre}} = 68.0\,\mathrm{mm}$ for pickup zero.

(b) Peak field at $r_{\mathrm{centre}} = 68.5\,\mathrm{mm}$ for pickup one.

Figure 4.34: Field strength peak gradient in the crystal as a function of the beam offset z_0 according to the CST simulations.

Analytically, the field-gradient g_C for small variations of the beam offset can be approximated by the derivative of the modulating field E_{LNB} with respect to the position r_0 (see appendix B):

$$g_C(r_0) = \frac{dE_{\mathrm{LNB}}(r_0)}{dr_0}[\mathrm{Vm}^{-1}\!\cdot\!\mathrm{mm}^{-1}] = -k_0\frac{N_p}{\beta\sigma\epsilon_z}\cdot\left[\frac{\mu_C(r_0)}{r_0^2} + \frac{g_C[\mathrm{mm}^{-1}]\cdot 10^3}{r_0}\right]\times 10^{-3}\,, \quad (4.7)$$

where k_0 is the peak-field decay constant defined in equation 3.13. With the SPS nominal values, that is, $\sigma = 0.25\,\mathrm{ns}$, $\beta \simeq 1$, $N_p = 1.15 \times 10^{11}$ protons, equation 4.7 makes the gradient $g_C(r_0)$ for pickup versions zero and one to take the values $-22.0\,\mathrm{Vm}^{-1}\cdot\mathrm{mm}^{-1}$ and $-86.8\,\mathrm{Vm}^{-1}\cdot\mathrm{mm}^{-1}$. The negative sign just indicates the modulating field increases

as the distance to the proton beam r_0 is reduced, or equivalently, the offset z_0 moves closer towards the pickup. Therefore, the results are indeed in very good agreement with those values obtained by CST.

4.5 Summary

This chapter basically tackles two crystal-integrated pickup designs: pickup zero interacts with a Coulomb field that propagates radially over the pipe section, while the upgraded model pickup one relies on concentrating more electric field lines in the crystal by introducing an attracting electrode, which effectively enhances the field strength. The simplified geometries of both designs have been defined in CST particle studio to estimate and characterise more precisely the field propagation across the crystal. According to the outcome produced by the numeric simulations, when upgrading from the first version to the electrode design, the field is increased approximately by a factor between 3.7 and 4.7 depending on what position in the crystal the laser is passing through. To give an indicator independent of the position, the voltage across the crystal thickness was incremented from 1.6 V across 5 mm for pickup zero, to 2.8 V across 2.5 mm for pickup one, according to CST.

Pickup one proposes a modest modification so the same buttons could be reused to investigate the floating electrode strategy. This constraint determined a simple electrode design that could be adapted to a given button body, which remained unchanged in both pickups. It is expected that this modification will increase the field a factor 3.7-4.7, which in combination with a ×1.8 longer crystal should lead to an overall EO signal increment factor between 6.7 to 8.7, according to the modulation equations 2.24 and 2.28. The shape of the electrode must be optimised in future designs to conduct the collected field towards the crystal more efficiently, so the field lines do not go through others paths, as depicted in Figure 4.20.

Very important simulations of HT instabilities were also performed to study the possible bandwidth limitations of the system. The results show that the modulating field inside the crystal can follow a mode 6 HT instability, but also reveal an after beam resonance that is caused mainly by the top electrode, and interferes with the HT profile. Although this residual artefact should cancel out in the differential field ΔE_{LNB}, the simulation method sums up the effect between opposing pickups, making worthless

to simulate any HT order beyond mode 8 for pickup one. The presence of the resonance in a single pickup can still be a major problem for the EO-BPM performance so further developments must redesign the top electrode to mitigate it. In fact, a potential modification that attenuates significantly the resonance and makes mode 8 detectable has been proposed.

Finally, the electromagnetic simulations draw another interesting conclusion: for variations of the beam position from the on-centre pipe axis within a few millimetres range, the maximum modulating field E_{LNB} in the crystal at the radial position around r_{centre} exhibits an almost linear behaviour with the beam offset, as Figures 4.34(a) and 4.34(b) demonstrate. In this scenario of small offset variations, the $1/r_0$ decay curve of the peak-field can be approximated by the linear-like response gradient, defined as the derivative of the peak field given by equation 4.7. This analytical approximation takes into account the dependency on r_0 of the coupling factor $\mu_c(r_0)$ also provided by CST and the LNB dielectric constant ϵ_z. As a consequence, the optical modulation and the field strength will also be linear with the beam position within that range.

Chapter 5

Crossed polarisers experimental setup

5.1 Optical setup

5.1.1 Optical arrangement

The EO-BPM follows the amplitude modulator scheme described in section 2.3.3. Thereby, the pickup presented in chapter 4 must be accompanied with an optical system. This section describes the optical setup developed to deliver the light beam into the pickups under polarisation controlled conditions [48].

The general setup is illustrated in Figure 5.1: the light beam source was a 780 nm fibre coupled laser placed in a control instrumentation room in CERN-HCA4, 160 m away from the pickups installed in the 4th sextant of the SPS ring (Fig. 1.4). The output laser is linearly polarised and connected to 160 m of Polarisation Maintaining (PM) fibre that carries out the Optical Beam (OB) from HCA4 to the prototype installed at SPS, keeping the optical polarisation state constant throughout the transfer by minimising the impact of the Polarisation Mode Dispersion (PMD) [59,60]. At the other extreme of the PM fibre, the OB is delivered vertically polarised by a 6.24 mm focal distance Fibre Collimator (FC). Furthermore, the vertical polarisation is again filtered by a polarising Plate Splitter (PS) that reflects at 90° the vertical component with an extinction ratio of 1:10000. Then, two mirrors M_1 and M_2 are used to align the optical path correctly towards the Knife-Edge Prism (KEP), which in turn, modifies the beam trajectory 90° into the EO pickup. Once the OB is reflected back after passing through the pickup, the KEP reflects it 90° again towards the return part of the system. The selection of the knife-edge prism as the optical element responsible for sending the light to the pickup, comes from the fact that its design

allows to separate 2 optical beams with a very narrow separation w_L, as it occurs in this system ($w_L \sim 15\,\text{mm}$). Since the alignment of this element is critical, the prism is mounted on a 3-axis stage attached to a fine movement rotation platform. In addition, the whole KEP system is resting on a Linear Actuator (LA) that permits to translate very finely (micrometer precision) the KEP along the z direction in Figure 5.1, that is, backward or towards the pickup. Consequently, bringing the KEP closer to the pickup leads to a wider w_L and vice-versa.
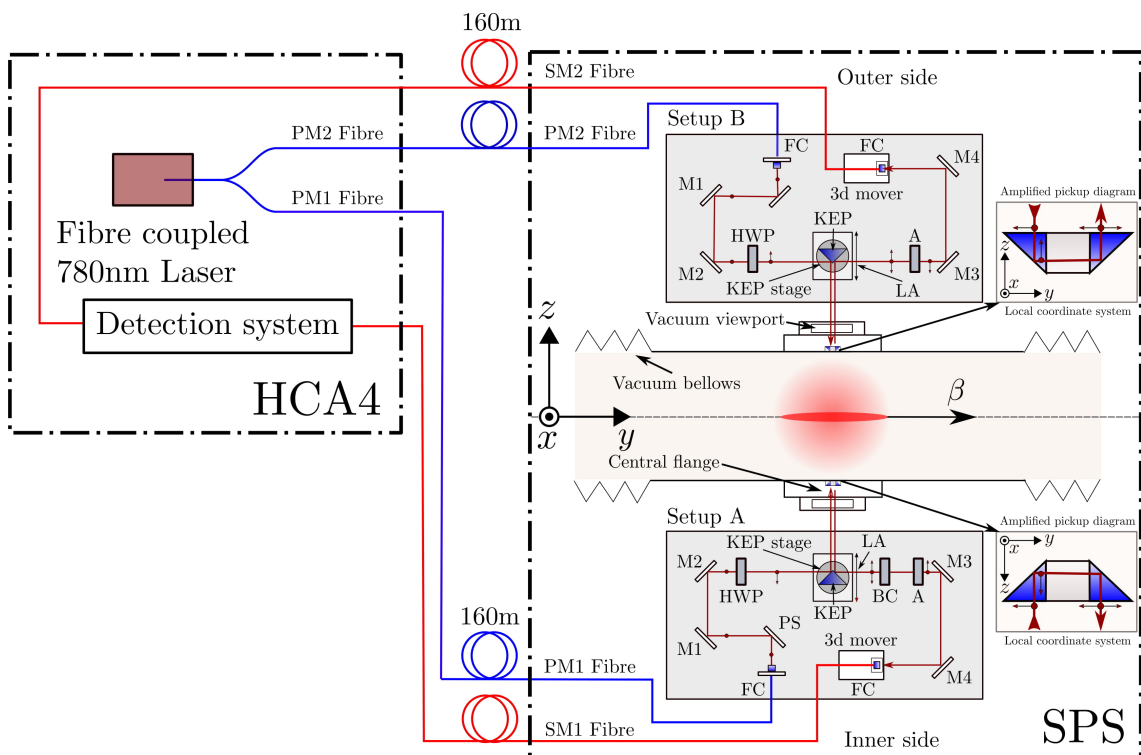
Figure 5.1: Layout of the optical setup for the EO-BPM experiment.

After the KEP, the light beam is conducted to a Fibre Coupler mounted in a 3d stage (3d FC) using a pair of mirrors M_3 and M_4. The OB is finally coupled by a $6.24\,\text{mm}$ lens into a Single Mode (SM) fibre that conveys the light $160\,\text{m}$ back to the detection system, installed in the same instrumentation room in HCA4 where the $780\,\text{nm}$ laser is located.

As depicted in Figure 5.1, the EO-BPM prototype consists of two fully equipped systems of pickup and optical setup on the horizontal plane at SPS. Thus, there exist two setups A and B, which are equivalent, providing optical beam to two opposing pickups. In terms of the arrangement, setups A and B are mirror images of each other with respect to the pipe longitudinal axis. In fact, both setups are oriented in such a way that the

Table 5.1: List of elements used in the experimental setup.

Component	Description
Laser	New Focus TLB-6800 (780 nm)
PM fibre	Nufern PM-S630-HP 175m 3.5μm core suitable wavelength range 630nm - 780 nm
SM fibre	Nufern S630-HP 175m 3.5μm core suitable wavelength range 630nm - 780 nm
PM splitter fibre	Gouldfiber optics PM coupler
Fibre Collimator (FC)	Thorlabs C110TMD-B - f = 6.24 mm mounted on a Thorlabs 1″ KS1T-SM1
Polarising Plate Splitter (PS)	Thorlabs PBSW-780 mounted on a 1″ Thorlabs KS1
Mirrors (M1 & M2)	Thorlabs 1″ BB1-E02 dielectric mirror mounted on a Thorlabs 1″KM100
Half-wave plate (HWP)	Thorlabs WPH10M-780 mounted on a 1″ remote stage Thorlabs PRM1Z8
Knife Edge Prism (KEP)	Thorlabs MRAK25-E03 prism mounted on a Newport 9411M stage attached to a linear actuator M-UMR825
Analyser (A)	Thorlabs WP25M-UB mounted on a 1″ remote stage Thorlabs PRM1Z8
Mirrors M3 & M4	Thorlabs 1″ BB1-E02 dielectric mirror mounted on a New Focus 8821 picomotor mount
3d Fibre Coupler (FC) stage	Thorlabs C110TMD-B - f = 6.24 mm mounted on a Thorlabs MAX302 - 3-Axis stage
Optical breadboard	Thorlabs MB4560/M*
Enclosure	Thorlabs XE25C9/M*

laser beam travels through the crystal in the same direction as the proton bunch. There is a single element breaking the symmetry, which is the Berek Compensator (BC) installed in setup A. This optical element works effectively as a retarder plate where the extent of the retardation can be manually adjusted. The Berek compensator allows to shift the output polarisation state after the crystal over the transmission curve, and consequently
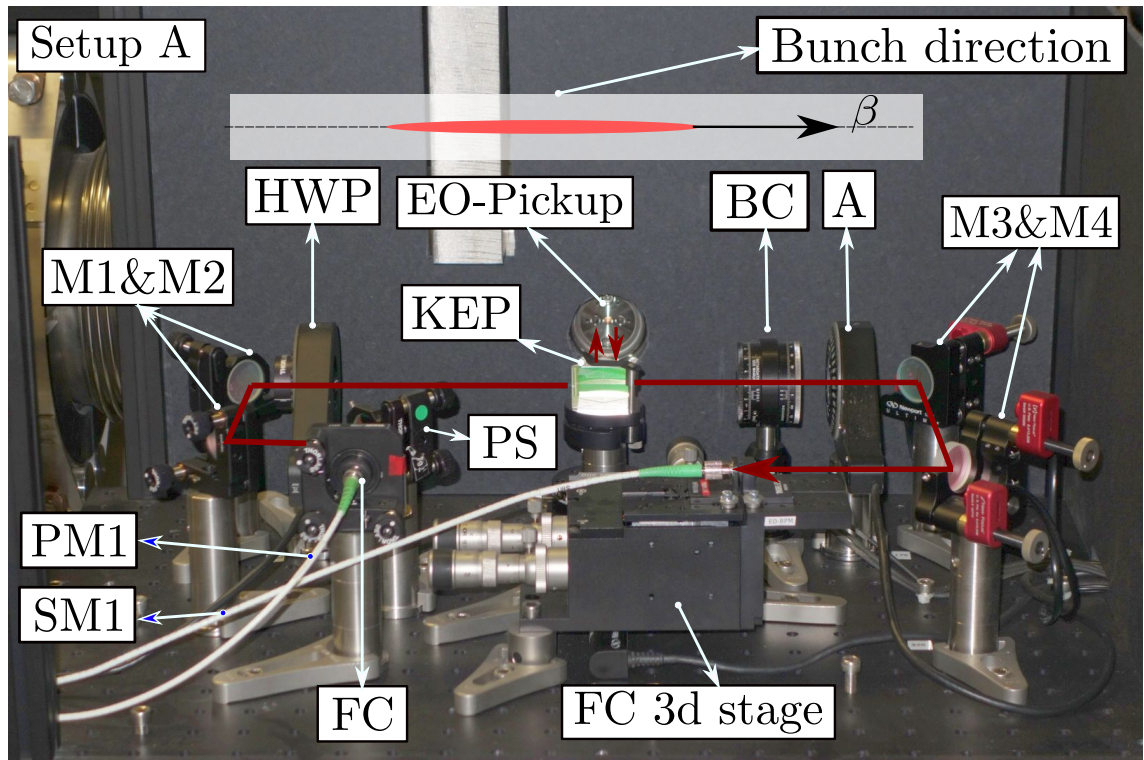
(a)
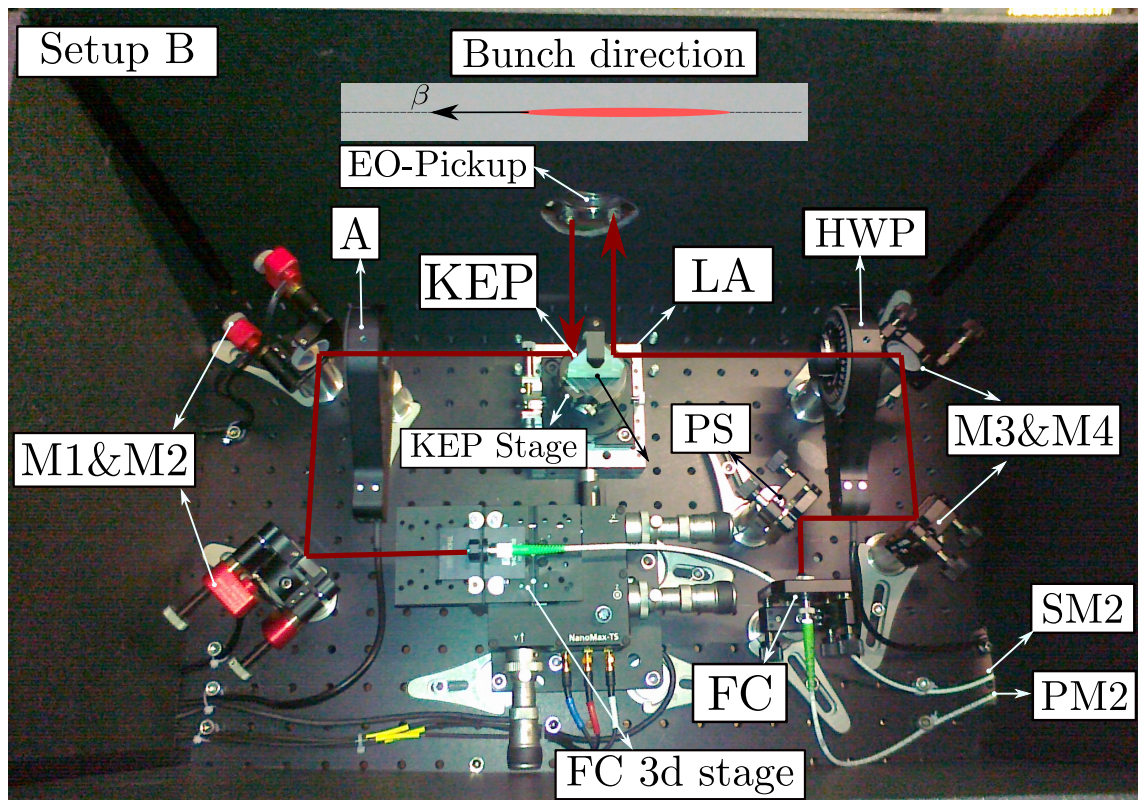
(b)

Figure 5.2: Front view of setup A (a) and top view of the equivalent setup B (b).

the sensitivity of the system (Fig. 2.11). The fibres PM1 and SM1 are the delivery and return fibres for setup A in the inner side of the ring, and similarly, PM2 and SM2 are the fibres for setup B in the outer part. In order to transfer the OB to both setups simultaneously, the laser could potentially be connected straight to both PM1 and PM2 by a PM fibre splitter.

Besides the optical elements involved in the alignment of the OB, the setup also includes two similar remote rotation stages: the first one holds a Half-Wave Plate (HWP) before the knife-edge prism. The objective of the HWP is to rotate the vertical polarisation vector of the incoming light beam by a certain angle 2θ, that corresponds to the physical rotation θ of the stage. The second one is situated in the optical path between the knife-edge prism and the mirror M3, after having passed through the crystal. This stage holds the Analyser (A), which is a radiation hard absorption polariser. As it has been detailed in the preceding chapters, the analyser will detect a variation in the component parallel to its transmission direction when the proton bunch is passing. The polarisation state set by the HWP before the KEP in the optical path is equivalent to the one in the input face of the crystal as it reflects twice: once in the KEP itself, and then again in the right angle prism. Equivalently, an output elliptical polarisation will be same handed after the KEP before reaching the analyser and at the output face of the crystal.

A detail of the optical elements is shown in the pictures of setups A and B in Figure 5.2. In addition, all the elements are listed in Table 5.1. Both setups are also enclosed to avoid laser beam exposure. Additionally, the HWP, analyser, and also the 3D stage are electrically connected through 12-pin Burndy cables to their control devices in HCA4, as specified in section 5.1.4.

5.1.2 Optical path alignment

The alignment of the OB is especially critical at the position of the knife-edge prism as it is the element that conducts the light in and out of the pickup, with a narrow separation between the incoming and outcoming beams. Figure 5.3 exemplifies in setup A the process carried out to ensure a good alignment in the system. The linear actuator is used to retract the KEP position backwards to permit a straight alignment from M1 to M2 with the assistance of a CCD camera (Fig. 5.3(a)). At that point, keeping the CCD camera at P in the figure, the prism is moved forward to intercept the OB and send it towards the pickup (Fig. 5.3(b)). The KEP orientation is finely adjusted with the stage in order

(a)   (b)
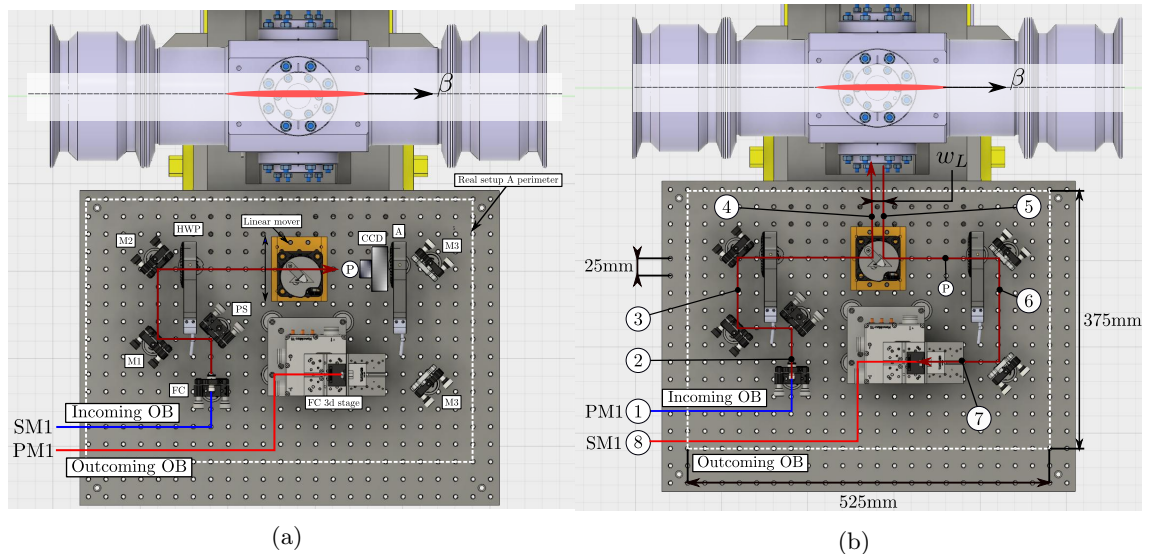
Figure 5.3: Example of the OB trajectory when the knife-edge prism is retracted (a) and placed in the final position (b) for setup A.

to align the OB at the same spot measured in the CCD when the KEP was retracted. Furthermore, the distance covered by the incoming beam from the collimator to the input face crystal, is the same as for the outcoming beam from the output face to the lens held by the 3d stage. The CCD camera also provided the diameter size of the collimated beam, which is approximately $900\,\mu$m. With that beam size, the optical power applied into the crystal input face never reached above $10\,$mW, so about $\sim 10\,$kW/m^2, which is significantly below $8\,$MW/m^2, that is, the power required to produce optical damage by inducing photorefractive effect at $780\,$nm in lithium niobate [61].

Table 5.2 shows the extrapolated optical power decay from an initial 1 mW along the whole optical path for each of the points depicted in Figure 5.3(b), based on the experimental readouts during the alignment process. The estimated coupling efficiency limit of both PM and SM fibres was found to be approximately $\sim 75\%$ ($1 \rightarrow 2$ and $7 \rightarrow 8$). Also, losses of roughly $\sim 9\%$ and $\sim 12\%$ were measured after the pickup in setups A and B, respectively.

Table 5.2: Laser light power decay along the optical path.

Point	1	2	3	4	5	6	7	8
Power [mW]	1	$\sim$0.75	$\sim$0.68	$\sim$0.68	$\sim$0.62	$\sim$0.57	$\sim$0.57	$\sim$0.43

In Figure 5.3 a perimeter that represents the position of the enclosure walls shown in Figure 5.2(a), is depicted as a discontinuous white line superimposed over the image. Since setup A is located in the inner side of the SPS ring next to the transport path of the accelerator, the original optical breadboard model presented in Figure 5.3 was cut along a new perimeter to avoid a possible collision, whereas setup B breadboard remained unchanged.

5.1.3 Laser Characterisation

According to the theory presented in chapter 2, the EO modulation is inversely proportional to the wavelength (eqn. 2.24). Nevertheless, the range of selection is limited by the photorefractive effect (section 2.4.1), which is very strong at wavelengths shorter than 633 nm, but sharply decays in the far infrared. Thereby, the chosen λ for the experiment presented in this thesis was 780 nm to keep it sufficiently short while ensuring the photorefractive damage in the crystal sample was minimum. Additionally, the final decision on the optimal wavelength was also driven by availability of high power diode lasers at 780 nm.

Furthermore, since the amplitude modulator pickup relies on the interferometric combination of different components after the crystal, a narrow laser linewidth is required. This way, the modulation occurs at a single wavelength, instead of over a range that would lead to a process where every wavelength component dephases by a different extent, inducing different optical modulations. The laser New Focus TLB-6800 offers a linewidth $\Delta\nu \leq 200$ kHz, which is related to $\Delta\lambda$ through Equation 5.1 [62, 63]:

$$\Delta\nu = \frac{c}{\lambda^2}\Delta\lambda\,, \tag{5.1}$$

where $\lambda = 780$ nm is the centre wavelength of the laser, then $\Delta\lambda = \lambda^2\,\Delta\nu/c \simeq 0.4$ fm. Then, $\Delta\lambda < 1$ fm is considered a short linewidth suitable for an interferometric application of this nature, as the birefringence Γ_0 (eqn. 2.23) could only vary over $\sim 1.5 \times 10^{-6}$ rad at 780 nm, if assuming $L_y = 5$ mm for LNB.

5.1.4 Control Instrumentation

To control remotely the input polarisation and the analyser positions, as well as the 3-axis fibre coupler stage described in previous sections, a hardware interface was required. The
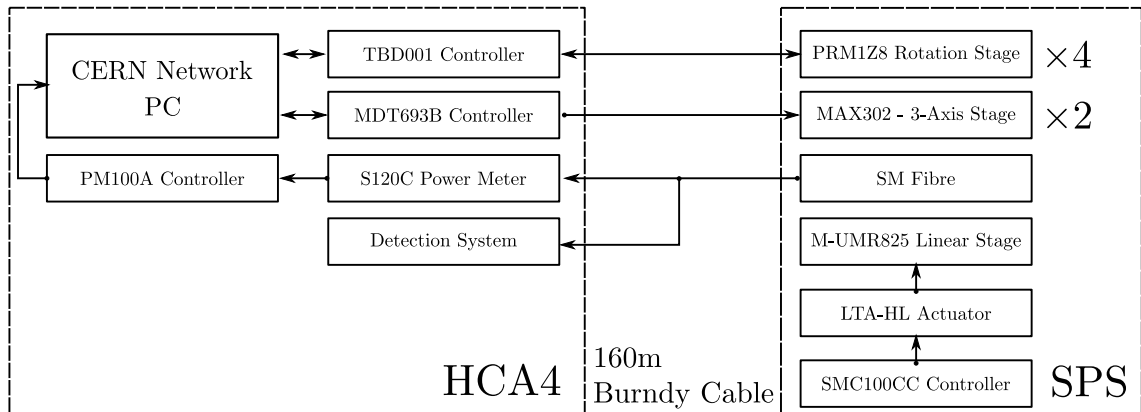
Figure 5.4: Flux diagram of the control instrumentation.

diagram 5.4 shows the separation of the system into two different locations: the Control Instrumentation room in HCA4 where the laser and the detection system are also installed, and the point at SPS where the optical setups and the EO pickups are mounted. The rotation stages PRM1Z8 holding the analyser and the HWP responsible for the input polarisation are connected to the TBD001 controllers (also known as T-cubes) in HCA4 through a 160 metres of Burndy cable. Likewise, the 3-axis stage in the optical setup is connected in the same way to the MDT693B controller in the instrumentation room. The diagram highlights that there are four rotation stages and two 3d stages, which corresponds to a set formed of an analyser, a HWP and a 3d stage per optical setup.

The return light coupled into the 3 axis stage was monitored by a S120C power meter connected to the other extreme of the SM fibre in HCA4. The power meter controller PM100A along with the controllers previously mentioned are in turn connected to a PC also located in HCA4. Figure 5.5 shows the screenshots of the Thorlabs software interface to monitor the readout from the power meter and also the 3d stage position. Therefore,

(a)

(b)
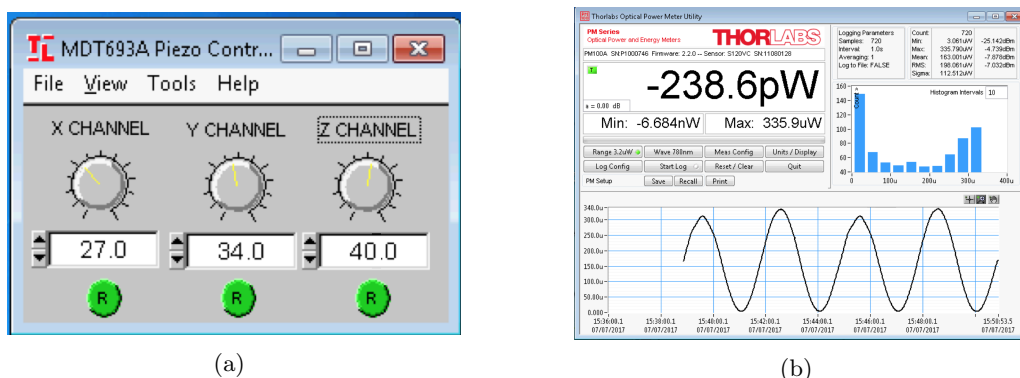
Figure 5.5: 3-axis panel control (a) and readout interface of the power meter software (b).

the efficiency coupling into the return fibres could potentially be improved remotely via software by the following readout feedback procedure: the user applies small displacements on the fibre stage and then checks the variation in power until reaching a maximum. Although the piezo actuators of the fibre coupler stage permit a very fine alignment of a $20\,\mu$m range, it is an open-loop system. Thus, during the alignment is not possible to record the real position of the stage but only the voltage applied in a range from 0 to $75\,$V, as displayed in Figure 5.5(a), however, this procedure was proved valid.

The rotation stages are controlled by the Thorlabs APT software, the interface of which is shown in Figure 5.6(a) along with the corresponding displacement direction for a numerically positive rotation in the panel, for each setup. The direct interaction with the stages has the disadvantage of having to apply the stage offset in each case. Figure 5.6(b) shows the interface panel of the LabVIEW software developed mainly by G. Boorman that allows us to control the remote stages and also integrates the power meter readout at the same time. This piece of software was specifically designed to record polarisation scans by plotting the power meter readout while moving the analyser, given a certain initial HWP position. This type of measurement determines the natural birefringence of the crystal as it was illustrated in section 2.4.3.

It should be noted that the Newport linear stages M-UMR825 are not managed from the instrumentation room, but from the tunnel by an actuator LTA-HL connected to a controller SMC100CC. This system was used for alignment purposes when a fine motion of the KEP was required during the interventions in SPS. Another additional machine parameters from other diagnostic devices such as bunch charge and length are logged independently and can be obtained through the CERN application TIMBER [64]. However, the bunch position for SPS requires specific logging from the CERN control centre.

5.2 Installation

As mentioned before, the EO-BPM prototype system consisted of two opposing pickups installed on the horizontal plane accompanied by an optical setup next to them. However, the entire system was not installed at once due to time constrains. It is important to highlight the fact that the access to the SPS machine is very limited, as it is reduced to very few short Technical Stops (TS) along the year of typically one or two days duration.
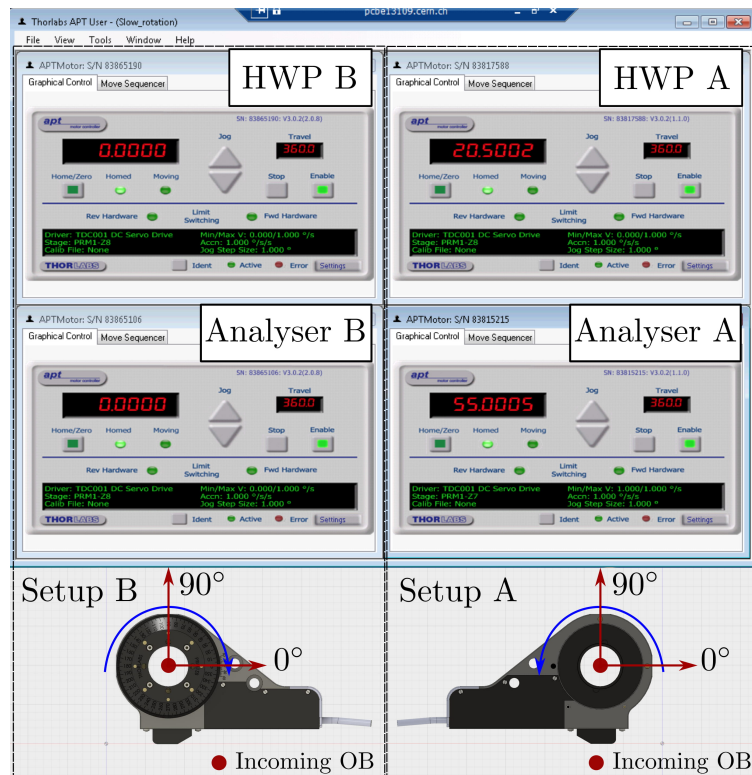
(a) Panel interface of the APT software associated with the remote stages controlling the HWP and analyser; on the left, for setup B, the rotation stage is depicted with the incoming beam direction and the corresponding control panels; on the right, equivalently, for setup A.
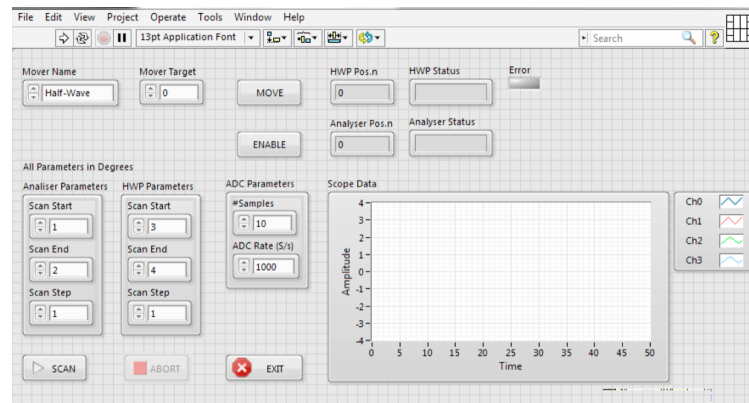
(b) LabVIEW control panel for measuring the crystal birefringence by acquiring polarisation scans.

Figure 5.6: Software interface screenshots of the main control tools of the experimental hardware.

During the period of this thesis experiments, there was also a long shutdown from the end of each year of a few months duration. The restricted access enforces the need of a remote control system over some of the most important setup parameters. The following list explains the points shown in Figure 5.7, which corresponds to the main milestones

that were achieved during the runs of pickup zero in 2016, and pickup one in 2017:
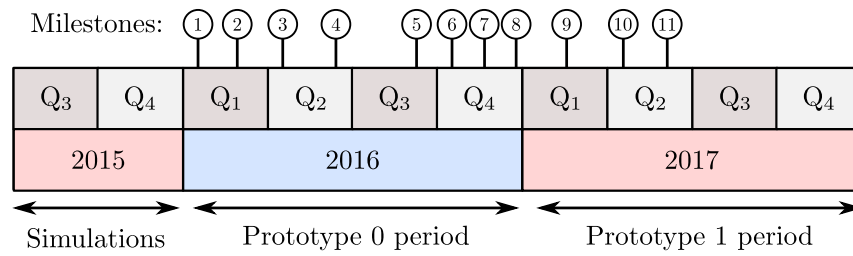
Figure 5.7: Installation calendar.

1. February, 2016: Installation of a pickup zero on the inner side and setup A next to it during the long shutdown.

2. March, 2016: Start of the 2016 run.

3. April, 2016: Installation of another three pickups zero during a short TS, two of them with metallic coated crystal samples on the vertical plane, and the missing one on the outer side. The pickups on the horizontal plane are equipped with non-coated crystals.

4. June 2016: Installation of setup B next to the outer side during a short TS.

5. September 2016: Installation of the narrow linewidth ($< 200\,\mathrm{kHz}$) $780\,\mathrm{nm}$ laser at HCA4 (previously there was an standard thorlabs 780 nm laser installed for alignment). The Berek polarisation compensator was also installed in setup A during a short TS.

6. November, 2016: Detection system finally integrated at HCA4.

7. December, 2016: First EO proton bunch detection with pickup zero.

8. December, 2016: End of the 2016 run.

9. February 2016: Replacement of the pickups on the vertical plane and on the inner side by upgraded model one pickups (long shutdown). The system on the outer side remained unchanged with a type zero prototype.

10. May, 2017: Start of the SPS 2016 run.

11. June, 2017: First EO detection of a passing proton bunch with pickup one. Later on in the same month, the first studies on beam position sensitivity for pickup one

were performed by applying beam bumps in SPS while working in machine Mode Development (MD).

12. July, 2017: Indirect detection in frequency domain of the betatron amplitude in the SPS with pickup one while working at low intensity coast beam.

13. August, 2017: Further measurements for pickup one with almost nominal intensity coast beam.

Figure 5.8(a) is a picture from inside the SPS pipe that corresponds to the first milestone, that is, the installation of a EO pickup zero in the inner side of the ring, in February, 2016. The optical system was not yet fully completed until November, 2016, when the high quality laser and also the horizontal setups were totally assembled and enclosed in the way shown in Figure 5.8(b). The Berek compensator did not allow remote control, so it was used only during the technical stops to shift the output polarisation towards a more sensitive point (Fig. 2.11).

(a)   (b)
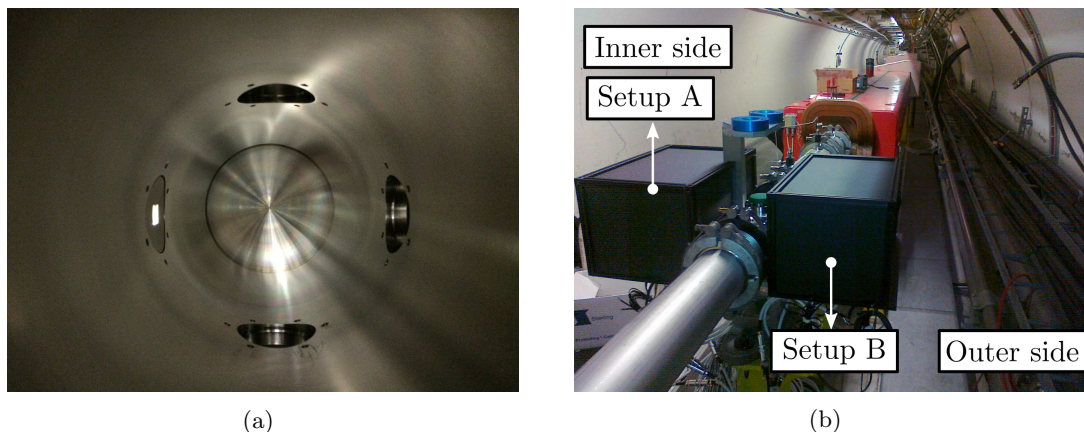
Figure 5.8: Picture inside the pipe with a single button installed next to setup A (a); the whole arrangement with the enclosed setups on the horizontal plane (b).

During the first pickup zero run, the signal from the prototype was obtained right after installing a detection system that suited the signal requirements, a week before the long shutdown in December 2016. This event constitutes the first detection of a proton beam by an EO device. Due to the limited remaining run time at SPS, only a single set of data was taken. The signal from pickup one was observed soon after the start of the 2017 SPS run, and several sets of data were taken at different conditions that will be explained in the succeeding chapter.

5.3 Detection system

The greatest extent of the EO amplitude modulation occurs when the system is set at crossed polarisers, that is to say 45° input polarisation and the analyser transmission line at −45°, or vice-versa. On the contrary, no amplitude modulation takes place when the input polarisation or the analyser position are set either horizontal or vertical. The polarisation after the EO crystal depends on the natural birefringence and determines the modulation sensitivity (Fig. 2.11), as well as the light power transmitted throughout the analyser, which corresponds with the point in the transfer function T_{crossed} with no field applied ($E_z = 0$).

The data acquisition system installed in the instrumentation room at HCA4 is shown in Figure 5.9; when the prototype is set at crossed polarisers, the return SM fibre transmits to HCA4 the baseline light power related with the natural birefringence of the pickup crystal. One can observe that the SM fibre is connected to a fast detector that has two different outputs: a DC type and a Radio Frequency (RF) signal. The former is proportional to the slow-changing light power baseline caused by the natural birefringence, and the latter transforms the EO modulation ΔP_{opt} conveyed 160 m from SPS to HCA4, into an electric signal that is magnified afterwards by an amplifier. Both DC and amplified RF signals, and also a trigger reference, were read by a 12-bit oscilloscope. Since the detection system was endowed with one fast detector, only the modulation from one pickup could be measured at the time.
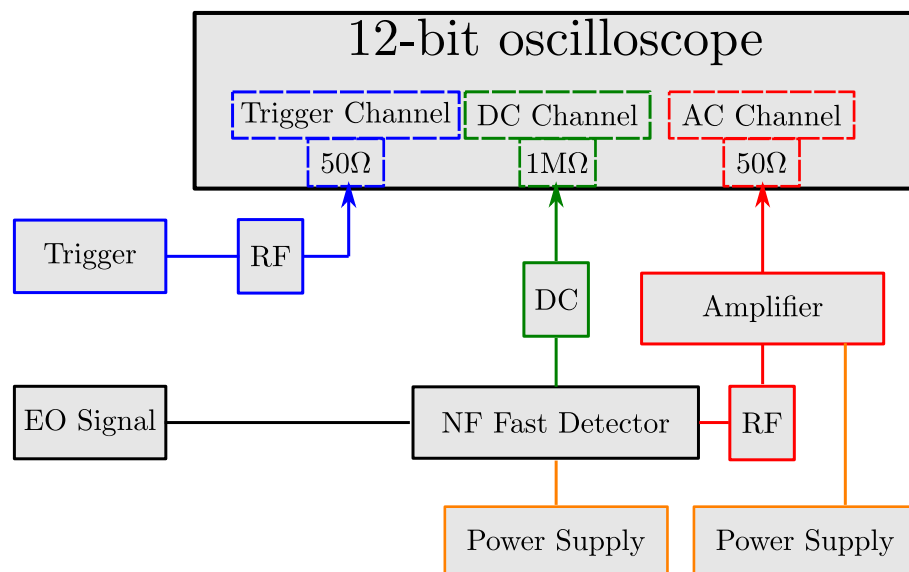
Figure 5.9: Detection scheme diagram.

5.3.1 Fast detector

The fast detector (PD) employed in the experiments presented in this thesis was a New Focus Model 1544-A [65]. The device contains an InGaAs diode sensitive to wavelengths ranging from 500 nm to 1630 nm. Figure 5.10 represents the technical drawings of the detector model. The light power comes from an FC/PC input fibre connector and is then applied on the diode generating an electric current signal. The current conversion efficiency depends on the responsivity $R(\lambda)$, which is in turn a wavelength-sensitive parameter. The SMA output connector provides the light power baseline as a DC voltage V_{DC}, and it is measured in one of the 12-bit channels terminated in $1\,M\Omega$. The DC detector's sensitivity S_{DC} can be characterised experimentally by the calibration curve, that is, the DC voltage V_{DC} against the input light power P_{DC}. Also, $V_{DC} = P_{DC} \times R(\lambda) \times G$ where $G = 1\,V/mA$ is the transimpedance gain associated to the detector preamplifier. Thus, the nominal sensitivity inferred from the detector's spreadsheet parameters is defined as $S_{DC} = R\,(780\,nm) \times \mid G \mid \simeq 0.2\,A/W \times 1000\,V/A = 200\,V/W$, which differs from the experimental calibration gradient of 140 V/W that is shown in Figure 5.11(b). The discrepancy is not relevant and can be explained considering that the responsivity curve $R(\lambda)$ is not necessarily the same in this detector, so the value at 780 nm can be different.
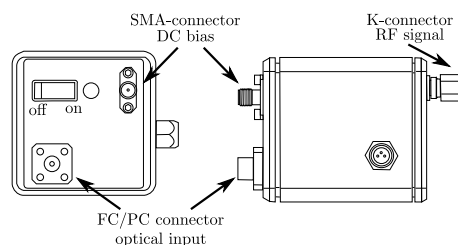
Figure 5.10: Technical drawing of the fast detector.

The calibration curves shown in Figure 5.11 are measured at 780 nm, and show how the sensitivity drops by almost the half when the wrong input termination FC/APC (instead of FC/PC) is connected to the detector, since the OB is applied less efficiently into the diode surface.

Besides the DC output, a K-connector supplies the outcome generated by fast changes in the input power light ΔP_{opt}, in a range from the cut-off frequency at 10 kHz up to 12 GHz, where the bandwidth (BW) is determined by the 32 ps rise time of the diode [65]. Therefore, an EO modulation in the order of 1 ns produces an RF signal at this output, which is acquired by the same 12-bit oscilloscope in a $50\,\Omega$-terminated chan-
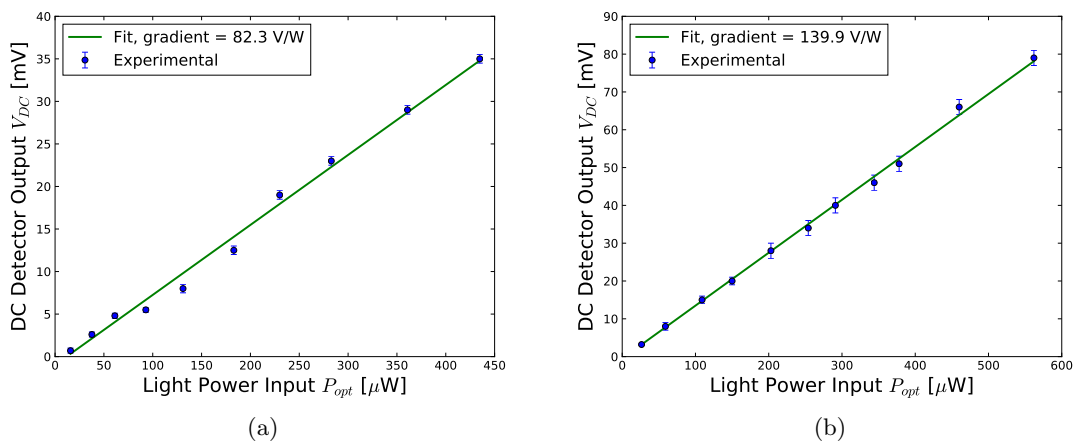
Figure 5.11: Fast detector DC calibration curve when the input fibre connection APC/PC (a) and PC/PC (b) for 780 nm.

nel. The RF readout results from the internal transimpidance amplification of the original diode signal inside the device.

From the spreadsheet, the maximum S_{RF} at 1550 nm can reach approximately between $-800\,\mathrm{V/W}$ and $-900\,\mathrm{V/W}$, which is assumed to correspond to the peak responsivity $R(\lambda = 1550\,\mathrm{nm}) \simeq 0.85\,\mathrm{A/W}$. However, according to the calibration curve at DC (Fig. 5.11), the RF sensitivity S_{RF} scales to $-140\,\mathrm{V/W}$ for the experimental working wavelength ($R(780\,\mathrm{nm}) = 0.14\,\mathrm{A/W}$), since $S_{\mathrm{DC}} = S_{\mathrm{RF}}$ [66].

There exist a certain noise level besides the signal induced by the optical modulation in the absence of an optical beam. The Noise Equivalent Power (NEP) is defined as the input optical power that results in a Signal-to-Noise Ratio (SNR) of one, when normalised per square root of one hertz output bandwidth. Essentially, the NEP expresses the minimum detectable optical power for a normalised bandwidth. Furthermore, the noise equivalent power depends on the optical wavelength too, since it scales inversely with the diode responsivity $R(\lambda)$, thereby:

$$\mathrm{NEP}(\lambda) = \mathrm{NEP}_{\lambda_0} \times \frac{R(\lambda_0)}{R(\lambda)} \, , \tag{5.2}$$

where λ_0 is the reference wavelength at which the parameter NEP is provided in the spreadsheet. Particularly for the detector employed in this experiment, $\mathrm{NEP}(\lambda_0) = \mathrm{NEP}(1550\,\mathrm{nm}) = 24\,\mathrm{pW}/\sqrt{\mathrm{Hz}}$. Table 5.3 contains the diode response $R(\lambda)$, the RF sensitivity S_{RF}, and the NEP obtained from equation 5.2, for the most important commercial wavelengths the diode is sensitive to.

The parameters at 780 nm and 633 nm resulted from scaling them according to the responsivity at each wavelength provided in the detector specifics:

Table 5.3: NEP and sensitivities as a function of the wavelength; (*) denotes the case when the efficiency coupling due to the APC fibre termination has been applied.

Wavelength λ [nm]	-	1550	780	633
$R(\lambda)$ [A/W]	Nominal & Experimental	~ 0.85	~ 0.14	~ 0.12
$S_{\mathrm{DC}}(\lambda)(=S_{\mathrm{RF}}(\lambda))$ [V/W]	Nominal & Experimental	~ -850	-140.1 ± 1.5	~ -120
$S_{\mathrm{DC}}^{*}(\lambda)(=S_{\mathrm{RF}}^{*}(\lambda))$ [V/W]	Experimental	-	-82 ± 3	-
NEP(λ) [pW/$\sqrt{\mathrm{Hz}}$]	Nominal & Extrapolated	~ 24	~ 145	~ 170

As was pointed out previously, the NEP value given in Table 5.3 is the standard normalised parameter to allow the comparison with other detectors in terms of noise. The actual NEP scales linearly with the square root of the bandwidth BW, thus:

$$P_{min} = \mathrm{NEP}(\lambda) \times \sqrt{\mathrm{BW}}, \tag{5.3}$$

where P_{min} represents the minimum optical power that provides a SNR of one for a certain bandwidth BW, given a wavelength λ. Figure 5.12 depicts the extrapolation at the previous commercial wavelengths of the weakest optical power P_{min} against the bandwidth obtained from applying equation 5.3:
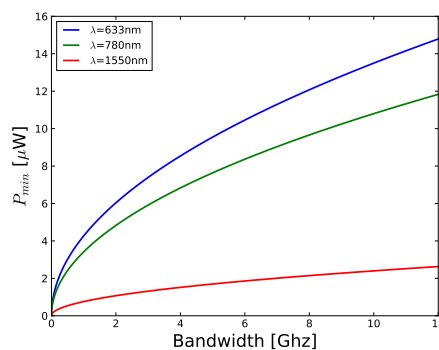
Figure 5.12: Noise Equivalent Power (NEP) against frequency bandwidth.

Figure 5.12 and also Table 5.3 show that the optimum wavelength for the fast detector is 1550 nm, as it provides the greatest responsivity R and the lowest detectable optical power. However, the optical modulation would drop by $\sim 50\%$ with a longer 1550 nm wavelength with respect to working at 780 nm. Ideally, the detection systems in future designs should have a NEP and response such that they are optimised for the working

wavelength, which would be in turn chosen to maximise the modulation. This concept will be extended in chapter 7.

5.3.2 Amplifier

Once the fast optical modulation is transformed into a voltage signal by the detector, its output signal is then magnified by a CERN in-house fabricated amplifier powered by an external supply, as depicted in the diagram of Figure 5.9. For this device, the output voltage V_G at its port 2 is the input signal V_{in} at port 1 amplified by a factor S_{21}, thus:

$$V_G = V_{in} \cdot 10^{\frac{S_{21}[\mathrm{dB}]}{20}} , \tag{5.4}$$

where the factor S_{21} is expressed in dB. Additionally, the parameters S_{11} and S_{22} are the reflections at ports 1 and 2 respectively. From the S-parameters depicted in Figure 5.13, the amplifier is characterised with a nominal gain $G = S_{21}(\mathrm{BW} = 0) = 33\,\mathrm{dB}$, and also a cutoff frequency of $210\,\mathrm{MHz}$ defined as the input signal frequency where the gain S_{21} drops by $3\,\mathrm{dB}$. Therefore, the amplification system can be interpreted as two different blocks formed of a first order $210\,\mathrm{MHz}$ Low-Pass Filter (LPF) with linear phase response, in combination with a $33\,\mathrm{dB}$ amplifier (appendix C). Although there exist $6\,\mathrm{GHz}$ models, this amplifier was chosen due to time and economic constrains, as it was freely available at CERN. However, this decision made impossible the Head-Tail detection. With this assumption, the interaction of the amplifier with the input signal V_{in} can lead to an effective gain G_e different to the nominal. Figure 5.14 shows a simulation of the effective gain G_e against a Gaussian bunch length signal, where it can be noticed how the amplifying factor decays as the bunch length shortens.
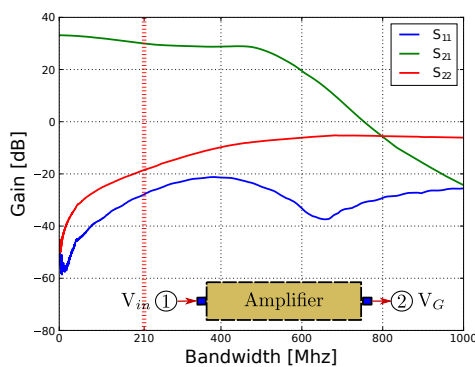
Figure 5.13: S-parameters against frequency for the external amplifier [67].
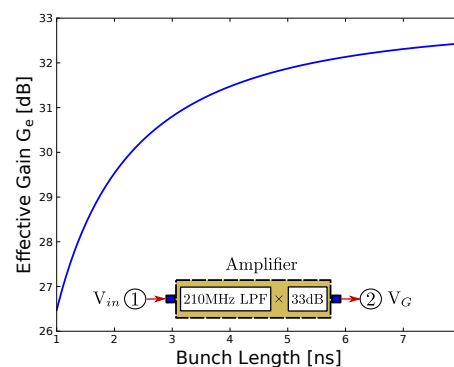
Figure 5.14: Effective gain for a simulated Gaussian bunch length signal.

Moreover, a total noise equivalent power η_{Total} is propagated along the detection chain, since the original NEP is then amplified by the same gain factor G_e. On top of the noise from the detector, the amplifier itself adds its own output noise η_{amp}, thereby:

$$\eta_{Total} = \sqrt{(\text{NEP}(\lambda))^2 \cdot 10^{\text{G}_e/20} + \eta_{amp}^2}, \tag{5.5}$$

or equivalently, assuming η_{PD} is the experimental noise from the detector:

$$\eta_{Total} = \sqrt{\eta_{PD}^2 \cdot 10^{\text{G}_e/20} + \eta_{amp}^2}. \tag{5.6}$$

5.3.3 Noise level analysis

Let us recall that Figure 3.12(c) shows the analytical simulation of the normalised EO modulation signal $\Delta T_{\text{crossed}}$ for a nominal SPS bunch (Table 3.1) at $r_0 = 68.0\,\text{mm}$ (SPS pipe radius). For the most sensitive case at circular polarisation, the expected signal is in the order of $0.4\%\,\Delta P_{opt}/P_{\text{DC}}$, where P_{DC} is the baseline optical power. According to the CST simulations, the field inside the crystal is enhanced in prototype one, which in combination to the crystal enlargement, would potentially result in an optical modulation in the order of $\sim 1\%\,\Delta P_{opt}/P_{\text{DC}}$. Therefore, the signal levels are predicted to be low and the impact of the output noise on the signal detection requires some particular analysis.

The total experimental noise η_{Total} when the fast detector is connected to the amplifier input was found to be $11.7\,\text{mV}$ RMS with no input light. Nevertheless, this value results from the combination of both devices given by virtue of equation 5.6. In order to isolate the contribution from the amplifier η_{amp}, the measurement was repeated with no input after removing the detector, obtaining $\eta_{amp} = 4.0\,\text{mV}$ RMS. According to equation 5.6, the contribution η_{amp} in the total noise from the detector is then $11\,\text{mV}$. However, this is the magnified output noise that can be divided by the amplifier nominal gain of $33\,\text{dB}$, resulting in $0.25\,\text{mV}$ RMS output noise coming out from the fast detector. Since the detection bandwidth is limited by the amplifier, only the noise within the 210 MHz range that gets significantly enlarged is considered. It should be noticed that this value can be compared to the noise obtained from applying the detector sensitivity S_{RF} to the NEP at $780\,\text{nm}$ for the same bandwidth, as equation 5.5 states. This gives $0.28\,\text{mV}$ output noise from the detector, and 13.0 mV after magnification including the amplifier noise.

Table 5.4 summarises the main noise values that will be used for the detection analysis in the following section and also in the overall results:

Table 5.4: Summary of the analysis on the system noise calculation.

Parameter	System noise	Experimental	Estimation
Total noise η_{Total}	Amplifier + PD	11.7 mV (RMS)	13.0 mV
Amplifier noise η_{amp}	Amplifier	4.0 mV (RMS)	-
Detector noise η_{PD} (at 210 MHz)	PD	0.25 mV	0.28 mV
NEP(780 nm) (at 210 MHz)	-	-	2.0 μW

5.3.4 Detection analysis

The detection chain is depicted in Figure 5.15: the optical signal ΔP_{opt} is transformed into a voltage output by the fast detector and is then magnified by the effective gain from the amplifier:
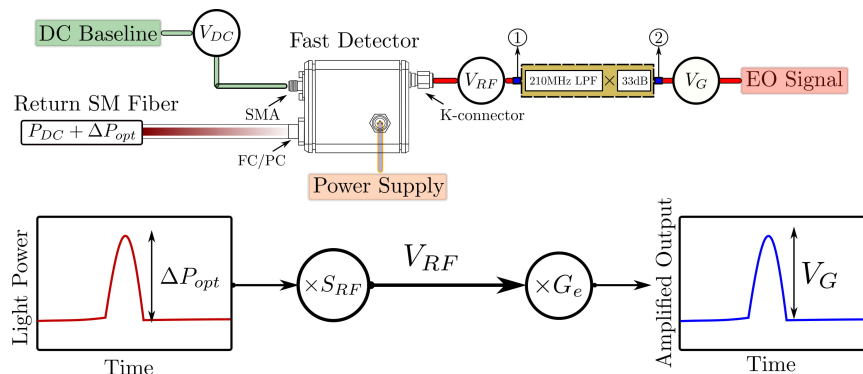
Figure 5.15: Detection chain diagram.

Let us assume an on-centre proton bunch at top energy passing by the experimental setup installed at SPS (Fig. 5.1), where the transfer function after the return SM fibre is such that the maximum value is equal to the nominal saturation power of the detector P_{sat}, that is, 1.0 mW. For a nominal SPS bunch of $4\sigma = 1$ ns, the effective gain G_e in the amplifier is 26.5 dB, as shown in Figure 5.14. For pickup zero, Figure 5.16(a) depicts the EO signal estimation ΔP_{opt} before the detection scheme, and Figure 5.16(b) shows the result of applying the detection chain illustrated above in Figure 5.15, together with the noise equivalent power at 210 MHz and the measured experimental noise (Table 5.4). Similarly, Figures 5.17(a) and 5.17(b) show an equivalent analysis for pickup one. Both Figures 5.16 and 5.17 are represented as a function of the dephase Γ_0, which indicates the
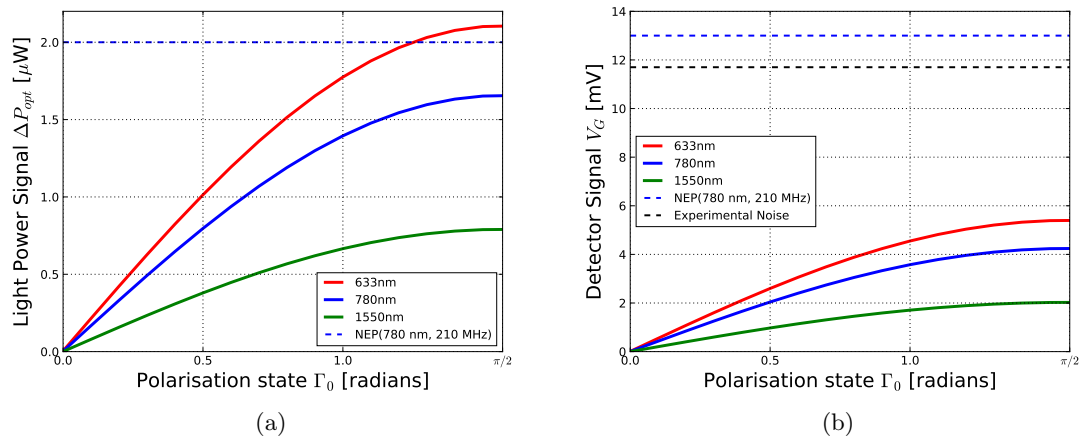
Figure 5.16: Optical power signal ΔP_{opt} (a) and detection signal voltage (b) as a function of the output polarisation, for the 5 mm cubic crystal in pickup zero modulated by 750 V/m electric field that corresponds to the SPS nominal bunch. The NEP at 780 nm and the experimental noise are also calculated.
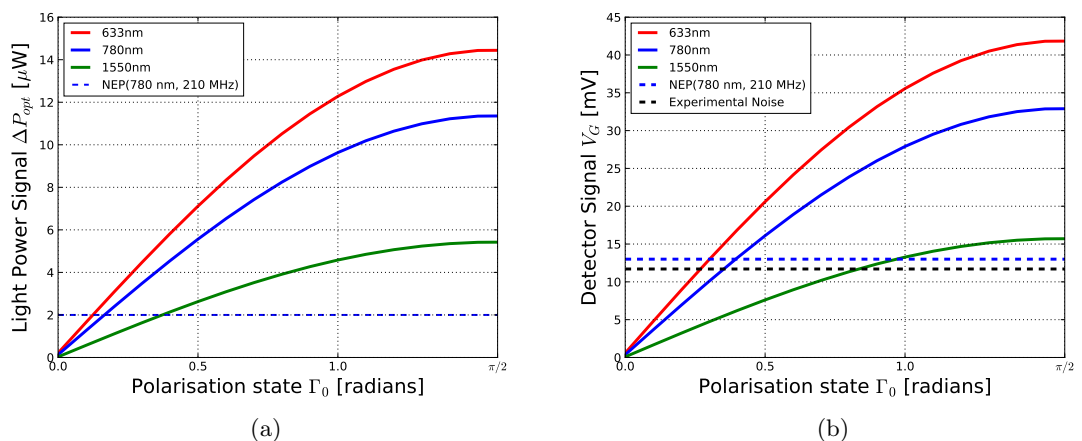
Figure 5.17: Optical power signal ΔP_{opt} (a) and detection signal voltage (b) as a function of the output polarisation, for the 9 mm long crystal in pickup one modulated by 2.86 kV/m electric field that corresponds to the SPS nominal bunch. The NEP at 780 nm and the experimental noise are also calculated.

birefringence of the crystal: $\Gamma_0 = \pi/2$ is the most sensitive state at circular polarisation, and $\Gamma_0 = 0$ is the non-sensitive state at linear polarisation. It can be observed that whereas the signal scales by the estimated factor ~ 8 from pickup zero to one, the noise equivalent power level remains unchanged and amplified by the nominal gain of 33 dB.

Since the EO modulation signal is notably below the RMS noise level for pickup zero, the detection would require averaging the signal over many turns, that is, passing bunches, in order to enlarge the SNR up to a detectable value. For instance, pickup zero would potentially require $N \simeq 750$ turns (equivalent to a noise reduction factor

$\sqrt{N} = 27.4$) to make the expected SNR of -9.0 dB (Table 5.5) to rise above the RMS noise and reach at least $\sim 20\,\mathrm{dB}$ ($= 20 \log \sqrt{N} \cdot V_G/\eta_{Total}$), that is, a RMS-SNR factor almost 10. Furthermore, the amplitude of the Peak-to-Peak (p-p) noise affecting the EO signal at the required bandwidth is typically 12 times larger than the RMS value assuming a white (Gaussian) noise distribution [68]. Thus in reality, a RMS-SNR of $0\,\mathrm{dB}$ would imply that the signal amplitude is still below the p-p noise level even for pickup one in the best scenario at circular output polarisation and assuming a nominal SPS bunch, just as the EO performance summary shown in Table 5.5 indicates. With the previous point in mind, pickup one would require fewer number of turns to achieve a similar SNR, but a single-shot acquisition is foreseen to remain unobtainable with the available detection system described in this section. In conclusion, the detection system has been designed to quantifying the EO modulation and compare it to the simulations, though it is not yet optimised to be capable of getting single-shot measurements, nor HT instability detection either.

Table 5.5: Summary of the simulated EO performance at $780\,\mathrm{nm}$ for the amplified New Port detector when the DC input power is selected to be $500\,\mu\mathrm{W}$ at circular natural bire-fringence ($\pi/2$ dephase). The simulation considers nominal SPS bunch conditions, which implies an effective gain of 26.5 dB and a modulating field E_{LNB} of $750\,\mathrm{V/m}$ and $2.86\,\mathrm{kV/m}$ for pickup zero and one, respectively. The RMS-SNR is calculated as $20 \log V_G/\eta_{RMS}$, and the peak-peak SNR as $20 \log \sqrt{N} \cdot V_G/12 \cdot \eta_{RMS}$

Pickup	ΔP_{opt} [μW]	V_{RF} [mV]	V_G [mV]	SNR (RMS) [dB]	SNR (p-p) [dB]
zero	1.7	0.2	4.9	-7.5	-29.1
one	11.4	1.6	33.6	9.2	-12.4

Let us now recall that the input DC power into the detector is $500\,\mu\mathrm{W}$ when the output polarisation is circular if the maximum of the transfer function is equal to the saturation power P_{sat}, $1\,\mathrm{mW}$ (Fig. 2.7). With those conditions, the typical EO signals are of the order of $1.7\,\mu\mathrm{W}$ and $11.4\,\mu\mathrm{W}$ for pickups zero and one, respectively (Table 5.5). Therefore, the signal-to-DC light relation ($\Delta P_{opt}/P_{\mathrm{DC}}$) is typically a per-mil effect for pickup zero, and a per-cent effect for pickup version one.

Another important aspect of the pickup design is the resolution of the signal versus position. According to equation 2.45, since $E_z \ll E_\pi$ for the prototype presented in this thesis, the EO signal is linearly proportional to the modulating electric field strength E_z; thereby, the signal sensitivity can be estimated from the field-position gradient. In fact,
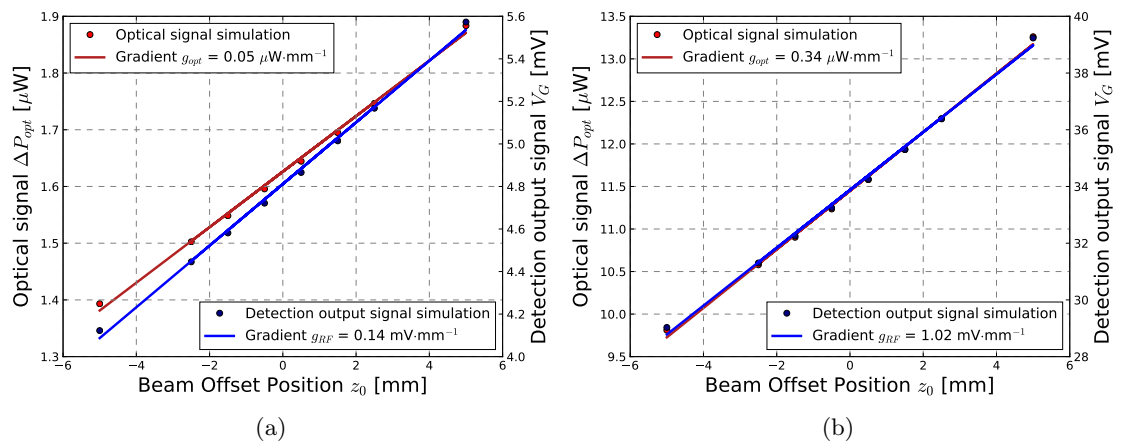
Figure 5.18: Gradients of the optical signal g_{opt} and the output detection system g_G as a function of the position for (a) pickup zero and (b) pickup one when the output polarisation estate is circular ($\Gamma_0 = \pi/2$).

Figures 5.18(a) and 5.18(b) depict the estimated optical signal ΔP_{opt} after the SM fibre, and the detection signal V_G as a function of the radial offset position of the bunch z_0 (Fig. 4.32). These values were calculated analytically from the field strength provided by CST and shown in Figure 4.34, particularly, by applying equations 2.24 and 2.28 correctly scaled, assuming a circular polarisation birefringence and keeping the same transfer function conditions employed previously, that is, a $500\,\mu$W input power into the detector as the transfer function maximum is 1 mW (Fig. 2.7). Table 5.6 summarises the gradients for both the optical g_{opt} and detection g_{RF} signals. One can appreciate that the signal sensitivity against the bunch position is approximately $\sim 0.26\,\mathrm{dBmm}^{-1}$ for both pickup versions, which is comparable to $0.52\,\mathrm{dBmm}^{-1}$ that corresponds to the resolution that would provide a button-like BPM of similar geometry [69] (see appendix D).

Table 5.6: Summary of the signal sensitivity for pickup zero and one. The values given in $\mathrm{dB} \cdot \mathrm{mm}^{-1}$ indicate the signal gradient within 1 mm offset displacement from the pipe centre.

Gradient	Pickup Zero	Pickup One
g_{opt} [μW/mm]	0.05	0.34
g_{opt} [dB/mm]	0.26	0.26
g_{RF} [mV/mm]	0.14	1.02
g_{RF} [dB/mm]	0.24	0.26

It should be stressed that the results above are obtained for the best case scenario in terms of natural birefringence, that is, at circular polarisation. However, the sensitivity is,

115

in turn, dependent on the output polarisation of the crystal as Figures 5.19(a) and 5.19(b) illustrate. One can realise how the pickup becomes non-sensitive at linear polarisations and reaches the maximum at circular, as expected when $E_z \ll E_\pi$.
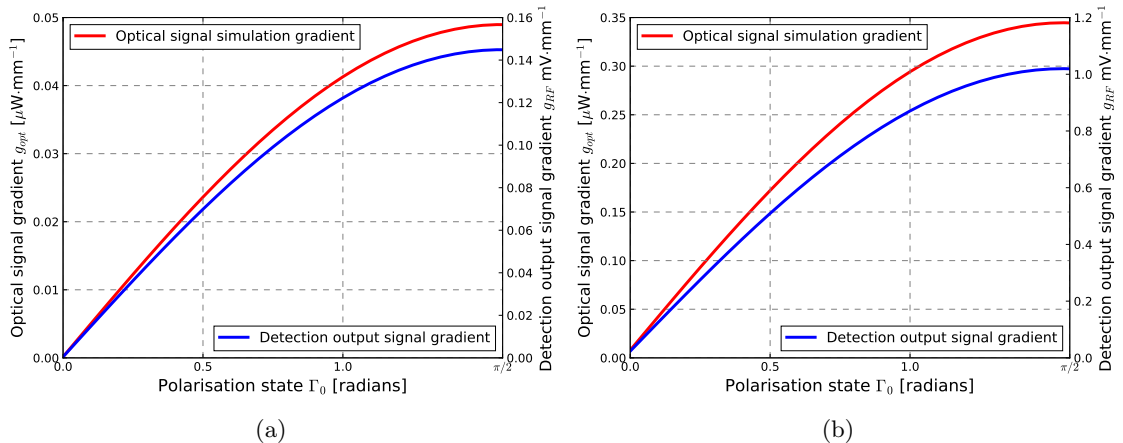
Figure 5.19: Gradients of the optical signal g_{opt} and the output detection system g_G as a function of the polarisation estate Γ_0 for pickup variants zero (a) and one (b).

5.4 Electro-optic characterisation of pickup version one

One of the most interesting features of pickup version one is the possibility to attach the electrode to a signal generator. Consequently, the design allows us to apply a voltage across the crystal along the z-direction, transversally to a laser beam passing through the LNB sample in the direction parallel to y. The setup presented in Figure 5.20 aims to recreate the conditions in the real scenario described in Figure 5.1, specially in terms of the field $E_z = E_{\mathrm{LNB}}$ that induces an optical modulation on the laser beam across the crystal. The laser source was a New Focus TLB-6800 at $780\,\mathrm{nm}$, which is the same model implemented in the experimental setup at SPS. Once the beam is delivered into the characterisation setup photographed in Figure 5.20, it follows the layout that is superimposed: a polarising splitter PS filters a vertical polarisation that is conducted towards the 3d fibre stage by a set formed of a mirror M1 and a KEP making the beam go through the EO pickup in the same way as in the real scenario. Of course, the setup also includes a HWP and an analyser placed respectively before and after the passage through the crystal. The optical elements are exactly the same as in the real scenario (Table 5.1) with the exception of the item labeled as KEP that now refers to a design functionally equivalent to a Knife-Edge Prism, based on two square mirrors assembled perpendicular one to the other. In the picture 5.20,

the viewport has been removed and the beam enters directly through the main flange. The pickup is held by a steel ring designed *ex professo* for this characterisation study, and the full voltage output was connected to an in-house designed plate clamped to the electrode of the EO button on the back side of the flange, which would be facing the particle beam once installed in the SPS ring.
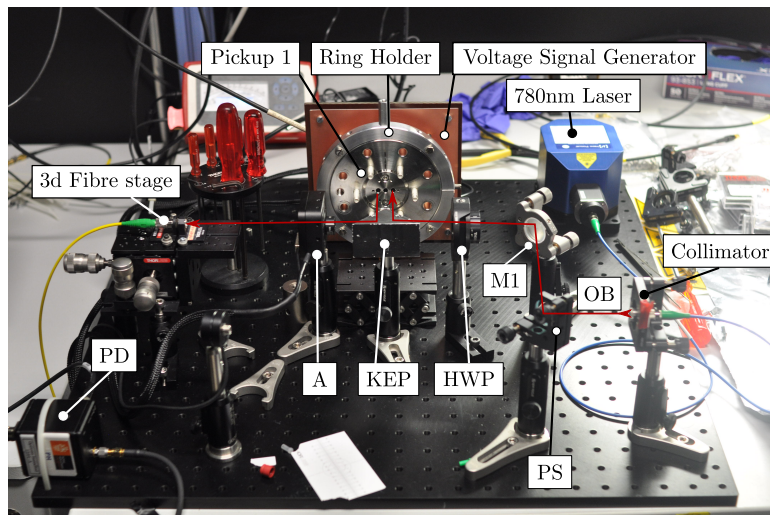
Figure 5.20: Pickup one characterisation setup.

The voltage signal V_{applied} translates to a modulating field E_{LNB} in the crystal. Since the transverse thickness of the crystal is $2.5\,\text{mm}$ for pickup one, the field strength will be $E_{\text{LNB}} = V_{\text{applied}}/2.5\,\text{mm}$ with the system being equivalent to a modulator configuration (Fig. 4.2(a)). Thereby, the voltage signals increasing up to ~ 12 peak voltage in the set of measurements shown in Figure 5.21, correspond to modulating electric fields ramping up to $\sim 4.8\,\text{kV/m}$.

The three version one pickups installed during the 2016-17 shutdown were characterised using the setup shown above before the installation to check the EO performance and ensure the reliability of the new EO pickup. The study required to investigate the signal output under time scale conditions similar to the real scenario and comparable field strengths. The fast pulses were produced by an avalanche signal generator built at RHUL based on a CERN design [70]. The pulser was triggered with a 2 Vpp, $4\sigma = 100\,\text{ns}$ trigger shots at $10\,\text{kHz}$. The pulser also had a built-in tuneable attenuator to adjust the pulse amplitude with two outputs: full voltage and voltage divided by 20, where the latter was read by the 12-bit oscilloscope. Both connections were made through a T-splitter terminated with $50\,\Omega$ to minimise reflections.

117

The graphs in Figure 5.21 illustrate the EO response in red along with the actual inducing voltage in blue across the crystal. The amplifier has been removed from the detection system (Fig. 5.9) and thus the EO signal corresponds directly to the fast detector output V_{RF}. All those set of results have been averaged typically over about ~ 200 turns triggering on the pulse rate to improve the initial poor SNR.

(a) Top pickup. Positive modulation.

(b) Top pickup. Negative modulation.

(c) Inner side pickup. Positive modulation.

(d) Inner side pickup. Negative modulation.

(e) Bottom pickup. Positive modulation.

(f) Bottom pickup. Negative modulation.
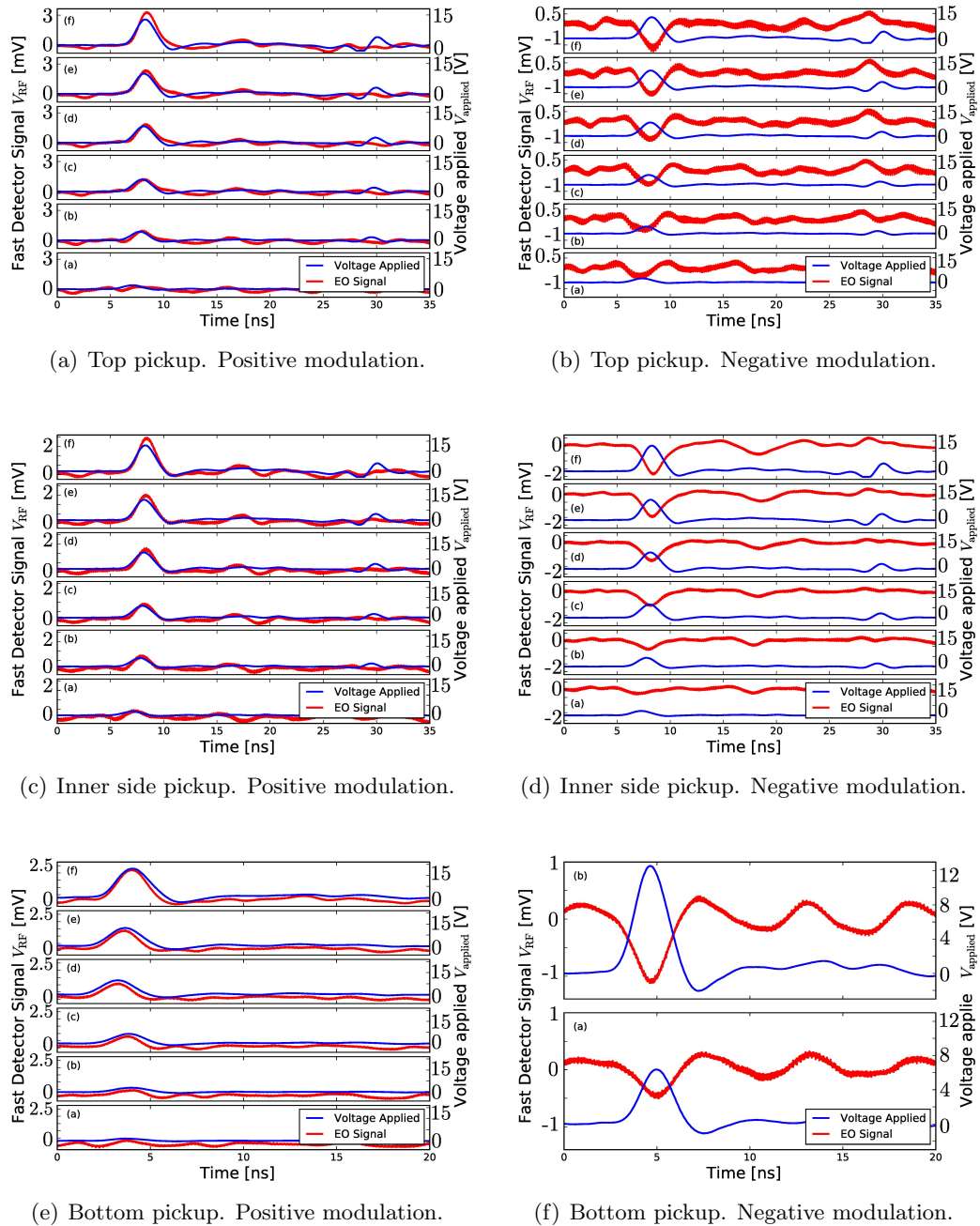
Figure 5.21: Averaged EO modulation when a fast voltage signal is applied on the electrodes of pickup one. The data recorded for Figure (f) only covered to 20 ns scope.

The voltage scaled up to $\sim 12\,\text{V}$ in 6 steps, where the studied cases are the following: $2\,\text{V}$ (a); $4\,\text{V}$ (b); $6\,\text{V}$ (c); $8\,\text{V}$ (d); $10\,\text{V}$ (e) and $12\,\text{V}$ (f), except from Figure 5.21(f) where only a pair cases for $6\,\text{V}$ (a) and $12\,\text{V}$ (b) were measured. Therefore, those values are within the expected order of magnitude in the real scenario at SPS, of about $\sim 2.86\,\text{kV/m}$, according to the CST simulations (Table 4.5). In particular, the closest case is (c) at $6\,\text{V}$, which corresponds to $2.4\,\text{kV/m}$.

Another important aspect of the pickup characterisation is the time-structure response. The generator allows us to apply a $2\,\text{ns}$ pulse on the crystal, which is comparable to the SPS bunch length. With these sort of pulses, one of the first conclusions looking at the experimental results is that the EO modulation matches well the signal applied. In fact, besides the main signal at $\sim 7\,\text{ns}$, the fast generator produces a reflection in the form of a weaker secondary pulse at $\sim 26\,\text{ns}$, that is followed by an EO modulation in its own scale, too. It is important to stress out that the amplifier, which is a bandwidth-limited element was not employed in the acquisition. One can observe that the experimental results are divided into two columns: positive and negative signals. As explained in Chapter 2, the sign of the modulation depends on the natural birefringence of the crystal at the moment of the acquisition, that is, the position in the transmission curve (Fig. 2.7) during the data-taking. Figure 5.22 represents a typical elliptical polarisation after the crystal, and also the Transmission Direction (TD) of the analyser superimposed; given that diagram, if, due to the action of the modulating field, the component oriented at $-45°$ is reduced implying that the component at $45°$ increases, then results in a negative modulation. Similarly, if the analyser was oriented along the $45°$-projection, this would lead to a positive modulation. Finally, since the sensitivity S_{RF} is negative, the detector output and the actual modulation have opposite signs. In order to illustrate this effect, two set of measurements taken under two different analyser positions perpendicular one to the other are presented in Figure 5.21.
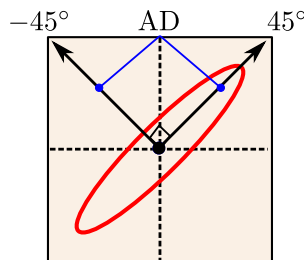
Figure 5.22: Diagram of the output face of the crystal sample with the possible positions of the analyser that lead to opposite sign modulations.

Let us now pay attention to either the positive or negative modulations aligned in columns. Since the sensitivity regime is such that the $E_{\text{applied}} \ll E_\pi$, the EO response in each case scales linearly with the field applied, as expected according to equation 2.45. This point is proved in Figure 5.23 where the peak detector signal is plotted as a function of the maximum modulating field in the crystal.

It is important to notice that, whereas in all the previous simulations the transfer function was assumed to have a 1 mW maximum for simplicity, on this occasion the estimation have been scaled according to the real maximum, $\sim 800\ \mu$W. The birefringence has also been featured in the calculation, in particular, although the output polarisation in the pickups was unknown, it is assumed to be at the $\sim 80\%$ of the maximum possible, at circular polarisation (Fig. 2.11). With those values, the maximum optical modulation and consequently the peak detector output V_{RF} were calculated for the maximum modulating field applied $E_{\text{applied}} \simeq 4.8\,\text{kV/m}$ ($V_{\text{applied}} = 12\,\text{V}$), and the values are presented in Table 5.7, in comparison with the experimental counterpart.

Table 5.7: Summary of the characterisation signal performance for pickup zero and one.

Pickup	Top	Inner side	Bottom
EO Signal Estimation (Positive Modulation) [mV]	2.0	2.0	2.0
Experimental EO Signal (Negative Modulation) [mV]	-1.32	-1.88	-1.12
Experimental EO Signal (Positive Modulation) [mV]	3.31	1.95	2.23

As a general note, the optical modulation is calculated applying the Jones formulation presented in Chapter 2, that is transformed into a detector signal V_{RF} by simply applying the device sensitivity, $-140\,\text{V/W}$ (Table 5.3), since the amplifier was removed. Table 5.7 confirms that the signal strength is in the correct order of magnitude, and also the change of sign observed when the analyser rotates $90°$ indicates that the EO behaviour is correct. The positive and negative modulations are foreseen to be symmetrical one to the other, that is, having both the same strength in absolute terms. Whereas this prediction is experimentally observed in the pickup installed on the inner side at the moment of the data-taking, pickups on the top and bottom do not show that equivalence in signal. The reason is found in the fact that the polarisation was quite circular, and thus the major and minor axes are probably shifted as was explained in section 2.4.3.
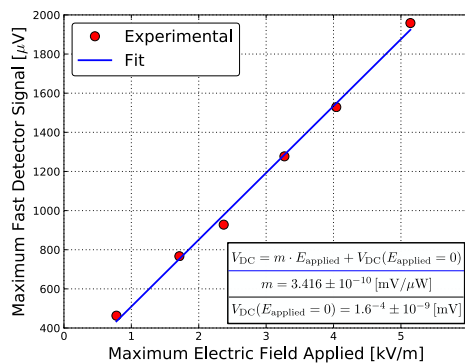
Figure 5.23: Maximum EO signal as a function of the field applied resulted from the characterisation of the inner side EO pickup one for positive signals.

5.4.1 Single-shot detection study

Once the correct EO performance has been demonstrated, this section tackles the task of determining the minimum modulating electric field E_{LNB} to ahieve a single-shot acquisition for pickup one. Since such a value depends mainly on the detection system, this study characterises the fast photo-diode from a point of view of the SNR and allows us to compare it with the previous estimations. Figure 5.24 plots a single shot EO signal taken directly from the fast detector when a 12.9 V pulse signal was applied on the LNB sample, which corresponds to a modulating electric field E_{LNB} of 5.16 kV/m. Since the SNR is approximately one, that value can be considered the minimum field to achieve an EO single-shot measurement given the experimental fast photo-diode employed in this thesis. Unfortunately, the fact that this threshold is below the expected modulating field at SPS (~ 2.8 kV/m) makes the detector unable to obtain a single-shot acquisition in the real case scenario.
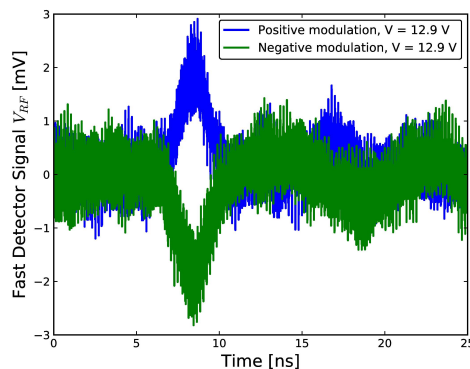
Figure 5.24: EO modulation acquisition at single shot taken during the characterisation for pickup one installed on the inner side adjacent to the setup A.

121

The optical power of the signal ΔP_{opt} is roughly estimated to be of the order of $16\,\mu\text{W}$ when applying equation 2.28, taking into account the birefringence and scaling according to the input laser power. Since the detector sensitivity is $\mid S_{\text{RF}}\mid= 140\,\text{V/W}$, the output signal will be $V_{\text{RF}} = 2.2\,\text{mV}$, which is indeed fairly close to the RMS output noise of the detector at full bandwidth, $2.8\,\text{mV}$. In other words, although strictly speaking, the minimum field for single-shot measurements also depends on the input power and the birefringence, the result above can be considered a good reference. Also, the results shown in Figure 5.21 have been averaged over many acquisitions to improve the SNR. For instance, the signal (c) displayed in 5.21(e) is modulated by $2.4\,\text{kV/m}$ and exhibits a SNR of $17.6\,\text{dB}$ (factor 7.6) after approximately 240 acquisitions. Therefore, the SNR at single-shot was $-6.16\,\text{dB}$ (factor 0.49), which is close to the expected $\sim -8.9\,\text{dB}$ (factor 0.35) obtained from the estimated signal of $1\,\text{mV}$ divided by experimental noise $2.8\,\text{mV}$. In any case, since the modulating electric fields in the real scenario lead to detector outputs below $1\,\text{mV}$, the amplifier is still required to enhance the signal.

5.5 Summary

This chapter describes the optical setup, its main elements and the acquisition system of the prototype. In the first place, the setup is designed to deliver a laser beam from a $780\,\text{nm}$ narrow bandwidth laser installed $160\,\text{m}$ away into the pickups in SPS, in conditions that could allow a remote control of the input polarisation and the analyser orientation so the system can replicate the amplitude modulator configuration. The remoteness of the HWP, the analyser, and other elements was managed through an specific software that has also been presented.

The acquisition system situated at the end of the optical path consists of a photo-diode detector connected to a $210\,\text{MHz}$ amplifier. This chapter includes detailed studies of the SNR to predict the detection performance when acquiring a real beam signal. Furthermore, an electro-optic characterisation of pickup one has also been carried out to test some of the principal elements in realistic conditions similar to the SPS. The outcome of the experiment confirms a correct optical behaviour, but also demonstrates the impossibility of acquiring a single-shot EO signal with the fast detector employed in this thesis. In addition, it should be noticed that the limited bandwidth of the amplifier, which was selected to simply deliver a EO signal, makes impossible the HT detection.

Beam test results of EO pickup at the CERN SPS

6.1 Prototype pickup zero: First electro-optic signal

This section presents the primary tests that culminated in the very first electro-optic detection of a proton beam in December, 2016 [71]. In particular, these first studies were performed with pickup zero; the aim was to observe an optical signal induced by the passing bunch Coulomb field in the form of a modulation in the light intensity through the system.

6.1.1 Beam conditions

The measurements were taken parasitically during the AWAKE experiment run in the SPS, providing an average bunch length of typically $4\sigma = 1.8\,\text{ns}$ and a bunch charge ranging from $1.5 \cdot 10^{11}$ to $3.5 \cdot 10^{11}$ protons [19]. Unfortunately, the detection scheme provided a low Signal-to-Noise Ratio (SNR), so it was necessary to average over the AWAKE cycle (digitising $\sim$600 turns over a total of approximately $\sim$40000 forming the entire cycle) to achieve detection [71]. In other words, single shot measurements were not performed, rather, an average EO signal was recorded during multiple revolutions of an AWAKE bunch within a CERN SPS cycle. Figure 6.1 is an screenshot of the CERN vistar's webpage where the AWAKE cycle is displayed [72].

The CERN web-tool Timber provides the mean bunch length and charge of each signal-related cycle [64]; given these parameters, the Coulomb field time-profile can be
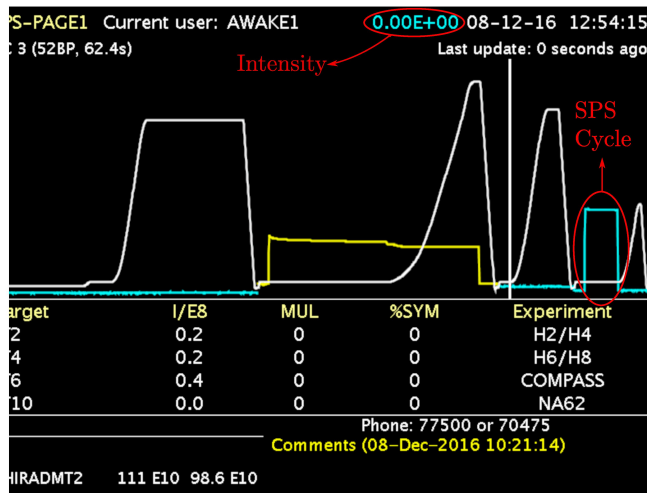
Figure 6.1: SPS control window displayed by the CERN vistar's tool [64].

estimated applying equation 3.5. The whole profile is then reduced by the effect of the LNB dielectric constant ϵ_z, and also the coupling factor $\mu_C(r_0)$ of the pickup determined by the numeric simulations in CST, just as described in equations 4.5 and 4.6. The beam offset information during the AWAKE cycles was not logged during the data-taking so the bunch has been assumed to be on-centre for the calculation ($\mu_C(z_0 = 0)$).

Once the modulating field E_{LNB} is estimated, it becomes one of the input parameters into the analytic simulation to calculate the light phase difference $\Gamma(E_{\mathrm{LNB}})$ (eqn. 2.22), which is in turn introduced into the Jones matrix representation of the crystal M (eqn. 2.18). After that, the polarisation vector E_{opt}^{in} (eqn. 2.21) parallel to the Input Polarisation direction (IP) at a given angle 2θ in the way depicted in Figures 2.5 and 2.15 (rotated θ by the HWP), is applied on M (eqn. 2.21) to obtain the output polarisation vector E_{opt}^{out}. Then, E_{opt}^{out} is multiplied by the analyser representation A, resulting in the final vector E_{trans}^{opt} (eqn. 2.26), whose modulus gives the output light intensity T_{crossed} (eqn. 2.28). Since the Coulomb field is a function of time so it is the output intensity, therefore, the optical modulation follows the field time-profile in this simulation.

In addition, the crystal sensitivity is scaled depending on the natural birefringence, which has been experimentally inferred by considering equation 2.28 with the values obtained from fitting the polarisation scans that are shown accompanying each set of EO signals, to equation 2.47. Finally, the optical signal ΔP_{opt} is also scaled by the actual experimental light power, which means that the realistic transfer function is deduced from the polarisation scan; in particular, the transfer function maximum employed to simulate the signal is equal to the sum of the minimum and maximum power of the polarisation

scan fit. It should be noticed that both polarisation state and maximum power can be different for each set of measurements, and indeed, the maximum power differs from the 1 mW value assumed in the simulations presented in the previous chapter.

According to the scheme presented in Figure 5.15, the next step in the analytical simulation consists in applying the detection chain, that is, the detector sensitivity factor $S_{\mathrm{RF}} = -140 \, \mathrm{V/W}$ (Table 5.3) and the bunch length-dependent effective gain G_e, which is fixed to be 28 dB (Fig. 5.14) for the typical AWAKE bunch length of $4\sigma = 1.8 \, \mathrm{ns}$. The peak value of the analytical signal results from multiplying those two factors but the shape does not account for the limited 210 MHz bandwidth, but has been forced to follow the actual bunch profile. Consequently, the time-structure of the estimated signal is slightly shifted leftwards and narrower so the experimental signal appears delayed and can be compared with the ideal faithful replica of the modulating field-profile. The entire signal simulation process can be followed in the flow diagram 6.2:
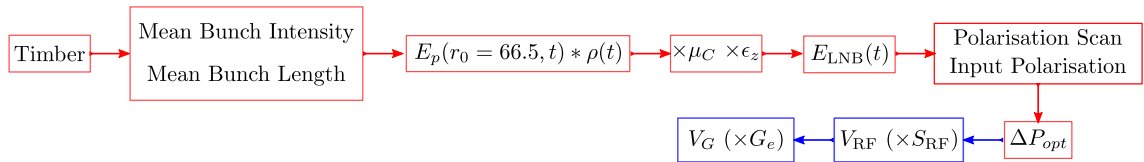
Figure 6.2: Flow diagram of the algorithm to calculate the EO signal estimation.

Figure 6.3 shows the typical appearance of the EO signal in the 12-bit scope display. The yellow line in channel 1 (C1) represents the amplified RF output V_G and Z1 is a zoomed depiction of the same signal; channel 2 (C2) in red shows the detector DC bias level V_{DC} and channel 3 (C3) in blue is the trigger signal obtained from the HT monitor placed downstream about a metre away from the EO pickups (Fig. 1.5).
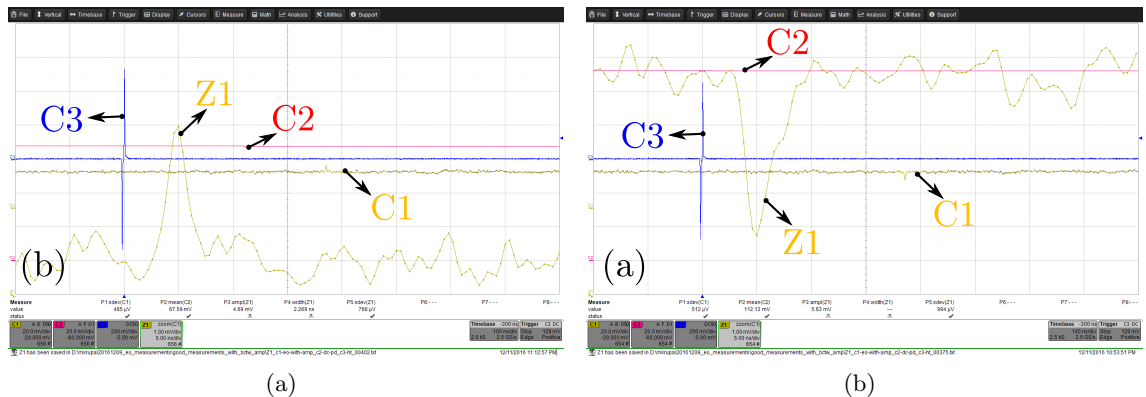
Figure 6.3: Example of the oscilloscope display appearance for a negative (a) and a positive (b) bunch-induced EO signal.

6.1.2 Analyser and HWP position studies for setup A

As a general note, the results presented in the following subsections show the experimental fast electro-optically induced signal V_G depicted as red dots averaged over multiple turns that were recorded by the 12-bit scope, in comparison with the analytical estimation in blue. For every set of measurements, the input polarisation was kept constant by fixing the HWP position, and each signal was obtained at a certain orientation θ_{TD} of the analyser Transmission Direction (TD) (Fig. 2.5 and Fig. 2.15). In addition, two different polarisation scans for each set of signals were recorded by rotating the analyser anticlockwise for setup A, and clockwise for setup B (note the rotation direction is illustrated in Figures
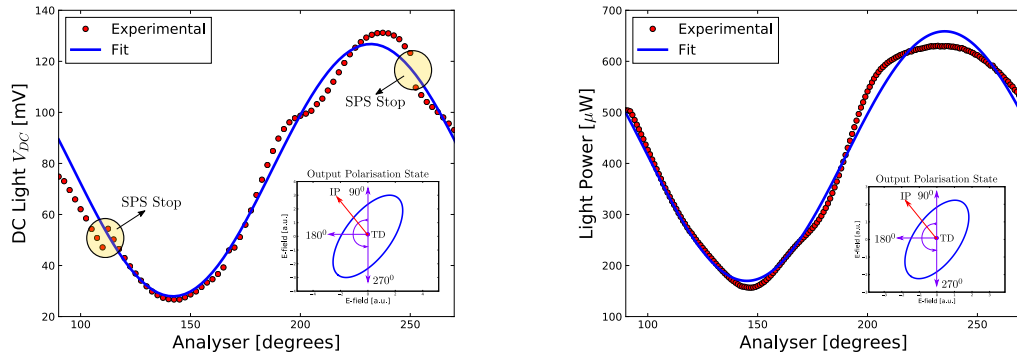
(a) Photodiode DC level scan during acquisition.

(b) Power Meter polarisation scan.
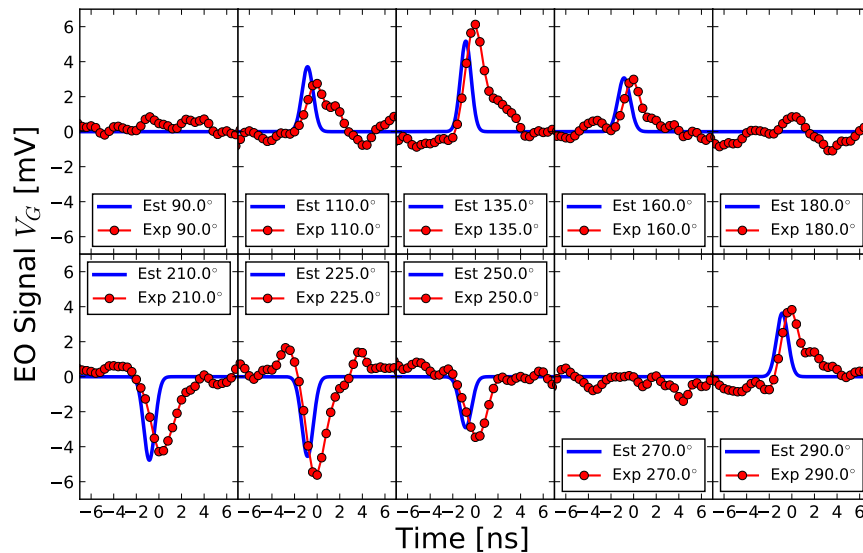
(c) EO Signal acquisition at different relevant analyser positions.

Figure 6.4: Polarisation conditions and EO Signal for pickup zero in setup A for a $-45°$ input linear polarisation. Two discontinuities are registered in the V_{DC} scan caused by a certain birefringence change during long SPS stops.

126

5.6 and 2.15): one of the scans was measured before the data-taking with the power meter (in μW), and also a DC level scan (in mV) was recorded during the acquisition with the fast photodiode. In fact, given the signal at a certain analyser position TD, the DC bias at that exact time can be checked in the DC scan. Furthermore, the scans were fit to equation 2.47, while the projection state is recovered by applying equation 2.48 to the fit curves. Likewise the signals, the readout in the polarisation scans is represented in red points, and the fit appears as a blue continuous line. Both experimental scans provide the output polarisation during each acquisition case determined by the Input linear Polarisation orientation (IP) and the birefringence.

The three figures shown in 6.4 correspond to the pickup type zero placed on the inner side of the CERN SPS ring next to setup A (Fig. 5.1), when the input polarisation direction IP was set at $-45°$ (135°). According to the CST numeric simulations, when using the typical values of the AWAKE cycle, the peak-field in the crystal is in the order of $E_{\mathrm{LNB}} = 750\,\mathrm{V/m}$ (Table 4.4), and the coupling factor μ_C is found to be 0.85 (eqn. 4.5). Those values are applied to the analytical calculations, in combination with the polarisation state and transfer function inferred from the experimental scans. In fact, Figures 6.4(a) and 6.4(b) are the photodiode DC and power meter scans, respectively, also including the polarisation state representation (eqn. 2.47) obtained from the fit curves (eqn. 2.48). By inspection, one can notice that both scans -DC level during the acquisition and the power scan right before- lead to similar polarisation states, which implies that the natural birefringence remained reasonably constant during the measurements. In general, the thermal drift is considered to be negligible during the data-takings, although in this case the DC scan registered two discontinuities due to a very slight change in the birefringence while the machine was stopped (Fig. 6.4(a)). Since the signal sensitivity is dependent on the birefringence, the polarisation output in this case leads to a value of about the 78% of the maximum at circular polarisation.

The EO signals are presented in Figure 6.4(c) for a selection of different relevant positions of the transmission direction (TD), starting from vertical at 90°, and rotating anticlockwise until reaching 290°. When the analyser is parallel to the input polarisation (IP) at 135° ($-45°$), or in the crossed polarisers scenario at 225° (45°), the EO modulation is expected to be maximum; when the analyser position is placed either vertical (90°) or horizontal (180°), the optical modulation will be undetectable. In the intermediate cases the signal decays or enhances accordingly. However, the optical power modulation

(a) Photodiode DC level scan during acquisition.

(b) Power Meter polarisation scan.
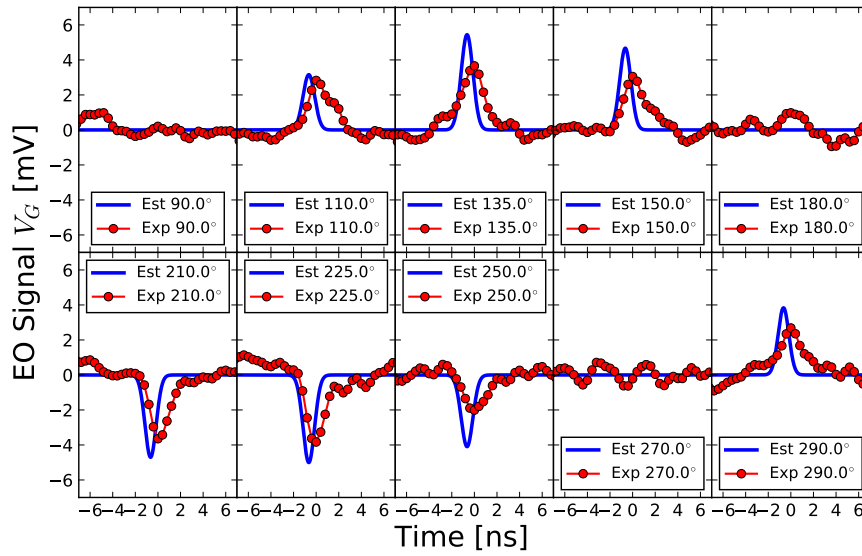
(c) EO Signal acquisition at different relevant analyser positions.

Figure 6.5: Polarisation conditions and EO Signal for pickup zero in setup A for a 120° input linear polarisation.

ΔP_{opt} also scales with the average bunch length and charge of each cycle, thus the peak height decrease does not have to be necessarily symmetrical around the maxima. Since the detector has a negative response, a positive signal indicates that the polarisation projection is decreasing when the beam is passing, and equivalently, the sign swaps from positive to negative when the analyser is transmitting a projection reduced by the passing bunch. For the set of measurements presented in Figure 6.4, the projection along the analyser position parallel to 135° (45°) is squeezed while the perpendicular direction at −45° is elongated.

The initial polarisation for the collection of signals shown in Figure 6.5 is set at $2\theta = 120°$ (90° + 30°). The minor axis of the elliptical polarisation state after the crystal is coincident with the analyser position TD where the power scan curve is minimum.

Thereby, one can observe how the minor and major axes of the elliptical state are rotated $\sim 30°$ towards the vertical, making the output state to become closer to a linear vertically-oriented polarisation. In the same way there is no signal when the analyser is horizontal or vertical. Furthermore, the sensitivity of the signal is reduced as the input polarisation is closer to either the vertical or horizontal direction. Subsequently, one can notice how the signal levels are significantly lower, even though the beam conditions remained similar.

6.1.3 Analyser and HWP position studies for box B

The following results are equivalent, *mutatis mutandis*, to the previous case, but now applied to the pickup zero installed on the outer side of the pipe adjacent to setup B.
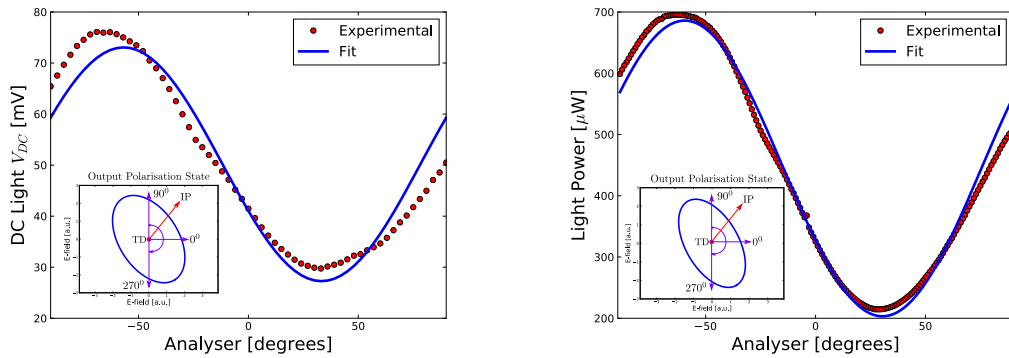
(a) Photodiode DC level scan during acquisition.

(b) Power Meter polarisation scan.
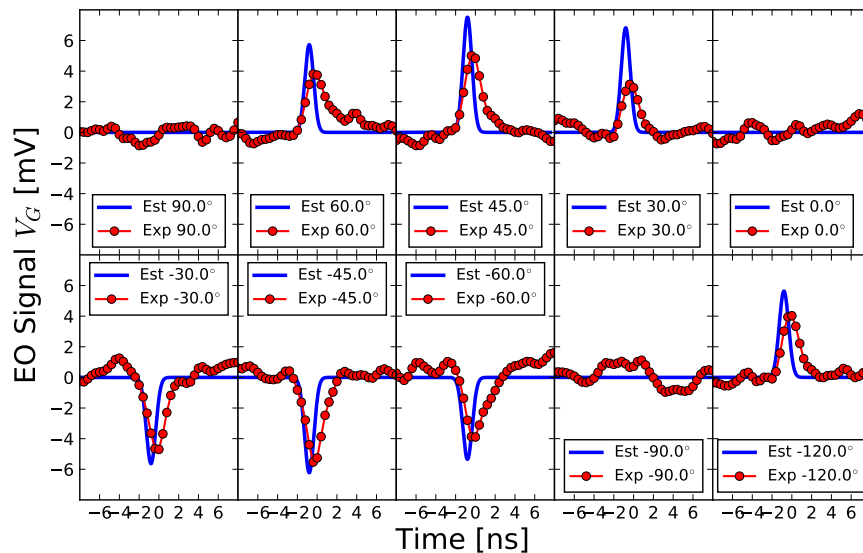
(c) EO Signal acquisition at different relevant analyser positions.

Figure 6.6: Polarisation conditions and EO Signal for pickup zero in setup B for a 45° input linear polarisation.
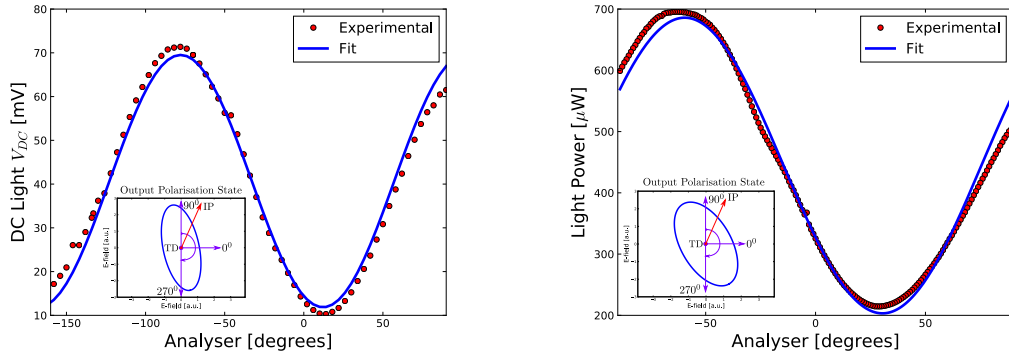
(a) Photodiode DC level scan during acquisition.

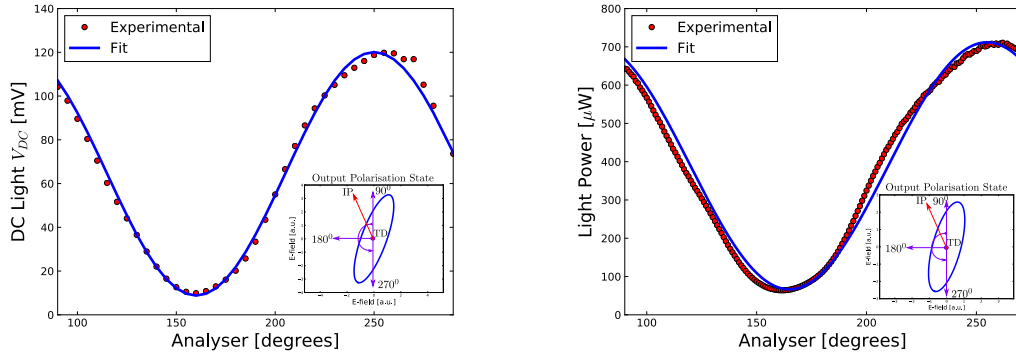
(b) Power Meter polarisation scan.
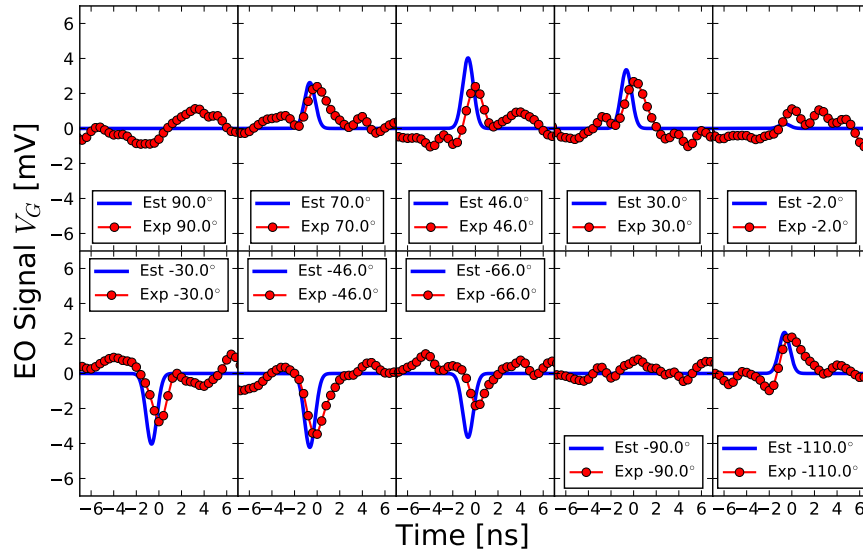
(c) EO Signal acquisition at different relevant analyser positions.

Figure 6.7: Polarisation conditions and EO Signal for pickup zero in setup B for a 67.5° input linear polarisation

Nevertheless, at this time the analyser rotation is clockwise from the vertical direction, and the position of the HWP is such that the input polarisation is a mirror image of the previous case. For instance, Figure 6.6 presents the results when the input linear polarisation into the crystal is set at 45° instead of −45° as in the setup A case.

Again, the EO signal performance variation with the analyser orientation θ_{TD} is consistent with the analytical estimation, reaching a maximum modulation at crossed (135°) or parallel polarisers (225°), and the signal disappears when the analyser is placed either vertical (90°) or horizontal (0°). One can also observe how the signal strength is attenuated approximately as expected when the input polarisation given by 2θ is set at 67.5° (90° − 22.5°) in Figure 6.7, leading to equivalent conclusions to those for setup A.

The output polarisation birefringence is measured by the contrast of the polarisation scan, which is defined as the ratio between the maximum and the minimum of the curve. Let us recall that the flatter the scan, the closer to the circular state. Therefore, if the polarisation drifts towards a very linear position, the contrast in the experimental scan will increase significantly making the sensitivity decay dramatically, according to Figure 2.11. As pointed out previously, the minimum (or maximum) in the polarisation scans correspond to the direction where the minor (or major) axis of the output polarisation is oriented. In theory, if assuming the input polarisation into the crystal to be perfectly linear and correctly oriented with respect to the crystal input face, the major and minor axes of the output polarisation must be always located along $45°$ or $-45°$, as illustrated in Figure 2.6. However, one can observe that in the experimental scans the minimum and maximum appeared shifted. This effect has already been explained in section 2.4.3, and tend to occur when the output polarisation is close to circular. In fact, Table 6.1 shows the measured birefringence defined this time as the phase difference between the vertical and the horizontal components $\phi_z - \phi_x$ obtained from the experimental DC and Power Meter (PM) scans, proving that the output polarisation was indeed above 77% of the circular state ($\phi_z - \phi_x = \pi/2$) for all the cases. Note that when the input polarisation was not set at $45°$ or $-45°$ the sensitivity is not provided as a percentage of the circular state, because it can never be achieved in that scenario.

Table 6.1: Summary of the experimental conditions during the signal data-taking for pickup zero that were used for the analytical simulated estimation.

Figure	6.4	6.5	6.6	6.7
Setup	A	A	B	B
Input Polarisation	135°	120°	45°	67.5°
Dephase ($\phi_z - \phi_x$) [radians] (DC)	0.90	-	1.14	-
Sensitivity [% circular] (DC)	78%	-	91%	-
Dephase ($\phi_z - \phi_x$) [radians] (PM)	0.98	-	1.00	-
Sensitivity [% circular] (PM)	83%	-	84%	-

6.1.4 Electro-optic modulation against light power

In the preceding section, the power through the crystal was kept constant during the data-taking and the analytical simulation was scaled accordingly given the information

provided by the polarisation scans. This section is a parametric study of the signal as a function of the input laser power into the crystal. Figure 6.8 depicts the EO modulation signals along with the Gaussian fits acquired under similar conditions, that is, averaging over a ~ 600 turns of an entire AWAKE cycle. One can observe that there are five different sets of measurements taken at a certain constant value of input light power. Specifically, the value shown for each collection corresponds to the power after the return fibre SM2 sent into the detector, hence, for pickup zero in setup B.
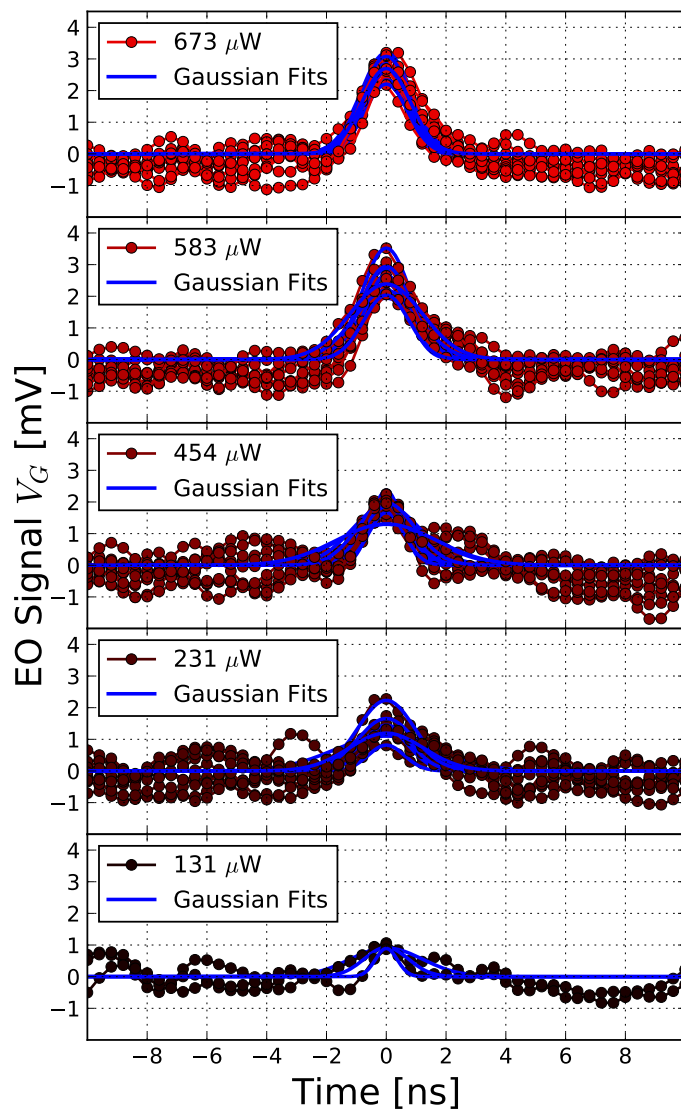
Figure 6.8: Experimental signal at different laser input power values with the baseline substracted.

Although the power was kept constant, each EO measurement is related to a different AWAKE cycle with an specific bunch length and intensity slightly different in every case. The averaging and the different bunch parameters induce a certain dispersion in the signal strength of each collection that is expected to be attenuated by taking several equivalent measurements. In fact, Figure 6.9 shows the mean peak collected from the maxima of the fits against the input light power. The error bars are the standard deviations associated with each set of peak signals except from the $131\,\mu$W case where the signal and error are in the same order so it was forced to be $0.8\,$mV. The transfer function (eqn. 2.28) should scale linearly with the input power as it happens in this case. It should be noticed though, that the regression provides a certain level of signal at non-light scenario, but in the order of the peak-peak noise of the detection system. Also, the unrecorded polarisation state for this set of measurements is assumed to be constant since the whole acquisition was done very rapidly, not allowing any polarisation drift to occur.
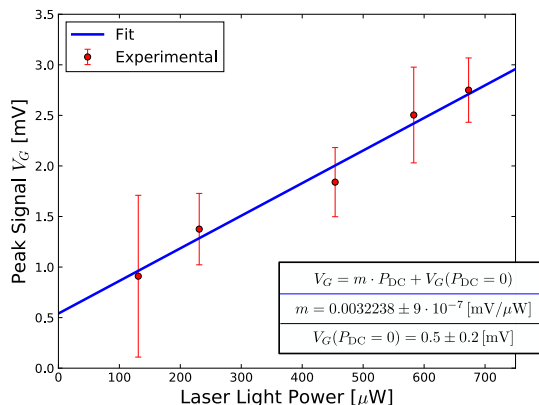
Figure 6.9: Linear relation between the EO peak signal against the input laser power.

This result in conjunction with the previous plots where the coherence of the EO performance under different scenarios was proven, lead to the confirmation of the first EO signal induced by the Coulomb field of a proton bunch. In conclusion, pickup zero successfully measured an EO signal that with development may lead to the realisation of a HT monitor.

Moreover, it is important to stress that the number of turns required to make the signal emerge was ranging from 500 to 600, which corresponds to a noise reduction factor in the order of ~ 25 from a hypothetical single-shot acquisition. This value is indeed in good agreement with the SNR foreseen in the study presented in section 5.3.4 under nominal SPS parameters, which are similar to the AWAKE conditions of this data-taking.

6.2 Prototype pickup one: Position sensitivity studies

6.2.1 Beam conditions

The upgraded pickup one was installed on the vertical plane and also on the inner side of the SPS pipe next to setup A (Fig. 5.1) when the 2016-17 winter shutdown took place. In fact, Figure 6.10 shows the very first signals delivered by the new pickup in May, 2017. In particular, the signal on the left corresponds to a modulation generated by a train of low-intensity bunches in the SPS, and the one on the right is a signal induced by an AWAKE cycle, just comparable to the beam conditions for pickup zero, but already providing a greater modulation in the order of 15 mV. The optical setup and acquisition system remained unmodified during the data-taking of the results presented in this section.

(a) (b)

Figure 6.10: Oscilloscope display of the EO signal (C1 and amplified Z1) with a button reference signal (C3 and amplified Z3) for a bunch of trains (a) and AWAKE beam (b).

In addition, the HWP was rotated to confirm the detection is electro-optically induced, following a similar procedure carried out for pickup zero. Figure 6.11 illustrates how the beam train of Figure 6.10(a) vanishes when the input polarisation at 2θ rotates from 135° to 180°, where no modulation is expected:
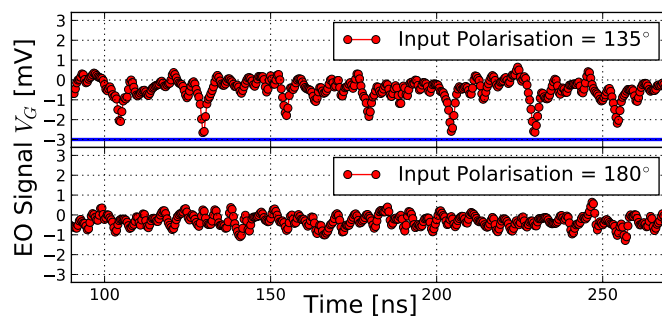
Figure 6.11: The train of signals disappears when the input polarisation is at 180°.

134

6.2.2 Orbit bump measurements

This study aims to measure a correlation between the induced EO modulation and the bunch position. The acquisition of the results shown in this section, took place with the SPS accelerator operating under Machine Development (MD) mode. In contrast to the data-taking for pickup zero, where the acquisition was carried out exploiting parasitically the AWAKE beam, on this occasion the MD2 user provided beam uniquely dedicated to our parametric study. The mean bunch length of the cycles employed for this set of measurements was significantly longer than SPS nominal as it varied between 4.5 ns and 4.7 ns, and the mean intensity range covered from 1.6×10^{11} to 1.95×10^{11} protons per bunch. Once again, the poor single-shot SNR required averaging over the entire cycle in order to achieve detection (SNR > 1). Nevertheless, whereas the experimental signal for pickup zero needed between 500 and 600 turns, the upgraded pickup one reduced this number by a half, that is, to about ~ 300 acquisitions of the MD2 cycle to obtain the EO signal. The MD2 cycle is shown in the SPS vistar's display in Figure 6.12. The modulating field E_{LNB} gradient with the bunch position can be approximated analytically by applying those parameters to equation 4.7, which leads to a estimated value of g_C between $25.6 \, \mathrm{Vm}^{-1} \cdot \mathrm{mm}^{-1}$ and $32.6 \, \mathrm{Vm}^{-1} \cdot \mathrm{mm}^{-1}$.
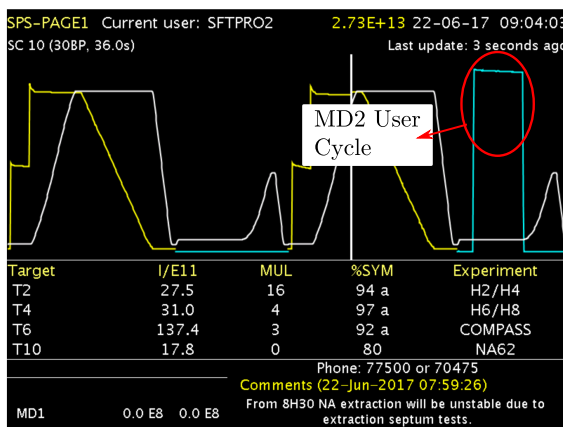
Figure 6.12: SPS vistar's page display indicating the MD2 user.

Figure 6.13(a) depicts the polarisation scan when the experiment was about to take place. One can appreciate that it is a high contrast curve, which means the polarisation is close to linear, thus the sensitivity is far from being in the most optimal point at circular state. To overcome the low sensitivity, the laser power was increased by a factor ~ 3 just before the data-taking so the total power crossing through the crystal scales up to 3.7 mW, though the input power into the detector still remains well below saturation as

the working point corresponds to the analyser position at $45°$ ($\sim 133\ \mu$W). The process of recording the results lasted approximately two hours and following that, the polarisation output scan was measured again and is shown in Figure 6.13(b).

(a) 19.0% of dephase at circular.

(b) 24.3% of dephase at circular.
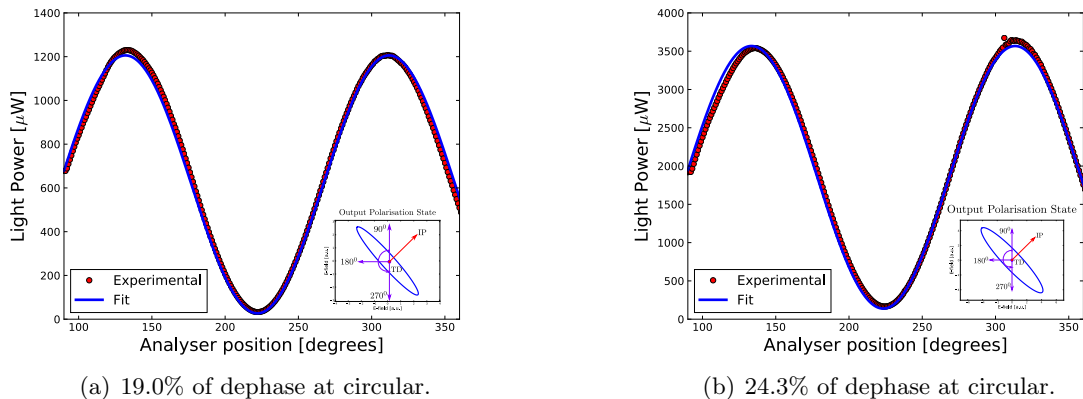
Figure 6.13: Polarisation output scan prior to the power increase by a factor 3 done just before the data-taking (a); after the experiment (b).

The polarisation states presented above report a variation in the sensitivity, since the crystal birefringence was found to be at the 19.0% of the circular polarisation before the start of the experiment, so the phase difference was $\phi_z - \phi_x = \pi/2 \times 19.0\%$, increasing up to 24.3% when it was measured some time after the data acquisition. The goal of minimising the impact of the non-optimal birefringence on the detection by pumping a significant amount of light power may implied a higher power absorption in the crystal, which entailed faster tendency of change in the polarisation state, as a consequence, on this occasion the output polarisation state cannot be assumed to be constant during the measurements. The best method to account for the polarisation drift is tracking how the DC optical power at crossed polarisers varies with time during the experiment period, that is, when the analyser position is oriented at $45°$; as a matter of fact, the chart of Figure 6.14(a) plots the input optical power P_{DC} -that equivalently translates into DC detector output V_{DC} (Fig. 5.15)- over the about two hours that took to complete the experiment. The DC power increment at crossed polarisers implies a reduction in the contrast, so the polarisation is driven towards a circular state and vice-versa. As Figure 2.11 reminds us, the closer to circular state, the pickup performance is more sensitive, however, the sensitivity does not scale in the same proportion as the polarisation contrast does; let us keep the most optimum point at circular polarisation as reference, then one can observe how the sensitivity along the experiment period shown in plot 6.14(b) varies

within a range from 31% to 45%, whereas the the DC level that determines the contrast in 6.14(a) more than doubles, from about $7\,\mathrm{mV}$ up to $16.5\,\mathrm{mV}$:
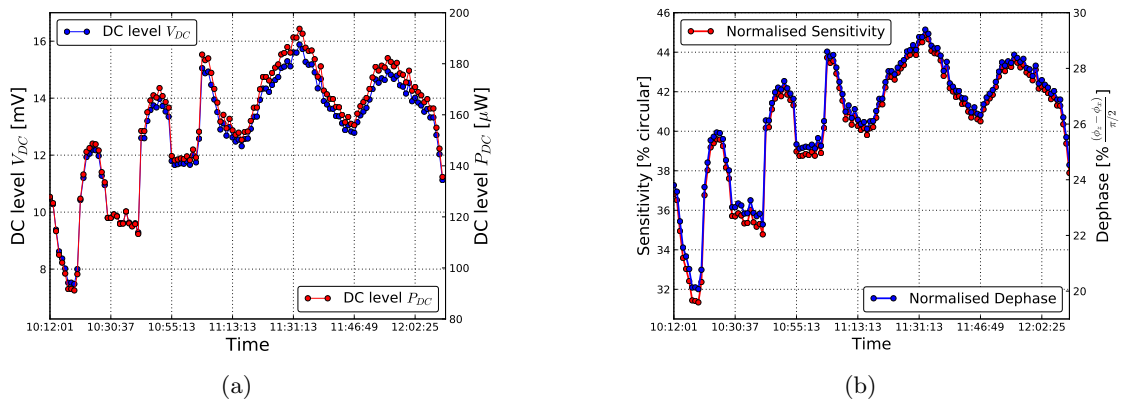
Figure 6.14: Optical P_{DC} and detector DC output V_{DC} drift during the data taking (a) and how that translates into the detection sensitivity as a function of the maximum point at circular polarisation (b).

Those values of sensitivity and power were employed to scale accordingly the subsequent analytical simulations replicating the same procedure described in section 6.1 for pickup zero under AWAKE conditions (Fig. 6.2). Since this machine development session was dedicated *ex professo* to investigate the EO pickup response, some orbit bumps were performed during the data-taking to determine wether the pickup is sensitive at all to the bunch position. For instance, Figure 6.15 depicts five examples of the experimental EO signal compared to the analytical simulation for different nominal bump amplitudes. Negative values of the bump amplitude indicate the proton beam is closer to the EO pickup and alternatively, positive bumps mean is further with the zero-bump amplitude as a reference for the geometrical pipe centre.
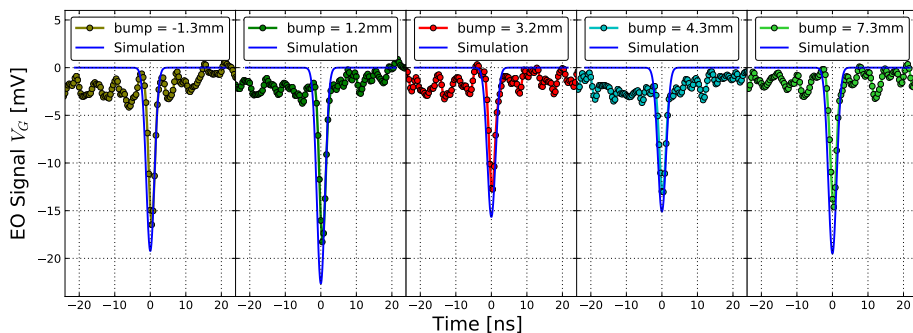
Figure 6.15: Set of experimental EO signals compared to the expected simulation for different orbit bump amplitudes. The offset bump value does not follow the signal amplitude as the beam conditions were different in each measurement.

Let us recall that the mean of the bunch length and also the intensity for each MD2 cycle are parameters that were retrieved from Timber to estimate the signal strength. In addition to those parameters, a system formed by a pair of BPMs with the EO prototype located in between registered the bunch position during the acquisition (Fig. 1.4). As a result, each signal in Figure 6.15 is labeled with the bump amplitude value z_0 obtained from this reference system readout interpolated at the position of the EO prototype. Thereby, along with the MD2 bunch intensity and length, the analytical simulation also used the beam position as an extra input to calculate the optical modulation ΔP_{opt}. As the beam parameters were different in each measurement, the relation between the offset bump and the signal peak is not necessarily linear. Finally, the detection chain was applied: in contrast to the pickup zero results where the amplification was fixed, now the gain in the calculations is case-sensitive. However, since the typical bunch length of the MD2 beam was quite long (~ 4.5 ns), the gain applied in most of the signals is typically the nominal value of the amplifier, 33 dB (Fig. 5.14). It is also important to point out that in this study the input fibre termination attached to the detector was APC/PC, which reduces the sensitivity by an almost factor 2 from $-140\,\mathrm{V/W}$ down to $-82\,\mathrm{V/W}$ (Table 5.3).

The next step in the analysis consists in extending the preceding example (Fig. 6.15) to the rest of measurements taken during the experiment. In order to visualise the match of the simulation to the experimental data over the whole set of results, Figure 6.16 shows a comparison between the normalised maxima of all the experimental signals (Fig. 6.16(a)) and the equivalent result obtained from the analytical simulation (Fig. 6.16(b)). Here, the term 'normalised' refers to the fact that the signal peaks displayed are divided by the total number of protons so the scaling effect of the intensity has been removed. Apart from that, the maxima are presented in absolute value for simplicity.

Every point of the plot shown in Figure 6.16(b) was calculated using the specific conditions that induced the equivalent experimental signal is compared to. In other words, the estimated modulating field E_{LNB} was scaled according to the intensity and mean bunch length of each corresponding cycle, where the latter also determined the effective gain G_e applied to the detector signal. In addition, every signal estimation takes into account the dependence of the coupling factor μ_c with the beam position z_0 (or r_0) through equation 4.5 for pickup one. On top of that, the sensitivity drift that is shown in Figure 6.14(b) has also been introduced in the analytical estimation to recalculate the new dephase and subsequent sensitivity of every point from the recorded DC level contrast.
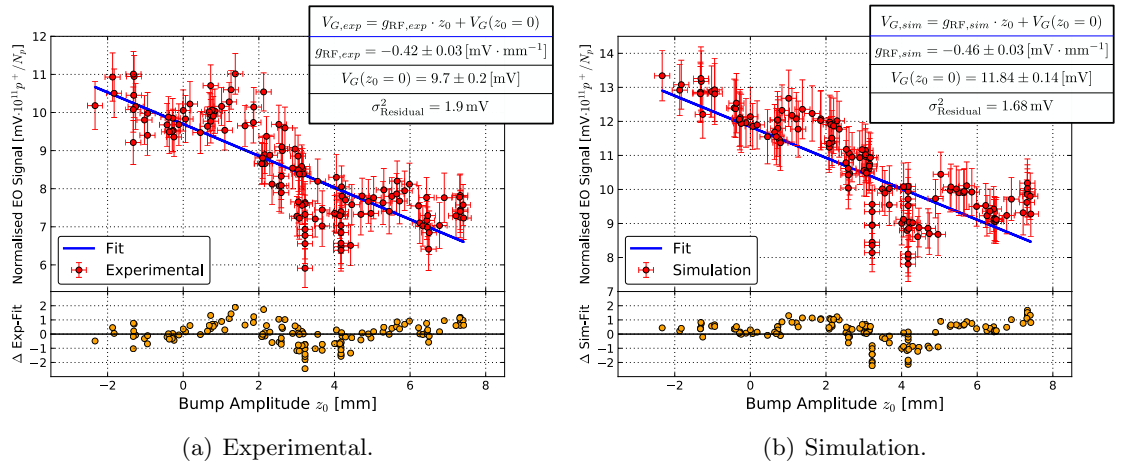
Figure 6.16: Experimental EO modulation peak V_G (a) compared to the expected simulation (b).

The experimental data are fitted by applying the Orthogonal Distance Regression model (ODR) assuming an error in the interpolated bump amplitude of $0.2\,\mathrm{mm}$. The fit leads to an experimental gradient $g_{\mathrm{RF,exp}} = -0.42 \pm 0.03\,\mathrm{mV} \cdot \mathrm{mm}^{-1}$ in the peak signal versus offset position. The gradient signal is caused by a modulating field E_{LNB} that can be roughly estimated by taking the least and most favourable range of beam parameters. This way, the lowest modulating field E_{LNB} is found to be $\sim 855\,\mathrm{V/m}$ when a $4\sigma = 4.7\,\mathrm{ns}$ bunch is formed by 1.6×10^{11} protons, similarly, the upper case occurs for $4\sigma = 4.5\,\mathrm{ns}$ and 1.95×10^{11} protons, leading to a field strength of $\sim 1060\,\mathrm{V/m}$. From this, the detector signal-beam position gradient $g_{\mathrm{RF,C}}$ can also be estimated from the field gradient g_C as follows:

$$g_{\mathrm{RF,C}} \simeq 82\,\mathrm{V/W} \times 10^{33\mathrm{dB}/20} \times \Big((\Delta P_{opt}(E_{\mathrm{LNB}}) - \Delta P_{opt}(E_{\mathrm{LNB}} + g_C)\Big). \qquad (6.1)$$

Let us now recuperate the analytic modulating field gradient approximation g_C procured by equation 4.7, that leads to absolute values ranging from $25.6\,\mathrm{Vm}^{-1} \cdot \mathrm{mm}^{-1}$ up to $32.6\,\mathrm{Vm}^{-1} \cdot \mathrm{mm}^{-1}$ when using the parameters indicated earlier for the best and worst scenarios. Thereby, applying equation 6.1 with the corresponding E_{LNB} and g_C in each case makes the detection signal gradient $g_{\mathrm{RF,C}}$ to vary between $-0.51\,\mathrm{mV} \cdot \mathrm{mm}^{-1}$ and $-0.66\,\mathrm{mV} \cdot \mathrm{mm}^{-1}$, if assuming the sensitivity to be constant by keeping the initial dephase ($24.8\% \times \pi/2$ according to Fig. 6.14(b)). The order of this less precise approach for the signal gradient seems to be comparable to the experimental outcome $g_{\mathrm{RF,exp}} = -0.42 \pm 0.03\,\mathrm{mV} \cdot \mathrm{mm}^{-1}$.

Alternatively, Figure 6.16(b) displays the linear fit obtained from all the points simulated to replicate every EO signal acquired during the experiment, assuming the same uncertainty in the bump offset and propagating the error in S_{RF} (± 3 V/W) to the estimated detector signal. With this approach, $g_{RF,sim} = -0.46 \pm 0.03$ mV·mm^{-1}, which is indeed coherent with the experimental result.

In the light of these results, the simulation generated from the mean parameters of the MD2 cycle have replicated the experimental acquisition precisely. On other note, in contrast to most of pickup zero signals, one can observe that in this case the time structure simulated in Figure 6.15 matches to a high degree the experimental signal time-profile due to lack of any bandwidth limitation when working with long bunches between 4.5 ns and 4.7 ns. Not only that, the order of the absolute signals between 10 mV and 20 mV draws one of the most important conclusions: the magnifying factor $\sim 6.7 - 8.7$ foreseen in section 5.3.4 has been measured.

In addition, the fit residuals have also been plotted on the bottom in Figure 6.16. From a qualitative point of view, one can appreciate how similar the distribution is in both cases for the experimental and simulated data. This pattern is actually induced by the sensitivity drift presented previously in Figure 6.14(b). In order to prove this point, Figure 6.17 shows an equivalent result after removing the DC drift obtained from scaling all the points with respect to the initial sensitivity, that is, the sensitivity of the first measurement (Fig. 6.14(b)), which is applied equally to both the raw data and the simulation; now, the pattern in the residuals vanishes and is replaced by a certain distribution centred along zero.

(a) Experimental.
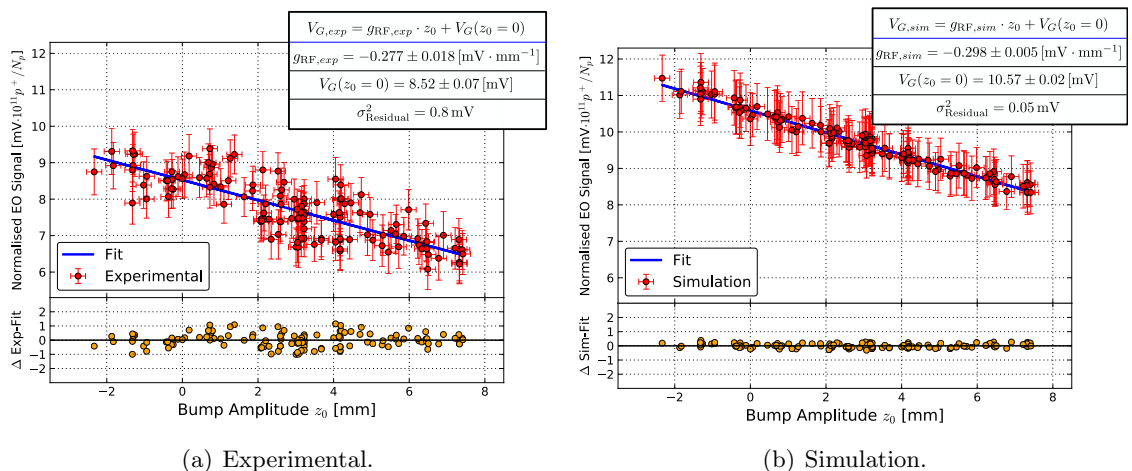
(b) Simulation.

Figure 6.17: Experimental EO modulation peak V_G (a) compared to the expected simulation (b) when the sensitivity drift has been removed.

Finally, Table 6.2 summarises the two pairs of gradients when the DC drift effect is removed and not. In both cases the estimated gradient $g_{\mathrm{RF,sim}}$ is coherent with the observed gradient $g_{\mathrm{RF,exp}}$ within the experimental error. Moreover, the gradients obtained are close to the lower case of the derivative approximation, $g_{\mathrm{RF,C}} = -0.51\,\mathrm{mV} \cdot \mathrm{mm}^{-1}$. From this result, the variation of the polarisation state had an obvious impact on the EO modulation along the data-taking period. In fact, the dispersion in the simulation represented in 6.17(b) is supposed to be uniquely caused, in turn, by the dispersion of the bunch-length itself, ranging between 4.5 ns and 4.7 ns. However, the experimental results exhibit a greater dispersion in general probably due to the uncertainties involved when averaging over an entire cycle in every measure. Although the estimated and experimental signal strengths and widths match well (Fig. 6.15), one can observe that there exist an offset of about 1.5 mV that separates the raw data from the analytical estimation, which implies that a certain scalar factor makes the difference between both set of points. This could be explained due to the fact that the non-optimal APC/PC fibre termination was attached to the photodiode, so the sensitivity S_{RF} and the baseline could have been slightly different in this experiment. Lastly, the gradients shown in Table 6.2 are also comparable to the resolution that would provide a button-like BPM with a geometry similar to pickup one, which is $0.52\,\mathrm{dBmm}^{-1}$ ($\simeq \times 1.06\,\mathrm{mm}^{-1}$) [69] (see appendix D).

Table 6.2: Summary of the experimental conditions during the signal data-taking for pickup zero that were used for the analytical simulated estimation.

Signal-gradient	$g_{\mathrm{RF,exp}}$ [mV·mm^{-1}]	$g_{\mathrm{RF,sim}}$ [mV·mm^{-1}]
Raw data	-0.42 ± 0.03 (0.36 dBmm^{-1})	-0.46 ± 0.03 (0.28 dBmm^{-1})
DC drift removed	-0.277 ± 0.018 (0.33 dBmm^{-1})	-0.298 ± 0.005 (0.24 dBmm^{-1})

6.2.3 Low intensity coast beam measurements

In the preceding section the energy of every bunch per cycle was ramping up and therefore implied a variation on the beam conditions during the acquisition, propagating a certain dispersion over the data as a consequence. In contrast, it is possible to make the SPS to operate in conditions of single bunch circulating at the revolution frequency of the machine, at constant energy. In this scenario, the intensity and bunch length are supposed to be also constant during the acquisition and the effect of these parameters on the signal can be

potentially removed. This operating mode is known by the term *Coast Beam* or *Coasting Beam* and can be very useful to investigate the performance of different instrumentation devices in the accelerator. In particular, the coasting beam conditions were very favourable for measurements of the EO pickup. Since the beam is stored at a constant energy, the pickup output signal can be averaged over a long time, which could potentially lead to a significant noise reduction. Additionally, due to the constant revolution frequency, indirect detection techniques in frequency-domain can also be applied. This section presents a set of measurements in time-domain at low intensity, alongside a synchronous detection of the revolution frequency and the sidebands that correspond to betatron oscillation components.

The first measurements under coast beam conditions were taken in July 2017, and the signal was again produced by the pickup one installed on the inner side of the SPS ring (Fig. 5.1). Figure 6.18(a) illustrates the characteristic vistar display for coast beam, with a fixed level that indicates a single proton bunch is circulating in the machine at constant intensity. Particularly, in this acquisition, the intensity was kept low of about 1.1×10^{10} protons per bunch stored in the SPS at 270 GeV energy for several hours during a so-called coasting beam operation. Unfortunately, the bunch length was not logged properly but the official logbook recorded a variation from $4\sigma = 1.7$ ns to 2 ns, approximately. However, for simplicity, a value $4\sigma = 1.65$ ns will be considered to be constant during the experiment for the analytical estimation. Also, the standard procedure was conducted to determine the sensitivity of the system, so Figure 6.18(b) depicts the polarisation scan at the output face of the LNB sample during the data-taking:
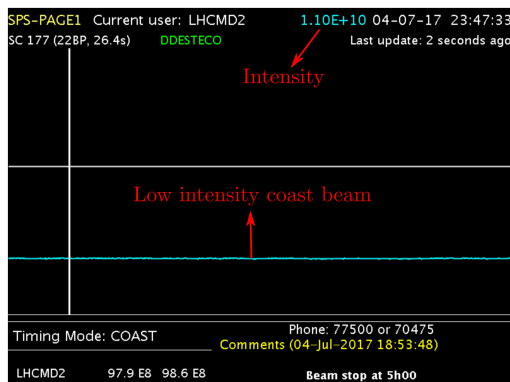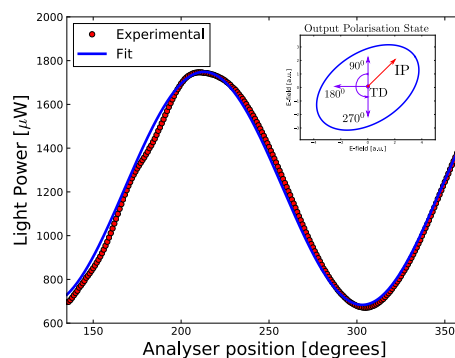
(a)   (b)

Figure 6.18: Screenshot of the SPS vistar's website showing the low intensity coast beam conditions (a) and the polarisation state after the crystal (b).

In principle, the coast beam also allows us to perform orbit bumps at different amplitudes, in fact, a similar parametric investigation on the signal response as a function of the beam offset was carried out for the following amplitudes: -2.2 mm, 0.0 mm, 1.6 mm and 3.0 mm. Once again, the positive sign indicates further away from the EO pickup. The potential goal of repeating the orbit bumps study with coast beam is the removal of any possible influence on the signal caused by the intensity and the bunch length that could be more dominating than the beam position itself. It is also important to point out that the input fibre termination attached to the detector was again APC instead of the correct PC-input, so the detector sensitivity remained being the half of the nominal -82 V/W, and the effective amplifier gain was 29.14 dB for the assumed bunch length of 1.65 ns. With the beam conditions mentioned earlier and taking a crystal birefringence at the 71.15% of the maximum sensitivity at circular (Fig. 6.18(b)), the course of action described in the diagram 6.2 was followed to simulate the estimation taking also into account the beam offset. Figure 6.19 shows a single experimental measurement per bump amplitude in comparison with the signal fit and prediction in blue. The beam circulating at constant frequency allowed a long acquisition averaging over ~ 25000 turns to improve the SNR at maximum:
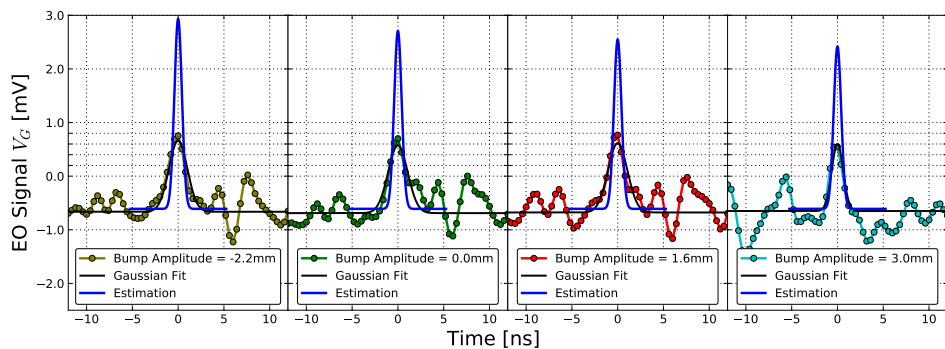
Figure 6.19: Set of experimental EO signals compared to the expected simulation for the low-intensity coast beam conditions.

Although the estimation is apparently correct within the order of magnitude, the degree of discrepancy with the experimental acquisition on this occasion is higher than in the previous results. Furthermore, the SNR of this set of measurements was very poor, insomuch as the beam intensity was only the 9% of the nominal SPS in combination with a specially noisy background during the data-taking, picked mainly from a 160 MHz component produced by the SPS clock in the instrumentation room and other unknown

sources. All these poor conditions might explain the disagreement between the simulation and the experimental signal. On top of that, the coasting beam in the SPS is a non standard operating mode so the BPM system requires special settings to measure orbit. It could have happened that these settings were not applied correctly during the experiment, which would imply that the bump amplitude z_0 recorded might not be correct. In principle, if the beam conditions had remained constant during the experiment, the beam offset would have solely been responsible for the signal scaling and at least, the difference between the experimental and estimated peaks should be constant. However, Figure 6.20 shows how none of those phenomena actually occurs, since the experimental peaks do not behave as expected, scaling up regularly for negative beam offsets. Even assuming the bumps went in correctly, it is likely that the bunch length varied slightly during the signal-acquisition. This could be another fundamental source of error, since the length is fixed constant in the simulation because the real value was not registered.
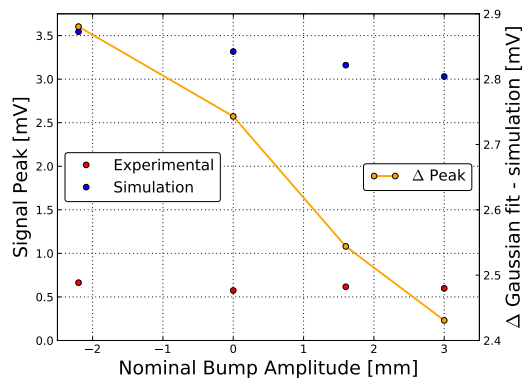
Figure 6.20: Analysis of the experimental and simulated peak signals related to the low intensity coast beam acquisition.

Certainly, it was not possible to exploit the advantages of measuring in time-domain with coast beam on this occasion. Indeed, the low SNR or the bunch-length effect domination made impossible for the system to directly observe the pickup's sensitivity to the transverse beam position. Nevertheless, after the time-domain measurements, the correlation of the betatron amplitude with the signal was indirectly observed while maintaining the same low-intensity coast beam mode, by detecting the narrow-band frequency spectrum around one of the higher harmonics of the SPS revolution frequency. By the time these frequency-domain measurements were carried out, a single bunch of about 2×10^{10} protons was circulating in the ring. The detection system was slightly modified as the amplifier was removed and thus, the photodiode output was directly connected to a spectrum

analyser Rohde Schwarz FSP13. The stored coast beam provided a constant revolution frequency that enabled to apply synchronous detection techniques which leads to further SNR improvement, in other words, the coast beam offers quite favourable conditions for indirect signal detection. In total, the data-acquisition was conducted with a noise floor of -100 dBm, which implies about $2\,\mu$V-RMS across a $50\,\Omega$ load. Figure 6.21 is the frequency spectrum of a pickup one output acquired around the 39.992 MHz component, which is the randomly chosen 922nd harmonic of the fundamental frequency, that is, the SPS revolution at 43.375 kHz.
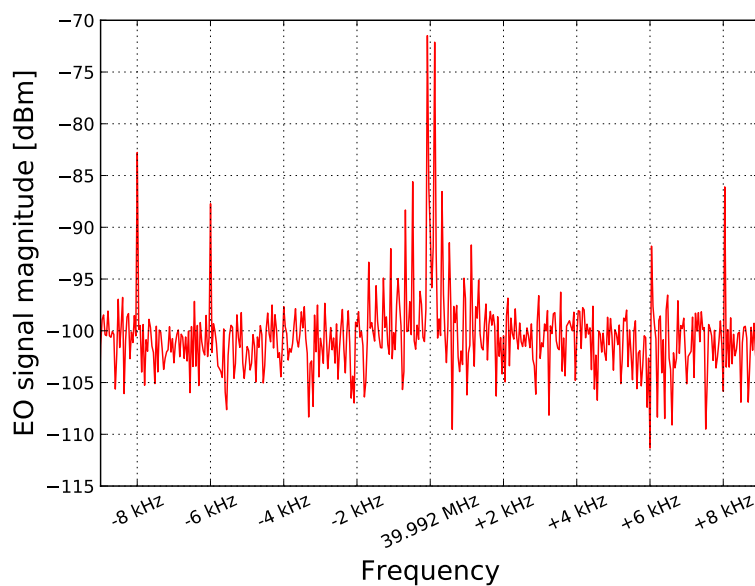
Figure 6.21: Frequency spectrum of the EO pickup signal around the 922nd harmonic of the SPS revolution frequency.

There are two sharp peaks on either side of the 39.992 MHz component at ±6 kHz and ±8 kHz. These frequencies correspond to the following fractions of the SPS revolution frequency (Table 1.1) [71]:

$$\frac{6}{43.375} = 0.138\,, \qquad \frac{8}{43.375} = 0.184\,. \tag{6.2}$$

In comparison, the nominal horizontal and vertical betatron tunes in the SPS are $Q_h = 0.13$ and $Q_v = 0.18$. These tunes represent the sidebands around the n-th revolution frequency harmonic [73]:

$$f_{Q_n} = n \times f_{rev} \pm Q \times f_{rev}\,. \tag{6.3}$$

During the coasting beam operation the SPS tunes drift slightly from their nominal values, then it is fair to conclude that the sidebands around the central peak at 39.992 MHz shown in Figure 6.21 correspond to the vertical and horizontal SPS tunes. Despite the time-domain measurements did not allow us to draw any conclusion on direct position sensitivity, it has been demonstrated by indirect means that pickup one is at least sensitive to the SPS betatron amplitude. This, in turn, reinforces that the EO prototype is sensitive to the transverse beam position.

6.2.4 High-intensity coast beam measurements

The results presented in this section correspond to the second set of measurements taken with coast beam, in August 2017. In this case, the coasting beam conditions were more favourable to repeat a similar bump offset study, insomuch as the intensity was higher around 1.05×10^{11} and remained fairly constant during approximately the hour and half that it took to complete the entire experiment, as can be appreciated in Figure 6.22(a). Furthermore, the persistent noise component at 160 MHz was totally removed on this occasion. Once again, the bunch length was not logged, but is assumed it varied approximately a 25% between approximately 1.7 ns and 2.1 ns, as it happened in the previous case. The number of turns digitised by the oscilloscope was again quite high between ~ 12000 and ~ 20000 thank to the constant revolution frequency, and the output polarisation defined by the polarisation scan shown in 6.22(b) leads to a sensitivity at the 87% of the best case scenario at circular:

(a)

(b)
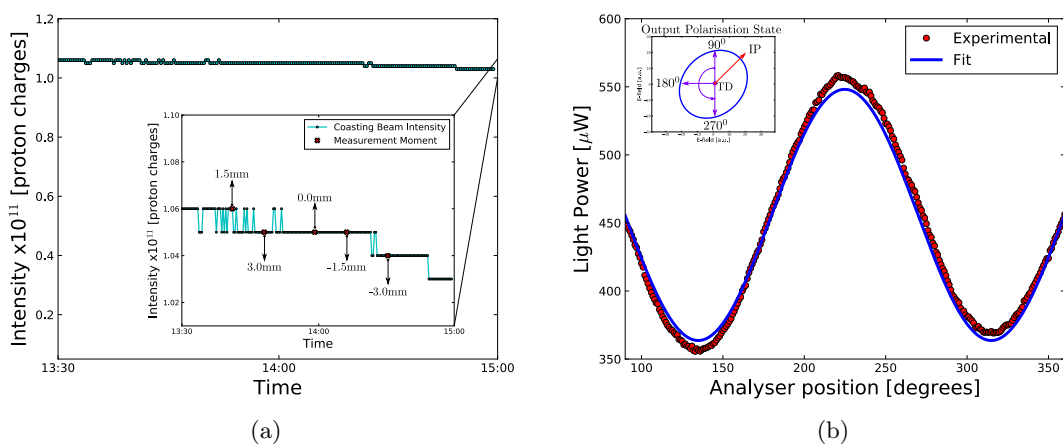
Figure 6.22: Beam intensity drift with time (a) and polarisation scan (b) for the high intensity coast beam measurements.

Although the intensity is higher than in the study case presented in the preceding section, the intensity still remains below the SPS nominal value of 1.15×10^{11} protons per bunch. However, one can appreciate in the figures presented in 6.23 that the EO signal is in the order of 10 mV, which is roughly 7 times above the equivalent signal shown in Figure 6.19 where the modulation strength was about ~ 1.5 mV being slightly less sensitive. This means that the signal scaled approximately linearly with the intensity if we assume exactly the same bunch length in both cases. In fact, since the bunch length for the coast beam during the experiment is unknown, the estimated signal was simulated for two different scenarios: in the first case, the input length put to use in the analytical simulation has been retrieved from a Gaussian fit to the experimental signal (Fig. 6.23(a)); in the second set (Fig. 6.23(b)), the bunch length value in the simulation is forced to be at the 65% with respect to the perfect Gaussian fit, motivated by the hypothesis that the signal does not follow the Coulomb profile due to the bandwidth-limited amplification when the bunch length is in that order. This approach covers a range from ~ 1.8 ns to ~ 3 ns, which is likely to be in a reasonable concordance with the real range of values during the acquisition. Even though the match between the experimental signal and the estimation is better when longer lengths are assumed, still the short bunches are in good agreement with the simulation within a factor 2. Regarding the detection system, the correct PC-fibre termination was connected into the detector and therefore the sensitivity was doubled up to 140 V/W. Also, the effective gain of the amplifier, given the typical bunch-lengths mentioned earlier, varied between 29 dB and 30 dB.

For every bump amplitude, four measurements were taken, and they all are displayed in Figure 6.23. Let us take the Gaussian fits as a reference to study how the bunch length varied during the experiment, then, it is clear that the EO strength is dominated by the bunch length rather than the bump amplitude. Figure 6.22(a) also contains the temporal sequence of every signal labeled with the bump amplitude that was used to scale the simulation accordingly. One can observe that the bunch length enlarges in the same order and thus the experimental signal peak decreases, just as as Figure 6.24(a) demonstrates.

The estimated peak signal for a perfect Gaussian fit and a 65% reduction are also plotted, along wich the difference of each of those cases with respect to the experimental measurement. Once again, the matching between the estimation and the experimental signal declines as the beam approaches to the pickup, as it happened in the previous coast beam experiment. Figure 6.24(a) also indicates that the optical modulation strength is not
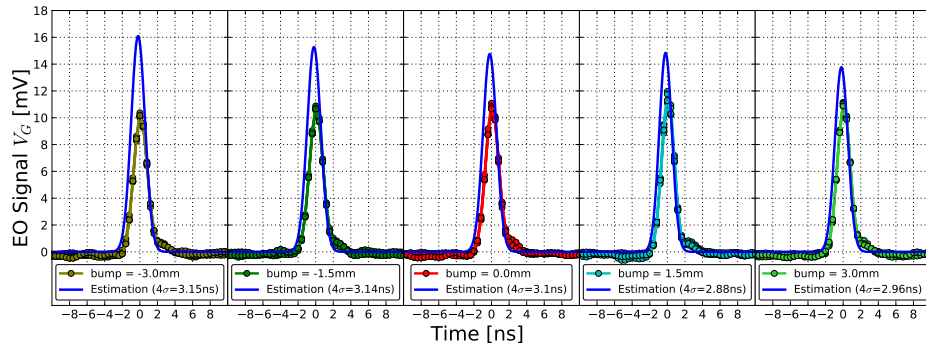
(a) Experimental measurements for each nominal bump amplitude in comparison with the prediction when assuming the bunch length obtained directly from the signal fit.
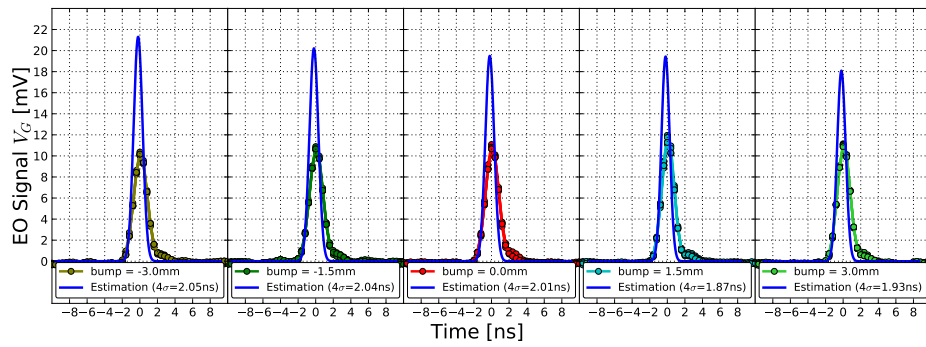
(b) Experimental measurements for each nominal bump amplitude in comparison with the prediction when the bunch length is shortened by 65% with respect the signal fit.

Figure 6.23: EO signal peaks obtained from pickup one under high intensity coasting beam conditions. The labels indicate the supposed bump amplitude case during the data taking.
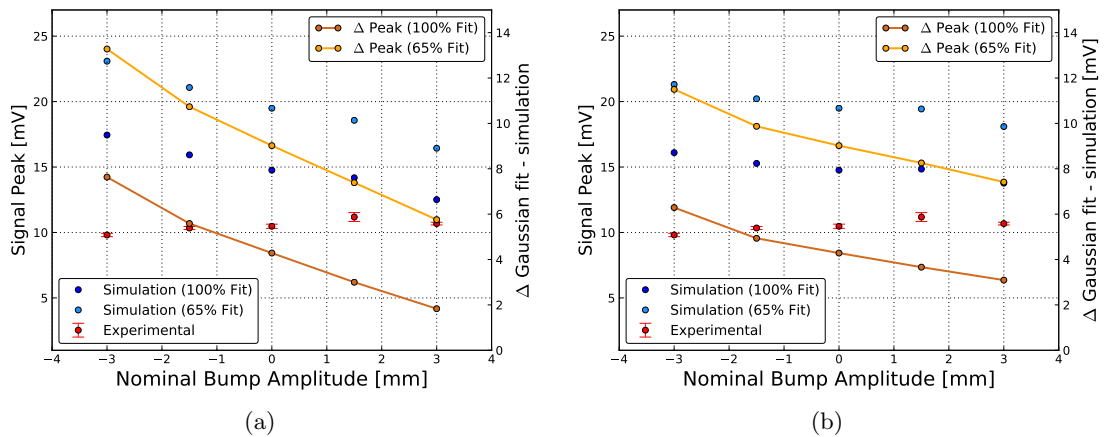
Figure 6.24: (a) Experimental and simulated signal maximum as a function of the bump amplitude, and the difference between them both for the perfect Gaussian fit (100%) and the 65% reduction in bunch length; (b) Peak signal scaled accordingly assuming a constant bunch length of 2.88 ns.

as sensitive to the beam position as the simulation suggests that it should be. In fact, even though Figure 6.24(b) shows a certain coherent behaviour when the simulated signals are scaled in such a way that the effect of the bunch length on the signal amplitude has been removed by making all of them equally long ($4\sigma = 2.88$ ns), still the peak increment occurs within a half milivolt and the signal taken at -3 mm remains inexplicable. In conclusion, the signal peak does not exhibit the kind of gradient that was observed in Figure 6.16(a), for instance.

In the coast beam, the bump amplitude is obtained from the interpolation of the BPM readouts installed downstream and upstream with respect to the prototype position (Fig. 1.4). Nevertheless, the coasting beam in the SPS is a non standard operating mode so the BPM system requires special settings to measure orbit. Given this situation, the diagnostics could have delivered a wrong readout of the bump amplitude. Therefore, if the orbit bump did not go in during the coast beam, or at least not with the amplitude that was read, this could explain why the experimental signal does not seem to be sensitive to the orbit bump in Figures 6.24(b) and 6.20, and also why the gradient is far from the one displayed in Figure 6.16, when the operation mode allowed a more reliable orbit position detection.

6.3 Summary

As a general overview, both prototype versions delivered EO signals in the expected order of magnitude according to the simulations: pickup zero produced an optical modulation of $1 - 3$ mV while the electrode-upgraded version one increased up to about 15 mV. In addition, since the SNR was actually quite poor in both cases, the acquisition required averaging over hundreds of turns, so unfortunately no single-shot measurements were taken. For instance, Table 6.3 is a comparison between two relevant examples chosen as study cases for pickup zero and one under comparable experimental conditions, specifically, when the signals were induced by different SPS cycles, AWAKE and MD2, respectively. In particular, for the pickup zero adjacent to setup B, the EO signal of strength $V_G = 6.3$ mV when the analyser was set at $45°$ in Figure 6.6 required 517 turns to achieve an experimental RMS-SNR of 20.53 dB (factor 10.62), thus, the experimental RMS-SNR extrapolated at single-shot was approximately -6.6 dB (factor 0.46). Similarly, an equivalent analysis for the signal induced by a 4.3 mm orbit bump amplitude depicted in Figure 6.15 is also

displayed. The estimated single-shot RMS-SNR is calculated by dividing the estimated signal peak obtained from the simulation by the RMS experimental noise $\eta_{total} = 11.7$ mV (Table 5.4), which leads to values in good agreement with the experimental counterpart in both cases. In general, the experimental results match fairly well the numeric-analytic simulations in terms of signal strength, and on top of that, the magnitude of the detected SNR draws the same conclusion.

Table 6.3: Comparison of the RMS SNR main conditions between pickup zero and one. The chosen representative case for pickup zero is when the analyser was set at 45° in Fig. 6.6, and equivalently, the signal labeled as 4.3 mm orbit bump amplitude in Fig. 6.15. The experimental single-shot RMS-SNR refers to the extrapolation of the measured RMS-SNR divided by $\sqrt{N}$ where N is the number of turns. Also, the estimated single-shot is resulted from dividing the estimated peak-signal calculated numeric-analytically by the experimental RMS noise $\eta_{total} = 11.7$ mV.

Pickup	Zero	One
Experimental RMS-SNR	20.53 dB (factor 10.62)	20.92 dB (factor 11.12)
Number of turns	517	314
Experimental single-shot RMS-SNR	-6.6 dB (factor 0.46)	-4.0 dB (factor 0.63)
Estimated single-shot RMS-SNR	-5.36 dB (factor 0.54)	2.15 dB (factor 1.28)

Qualitatively, the dependency upon the analyser position has been studied for pickup zero, in order to double check the electro-optic nature of the signal and confirm the experimental outcome as a proof of concept. Beyond those results, several parametric studies to relate the beam position to the signal strength have been conducted with pickup one. In particular, Figure 6.16(a) demonstrates that the EO prototype is sensitive to the beam position with a gradient of value $g_{\mathrm{RF,exp}} = -0.42 \pm 0.03\,\mathrm{mVmm}^{-1}$, or equivalently, $g_{\mathrm{RF,exp}} = 0.36\,\mathrm{dBmm}^{-1}$. Although similar parametric investigations under coast beam were performed, any relevant position-related pattern was observed, on the contrary, the bunch length dependence seemed to be the dominant effect. In fact, this mode did not ensure suitable monitor conditions during the experiments. Moreover, the mismatch between the estimation and the observed EO signal is greater when the bunch length was shorter with coast beam, which could indicate that the approximation derived to calculate the effective gain G_e is not very precise, as for longer bunches where the nominal gain of the amplifier was applied the coincidence is much better. On the plus side however, Figure 6.21 represents an indirect measurement in frequency-domain with coast beam that proves the EO pickup is at least sensitive to the SPS betatron oscillation amplitudes.

Chapter 7

Outlook and conclusions

7.1 Future work

7.1.1 Electro-optic performance upgrade

There are two clear different parts in the EO system that work independently. On one side, the optical setup covers everything from the laser source until the detection system, which constitutes itself the second part of the device. The optical setup is responsible for the electro-optic performance, which is in turn determined by the ratio E_{LNB}/E_π. If the modulating field increases with respect to the EO parameter E_π, then the pickup is more sensitive and vice-versa. With this in mind, the possible ways to improve the signal are the following:

1. **Reducing E_π by increasing the crystal length**: Equation 2.24 reminds us that E_π is inversely proportional to the crystal length, thereby, enlarging the crystal along the modulating y-direction is probably the most obvious way to enhance the signal. However, equation 2.53 in section 2.5 indicates that as the crystal length increases the detection bandwidth decreases, which is an important disadvantage of this strategy. From the introduction, the final system is aiming to a minimum required bandwidth of 6 GHz for Head-Tail detection, thereby, the crystal length should not get any longer than 11.40 mm (Table 2.3), which would reduce E_π a factor ~ 0.8 with respect to pickup one.

2. **Reducing E_π by reducing the wavelength**: The parameter E_π is proportional to the laser wavelength λ. Therefore, a shorter λ leads to a more sensitive pickup.

Nevertheless, the operative shortest wavelength that can be reached when working with LNB corresponds to red light (633 nm), as for shorter wavelengths the photorefractive effect reported in section 2.4.1 emerges and damages the crystal sample. Then, the potential reduction of E_π is limited also to ~ 0.8 with respect 780 nm.

3. **Increasing E_{LNB} by increasing the parameter μ_C**: Future designs of the floating electrode can potentially lead to higher density of Coulomb field lines and the subsequent increase of the coupled modulating field E_{LNB} into the crystal. Later on the extent of improvement of this strategy is described.

4. **Increasing E_{LNB} by reducing the permittivity ϵ_z**: The dielectric constant of LNB makes the image field coupled between the electrodes to drop by a factor $1/\epsilon_z$. Seeking a different EO crystal that could potentially offer a better balance between a lower dielectric constant and high linear EO coefficients can effectively enhance the modulation. If organic crystals are not considered due to their poor resistance to radiation, it is unlikely to obtain a factor any greater than $\sim 3 - 4$.

5. **Increasing E_{LNB} by reducing the pipe radius**: This is indeed an obvious way of increasing the modulating field. The EO-BPM is aiming to be installed at Hi-Lumi LHC where the typical pipe radius is about 30 mm. In that scenario, the field strength increases some factor ~ 2 as the peak field along the $1/r_0$ curve is closer to the pipe-centre (eqn. 3.12). Moreover, the modulating field-gradient μ_C (eqn. 4.7) at 30 mm ($\sim -320\,\text{V} \cdot \text{m}^{-1} \cdot \text{mm}^{-1}$), is at least a factor ~ 3.5 times higher than at 68.5 mm ($\sim -86\,\text{V} \cdot \text{m}^{-1} \cdot \text{mm}^{-1}$) under SPS nominal beam and assuming the same μ_C gradient as pickup one, which is likely to be actually even more propitious. Consequently, the overall effect would impact very positively on the beam offset signal gradient.

6. **Increasing the sensitivity by applying an interferometric configuration**: If, keeping a similar pickup hardware, the system is transformed into an interferometric configuration where the polarisation is vertical through the crystal parallel to the z-direction and combined afterwards, the sensitivity will increase. In particular, by doing so, a factor 1.45 is predicted by equation 2.44.

To sum up in terms of electro-optic performance, Table 5.5 gives a good approach to the order of magnitude of each prototype model. Let us recall that the standard parameters

of simulation have been chosen to be the nominal SPS beam (Table 1.1), with a maximum laser power of 1 mW. In this scenario, pickup models zero and one present, respectively, optical modulations of about $\sim 1.4\,\mu$W and $\sim 11\,\mu$W. Also, since the maximum laser power is 1 mW, the DC power P_{DC} into the detector is 500 μW at circular output polarisation, then, pickup zero can be labeled as a a per-mil effect model ($\Delta P_{opt}/P_{DC} \sim 0.3\%$), and equivalently pickup one is a per-cent effect model ($\Delta P_{opt}/P_{DC} \sim 2.2\%$). In fact, the first analytic simulations presented in Figure 3.11(c) where the factor μ is not applied, already foresaw a typical per-mil effect ($\sim 0.4\%$) for model zero even before the correction introduced by the more detailed numeric-analytic calculations shown in chapter 4.

Let us now propose two possible upgrades of the pickup design on the grounds of the crystal length and an optimisation of the parameter μ_C: the first proposal is the so-called pickup 10-10 because it consists of a 10 mm long crystal embedded in a button with a hypothetical floating electrode design such that the modulating field E_{LNB} increases up to 10 kV/m; the second proposal is named pickup 15-15 as now a 15 mm crystal would be modulated by an 15 kV/m field through another even more optimised electrode design. Figure 7.1 depicts the optical signal assuming the standard simulation conditions with 1 mW maximum laser power at 3 different typical commercial wavelengths, 1550 nm, 780 nm and 633 nm, replicating Figures 5.16(a) and 5.17(a) for the new pickups. One can observe that the electro-optic performance improves as the wavelength gets shorter, though the detector responsivity changes with wavelength too. Also, the reader must bear in mind that is not possible to get any shorter than 633 nm due to the photorefractive effect when using a LNB sample.

(a) pickup 10-10.

(b) Pickup 15-15.
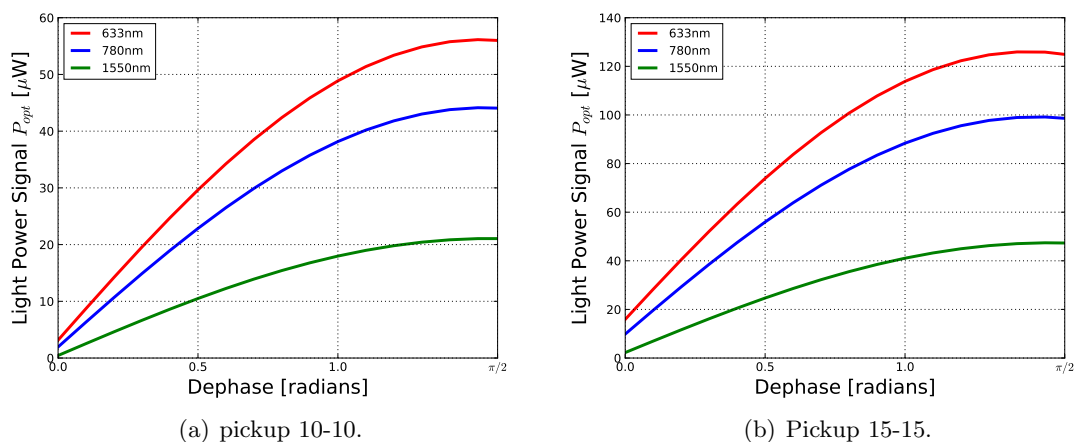
Figure 7.1: Optical signal as a function of the output polarisation for pickups 10-10 (a) and 15-15 (b).

Table 7.1 makes a comparison of the electro-optic performance at 780 nm between the prototype variants zero and one and the hypothetical pickups 10-10 and 15-15 when the crystal birefringence is circular and the maximum optical power is 1 mW. From a percent effect for the prototype, the ratio $\Delta P_{opt}/P_{\mathrm{DC}}$ scales up a significant proportion until almost reaching a per-ten modulation (8.8%) precisely for pickup 10-10, in fact, it would take a value of 11.2% at 633 nm. Additionally, according to equation 2.53, the 10 mm crystal length can achieve ~ 6.8 GHz bandwidth, whereas the 15 mm crystal is limited up to ~ 4.6 GHz, though the optical modulation displayed in Table 7.1 corresponds to a linear response scenario at low modulating frequencies. Interestingly, the almost 9% variation over the transmission curve (Fig. 2.7) shown by 10-10 model is actually comparable to the typical performance of some commercial EO modulators. This implies that once connected to a proper detection system, should be able to produce a good quality EO signal.

Although pickups 10-10 and 15-15 are presented as hypothetical designs, recent preliminary studies on new floating electrode geometries suggest that at least pickup 10-10 is actually possible [74]. Furthermore, as mentioned earlier, this model would actually improve a factor not less than ~ 3.5 if installed in a 30 mm pipe radius at LHC, but further simulations in CST are required to determine the exact extent of improvement. In conclusion, the 10-10 proposal model emerges as a promising candidate capable of producing a significant leap forward in terms of electro-optic performance.

Table 7.1: Summary of the simulated electro-optic performance at 780 nm under nominal SPS beam conditions, where the DC input power into the detector is selected to be 500 μW when the birefringence is circular ($\pi/2$ dephase).

Pickup	L_y [mm]	E_π [kV/m]	E_{LNB} [kV/m]	$\frac{E_{\mathrm{LNB}}}{E_\pi}$ [%]	ΔP_{opt} [μW]	$\frac{\Delta P_{opt}}{P_{\mathrm{DC}}}$ [%]
zero	5	711.3	0.75	0.10	1.66	0.33
one	9	395.2	2.86	0.72	11.4	2.28
10-10	10	355.7	10	2.81	44.1	8.8
15-15	15	237.1	15	6.33	98.7	19.7

In Table 7.1, the magnitude $\Delta P_{opt}/P_{\mathrm{DC}}$ is $0.5 \times \Delta P_{opt}/P_{sat}$, where P_{sat} is the saturation power of the detector that by convention is taken equal to the maximum of the transfer function. For models 10-10 and 15-15, the working point in the transfer function can be taken around the circular polarisation to couple the modulating field along the linear region of the function, making the EO signal shape a replica of the input field. In

this case, it would be possible to keep the working point below the circular state to reduce P_{DC}, and consequently the system noise. However, it should be noticed that the electro-optic performance defined as $\Delta P_{opt}/P_{\mathrm{DC}}$ is limited up to 20%-25%, because beyond that value the signal is no longer linear with the field along the transfer function. While the prototype models are far off from that limit, the optical modulation strength for pickups 10-10 and 15-15 are actually much closer, which indicates that the upgraded versions could potentially produce considerable signals, in the order of the commercial EO modulators.

7.1.2 Acquisition system upgrade

The optical setup, specially the pickup design, is the responsible for the electro-optic performance, which is determined by the ratio E_{LNB}/E_{π}. The detection system works independently and its mission consists in transforming the optical modulation into an electric output to be acquired by, for instance, an oscilloscope in the time-domain or alternatively, a spectrum analyser. Although the preliminary acquisition system employed in the prototype has proven sufficient to achieve the first proton-induced EO signal and also conduct several parametric studies, it is obvious that it requires a profound optimisation due to the very poor Signal-to-Noise Ratio (SNR). In particular, for the system presented in this thesis, the SNR in decibels is defined by the following expression:

$$\mathrm{SNR\ [dB]} = 20 \cdot \log \frac{\Delta P_{opt} \times S_{\mathrm{RF}} \times G_e}{F \times \eta_{\mathrm{RMS}}} = 20 \cdot \log \frac{V_G}{F \times \eta_{\mathrm{RMS}}}\,, \tag{7.1}$$

where the numerator V_G is the product of the optical signal ΔP_{opt} by the photodiode sensitivity S_{RF}, and also the effective gain factor of the amplifier G_e; if $F = 1$ the denominator is simply the RMS noise η_{RMS}, which leads to the RMS-SNR or $\mathrm{SNR_{RMS}}$, and the peak-peak noise is defined as $\eta_{\mathrm{p-p}} = 12 \cdot \eta_{\mathrm{RMS}}$, then $F = 12$ for the peak-peak SNR or $\mathrm{SNR_{p-p}}$. The reader should notice that equation 7.1 only considers the RF signal so this analysis does not take into account the noise related to the DC light power P_{DC}. In fact, if equation 7.1 is applied on the optical modulations tabulated in Table 7.1, the result is the set of SNR values depicted in Table 7.2, which extends the analysis for the prototype variants already shown in Table 5.5 to the new pickups 10-10 and 15-15.

Let us now compare prototype variants zero and one in a similar operational framework when the proton beam was delivered in cycles. The EO signal of pickup zero under AWAKE beam required some $N \simeq 600$ turns to achieve detection, whereas pickup one

Table 7.2: Summary of the detection performance under nominal SPS beam conditions, at $780\,\mathrm{nm}$, where the DC input power into the detector is selected to be $500\,\mu\mathrm{W}$ when the birefringence is circular ($\pi/2$ dephase). The photodiode sensitivity S_{RF} is $140\,\mathrm{V/W}$ and the effective amplifier is $G_e = 26.5\,\mathrm{dB}$ as $4\sigma = 1\,\mathrm{ns}$ the noise employed for the calculation is the experimental value $\eta_{\mathrm{RMS}} = 11.7\,\mathrm{mV}$. Also, $F = 1$ and $F = 12$ for $\mathrm{SNR}_{\mathrm{RMS}}$ and $\mathrm{SNR}_{\mathrm{p-p}}$, respectively.

Pickup	ΔP_{opt} [μW]	V_{RF} [mV]	V_G [mV]	$\mathrm{SNR}_{\mathrm{RMS}}$ [dB]	$\mathrm{SNR}_{\mathrm{p-p}}$ [dB]
zero	1.7	0.2	4.1	-9	-30.6
one	11.4	1.5	32.7	8.9	-12.6
10-10	44.1	6.2	130.0	20.9	-0.7
15-15	98.7	13.8	309	29.7	6.3

under MD2 cycle reported in section 6.2.2 needed fewer turns to get a similar signal quality, in particular about $N \simeq 300$ turns. Since the square root of the number of turns $\sqrt{N}$ is the noise reduction factor, in similar experimental conditions the detection system should improve the SNR a factor ~ 25 and ~ 18 for variants zero and one respectively in order to obtain a single-shot acquisition, although a signal suitable for an operative BPM is even more higher. On top of that, the bandwidth performance is limited by the amplifier that widens the time structure of the signal when the time-profile is shorter than about $\sim 2\,\mathrm{ns}$. That is why the signal width does not match the estimation for pickup zero, as on that occasion the typical AWAKE bunch is shorter than $2\,\mathrm{ns}$, whereas the profile is quite similar for pickup one results under MD2 when the bunch lengths were in the order of $4.5\,\mathrm{ns}$. In fact, the effective gain G_e applied on pickup one signals is just the equivalent-circuit approximation derived in appendix C. This approach could not be sufficiently precise, leading to a certain mismatch with the prediction for short bunches as it occurs in the signals under coast beam conditions.

In the simulation of the upgraded version 10-10 shown in Table 7.2, the optical modulation is a $\sim 9\%$ of the input DC power level, that is transformed into a noteworthy detection signal of $130\,\mathrm{mV}$. However, even though this signal is significant, the associated SNR barely reaches a factor 10 at the final output, thereby, the acquisition system yield does not quite match the improved EO pickup performance. Consequently, the detection hardware must be greatly improved aiming to a good quality and high SNR EO signal that could allow not only single-shot detection, but also beam-position measurements.

There are two straightforward manners to improve the SNR: either the signal is increased or the noise is reduced. On one side the signal can be enhanced directly by pumping more light intensity through the crystal which would imply, from the point of view of the detection, to employ an acquisition element with higher saturation power P_{sat}. The second strategy consists in finding a less noisy detector, which would translate into lower NEP. Normally, the dominant source of noise tends to be shot noise in biased photodiodes, specially when large loads R_L to generate the voltage signals are coupled into them. Additionally, when time response is important, the transimpedance amplifiers also known as operative amplifiers (op-amp) are one of the best choices; in that scenario, the feedback resistor R_F responsible of the amplification gain operate as a signal-generator load ($R_F = R_L$), in our case, $1 \, \text{k}\Omega$. This is the reason why diode materials with low dark currents are preferable, for instance, GaAs is better option than InGaAs since the wider band gap of the former leads to a lower dark current I_0. In general, the noise associated with the photocurrent I_λ of the detector is defined by the following equation [75]:

$$\text{SNR [dB]} = 20 \cdot \log \sqrt{\frac{R_L \, I_\lambda^2}{2 \, e \, (I_\lambda + I_0) \, R_L \, \text{BW} + 4 \, k_B \, T \, \text{BW}}} \, , \qquad (7.2)$$

where e denotes the electron charge, BW the detector bandwidth, and $4 \, k_B \, T \, \text{BW}$ is the thermal noise at a temperature T, with k_B the Boltzmann constant. Ideally, the photocurrent is much higher than the dark current ($I_\lambda \gg I_0$) and also $I_\lambda R_L \gg k_B T/e$, since then $\text{SNR}_{\text{RMS}} \approx I_\lambda/(2 \, e \, \text{BW})$ is only dependent on the BW. However, in our case the signal is weak ($I_\lambda \ll$), and the the feed resistance of the op-amp integrated in the detector is not very large ($R_F = R_L = 1 \, \text{k}\Omega$), as it is designed to deliver high bandwidth signals at $12 \, \text{GHz}$. Given this, for the measurements shown in this thesis, equation 7.2 becomes:

$$\text{SNR [dB]} = 20 \cdot \log \sqrt{\frac{I_\lambda^2 \, R_L}{4 \, k_B \, T \, \text{BW}}} \, . \qquad (7.3)$$

Then, the way to improve the SNR if the photocurrent remains weak is to increase R_L (the EO signal would scale linearly with R_L, whereas the noise with $\sqrt{R_L}$). However, increasing R_L degrades the response time due to RC constant effects. With this in mind, It could be interesting to explore slower detectors with higher resistance loads but still above the lower limit of $6 \, \text{GHz}$, imposed by the head-tail detection requirements (see section 1.2.1).

Let us now focus on Metal-Semiconductor-Metal (MSM) detectors that have been proposed as an interesting alternative due to the very low Noise Equivalent Power (NEP) [76]. For instance, some MSM models present NEP values of $3 \cdot 10^{-15}\,\mathrm{W}/\sqrt{\mathrm{Hz}}$, which is 4 orders of magnitude below the detector used in the prototype ($24 \cdot 10^{-12}\,\mathrm{W}/\sqrt{\mathrm{Hz}}$), though this value is before any amplification [65, 77]. Table 7.3 tabulates the electro-optic performance of all the different pickup options when assuming a noiseless op-amp is connected to a MSM detector (that is, amplifies the detector noise, but does not contribute): the optical modulation scales up a factor 5 due to the new $5\,\mathrm{mW}$ saturation power P_{sat}; the photocurrent I_λ is generated by $0.2\,\mathrm{A/W}$ responsivity at $780\,\mathrm{nm}$, which is transformed by a transimpedance gain of $1\,\mathrm{k\Omega}$ into the detector output V_{RF}:

Table 7.3: Comparison of the overall EO signal performance of the prototype pickups, and the models 10-10 and 15-15 at $780\,\mathrm{nm}$, when considering a MSM detector with $P_{sat} = 5\,\mathrm{mW}$, and $I_0 = 100\,\mathrm{pA}$ at $12\,\mathrm{GHz}$ bandwidth.

Pickup	ΔP_{opt} [μW]	I_λ [μA]	V_{RF} [mV]	$\mathrm{SNR_{RMS}}$	$\mathrm{SNR_{p-p}}$ [dB]
zero	7	1.4	1.4	26.6	14.8
one	55.5	11.1	11.1	34.6	23.8
10-10	220.5	44.1	44.1	40.6	29.8
15-15	492	98.4	98.4	44.0	33.3

The acquisition circuitry should include a lower frequency cutoff to obtain the RF signal V_{RF} separated from the DC baseline. The SNR shown in Table 7.3 is obtained from equation 7.2

In Figure 7.2 the x-axis represents the electro-optic performance and covers mostly the linear response region of the transfer function until $\Delta P_{opt}/P_{\mathrm{DC}}$=25%. It compares graphically the $\mathrm{SNR_{p-p}}$ ($F = 12$) for the prototype acquisition system formed by the New Port detector plus the in-house CERN $27\,\mathrm{dB}$ amplifier (NP) and the hypothetical MSM performance calculated from equations 7.1 and 7.2, respectively, which also correspond to the values displayed in Tables 7.2 and 7.3.

Although it is important to bear in mind that some quite favourable conditions have been assumed in the previous analysis, such as a noiseless op-amp, it is also clear that the MSM detection exhibits a priori much better SNR performance. This is specially true at low power signals, e.g. the MSM SNR is ~ 60 times higher with respect to the prototype acquisition system for pickup zero, whereas for pickup 10-10 is only a factor 10 better. This
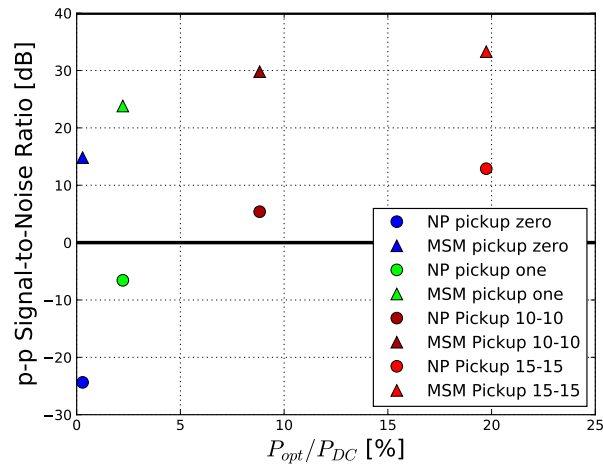
Figure 7.2: SNR$_{\mathrm{p-p}}$ comparison between the prototype acquisition system (NP) and MSM detector.

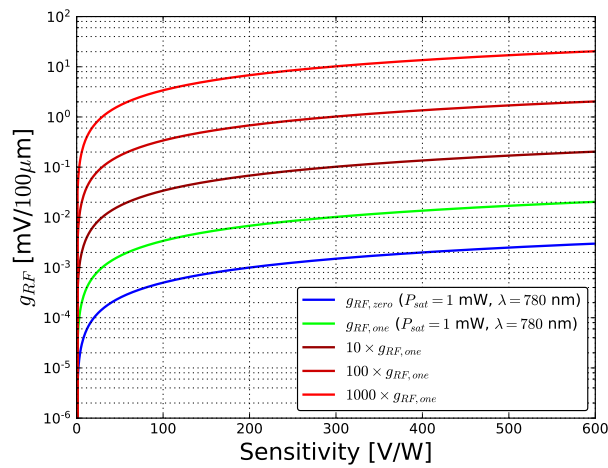Figure 7.3: Isogradient curve for $g_{\mathrm{RF}} = 1\,\mathrm{mV}/100\mu\mathrm{m}$ at $780\,\mathrm{nm}$, with $P_{sat} = 1\,\mathrm{mW}$.
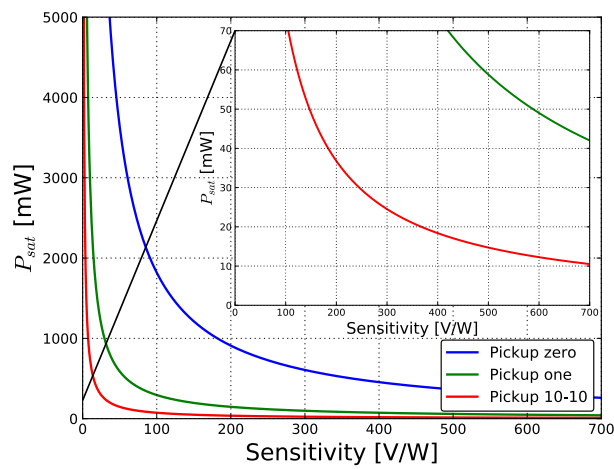
Figure 7.4: Isogradient curves for $g_{\mathrm{RF}} = 1\,\mathrm{mV}/100\,\mu\mathrm{m}$ at $780\,\mathrm{nm}$.

159

type of analysis can be generalised to other options of detection. Furthermore, the actual SNR of different candidates can be checked experimentally in the ring setup presented in section 5.4, by repeating the same kind of study on single-shot acquisition.

Let us now assume a suitable low-noise detector has been found so single-shot measurements are potentially possible. The next step consists in investigating the beam-transverse position resolution of the detector. There exist a simple approach to calculate the detector signal gradient g_{RF} as a function of the estimated optical gradient g_{opt}, the detector saturation power P_{sat} and detector sensitivity denoted as S_{RF}:

$$g_{\mathrm{RF}} = g_{opt} \cdot S_{\mathrm{RF}} \cdot P_{sat} \,. \tag{7.4}$$

For instance, Table 5.6 provides the optical gradient for pickups zero and one. Since the gradient is expected to scale at least in the same proportion as the optical modulation itself, g_{RF} would potentially increase a factor ~ 4 for pickup 10-10 with respect to pickup one, and similarly, a factor ~ 9 for model 15-15. Figure 7.3 shows the gradient g_{RF} in logarithmic scale for pickup zero, one, and also 3 extra hypothetical cases where the gradient is increased 10, 100 and 1000 times above the optical gradient of pickup one. The gradient unit is defined as the detector signal difference in mV per $100\,\mu$m displacement in the transverse offset position of the beam.

Let us take g_{opt} for pickup one, which is $34 \cdot 10^{-3}\,\mu$W/$100\,\mu$m when $P_{sat} = 1\,$mW. Then, applying the sensitivity $S_{\mathrm{RF}} = 140\,$V/W of the prototype detector (but not the amplifier gain), a signal gradient $g_{\mathrm{RF}} = 4.76\,\mu$V·mm^{-1} is obtained. Equivalently, if the optical sensitivity is 4 times grater for the 10-10 model, then an optical gradient $g_{opt}(P_{sat} = 1\,$mW$) = 136 \cdot 10^{-3}\,\mu$W/$100\,\mu$m is obtained. If, for instance, now $P_{sat} = 15\,$mW, then the gradient scales as $g_{opt}(P_{sat} = 15\,$mW$) = 15 \times g_{opt}(P_{sat} = 1\,mW) = 2.04\,\mu$W/$100\,\mu$m. With $S_{\mathrm{RF}} = 500\,$V/W, the detection sensitivity results $g_{\mathrm{RF}} = 1.02\,$mV/$100\,\mu$m, which might be sufficiently good to detect bunch rotation induced by crab cavities in some scenarios [23].

Let us set the goal of future designs to be a gradient of at least $1\,$mV per $100\,\mu$m (Fig. 7.3), then each element will require a certain degree of improvement. For instance, assuming it is possible to achieve a modulating field $E_{\mathrm{LNB}} = 25\%\,E_\pi \simeq 100\,$kV/m (factor $\times 35$ with respect to pickup one) in a $9\,$mm LNB crystal, so the linear region of the transfer curve is covered, and with $S_{\mathrm{RF}} = 300\,$V/W (factor $\times 2$), then the saturation power of the detector should be about $P_{sat} \simeq 3\,$mW (factor $\times 3$) to achieve the objective. The gradient can also be used as a reference to set the expected noise level of the detector enough below

the gradient itself. As a final note on beam transverse position detection, the previous value is obtained assuming a SPS pipe radius, but the reader should keep in mind that at least an extra factor 3.5 is expected for the typical LHC radius.

The optical gradients are fixed independently before applying the detection scheme and are determined by the pickup designs. Therefore, if the signal gradient objective is set to be $g_{\mathrm{RF}} = 1\,\mathrm{mV}/100\,\mu\mathrm{m}$, the result, according to equation 7.4, is an *isogradient* curve like the ones shown in Figure 7.4 for pickups zero, one, and 10-10, when plotting the saturation power P_{sat} against the sensitivity S_{RF}. For the prototype models, the pair $(P_{sat}, S_{\mathrm{RF}})$ required to obtain the final goal is probably hard to achieve, whereas the improved pickup 10-10 present more reasonable values within a range offered by some commercial detectors.

Of course, all the previous analysis on beam position detection is optimised for signal subtraction. That means that if the gradient is $1\,\mathrm{mV}/100\,\mu\mathrm{m}$ in each pickup, the absolute difference Δ between opposite pickup signals on the same plane would be $20\,\mathrm{mV}$ per beam offset millimetre. Nevertheless, the system performance would not need to be this demanding if were instead optimised to the single interferometric configuration (Fig. 3.10(b)). In this case, rather than subtracting two large single-shot signals from opposite pickups, the difference is done optically. Thereby, the acquisition could be just focus on acquiring a single EO signal per plane, which would simplify notably the detection requirements, as for instance, the saturation power will not be exploited in producing a single pickup modulation, but directly in amplifying the signal difference.

Lastly, it is important to draw attention to a particular aspect of Figure 7.1, where the electro-optic performance for the hypothetical designs 10-10 and 15-15 is shown as a function of the crystal birefringence. In these models, the modulating field E_{LNB} is no longer negligible with respect to E_π. As a consequence, the new pickups start being sensitive even when the crystal output polarisation is linear. In fact, if the birefringence were controllable in the upgraded models, it could be potentially possible to set the system in crossed polarises letting almost no light to reach the detector, which translates into no DC signal in the absence of beam. Once the beam is passing, the optical modulation would then occur. This fact would allow us to apply different acquisition techniques, in particular, these very dark conditions make Photo-Multipliers Tubes (PMT) an interesting option to detect passing beams.

7.1.3 Further studies

With the exception of the crystal and the right-angled prisms, most of the optical elements are outside the pickup body in the prototype presented in this thesis. One important task to be developed in future models consists in integrating the optics inside the button in a very compact way. Ideally, the final design would be featured with fibres connectors to easily click-in the delivery and return fibres into the pickup. In principle, all the different elements should be pieced together in vacuum, however, future electrode designs could potentially eliminate the necessity of vacuum integration; this could simplify the installation and also any possible intervention to upgrade or modify the system during the operation year, since breaking the vacuum would not be required.

As mentioned before, the interferometric design is a promising proposal and very interestingly, all the work developed on crystal-vacuum integration, pickup hardware design, and also the calculation of the modulating field, is easily transferable into a novel interferometric configuration. On the down side, the interferometric arrangement requires a high level of mechanical stability.

A random variation of the output polarisation, that is, the crystal birefringence, has been measured and monitored during different experiments, specially for pickup one. For instance, Figure 6.14 acknowledges this effect that had a relevant impact on some results, as reported in section 6.2.2. In this regard, the worst case occurred on one occasion when, even with favourable beam conditions, no signal at all was observed due to the fact that the crystal birefringence at that moment was actually very linear; that no-signal result confirms, in turn, the sensitivity behaviour predicted in Figure 2.11.

Future designs must find solutions to this problem insomuch as each of the EO pickups working as a BPM require to be equally well-sensitive. Only this ensures that the combination of signals on the same plane could lead to a linear-dependent response to the beam transverse position. Not just that, the control of the output polarisation would also determine the input DC light into the acquisition system. Possible ways to overcome this constraint are the addition of remotely controllable elements that act as phase retarders such as Babinet compensators or Pockels cells before the pickup crystal in the optical path, or alternatively, the direct application of voltage on the crystal. Both proposals would bias the birefringence by keeping a fixed position along the transmission curve. Alternatively, a frequency tuneable laser could be an easy solution to modify the relation $E/E_\pi(\lambda)$ in order to offset the output polarisation.

7.2 Conclusions

In this thesis, two different prototype variants of EO-BPM pickups were set up, commissioned and tested in the CERN SPS. In fact, this prototype constitutes the first attempt of producing a BPM pickup based on electro-optic technology for proton beam diagnostics at CERN.

The variant zero represents the basic design where the crystal is directly exposed to the Coulomb field. Although the signal strength was typically weak in the order of few millivolts, it is very important to highlight that the crystal was placed 66.5 mm away from the beam, detecting modulating fields below one kV/m. Most of those results match within less than a factor two with the numeric-analytic simulations carried out to estimate the signal amplitude. Moreover, the linearity of the optical strength with the light intensity and the relation with the analyser position have also been investigated. The observations lead to conclude that the signal is generated by the linear EO mechanism described in chapter 2. Therefore, the studies conducted with pickup zero have successfully delivered a proof of concept and the results reported in this thesis constitute the first ever detection of a passing proton beam by electro-optic means.

Pickup one differs from the original version zero mainly in two features: in the first place, the longer crystal contributes to enhance the signal by 80%, and on top of that, the addition of a floating electrode increases the modulating field itself due to a higher concentration of field lines across the crystal. The synergy of those effects translates into an overall improvement factor of roughly ~ 8. In particular, the upgraded performance has actually been demonstrated to scale correctly to the extent predicted by the simulations. Furthermore, the signals at low bandwidth obtained from pickup one show a non-distorted Gaussian profile, and important HT simulations indicate that this model can potentially detect high order modes 6 and 8 after modifying the top electrode shape, which is causing a resonant artefact.

Above that, Figure 6.16(a) is probably the most important outcome of this thesis as it demonstrates for first time that the EO response is linearly sensitive to the beam transverse position. A cloud of 130 experimental points at different orbit bump amplitudes were piled up to reduce the statistical error. As a result, the sensitivity gradient for the EO prototype was obtained to be $g_{\mathrm{RF,exp}} = -0.42 \pm 0.03\,\mathrm{mV \cdot mm^{-1}}$ directly from the raw data, and $g_{\mathrm{RF,exp}} = -0.277 \pm 0.018\,\mathrm{mV \cdot mm^{-1}}$ once a correction factor was applied to rectify

the DC drift. Those values translate to resolutions of $0.36\,\mathrm{dBmm^{-1}}$ and $0.33\,\mathrm{dBmm^{-1}}$, respectively, which is a factor $\sim 1.04\,\mathrm{mm^{-1}}$. This is comparable to the performance of a BPM button with a similar geometry, $0.52\,\mathrm{dBmm^{-1}}$ ($\simeq \times 1.06\,\mathrm{mm^{-1}}$) [69] (see appendix D). Additionally, even though the experimental conditions during coast beam were not very propitious in terms of noise, bunch intensity and BPM monitoring, this mode allowed the indirect detection of the SPS betatron frequencies.

Nevertheless, all the signals shown in the previous chapter correspond to a single pickup exclusively, without recording the signal from the opposite pickup. It is then important to stress that the prototype has not measured the absolute bunch position on the course of the investigations reported in this thesis. In fact, not even single-shot measurements have been obtained due to the very poor SNR, which is undoubtedly the biggest obstacle at this stage to achieve an operative EO-BPM. Another important drawback of the detection is the limited bandwidth performance of the amplifier that widens the time structure of the signal when the time-profile is shorter than about $\sim 2\,\mathrm{ns}$.

Although the preliminary detection system has proven itself sufficiently good to produce the very first proton-induced signals, it is obvious that also constitutes a big limiting factor, therefore a profound optimisation is required to reduce significantly the noise and also remove the bandwidth restriction.

Besides the low SNR, a persistent drift of the EO crystal birefringence has been observed, whereby, according to the theoretical prediction about signal-birefringence dependency, a random variation of the pickup sensitivity was induced during some experiments. This effect, that was incorporated into the simulations to make the signal scale accordingly, has indeed also been confirmed experimentally. In particular, the measurements verify that the circular output polarisation is the best case scenario in terms of sensitivity and thus near this point should be the preferential working state of the system; on the contrary, the linear polarisation state should be avoided since is non-sensitive when $E_{\mathrm{LNB}} \ll E_{\pi}$, and in general, far from the optimum point. In consideration of this problem, it is essential to find mechanisms such us pockels cells or phase retarders to offset the pickup crystal natural birefringence and fix it at the best position, in order to keep each of them equally well sensitive as a BPM.

Another important milestone is the development *ex professo* of the opto-mechanical design of the entire pickup, specially the button body, that was manufactured in-house and culminated in a successful installation at SPS. As a result, a novel device with a vacuum-

integrated optical arrangement has been tested in the SPS ring environment, proving the system to be reliable in terms of optical alignment and control. Furthermore, the crystals have been kept under radiation conditions during at least a year of operation exhibiting no signal of deterioration, such as an increment of light absorption. In fact, the crystal samples that were removed afterwards seem undamaged. Therefore, the conceptual idea for the button design has been consolidated and more importantly, the acquired know-how is easily transferable to the interferometric configuration and other options. However, future models should advance towards more compact integration of all the optical elements.

Lastly, in the light of all the comparisons between the numeric-analytic simulations and the experimental results, the methodology developed to predict the EO signal has been proved correct and is indeed a powerful tool to optimise future designs. The general procedure is conducted in two steps: the numeric simulations in CST set the relation between the Coulomb field and the modulating field in the crystal, that is in turn rescaled as a function of the bunch length and intensity; subsequently, the extent of the optical modulation is obtained applying the crystal birefringence and length following the Jones calculus framework deployed in the theory chapter. This definitely constitutes one of the main achievements since it allows us to extrapolate the performance of the new pickups to come. On this point, it has been proposed a reliable and promising model candidate named pickup 10-10 that could potentially produce $10\,\mathrm{kV/m}$ modulating field by optimising the electrode design on a $10\,\mathrm{mm}$ LNB crystal.

While models zero and one have shown EO modulations in the order of per-mil and per-cent over the input DC level, the hypothetical pickup 10-10 should be capable to get a significant improvement reaching almost a 10% modulation in similar conditions. This, in combination with an optimised acquisition system with a higher SNR should aim to reach a beam position sensitivity of at least $1\,\mathrm{mV}/100\,\mu\mathrm{m}$, which is expected to be sufficient to detect bunch kicks induced by crab cavities in some scenarios (see 1.2.1). In order to achieve this goal, an overall increase factor no less than 200 with respect to the observed beam-position gradient $g_{\mathrm{RF,exp}}$ for pickup one must be obtained. In any case, the whole upgrade in both modulation and detection can be applied indistinctly on interferometric detection, which would simplify the requirements of the detection system.

In conclusion, the studies on the EO prototype presented in this thesis constitute the proof of concept of this novel technology, and not just that, the results indicate excellent prospects for future research towards the next fully developed EO BPM at CERN.

Derivation of the bunch Coulomb field

Let us take the Fourier transformation F of a function f defined as follows:

$$F(\omega) = \mathrm{FT}[f] = \frac{1}{\sqrt{2\pi}} \int_{-\infty}^{\infty} f(t) e^{-j\omega t} dt \tag{A.1}$$

where t and ω represent the time and the angular frequency respectively, and j the imaginary number. Then, with the normalisation factor $1/\sqrt{2\pi}$ in the forward Fourier definition, the convolution theorem leads to the following relation [78]:

$$\mathrm{FT}[f * g] = \sqrt{2\pi} \cdot \mathrm{FT}[f] \cdot \mathrm{FT}[g] \tag{A.2}$$

If $f = \rho(t)$ is the charge density distribution of the bunch (eqn. 3.4), applying the Fourier transformation introduced in A.1:

$$\mathrm{FT}[\rho(t)] = \frac{1}{\sqrt{2\pi}} e^{-\frac{1}{2}\sigma^2\omega^2} \tag{A.3}$$

where σ is the standard deviation of the gaussian distribution. Similarly, with $g = E_p(r_0, t)$ (eqn. 3.7):

$$\mathrm{FT}[E_p(r_0, t)] = \frac{e_0}{2\sqrt{2}\pi^{3/2}\gamma v^2 \epsilon_0} \mid \omega \mid \mathrm{K}_1(\frac{\omega}{\beta\gamma c} r_0) \tag{A.4}$$

Therefore:

$$E_{\mathrm{bunch}}(r_0, \omega) = \sqrt{2\pi} \cdot \mathrm{FT}[\rho(t)] \cdot \mathrm{FT}[E_p(r_0, t)] = \frac{N_p e_0}{2\sqrt{2}\pi^{3/2}\gamma v^2 \epsilon_0} \mid \omega \mid e^{\frac{1}{2}\sigma^2\omega^2} \mathrm{K}_1(\frac{\omega}{\beta\gamma c} r_0) \tag{A.5}$$

Appendix B

Derivation of the modulating field gradient

The gradient μ_C is defined as the derivative of the modulating field with respect the radial position r_0:

$$
\begin{aligned}
g_C = \frac{dE_{\mathrm{LNB}}(r_0)}{dr_0} &= \frac{d}{dr_0}\Big(E_{\mathrm{bunch}}(r_0) \cdot \frac{\mu_C(r_0)}{\epsilon_z}\Big) = \\
&= \frac{1}{\epsilon_z}\Big(\frac{dE_{\mathrm{bunch}}}{dr_0}\mu_C + E_{\mathrm{bunch}}\frac{\mu_C(r_0)}{dr_0}\Big) = \frac{1}{\epsilon_z}\cdot\Big(-k\mu_C(r_0)\frac{N_p}{\beta\sigma r_0^2} + k\frac{N_p}{\beta\sigma r_0}\frac{d\mu(r_0)}{dr_0}\Big) = \\
&= -k\frac{N_p}{\beta\sigma\epsilon_z}\cdot\Big(\frac{\mu_C(r_0)}{r_0^2} - \frac{1}{r_0}\frac{d\mu(r_0)}{dr_0}\Big)
\end{aligned}
\tag{B.1}
$$

with $\mu_C(r_0) = (r_{\mathrm{centre}} - r_0)\cdot g_C + \mu_0(r_0)$ the focusing factor μ around the position r_0, which takes the value 68.0 mm for model zero, and 68.5 mm for model one:

$$
\frac{dE_{\mathrm{LNB}}(r_0)}{dr_0} = -k\frac{N_p}{\beta\sigma\epsilon_z}\cdot\Big(\frac{\mu_C(r_0)}{r_0^2} + \frac{g_C}{r_0}\Big)
\tag{B.2}
$$

In I.S., the focusing factor gradient g_C is expressed as $g_C[\mathrm{mm}^{-1}]$:

$$
\frac{dE_{\mathrm{LNB}}(r_0)}{dr_0}[\mathrm{I.S.}] = -k\frac{N_p}{\beta\sigma\epsilon_z}\cdot\Big(\frac{\mu_C(r_0)}{r_0^2} + \frac{g_C[\mathrm{mm}^{-1}]\cdot 10^3}{r_0}\Big)
\tag{B.3}
$$

thereby:

$$
g_C = \frac{dE_{\mathrm{LNB}}(r_0)}{dr_0}[\mathrm{Vm}^{-1}\mathrm{mm}^{-1}] = -k\frac{N_p}{\beta\sigma\epsilon_z}\cdot\Big(\frac{\mu_C(r_0)}{r_0^2} + \frac{g_C[\mathrm{mm}^{-1}]\cdot 10^3}{r_0}\Big)\times 10^{-3}
\tag{B.4}
$$

Derivation of the amplifier effective gain

If the amplification is not bandwidth-dependent, the signal should follow the charge density distribution ρ of the proton bunch, that is, $\rho(t) = \frac{N_p}{\sigma\sqrt{2\pi}}e^{-t^2/2\sigma^2}$. Let us now apply a first order low-pass filter $\mathrm{LPF}(\rho)$ with a cutoff frequency f_cutoff to obtain $\rho_\mathrm{filter}(t)$:

$$\rho_\mathrm{filter}(t) = \mathrm{LPF}(\rho(\mathrm{t})) = 2\pi \cdot \Delta\mathrm{t} \cdot \mathrm{f}_\mathrm{cutoff} \cdot \left(\mathrm{e}^{-2\pi\mathrm{f}_\mathrm{cutoff}\mathrm{t}} * \rho(\mathrm{t})\right) \tag{C.1}$$

where Δt is the time resolution of the signal and $f_\mathrm{cutoff} = 210\,\mathrm{MHz}$ in this case. The effective gain G_e is defined as follows:

$$G_e = G + 20\log_{10}\left[\frac{\max(\rho_\mathrm{filter(t)})}{\max(\rho(t))}\right] \tag{C.2}$$

with $G = 33\,\mathrm{dB}$ is the nominal gain of the amplifier.

Appendix D

Estimation of the signal resolution as a traditional button pickup

From the paper on beam position monitoring by Robert E. Shafer [69], the resolution g_B for a button pickup of diameter d_B installed in a pipe with diameter $d = 2b$ can be obtained from the coverage angle α_B as follows:

$$g_B[\text{dB}] = \frac{160}{\log 10} \frac{\sin(\alpha_B/2)}{\alpha_B} \frac{x}{b} \tag{D.1}$$

Our electro-optic pickup type one can be estimated assuming the bottom electrode acts as a traditional button of diameter $d_B \simeq 8\,\text{mm}$ (fig. 4.5) installed in a pipe with diameter $d = 133\,\text{mm}$. In that case, $\alpha_B = \frac{2\pi d_B}{d\pi} = \frac{2\pi 8}{133\pi} = 0.12\,\text{rad}$ (see fig. D.1). The outcome of equation in D.1 when plugging those values for a displacement $x = 1\,\text{mm}$ from the pipe centre is $0.52\,\text{dBmm}^{-1}$.
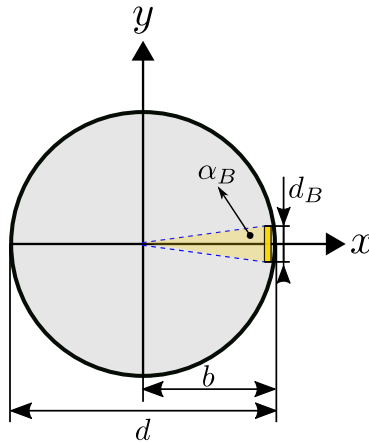

Figure D.1: Diagram illustrating the coverage angle α_B for a traditional button pickup.

Bibliography

[1] L. Evans, P. Bryant, LHC Machine, Journal of Instrumentation 3 (2008) S08001.
`doi:10.1088/1748-0221/3/08/S08001`.
URL `https://doi.org/10.1088/1748-0221/3/08/S08001`

[2] CMS Collaboration, Observation of a new boson at a mass of 125 GeV with the CMS experiment at the LHC, Physics Letters B 716 (2) (2012) 30 – 61.
URL `https://doi.org/10.1016/j.physletb.2012.08.021`

[3] Observation of a new particle in the search for the Standard Model Higgs boson with the ATLAS detector at the LHC, Physics Letters B 716 (1) (2012) 1 – 29.
URL `https://doi.org/10.1016/j.physletb.2012.08.020`

[4] Collaboration CMS, Collaboration LHCb, Observation of the rare decay $B_s^\circ \to \mu^+\mu^-$ from the combined analysis of CMS and LHCb data, Nature 522 (7554) (2015) 68–72.
URL `http://dx.doi.org/10.1038/nature14474`

[5] M. Krammer, The update of the european strategy for particle physics, Physica Scripta 2013 (T158) (2013) 014019.
URL `http://stacks.iop.org/1402-4896/2013/i=T158/a=014019`

[6] C. Lefévre, The CERN accelerator complex (2008).
URL `https://cds.cern.ch/record/1260465`

[7] Y. Miyahara, Luminosity of angled collision of strongly focused beams with different gaussian distributions, Nucl. Instr. Meth. Phys. Res. A 588 (3) (2008) 323 – 329.
URL `https://doi.org/10.1016/j.nima.2007.12.039`

[8] F. J. Sacherer, Transverse bunched-beam instabilities, Tech. Rep. CERN-PS-BR-76-21, CERN, Geneva (1976).
URL https://cds.cern.ch/record/322533

[9] F. J. Sacherer, Transverse bunched beam instabilities - theory (CERN-MPS-INT-BR-74-8) (1974) 5.
URL http://cds.cern.ch/record/322645

[10] J. Gareyte, F. Sacherer, Head-tail type instabilities in the CERN PS and booster, in: Proc. of HEACC, 1974, pp. 341–346.
URL http://inspirehep.net/record/94029/files/HEACC74_362-367.pdf

[11] T. Levens, K. Łasocha, T. Lefévre, Recent developments for instability monitoring at the LHC, in: Proc. of IBIC 2016, Barcelona, Spain, 2016, THAL02. doi:10.18429/JACoW-IBIC2016-THAL02.
URL http://inspirehep.net/record/1639642/files/thal02.pdf

[12] N. Catalan-Lasheras, Fartoukh, S. David, R. Jones, Recent advances in the measurement of chromaticity via head-tail phase shift analysis (CERN-AB-2003-058-BDI) (2003) 4.
URL https://cds.cern.ch/record/624191

[13] R. Steinhagen, T. Lucas, M. Boland, A multiband-instability-monitor for high-frequency intra-bunch beam diagnostics, in: Proc. of IBIC 13, Oxford, UK, 2013, TUBL3.
URL http://accelconf.web.cern.ch/accelconf/ibic2013/papers/tubl3.pdf

[14] G. Apollinari et al., High-Luminosity Large Hadron Collider (HL-LHC): Technical Design Report v. 0.1, Tech. rep., Geneva (2017).
URL https://cds.cern.ch/record/2284929

[15] P. Forck, P. Kowina, D. Liakin, Beam position monitor, in: Presented as the CERN Accelerator School in Dourdan, France, 2009, p. 187.
URL https://cdsweb.cern.ch/record/1071486/files/cern-2009-005.pdf

[16] E. Wilson, E. Wilson, An Introduction to Particle Accelerators, An Introduction to Particle Accelerators, Oxford University Press, 2001.
URL https://books.google.co.uk/books?id=hOseyyFa394C

[17] CERN SPS layout.
URL https://emetral.web.cern.ch/emetral/SPSmachine/spsvcpeb0133.pdf

[18] The Super Proton Synchrotron.
URL http://cds.cern.ch/record/1997188

[19] E. Gschwendtner et al., AWAKE, the advanced proton driven plasma wakefield acceleration experiment at cern, Nuclear Instruments and Methods in Physics Research Section A: Accelerators, Spectrometers, Detectors and Associated Equipment 829 (2016) 76 – 82, 2nd European Advanced Accelerator Concepts Workshop - EAAC 2015.
URL https://doi.org/10.1016/j.nima.2016.02.026

[20] F. Ruggiero, Nominal LHC parameters, in: 7th LTC meeting, CERN, 2003.
URL https://lhc-data-exchange.web.cern.ch/lhc-data-exchange/ruggiero.pdf

[21] G. Apollinari, O. Bröning, L. Rossi, High Luminosity LHC project description, Tech. Rep. CERN-ACC-2014-0321, CERN, Geneva (12 2014).
URL https://cds.cern.ch/record/1974419

[22] E. Shaposhnikova, Current LHC beam parameters in the SPS.
URL https://care-hhh.web.cern.ch/

[23] A. Alekou, F. Antoniou, H. Bartosik, R. Calaga, R. Appleby, G. Arduini, C. Welsch, Y. Papaphilippou, Preparation of the Crab Cavity Test in the SPS: results with beam and simulations, plans, minimum performance requirements, in: HL-LHC Collaboration Meeting, Madrid, Spain, 2017.
URL https://indico.cern.ch/event/647714/contributions/2646109/attachments/1558696/2455284/AAlekou_CIEMAT_Nov17.pdf

[24] D. Oepts, G. Knippels, Direct measurement of the shape of short electron bunches, in: Proc. of FEL, Thomas Jefferson National Accelerator Facility (U.S.), 1998.

[25] I. Wilke, A. M. MacLeod, W. A. Gillespie, G. Berden, G. M. H. Knippels, A. F. G. van der Meer, Single-shot electron-beam bunch length measurements, Phys. Rev. Lett. 88 (2002) 124801. doi:10.1103/PhysRevLett.88.124801.
URL https://link.aps.org/doi/10.1103/PhysRevLett.88.124801

[26] A. Azima, S. Dusterer, H. Schlarb, J. Feldhaus, A. Cavalieri, D. Fritz, K. Sengstock, Jitter measurement by spatial electro-optical sampling at the flash free electron laser, 2006, MOPCH011.
URL http://accelconf.web.cern.ch/AccelConf/e06/papers/mopch011.pdf

[27] G. Berden, S. P. Jamison, A. M. MacLeod, W. A. Gillespie, B. Redlich, A. F. G. van der Meer, Electro-optic technique with improved time resolution for real-time, nondestructive, single-shot measurements of femtosecond electron bunch profiles, Phys. Rev. Lett. 93 (2004) 114802.

[28] S. P. Jamison, G. Berden, P. Phillips, W. Gillespie, A. M. MacLeod, Upconversion of a relativistic coulomb field terahertz pulse to the near infrared 96 (2010) 231114 – 231114.

[29] B. R. Steffen, Electro-optic methods for longitudinal bunch diagnostics at flash, Ph.D. thesis (2007).

[30] R. Pan, Electro-optic diagnostic techniques for the clic linear collider, Ph.D. thesis (2015).

[31] T. Tsang, V. Castillo, R. Larsen, D. M. Lazarus, D. Nikas, C. Ozben, Y. K. Semertzidis, T. Srinivasan-Rao, Electro-optical measurements of picosecond bunch length of a 45 MeV electron beam, Journal of Applied Physics 89 (2001) 4921.

[32] M. A. Brubaker, C. A. Ekdahl, C. P. Yakymyshyn, Electro-optic beam position and pulsed power monitors for the second axis of darht, in: Proceedings of the 2001 Particle Accelerator Conference (Cat. No.01CH37268), Vol. 1, 2001, pp. 534–538 vol.1.

[33] Y. Okayasu et al., The first electron bunch measurement by means of dast organic eo crystals, in: Proc. of IBIC, 2012, MOCC03.
URL http://accelconf.web.cern.ch/AccelConf/IBIC2012/papers/mocc03.pdf

[34] J. Doherty, R. Steinhagen, The electro-optic beam position monitor, Tech. rep., CERN, summer Student internship report (2013).

[35] A. Angelovski, A. Penirschke, R. Jakob, Time domain pickup signal characterisation for low charge arrival-time measurements at flash, in: Proc. of IBIC, 2014, MOPD25.
URL http://accelconf.web.cern.ch/AccelConf/IBIC2014/papers/mopd25.pdf

[36] A. Angelovski, A. Kuhl, M. Hansli, A. Penirschke, S. M. Schnepp, M. Bousonville, H. Schlarb, M. Kristin Bock, T. Weiland, R. Jakoby, High bandwidth pickup design for bunch arrival-time monitors forfree-electron laser, Physical Review Special Topics - Accelerators and Beams 15 (2012) 112803.
URL `https://journals.aps.org/prab/pdf/10.1103/PhysRevSTAB.15.112803`

[37] A. Angelovski, M. Kuntzsch, M. Kristin Czwalinna, A. Penirschke, M. Hansli, C. Sydlo, V. Arsov, S. Hunziker, H. Schlarb, M. Gensch, V. Schlott, T. Weiland, R. Jakoby, Evaluation of the cone-shaped pickup performance for low charge sub-10 fs arrival-time measurements at free electron laser facilities, Physical Review Special Topics - Accelerators and Beams 18 (2015) 012801.
URL `https://journals.aps.org/prab/pdf/10.1103/PhysRevSTAB.18.012801`

[38] R. W. Boyd., Nonlinear Optics, Academic Press, 3rd edition, 2008, Ch. 2.

[39] A. Yariv, P. Yeh, Optical waves in crystals, Willey-interscience, 2003.

[40] R.S.Weis, T.K.Gaylord, Lithium niobate: Summary of physical properties and crystal structure, Applied Physics A 37 (1985) 191–203.

[41] M. Luennemann, U. Hartwig, K. Buse, Electrooptic properties of lithium niobate crystals for extremely high external electric fields, Applied Physics B 76 (2003) 403–406.

[42] A. M., J. Salvestrini, M. Fontana, M. Aillerie, Frequency and wavelength dependences of electro-optic coefficients in inorganic crystals, Applied Physics B 6 (7) (2003) 765–769. `doi:10.1007/s00340-003-1196-5`.
URL `https://doi.org/10.1007/s00340-003-1196-5`

[43] M. Weber, Handbook of Optical Materials, CRC Press, 2003.

[44] A. A. Savchenkov, A. B. Matsko, D. Strekalov, V. S. Ilchenko, L. Maleki, Enhancement of photorefraction in whispering gallery mode resonators, Phys. Rev. B 74 (2006) 245119. `doi:10.1103/PhysRevB.74.245119`.
URL `https://link.aps.org/doi/10.1103/PhysRevB.74.245119`

[45] Y. Yang, D. Psaltis, M. Luennemann, D. Berben, U. Hartwig, K. Buse, Photorefractive properties of lithium niobate crystals doped with manganese, J. Opt. Soc. Am.

B 20 (7) (2003) 1491–1502. `doi:10.1364/JOSAB.20.001491`.
URL `http://josab.osa.org/abstract.cfm?URI=josab-20-7-1491`

[46] D. E. Zelmon, D. L. Small, D. Jundt, Infrared corrected Sellmeier coefficients for congruently grown lithium niobate and 5 mol.% magnesium oxide-doped lithium niobate, J. Opt. Soc. Am. B 14 (12) (1997) 3319–3322. `doi:10.1364/JOSAB.14.003319`.
URL `http://josab.osa.org/abstract.cfm?URI=josab-14-12-3319`

[47] J. D. Jackson, Classical Electrodynamics, John Wiley and sons, Inc., 3rd edition, 1999, Ch. 11.

[48] A. Arteche, A. Bosco, N. Chritin, D. Draskovic, S. Gibson, T. Lefévre, T. Levens, Development of a prototype electro-optic beam position monitor at the CERN SPS, in: Proc. of IBIC, 2016, WEPG09. `doi:10.18429/JACoW-IBIC2016-WEPG09`.
URL `http://inspirehep.net/record/1640128/files/wepg09.pdf`

[49] S. Gibson, A. Arteche, G. Boorman, A. Bosco, P.-Y. Darmedru, T. Lefévre, T. Levens, High frequency electro-optic beam position monitors for intra-bunch diagnostics at the LHC, in: Proc. of IBIC, 2015, WEDLA02. `doi:10.18429/JACoW-IBIC2015-WEDLA02`.
URL `http://inspirehep.net/record/1480738/files/wedla02.pdf`

[50] P. Y. Darmedru, Conception mécanique d´un instrument de mesure de position d´un faisceau de particules, Tech. rep., CERN, CERN EN report, Groupe 2A04 (2015).

[51] A. Demougeot, High frequency electro-optic BPM, Tech. rep., CERN, 1554546 v.1.
URL `https://edms.cern.ch/document/1554546/1`

[52] A. Demougeot, High frequency electro-optic BPM type b, Tech. rep., CERN, 1752924 v.1.
URL `https://edms.cern.ch/document/1752924/1`

[53] G. Bregliozzi, Vacuum acceptance tests for particle accelerator equipment, in: Presentation contribution at CERN Accelerator School (CAS), 2017.

[54] A. Demougeot, High frequency electro-optic BPM - instrument assembly, Tech. rep., CERN, SPSBPMEA0003.
URL `<https://edms.cern.ch/document/1551069/0>`

[55] A. Demougeot, High frequency electro-optic BPM - instrument assembly - type b, Tech. rep., CERN, SPSBPMEB0002.
URL `https://edms.cern.ch/document/1752806/0`

[56] A. Demougeot, High frequency electro-optic BPM - crystal / mirror support assy., Tech. rep., CERN, 1554407 v.0.
URL `https://edms.cern.ch/document/1554407/0`

[57] A. Demougeot, High frequency electro-optic BPM / mirror support assy., Tech. rep., CERN, 1752807 v.0.
URL `https://edms.cern.ch/document/1752807/0`

[58] Computer Simulation Technology, `http://www.cst.com`.

[59] A. Mecozzi, Theory of polarization mode dispersion with linear birefringence, Opt. Lett. 33 (12) (2008) 1315–1317. `doi:10.1364/OL.33.001315`.
URL `http://ol.osa.org/abstract.cfm?URI=ol-33-12-1315`

[60] R. Paschotta, article on 'Polarization Mode Dispersion' in the Encyclopedia of Laser Physics and Technology, Wiley-VCH, accessed on 15-01-2018.
URL `https://www.rp-photonics.com/polarization_mode_dispersion.html`

[61] A. A. Savchenkov, A. B. Matsko, D. Strekalov, V. S. Ilchenko, L. Maleki, Enhancement of photorefraction in whispering gallery mode resonators, Phys. Rev. B 74 (2006) 245119. `doi:10.1103/PhysRevB.74.245119`.
URL `https://link.aps.org/doi/10.1103/PhysRevB.74.245119`

[62] R. Paschotta, article on 'Bandwidth' in the Encyclopedia of Laser Physics and Technology, Wiley-VCH, accessed on 15-01-2018.
URL `https://www.rp-photonics.com/bandwidth.html`

[63] G. D. Domenico, S. Schilt, P. Thomann, Simple approach to the relation between laser frequency noise and laser line shape, Appl. Opt. 49 (25) (2010) 4801–4807. `doi:10.1364/AO.49.004801`.
URL `http://ao.osa.org/abstract.cfm?URI=ao-49-25-4801`

[64] CERN, Timber tool, `<https://cern.ch/timber.html>`.

[65] New Focus, 12 GHz Amplified Photoreceivers, User's guide, model 1544-A.

[66] Internal communication from Newport.

[67] Data obtained from M. Krupa (CERN BE/BI) by internal communication.

[68] R. Mancini, Op Amps For Everyone, Texas Instruments, Ch. 10: Op Amp Noise Theory and Applications.

[69] R. E. Shafer, Beam position monitoring, AIP Conference Proceedings 212 (1) (1990) 26–58. `doi:10.1063/1.39710`.
URL `https://aip.scitation.org/doi/abs/10.1063/1.39710`

[70] M. Krupa, Application of Avalanche Generators in Laboratory Measurements, CERN, internal report.

[71] A. Arteche, S. E. Bashforth, G. Boorman, A. Bosco, S. M. Gibson, N. Chritin, M. Krupa, T. Lefévre, T. Levens, First beam tests at the CERN SPS of an electro-optic beam position monitor for the HL-LHC, in: Proc. of IBIC, 2017, TUPCF23.

[72] CERN vistar website, `https://op-webtools.web.cern.ch`.

[73] M. Gasior, R. Jones, The principle and first results of betatron tune measurement by direct diode detection, Tech. rep., CERN (2005).

[74] A. Arteche, Electro-optic BPM project review: EO-simulations and tests on SPS, presentation (Internal presentation report).
URL `https://indico.cern.ch/event/669811/`

[75] R. S. Quimby, Photonics and Lasers: An Introduction, John Wiley & Sons, Inc., 2006, Ch. 14.

[76] R. Steinhagen, M. Boland, T. Lucas, R. Rassool, T. Mitsuhashi, Application of metal-semiconductor-metal (MSM) photodetectors for transverse and longitudinal intra-bunch beam diagnostics, in: Proc. of IBIC, 2013, MOP20.
URL `http://accelconf.web.cern.ch/AccelConf/ibic2013/papers/mopc20.pdf`

[77] Hamamatsu, Ultrafast MSM photodetectors, G4176-01.

[78] T. Bultz, Fourier transformation for pedestrians, 2nd Edition, Sprinter, Ch. 2.